Studies on Biochemical and Molecular Aspects of Theranostic Redox Modulatory Nanomaterials in Preclinical Disease Model

THESIS

SUBMITTED FOR THE DEGREE OF

DOCTOR OF PHILOSOPHY (SCIENCE)

IN BIOCHEMISTRY

BY

SUSMITA MONDAL

DEPARTMENT OF BIOCHEMISTRY

UNIVERSITY OF CALCUTTA

2023

To my family and my supervisor

Acknowledgement:

The successful completion of my Ph.D. and writing this dissertation has been like a roller coaster ride. Through out this wonderful and most happening journey of my life I was encourgaed, spported and tolarated by a number of outstading people. These five years was an opportunaty of learning at each and every moment. Also in these years I got an excellent chance to become a better and independent version of myself. At the end of this journey I would like to acknowledge all those people who were with me.

Firstly, I convey my gratitude to my supervisor, Prof. S. K. Pal for his unconditional support. All those scientific discussion and his brilliant ideas has helped me to become a potent researcher. His energy and enthusiasm about the work has always served as a source of motivation even in the darkest phase of life. His strong work ethics and hardworking nature has influenced me to keep going on. Not only in the field of research, in my personal life also, his influence is remarkable. His fatherly affection saved me from many internal and external turmoil of my life. During these five years, there were innumerable occasions where I could not believe in myself but he never lost his trust on me. He always protected me from every storm. Thank you very much sir for being with me in this uphill journey and inspiring me to believe that "sky is the limit".

I am specially grateful to you Dr. Aniruddha Adhikari for his support. Without your support the journey to success was not possible.

I am also thankful to you, Soumendra Da (Dr. Soumendra Darbar). You are the person who though me the minute details of the animal studies and supported me in every phases of this Ph.D.

A special thanks goes to Monojit Da, Lopamudra, Nivedita and Manali for their unconditional support. You supported me in every bit of my life. The funny moments you shared at or outside lab will always remain as twinkling stars in the sky of my mind.

All of the members of ultrafast spectroscopy lab at SNBNCBS have provided me with encouragement, training, good laughs, and great fellowship. I want to thank all former and current members of the lab for helpful discussions and creating an atmosphere, which made the whole work fun! Thank you: Jayita Di, Priya Di, Damayanti Di, Probir Da, Soumendra Da, Pritam Da, Animesh Da, Prosenjit da, Tuhin Da, Debanjana, Ria, Neha, Amrita, Deepshika, Nur, Dipanjan, Aman, Debdutta, Arpan Da, Arka Da, Tanusree Di, Sumana Di.

Special thanks to Monojit Da, Lopamudra, Nivedita, Nur for carefully proofreading my thesis.

Furthermore I express my gratitude to Prof. Bimalendu Bhusan Bhattacharya for his valuable advices and guide. He was the person who introduced me with Prof. Samir Kumar Pal.

I owe my thanks to all my teachers at Dept. of Biochemistry, University of Calcutta for teaching me the basics in the field of biological research.

Working tirelessly to complete the thesis work would have been a painful experience without some great friends. There were innumerable occasions when I had failed to be at their side. But even after that, they never left my side. Silajit, Geetashree, Lopa, Shukti, Anisha, and Moupali, I don't know how I could survive this uphill journey without your constant support. These people willingly sacrificed their sleep to solve my chaos, console me in my setbacks, or only give me company. I know a mere thank you is not enough for all this. However, I can promise to be a better friend in future.

Some people come to life without any defined purpose. But their presence leaves a sustainable impact on life. I am fortunate enough to have such a person in my life. Writing this thesis would have been very difficult without the constant support from that person. Thank you for your time, kindness, those little adventures and highly intellectual conversations. Also, a special thanks to you for becoming my "Schrödinger's cat" and making me believe in the paradox of quantum superposition.

I would like to express my gratitude to you Siddhartha Sir (Siddhartha Das), because of you I found interest in Biology. Your amazing classes and interactions helped me to become inquisitive and encouraged me for the research work.

I am really thankful to SNBNCBS for providing such a wonderful working environment and also for accommodation facilities during these two months.

I also like to thank all my previous teachers at college and schools for giving me the light of education and directing me towards my passion. Thanks to all those technicians and support stuffs I met during the student life.

Finally, a great deal of gratitude is due to my family, my mother, father, sister, borther-in-law, Sister-in-law and specially my niece and nephew, without their continuous courage and unconditional love I can never proceed in my studies. They were always with me, they protect me and fulfill my every wish. Thank you.

Sector-III, Salt Lake City
Kolkata-98
August, 2017

Susmita Mondal

CONTENTS

Chapter 3: Instrumentation and Sample Preparation

CHAPTER 1

Introduction

1.1. Background:

The prosperity of modern lifestyle has gifted us with various complicated diseases. Intake of processed and fast food, smoking, alcohol consumption, and environmental pollution, i.e. the exposome is enhancing the risk of many deadly diseases like cancer, inflammatory bowel disease (IBD), metal poisoning, Covid-19 infection, Alzheimer's disease, Parkinson's disease etc. Not only the cure of these diseases are challenging but the diagnosis of these deadly diseases are also troublesome. In most cases, separate diagnosis and therapy for these life-threatening diseases are costly and time-consuming. In many cases, early detection of the disease helps to reduce the severity as well as the mortality rate. Therefore, to overcome such problems, researchers have been trying to develop a unique solution by the means of "theranostics", where both therapy and diagnosis can be achieved simultaneously using a single agent.

The word "theranostic" arises from the fusion of two words, therapeutics and diagnosis. In this regard, the potential of nanomaterials is a better exemplary than the conventional drugs due to their unique physical, chemical, optical and magnetic properties [1-11]. The exploitation of their multi-functionality can impart exhaustive improvement to the currently available diagnosis and therapeutics. A convenience in constructing such function-integrated agents is that many nanoplatforms are already, themselves, imaging agents. Their well-developed surface chemistry makes it easy to load them with pharmaceutics and promotes them to be theranostic nanosystems [12-14]. It adds to the previous paradigm for allowing imaging to be performed not only before or after, but also during a treatment regimen. Hence, these nanomaterials can provide an effective and integrated strategy for better management of these diseases which are causing a great economic burden and mortality around the globe.

1.2. Theranostic Redox Modulatory Nanomaterials:

1.2.1. Definition: Nanomaterials can be defined as materials possessing, at minimum, one external dimension measuring 1-100 nm [15, 16]. The definition given by the European Commission states that the particle size of at least half of the particles in the number size distribution must measure 100 nm or below [15]. Due to the ability to generate the materials in a particular way to play a specific role, the use of nanomaterials spans across various industries, from healthcare and cosmetics to environmental preservation and air purification. In this thesis, we will only discussion the role of nanomaterials in healthcare and the scope of improvement of their use in the medicinal field.

As mentioned previously, the term "theranostic" is combined of two words i.e. therapy and diagnosis. Hence, the theranostic nanomaterials are nano-constructs those can simultaneously provide a diagnostic platform as well as a therapeutic strategy. Iron oxide nanoparticles, quantum dots, carbon nanotubes, gold nanoparticles, manganese nanoparticles and silica nanoparticles, have been previously well investigated in the imaging setting [4, 6, 7, 9, 10]. These nanomaterials have also shown some fantastic therapeutic efficacy against life-threatening diseases. Therefore, a critical engineering of these nanomaterial can be the foundation of theranostic in the field of medicine.

One of the unique features of these new-edge nanomaterials is redox modulation of a given system, i.e., they can act either as a pro-oxidant or an anti-oxidant depending upon the redox state of the system and helps to maintain the cellular redox homeostasis. This property imparts a great deal of advantage of using such nanomaterials in comparison with the anti-oxidant drugs traditionally used against many life-threatening diseases.

1.2.2. Advantages of Using Theranostic Redox Modulatory Nanomaterial in the Medical Field: New-edge nanomaterials are exerting excellent efficacy in the healthcare sector. Due to their tuneable optical, biological and magnetic properties, one can engineer a single nanomaterial to perform various different functions. Due to their higher surface-to-volume ratio, a very small amount of material can provide the necessary effect in the physiological milieu [17]. Critical surface engineering can increase their solubility by many folds so that they can be excreted out of the system

very easily. Also, only by changing their surface ligand, the same nanomaterial can be specifically targeted to various different organs [18-21]. Their inbuilt magnetic and optical properties also give them the advantages to be an efficient imaging agent [4, 20]. The ability to generate as well as passivate the radicals present in systems promotes unique therapeutic strategies against various redox imbalance-related diseases [11, 22-24]. The use of iron oxide, gold, silver, zinc and manganese nanoparticles as contrasting agents in conventional MRI and X-ray is very promising for easy detection of many critical diseases [4, 9, 20, 25-27]. Also, their therapeutic efficacy as photodynamic therapy (PDT) agent, or as an anti-oxidant agent make remarkable progress for the cure of some deadly diseases. The combination of these diagnostic and therapeutic potentials will help to decrease the cost of separate diagnosis and therapy and also will reduce the time between the diagnosis and therapy so that a disease can be cured within the minimal time span after diagnosis or simultaneously.

1.2.3. Challenges of Using Nanomaterial in the Field of Medicine: The bio-distribution of nanoparticles, and of any other agent, is primarily governed by their ability to negotiate biological barriers [28]. Several extremely effective physiological obstacles, called biological barriers, largely prevent injected chemicals, biomolecules, nanoparticles and any other foreign agents from reaching their intended destinations and manifesting their effects. These barriers include: the reticuloendothelial system, endothelial or epithelial membranes, complex networks of blood vessels, abnormal flow of blood, and interstitial pressure gradients [29]. Understanding the mutual association between biology and nanotechnology, including the influence of disease pathophysiology on nanomaterials accumulation, distribution, retention and efficacy, as well as the biopharmaceutical correlation between their inherent properties and *in vivo* behaviour in animals (eventually in humans) are essential determinants for the successful translation of nanomaterials [30]. Another major concern regarding the growing number of nanomaterials for applications in healthcare is their potential adverse health effects, i.e. the toxicity. Knowledge about the interactions of nanostructures with biological systems with an emphasis on elucidating the relationship between the physical and chemical properties (e.g. size, shape, surface chemistry, composition, and aggregation) of nanostructures with induction of toxic biological responses is becoming an

important factor for the rational design of nanoparticles [31-33]. In the last decade, mainstream nanotoxicity research has been concentrated on cell culture systems; however, the results from these studies could be deceptive and necessitates the need for authentication from animal experiments [31]. It is worth mentioning here that *in vivo* systems are extremely complicated and the interactions of the nanostructures with biological components, such as proteins and cells, could lead to unique bio-distribution, clearance, immune response, and metabolism [34, 35]. An understanding of the relationship between the physical and chemical properties of the nanostructure and their *in vivo* behaviour is extremely needed to provide a basis for assessing toxic response and more importantly could lead to predictive models for assessing toxicity [36, 37]. These parameters need to be well-investigated based on dose, dosage form and route of administration to establish safe limits prior to clinical trials [30, 38].

1.3. Scope of the Thesis:

Lack of specificity, undesirable side-effects, poor solubility and some serious issues regarding bio-availability and bio-distribution limited the uses of traditional small molecules as a drug in the medical field. The failure of conventional small molecules against various diseases indicates the necessity for the development of alternative strategies in the healthcare [39, 40]. Also the conventional diagnosis strategies are proving inefficient to meet the need of precise, quick and cost-effective diagnosis [41, 42].

In the past decade, oxidative stress and reactive oxygen species (ROS) in physiological milieu have been established as one of the major cause behind these life-causing diseases [43-46]. The involvement of ROS in the pathogenesis of various diseases are well-documented. Though the role of ROS in disease pathogenesis is evident but emerging researches and clinical case studies report the failure of conventional anti-oxidants against these diseases [39]. To, counter this failure of anti-oxidant molecules, new school of thoughts regarding the oxidative stress has been founded [47-51]. The redox state of physiological milieu has been classified as "oxidative eustress" and "oxidative distress" [49]. In the oxidative eustress condition cells maintain a basal level of ROS within it where they help, mainly as a signaling molecule, to carry-out the normal function of cells [49, 51]. But in oxidative distress

the level of ROS within cells exceeds the optimum level and started to damage the cell organelles, nucleus and cell membrane. The pathogenesis of cancer, IBD etc. are predominantly due to the excess ROS within the cells [45, 46]. However, the conventional anti-oxidant therapy fails to cure these conditions because they quench all the ROS present in the system, so that the normal functions of cells driven by ROS get hampered. Therefore, a clinical strategy that can minutely maintain the cellular redox homeostasis is a perfect solution against this redox associated diseases.

Hence, the development of theranostic redox modulatory nanoparticles will be an excellent solution against these life-threatening diseases those are creating a huge economic, social burden and also causing thousands of life every year around the globe.

1.4. Objectives:

The thesis work mainly focused to develop low-cost, redox modulatory nanoparticles and to determine their efficacy as theranostic nanoagents against redox associated diseases. Hence the key objectives of this thesis are as follows:

i. Synthesis of bio-compatible, surface functionalized nanomaterials.

ii. Evaluation of diagnostic ability of surface functionalized nanomaterials against various diseases.

iii. Potential therapeutic effect of surface functionalized nanomaterials against various diseases in preclinical models.

iv. Evaluation of surface modulated metal oxide nanoparticle as Photodynamic therapy against cancer.

v. Design a unique nanotherapeutic strategy for effective treatment against inflammatory bowel diseases and hyperbilirubenemia.

vi. Development of a unique nanothenostic strategy against metal toxicity.

vii. The underlying mechanism of action of the nanomaterials, their bio-distribution, pharmacokinetics and pharmacodynamics. Particularly how they are tuning the redox state of the cell to treat the diseases.

viii. Toxicity of the nanomaterials, specifically the systemic acute and chronic toxicity studies.

1.5. Summary of the Work Done:

1.5.1. Synthesis and Characterization of a Nanomaterial with Industrial Scaling-up Possibility for Photodynamic Therapeutic Application:

1.5.1.1. Novel One Pot Synthesis and Spectroscopic Characterization of Folate-Mn_3O_4 Nanoparticle for Potential Photodynamic Therapeutic Application [52]: Treatment of cancer using nanoparticles made of inorganic and metallic compounds has been increasingly used, owing to their novel intrinsic physical properties and their potential to interact with specific cellular sites, thereby significantly reducing severe secondary effects. In this study, we report a facile strategy for synthesis of folate capped Mn_3O_4 nanoparticles (FA-Mn_3O_4 NPs) with high colloidal stability in aqueous media using a hydrothermal method for potential application in photodynamic therapy (PDT) of cancer. The capping of FA to Mn_3O_4 NPs was confirmed using various spectroscopic techniques. In adenocarcinomic human alveolar basal epithelial cells (A549), the nanoparticle synthesised with a combination of FA and Mn_3O_4 shows remarkable PDT activity via intracellular ROS generation (singlet oxygen). As established by a DNA fragmentation assay and fluorescence studies, the nanoparticle can cause significant nuclear DNA damage by light induced enhanced ROS generation. In the assessment of Bax, Bcl2 provides strong evidence of apoptotic cellular death. Cumulatively, the outcomes of this study suggests that these newly synthesized FA-Mn_3O_4 NPs can specifically destroy cells with overexpressed folate receptors, thereby providing a solution in the journey of cancer eradication.

1.5.2. Synthesis and Characterization of a Nanomaterial for its Potential Application as a Nanoceutical Fabric Against Airborne Diseases:

1.5.2.1. Nanoceutical Fabric Prevents COVID-19 Spread Through Expelled Respiratory Droplets: A Combined Computational, Spectroscopic, and Antimicrobial Study [53]: Centers for Disease Control and Prevention (CDC) warns the use of one-way valves or vents in face masks for potential threat of spreading COVID-19 through expelled respiratory droplets. Here, we have

developed a nanoceutical cotton fabric duly sensitized with non-toxic zinc oxide nanomaterial for potential use as a membrane filter in the one-way valve for the ease of breathing without the threat of COVID-19 spreading. A detailed computational study revealed that zinc oxide nanoflowers (ZnO NFs) with almost two-dimensional petals trap SARS-CoV-2 spike proteins, responsible to attach to ACE-2 receptors in human lung epithelial cells. The study also confirmed significant denaturation of the spike proteins on the ZnO surface, revealing removal of the virus upon efficient trapping. Following the computational study, we have synthesized ZnO NF on a cotton matrix using a hydrothermal-assisted strategy. Electron-microscopic, steady-state, and picosecond-resolved spectroscopic studies confirm attachment of ZnO NF to the cotton (i.e., cellulose) matrix at the atomic level to develop the nanoceutical fabric. A detailed antimicrobial assay using Pseudomonas aeruginosa bacteria (model SARS-CoV-2 mimic) reveals excellent antimicrobial efficiency of the developed nanoceutical fabric. To our understanding, the nanoceutical fabric used in the one-way valve of a face mask would be the choice to assure breathing comfort along with source control of COVID-19 infection. The developed nanosensitized cloth can also be used as an antibacterial/anti CoV-2 washable dress material in general.

1.5.3. Characterization of Oxidative Stress-induced Disorders and Modulation Reactive Oxygen Species in Biologically Relevant System for Potential Therapeutic Applications:

1.5.3.1. Synthesis And Spectroscopic Characterization of a Target-Specific Nanoparticle for Redox Buffering in Cellular Milieu [54]: A crucial balance between oxidative eustress and distress is important for maintaining redox homeostasis in the cellular *milieu*. Therefore, sustaining the intracellular redox buffer condition with exogenous agents could be a therapeutic strategy against diseases caused by redox imbalance. Here, we synthesized chitosan functionalized Mn_3O_4 nanoparticles (Ch-Mn_3O_4 NPs) and tested their redox buffering capability in *in-vitro* and *in-cellulo*. Chitosan is easily absorbed by the intestine and can be used as target-specific delivery agent to the intestine, while Mn_3O_4 NPs have redox modulatory properties. Therefore, combination of chitosan and Mn_3O_4 NPs provide the opportunity for targeted redox buffering. Targeted delivery of a drug and

remediation or the corresponding indication qualify the drug to be a theranostic agent. Spectroscopic studies suggest ROS generation as well as antioxidant ability of Ch-Mn_3O_4 NPs. *In cellulo* studies using A549 cell-lines confirmed the efficacy of the nanohybrid in redox homeostasis. The outcomes suggest that Ch-Mn_3O_4 nano-hybrid has the potential to function as a target-specific redox buffering agent in both *in vitro* and *in cellulo* systems.

1.5.3.2. Spectroscopic Study on the Interaction Of Co^{2+} with Citrate-Mn_3O_4: towards the Development Of Nanotherapy Against Cobalt Toxicity [55]: Cobalt (Co) although, an essential element playing a key role in several physiological and biological pro- cesses, can transform into a potential toxin when present in higher amounts or in certain chemical forms. The increasing usage of transition metals in industries, agriculture, medicines and technology has led to an alarming rise in cobalt poisoning cases. Exposure to cobalt can cause several health hazards including neurodegenerative disorders like Alzheimer's disease, Parkinson's disease, etc. Cobalt may interact with several proteins in the cellular milieu, generating reactive oxygen species (ROS) and thereby triggering apoptosis of the neural cells via DNA damage. The most common method of removal of such metals from the body is by the use of metal chelators. In this study, we report a facile strategy for the clearance of Co(II) from the physiological milieu using citrate functionalized Mn_3O_4 NPs (C-Mn_3O_4 NPs). The chelation ability of C-Mn_3O_4 NPs has been evaluated using steady state and pico-second resolved optical spectroscopy. Our studies reveal that C-Mn_3O_4 NPs form a stable complex with cobalt ions, thereby reducing the ability of Co^{2+} to produce reactive oxygen species (ROS) via Fenton like reaction and hence function as a novel nanotherapeutic for the detoxification of cobalt in the human system.

1.5.4. Synthesis and Characterization of Nanomaterial for Therapeutic and Diagnostic Biological Applications:

1.5.4.1. Interaction of a Jaundice Marker Molecule with Redox Modulatory Nano Hybrid: A Combined Electrochemical and Spectroscopic Study Towards the Development of a Theranostics Tool [56]: This study explores a combined electrochemical and spectroscopic approach to investigate the degradation of bilirubin, a molecular marker of jaundice in humans using a biocompatible

nanohybrid (citrate-functionalized Mn_3O_4 nanohybrid; C-Mn_3O_4 NH).The approach is aimed at the development of a facile theranostic tool for treatment, detection, and prognosis of jaundice. Linear sweep voltammetry (LSV) studies on bilirubin, C-Mn_3O_4 NH, a model carrier protein, and its complex with bilirubin reveal the efficacy of the nanohybrid for both degradation and detection of bilirubin. Furthermore, spectroscopic studies depict that distal electron transfer to be the probable mechanism behind the observed bilirubin degradation in physiological milieu.

1.5.4.2. In-Vitro and Microbiological Assay of Functionalized Hybrid Nanomaterials to Validate Their Efficacy in Nano-Theranostics: A Combined Spectroscopic and Computational Study [57]: Functionalized nanoparticles reveal new frontiers in therapeutics and diagnostics simultaneously, called theranostics. Functionalization of an inorganic nanoparticle with an organic ligand mostly predominates its interaction of the functionalized nanoparticles (NPs) with various cellular components leading to therapeutic effect diminishing the adverse side effects. Apart from the therapeutic effect of the nanoparticles other physical properties of the organic-inorgaic complex (nanohybrid) including fluorescence, X-ray or MRI contrast offer diagnosis of the anomalous target cell. Here we have functionalized Mn_3O_4 nanoparticles with organic citrate (C-Mn_3O_4) and folic acid (FA-Mn_3O_4) ligand and investigated their antimicrobial activities using Staphylococcus hominis as a model bacteria, which can be remediated through their membrane rupture. While, high resolution transmission microscopy (HR-TEM), XRD, DLS, absorbance and fluorescence spectroscopy have been used for the structural characterisation of the functionalised nanoparticles, zeta potential measurement, temperature dependent ROS generation reveal the drug action of the NPs. We have used high end density functional theory (DFT) calculation to rationalise the specificity of the drug action of the NPs. Pico-second resolved FRET studies confirm the enhanced affinity of FA-Mn_3O_4 to the bacteria compared to C-Mn_3O_4 leading to enhanced anti-microbial activity. We have shown that the functionalised nanoparticles offer significant X-ray contrast in in-vitro studies indicating the FA-Mn_3O_4 NPs to be a potential theranostic agent against bacterial infection.

1.5.4.3. Functionalised Two Dimension Carbon Nitride Nanodots Detect and Reverse Lead Toxicity in The Physiological Milieu [58]: Despite significant

development of graphitic Carbon Nitride (g-C_3N_4) as a catalytic material, the biomedical application of the same is rarely discussed in the excising literature. For the first time, we report on the synthesis of citrate capped C_3N_4 nanodots (C-C_3N_4 NDs) and their potential application as nanomedicine against lead poisoning. The physioco-chemical properties of the nanodots have been explored extensively using microscopic and spectroscopic tools. The generation of a significant amount of reactive oxygen species (ROS) has been witnessed for the as synthesized citrate capped nanodots. The C-C_3N_4 NDs can effectively bind to Pb(II) leading to the formation of a stable, soluble complex to eliminate Pb(II) from circulation. In addition, it has been demonstrated that the complex can be detected using spectroscopic tools thereby making the nanodots as potential markers for Pb(II) detection. These bio-compatible NDs have also been found to have potential to protect cellular components from ROS associated damages while maintaining the cellular eustress condition. The present study establishes the dual action of C-C_3N_4 NDs as a potential lead detector as well as an alternative, non-toxic, biocompatible solution against lead toxicity.

1.5.5. Developments of Nanoparticles and Their Biochemical and Molecular Aspects in Preclinical Disease Model:

1.5.5.1. Chitosan Functionalized Mn_3O_4 Nanoparticle Counteracts Ulcerative Colitis Through Modulation of Reactive Oxygen Species [59]: Crucial balance of reactive oxygen species (ROS) in physiological condition revealing oxidative distress (elevated level of ROS) and oxidative eustress play a central role in cellular redox signaling via different post translational modifications. In the present study, we have synthesized a nanoparticle consisting chitosan functionalized Mn_3O_4 in counteracting ulcerative colitis (UC) in a preclinical study confirming the nanoparticle to be excellent nanomedicine for the disease due to redox imbalance. Our *in-vitro* characterization of the developed nanoparticle confirms critical electronic transitions in the nanoparticle to be important for the redox buffering activity in the animal model. The physiological observations including fecal blood and frequency in the bowel movement and elevated inflammatory molecular markers established the inflammatory UC in the mice model upon induction through dextran sulfate sodium (DSS). A careful administration of the developed nanoparticle not only reduces the inflammatory marker in the animals, also reduces

the significant mortality rate from the induced disease. To our understanding, the novel use of the nanoparticles for the remediation of UC is one of the examples of modulation of molecular factors like mitochondrial stress, inflammatory cytokines via modulating the cellular redox state.

1.5.6. Use of Theranostic Nanomaterials in Preclinical Mice Model:

1.5.6.1. Organ Specific Therapeutic Nanoparticles Generates Radiolucent Reactive Oxygen Species for Potential Nanotheranostics Using Conventional X-ray Technique in Mammals [60]: Here we report the use of citrate functionalized Mn_3O_4 nanoparticles (C-Mn_3O_4 NPs) for targeted delivery in lungs and brain in mice model. While the bio-distribution of the NPs is reported earlier and found to be useful for the reversal of disorders in some specific organs, we report the direct observation of the accumulation of reactive oxygen species (ROS) by using X-ray induced radiolucency. Our detailed analysis on X-ray images of lungs in mice model reveals lower contrast compared to that of the control group indicating NPs induced ROS in the organs. Various lobes of NP treated mice brain are also clearly visible compared to that of the control group.

1.6. Plan of the Thesis:

The plan of the thesis is as follows:

Chapter 1: This chapter provides a brief introduction to the scope and motivation behind the thesis work. A brief summary of the work done is also included in this chapter.

Chapter 2: This chapter gives a brief overview of the different steady state and dynamical tools, animal models and chemical probes used in the experiments.

Chapter 3: This chapter describes the instrumental details, experimental protocols and data analysis procedures.

Chapter 4: In this chapter, the role of folate functionalized Mn_3O_4 nanoparticles as photodynamic therapeutic agent against cancer has been investigated using adenocarcinomic human alveolar basal epithelial cells.

Chapter 5: In this chapter, the efficacy of a nanoceutical fabric (ZnO coated) used in the one-way valve of a face mask against COVID-19 Spread through Expelled

Respiratory Droplets has been accessed using Pseudomonas aeruginosa bacteria, a SARS-CoV-2 mimic.

Chapter 6: In this chapter, the efficacy of chitosan functionalised Mn_3O_4 nanoparticle and citrate functionalised Mn_3O_4 nanoparticle to maintain the cellular redox homeostasis has been explored using biologically relevant systems.

Chapter 7: In this chapter, the theranostic efficacy of citrate functionalised Mn_3O_4 nanoparticle and citrate functionalised carbon nitrate nanodots has been investigated against various redox modulatory diseases.

Chapter 8: In this chapter, the therapeutic efficacy of chitosan functionalised Mn_3O_4 nanoparticle against ulcerative colitis has been accessed using dextran sulphate sodium intoxicated mice model.

Chapter 9: In this chapter, the theranostic efficacy of citrate functionalised Mn_3O_4 nanoparticles has been studied using the preclinical mice model. This chapter describes the ROS induced negative contrast using the conventional X-ray technique.

Reference

[1] F. Chen, E.B. Ehlerding, W. Cai, Theranostic nanoparticles, *J. Nucl. Med.*, 55 (2014) 1919.

[2] J.V. Jokerst, S.S. Gambhir, Molecular imaging with theranostic nanoparticles, *Acc. Chem. Res.*, 44 (2011) 1050.

[3] D. Wang, B. Lin, H. Ai, Theranostic nanoparticles for cancer and cardiovascular applications, *Pharm. Res.*, 31 (2014) 1390.

[4] S.M. Dadfar, K. Roemhild, N.I. Drude, S. von Stillfried, R. Knüchel, F. Kiessling, T. Lammers, Iron oxide nanoparticles: Diagnostic, therapeutic and theranostic applications, *Adv. Drug Deliv. Rev.*, 138 (2019) 302.

[5] L. Zhu, Z. Zhou, H. Mao, L. Yang, Magnetic nanoparticles for precision oncology: Theranostic magnetic iron oxide nanoparticles for image-guided and targeted cancer therapy, *Nanomed.*, 12 (2017) 73.

[6] T. Curry, R. Kopelman, M. Shilo, R. Popovtzer, Multifunctional theranostic gold nanoparticles for targeted CT imaging and photothermal therapy, *Contrast Media Mol. Imaging.*, 9 (2014) 53.

[7] V. De Matteis, M. Cascione, C.C. Toma, S. Leporatti, Silver nanoparticles: Synthetic routes, in vitro toxicity and theranostic applications for cancer disease, *Nanomater.*, 8 (2018) 319.

[8] M. Qasim Nasar, T. Zohra, A.T. Khalil, S. Saqib, M. Ayaz, A. Ahmad, Z.K. Shinwari, Seripheidium quettense mediated green synthesis of biogenic silver nanoparticles and their theranostic applications, *Green Chem. Lett. Rev.*, 12 (2019) 310.

[9] M.W. Ambrogio, C.R. Thomas, Y.-L. Zhao, J.I. Zink, J.F. Stoddart, Mechanized silica nanoparticles: A new frontier in theranostic nanomedicine, *Acc. Chem. Res.*, 44 (2011) 903.

[10] A. Adhikari, S. Mondal, T. Chatterjee, M. Das, P. Biswas, R. Ghosh, S. Darbar, H. Alessa, J.T. Althakafy, A. Sayqal, Redox nanomedicine ameliorates chronic kidney disease (CKD) by mitochondrial reconditioning in mice, *Commun. Biol.*, 4 (2021) 1013.

[11] M. Zare, K. Namratha, K. Byrappa, D. Surendra, S. Yallappa, B. Hungund, Surfactant assisted solvothermal synthesis of ZnO nanoparticles and study of their antimicrobial and antioxidant properties, *J. Mater. Sci. Technol.*, 34 (2018) 1035.

[12] Y. Liu, G. Yang, S. Jin, L. Xu, C.X. Zhao, Development of high-drug-loading nanoparticles, *ChemPlusChem*, 85 (2020) 2143.
[13] J.S. Petschauer, A.J. Madden, W.P. Kirschbrown, G. Song, W.C. Zamboni, The effects of nanoparticle drug loading on the pharmacokinetics of anticancer agents, *Nanomedicine (Lond).* 10 (2015) 447.
[14] R. Singh, J.W. Lillard Jr, Nanoparticle-based targeted drug delivery, *Exp. Mol. Pathol.*, 86 (2009) 215.
[15] TWI, What is a nanomaterial? - Definition, examples and uses, 2023.
[16] E. Roduner, Size matters: Why nanomaterials are different, *Chem. Soc. Rev.*, 35 (2006) 583.
[17] A.B. Asha, R. Narain, Nanomaterials properties, Polymer Science and Nanotechnology, *Elsevier,* Amsterdam, 2020, 343.
[18] M. K. Amin, J. Boateng, Surface functionalization of PLGA nanoparticles for potential oral vaccine delivery targeting intestinal immune cells, *Colloids Surf. B*, 222 (2023) 113121.
[19] J. Lazarovits, Y.Y. Chen, E.A. Sykes, W.C. Chan, Nanoparticle–blood interactions: The implications on solid tumour targeting, *Chem Comm*, 51 (2015) 2756.
[20] J.M. Bergen, H.A. Von Recum, T.T. Goodman, A.P. Massey, S.H. Pun, Gold nanoparticles as a versatile platform for optimizing physicochemical parameters for targeted drug delivery, *Macromol. Biosci.*, 6 (2006) 506.
[21] R. Mout, D.F. Moyano, S. Rana, V.M. Rotello, Surface functionalization of nanoparticles for nanomedicine, *Chem. Soc. Rev.*, 41 (2012) 2539.
[22] A. Giri, N. Goswami, M. Pal, M.T.Z. Myint, S. Al-Harthi, A. Singha, B. Ghosh, J. Dutta, S.K. Pal, Rational surface modification of Mn_3O_4 nanoparticles to induce multiple photoluminescence and room temperature ferromagnetism, *J. Mater. Chem. C*, 1 (2013) 1885.
[23] A. Adhikari, P. Biswas, S. Mondal, M. Das, S. Darbar, A.M. Hameed, A. Alharbi, S.A. Ahmed, S.S. Bhattacharya, D. Pal, S.K. Pal, A smart nanotherapeutic agent for in vitro and in vivo reversal of heavy-metal-induced causality: Key information from optical spectroscopy, *ChemMedChem*, 15 (2020) 420.

[24] N. Yakimovich, A. Ezhevskii, D. Guseinov, L. Smirnova, T. Gracheva, K. Klychkov, Antioxidant properties of gold nanoparticles studied by ESR spectroscopy, *Russ. Chem. Bull.*, 57 (2008) 520.

[25] Z. Zhao, H. Fan, G. Zhou, H. Bai, H. Liang, R. Wang, X. Zhang, W. Tan, Activatable fluorescence/MRI bimodal platform for tumor cell imaging via MnO_2 nanosheet–aptamer nanoprobe, *J. Am. Chem. Soc.*, 136 (2014) 11220.

[26] M. Zhang, L. Xing, H. Ke, Y.-J. He, P.-F. Cui, Y. Zhu, G. Jiang, J.-B. Qiao, N. Lu, H. Chen, MnO_2-based nanoplatform serves as drug vehicle and MRI contrast agent for cancer theranostics, *ACS Appl. Mater. Interfaces.*, 9 (2017) 11337.

[27] M.H. Cho, E.-S. Choi, S. Kim, S.-H. Goh, Y. Choi, Redox-responsive manganese dioxide nanoparticles for enhanced MR imaging and radiotherapy of lung cancer, *Front. Chem.*, 5 (2017) 109.

[28] M. Ferrari, Cancer nanotechnology: Opportunities and challenges, *Nat. Rev. Cancer.*, 5 (2005) 161.

[29] W.R. Sanhai, J.H. Sakamoto, R. Canady, M. Ferrari, Seven challenges for nanomedicine, *Nat. Nanotechnol.*, 3 (2008) 242.

[30] S. Hua, M.B. De Matos, J.M. Metselaar, G. Storm, Current trends and challenges in the clinical translation of nanoparticulate nanomedicines: Pathways for translational development and commercialization, *Front. Pharmacol.*, 9 (2018) 790.

[31] H.C. Fischer, W.C. Chan, Nanotoxicity: The growing need for in vivo study, *Curr. Opin. Biotechnol.*, 18 (2007) 565.

[32] A.D. Maynard, R.J. Aitken, T. Butz, V. Colvin, K. Donaldson, G. Oberdörster, M.A. Philbert, J. Ryan, A. Seaton, V. Stone, Safe handling of nanotechnology, *Nature*, 444 (2006) 267.

[33] J. Tsuji, A. Maynard, P. Howard, J. James, Research strategies for safety evaluation of nanomaterials, part iv: Risk assessment of nanoparticles, *Toxicol. Sci.*, 89 (2006) 42.

[34] D.A. Casciano, S.C. Sahu, Nanotoxicity: From in vivo and in vitro models to health risks, *John Wiley & Sons,* New York, 2009.

[35] A.M. Alkilany, C.J. Murphy, Toxicity and cellular uptake of gold nanoparticles: What we have learned so far?, *J. Nanopart. Res.*, 12 (2010) 2313.

[36] J.M. Hillegass, A. Shukla, S.A. Lathrop, M.B. MacPherson, N.K. Fukagawa, B.T. Mossman, Assessing nanotoxicity in cells in vitro, *Wiley Interdiscip. Rev.: Nanomed. Nanobiotechnology*, 2 (2010) 219.

[37] A. Sukhanova, S. Bozrova, P. Sokolov, M. Berestovoy, A. Karaulov, I. Nabiev, Dependence of nanoparticle toxicity on their physical and chemical properties, *Nanoscale Res. Lett.*, 13 (2018) 1.

[38] R. Gaspar, R. Duncan, Polymeric carriers: Preclinical safety and the regulatory implications for design and development of polymer therapeutics, *Adv. Drug Deliv. Rev.*, 61 (2009) 1220.

[39] S.R. Steinhubl, Why have antioxidants failed in clinical trials?, *Am. J. Card.*, 101 (2008) S14.

[40] S. Baker, S. Pereira, A. Begum, Failure of vitamin E therapy in the treatment of anemia of protein-calorie malnutrition, *Blood*, 32 (1968) 717.

[41] B. Gümrü, B. Tarçın, Imaging in endodontics: An overview of conventional and alternative advanced imaging techniques, *J. Marmara Univer. Insti. Health Sci.*, 3 (2013) 55.

[42] S. Patel, A. Dawood, E. Whaites, T. Pitt Ford, New dimensions in endodontic imaging: Part 1. Conventional and alternative radiographic systems, *Int. Endod. J.*, 42 (2009) 447.

[43] S. Yang, G. Lian, ROS and diseases: Role in metabolism and energy supply, *Mol. Cell. Biochem.*, 467 (2020) 1.

[44] A. Popa-Wagner, S. Mitran, S. Sivanesan, E. Chang, A.-M. Buga, ROS and brain diseases: The good, the bad, and the ugly, *Oxid. Med. Cell. Longev.*, 2013 (2013) 1.

[45] G.-Y. Liou, P. Storz, Reactive oxygen species in cancer, *Free Radic. Res.*, 44 (2010) 479.

[46] A. Roessner, D. Kuester, P. Malfertheiner, R. Schneider-Stock, Oxidative stress in ulcerative colitis-associated carcinogenesis, *Pathol. Res. Pract.*, 204 (2008) 511.

[47] H. Sies, Hydrogen peroxide as a central redox signaling molecule in physiological oxidative stress: Oxidative eustress, *Redox Biol.*, 11 (2017) 613.

[48] H. Sies, Oxidative eustress: On constant alert for redox homeostasis, *Redox Biol.*, 41 (2021) 101867.

[49] H. Sies, Oxidative eustress and oxidative distress: Introductory remarks, Oxidative Stress, *Elsevier,* Amsterdam, 2020, 3.

[50] C.R. Reczek, N.S. Chandel, ROS-dependent signal transduction, *Curr. Opin. Cell Biol.*, 33 (2015) 8.

[51] M. Schieber, N.S. Chandel, ROS function in redox signaling and oxidative stress, *Curr. Biol.*, 24 (2014) R453.

[52] S. Mondal, A. Adhikari, M. Das, S. Darbar, A. Alharbi, S.A. Ahmed, S.S. Bhattacharya, D. Pal, S.K. Pal, Novel one pot synthesis and spectroscopic characterization of a folate-Mn_3O_4 nanohybrid for potential photodynamic therapeutic application, *RSC Adv.*, 9 (2019) 30216.

[53] A. Adhikari, U. Pal, S. Bayan, S. Mondal, R. Ghosh, S. Darbar, T. Saha-Dasgupta, S.K. Ray, S.K. Pal, Nanoceutical fabric prevents covid-19 spread through expelled respiratory droplets: A combined computational, spectroscopic, and antimicrobial study, *ACS Appl. Bio Mater.*, 4 (2021) 5471.

[54] S. Mondal, A. Adhikari, R. Ghosh, M. Singh, M. Das, S. Darbar, S.S. Bhattacharya, D. Pal, S.K. Pal, Synthesis and spectroscopic characterization of a target-specific nanohybrid for redox buffering in cellular milieu, *MRS Adv.*, 6 (2021) 427.

[55] S. Mondal, A. Adhikari, M. Singh, R. Ghosh, M. Goswami, P. Biswas, S.K. Pal, Spectroscopic study on the interaction of Co^2+ with citrate-Mn_3O_4: Towards the development of nanotherapy against cobalt toxicity, *Mater. Today: Proc.*, 43 (2021) 3692.

[56] S. Mondal, N. Pan, R. Ghosh, A. Bera, D. Mukherjee, T.K. Maji, A. Adhikari, S. Ghosh, C. Bhattacharya, S.K. Pal, Interaction of a jaundice marker molecule with a redox-modulatory nano-hybrid: A combined electrochemical and spectroscopic study toward the development of a theranostic tool, *ChemMedChem*, 17 (2022) e202100660.

[57] S. Mondal, R. Ghosh, A. Adhikari, U. Pal, D. Mukherjee, P. Biswas, S. Darbar, S. Singh, S. Bose, T. Saha-Dasgupta, In vitro and microbiological assay of functionalized hybrid nanomaterials to validate their efficacy in nanotheranostics: A combined spectroscopic and computational study, *ChemMedChem*, 16 (2021) 3739.

[58] S. Mondal, S. Bayan, R. Ghosh, M. Das, A. Adhikari, D. Mukherjee, A.K. Mallick, S.K. Ray, S.K. Pal, Functionalized two-dimensional carbon nitride

nanodots detect and reverse lead toxicity in the physiological milieu, *ACS Appl. Mater. Interfaces.*, 14 (2022) 27002.

[59] S. Mondal, M. Das, R. Ghosh, M. Singh, A. Adhikari, S. Darbar, A.K. Das, S.S. Bhattacharya, D. Pal, D. Bhattacharyya, A.S.A. Ahmed, A.K. Mallick, M.A.R. Munirah, Z. Moussa, S.A. Ahmed, S.K. Pal, Chitosan functionalized Mn_3O_4 nanoparticles counteracts ulcerative colitis in mice through modulation of cellular redox state, *Commun. Biol.*, 6 (2023) 647.

[60] S. Mondal, M. Das, R. Ghosh, S. Singh, S. Darbar, N. Bhattacharyya, A. Adhikari, A.K. Das, S.S. Bhattacharya, D. Pal, Organ-specific therapeutic nanoparticles generates radiolucent reactive species for potential nanotheranostics using conventional X-ray technique in mammals, *Appl. Nanosci.*, 12 (2022) 3851.

CHAPTER 2

Overview of Experimental Techniques and Animal Models

In order to investigate the various processes involved in synthesis, characterization and potential biomedical applications of the nanomaterials and ethnobotanical ingredients, different steady state and dynamical tools including molecular quenching, time correlated single photon counting, dynamic light scattering have been used. To understand therapeutic efficacy of the developed nanomaterials, preclinical models were employed to mimic the human disease conditions. In this chapter, a brief overview of the theoretical aspects of the spectroscopic tools and insights about the animal models are provided. Also, particulars about various systems used in different studies have been discussed.

2.1. Fluorescence Quenching:

Fluorescence quenching is the non-radiative loss of excitation energy from a fluorophore through interaction with another molecule, called quencher, resulting into decrease in fluorescence intensity. The stationary and time-dependent observations of such processes can reveal the deactivation mechanism of the excited molecule and can be used to probe bimolecular interactions.

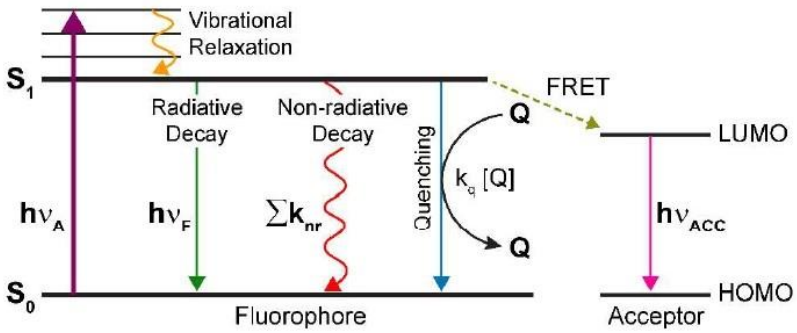

Figure 2.1*: Schematic representation of modified Jablonski diagram.*

Quenching can occur through numerousmechanisms including excited-state reactions, molecular rearrangements, energy transfer, ground-state complex

formation, and collision. However, there are two main classes of mechanisms of fluorescence quenching namely dynamic and static.

2.1.1. Dynamic or Collisional Quenching: Dynamic or collisional quenching is a process where depopulation of excitedstate takes place upon collisional encounter between fluorophore and the quencher (illustrated on the modified Jablonski diagram in Figure 2.1). Herein, the excited state fluorophore is returned to the ground state without any chemical alterations through a diffusive encounter with the quencher. The collisional quenching is described by the popular Stern-Volmer equation (Eq. 2.1.)

$$\frac{F_0}{F} = 1 + k_q \tau_0 [Q] = 1 + K_D [Q] \qquad (2.1)$$

Here, F_0 and F are the fluorescence intensities of the fluorophore in presence and absence of quencher, kq is the bimolecular quenching constant and τ_0 is the initial lifetime of the fluorophore. K_D is the Stern-Volmer quenching constant and [Q] is the quencher concentration. K_D points toward the sensitivity of the fluorophore to a quencher. Larger K_D values indicate more accessibility of the fluorophore to aquencher. If the quenching is identified to be dynamic, the Stern-Volmer constant is represented by K_D. Otherwise it is replaced with K_{SV}.

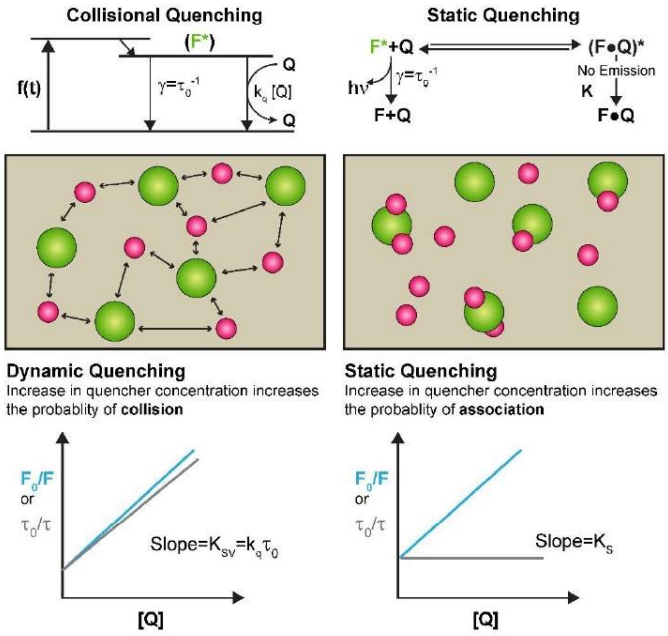

Figure 2.2: *Schematic representation of collisional (i.e., dynamic) and static quenchingphenomena. quencher.*

2.1.2. Static Quenching: In static quenching, a complex formation happens between the fluorophore and the quencher at the ground state, and this complex is non-fluorescent. When this complex absorbs light it immediately returns to the ground state without emission of a photon. Static quenching can be described by Eq. 2.2.

$$\frac{F_0}{F} = 1 + K_S[Q] \tag{2.2}$$

In this expression, K_S is the association constant. It has to be noted that unlike dynamic quenching, static quenching causes no change to the fluorescence lifetime [1]. Quenching data are usually presented as plots of F_0/F versus [Q]. This is because F_0/F is expected to be linearly dependent upon the concentration of quencher. A plot of F_0/F versus [Q] yields an intercept of one on the y-axis and a slope equal to K_D or K_S (Figure 2.2). The possible mechanistic diagram of dynamic and static quenching are shown in Figure 2.2.

2.1.3. Combined Dynamic and Static Quenching: Often, collisional quenching and ground state complex formation simultaneously occurs between the fluorophore and the quencher, causing an upward curvature of the Stern-Volmer plot (Figure 2.3).

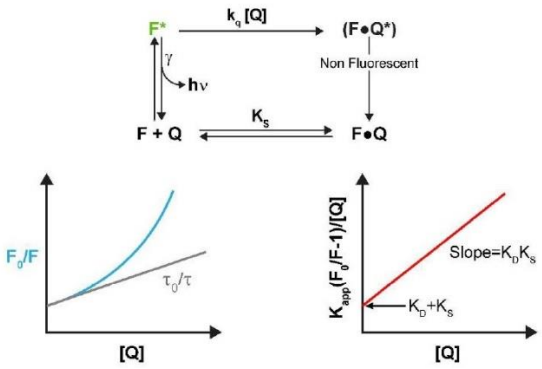

Figure 2.3: *Dynamic and static quenching of the same population of fluorophores.*

This kind of mixed quenching can be expressed using Eq. 2.3 and 2.4.

$$\frac{F_0}{F} = (1 + K_D[Q])(1 + K_S[Q]) \tag{2.3}$$

$$\frac{F_0}{F} = K_{app}[Q] \tag{2.4}$$

Here, K_{app} is the apparent quenching constant which is calculated at each quencher concentration. A plot of K_{app} versus [Q] yields a straight line with an intercept of K_D+K_S and a slope of K_SK_D (Figure 2.3)

2.2. Fluorescence Lifetime:

The fluorescence lifetime of a fluorophore is defined by the average time the molecule spends in the excited state before returning to the ground state via loss of energy through fluorescence and other non-radiative processes (Figure 2.4).

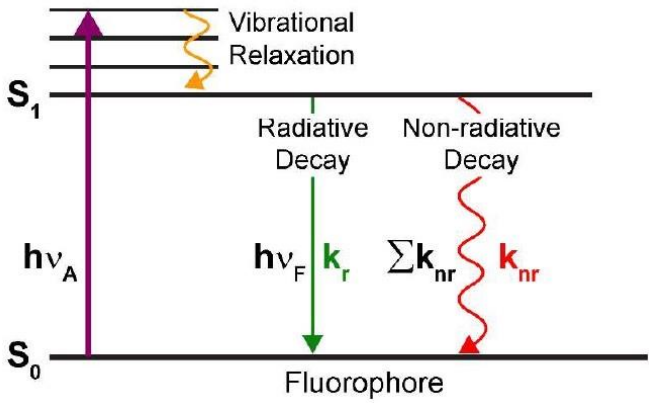

Figure 2.4: *A simplified Jablonski diagram to illustrate the meaning of fluorescence lifetime. k_r and $k_{nr}$are the radiative and non-radiative rates of decay.*

2.2.1. Theory: The excited state lifetime, τ, is defined by the following equation (Eq. 2.5).

$$\tau = \frac{1}{k_r+k_{nr}} \tag{2.5}$$

Where, k_r and k_{nr} is the radiative and non-radiative rates of decay. The lifetime of the fluorophore in the absence of non-radiative processes is called the intrinsic or natural lifetime, and is given by, $\tau = \frac{1}{k_r}$

2.2.2. Experimental Methods: The fluorescence transients were measured with commercially available time correlated single photon counting (TCSPC) setup from Edinburgh Instruments Ltd. (Livingston, UK) having an instrument response function, IRF=80 ps.

Curve fitting of the time-resolved fluorescence transients was performed using a nonlinear least square fitting procedure to a function (Eq. 2.6.) comprised of

convolution of the IRF (E(t)) with a sum of exponentials (Eq. 2.7.) with preexponential factors (B_i), characteristic lifetimes (τ_i), and a background (A).

$$X(t) = \int_0^t E(t')R(t-t')dt' \tag{2.6}$$

$$R(t) = A + \sum_{i=1}^{N} B_i e^{\frac{-t}{\tau_i}} \tag{2.7}$$

Relative concentration in a multi-exponential decay is expressed as Eq. 2.8.

$$C_n = \frac{B_n}{\sum_{i=1}^{N} B_i} \times 100 \tag{2.8}$$

The average lifetime (amplitude-weighted) of a multi-exponential decay is finally expressed as Eq. 2.9.

$$\tau_{avg} = \sum_{i=1}^{N} C_i \tau_i \tag{2.9}$$

The quality of the curve fitting is evaluated by reduced $\chi 2$ and residual data.

2.3. Dynamic Light Scattering:

According to semi-classical theory of light scattering, when light impinges onmatter, the electric field of the light induces an oscillating polarization of electrons inthe molecules. Hence, the molecules provide a secondary source of light andsubsequently scatter light. The frequency shift, the angular distribution, thepolarization, and the intensity of scattered light are determined by size, shape andmolecular interactions in the scattering material. Dynamic light scattering (DLS) alsoknown as photon correlation spectroscopy (PCS) or quasi-elastic light scattering (QELS) is one of the most popular techniques used to determine the size of the particle.

2.3.1. Theory: DLS experiments are based on two assumptions:

A) Particles exhibit Brownian motion (also called 'random walk'). The probability density function is given by the formula,

$$P(r,t|0,0) = (4\pi DT)^{\frac{3}{2}} e^{\frac{-r^2}{4Dt}} \tag{2.10}$$

Where D is the translational diffusion coefficient.

B) The particles are spherical in shape with particles of molecular dimensions. If it is so, then it is possible to apply the Stoke-Einstein relation and hence have a formula that easily gives the diffusion constant,

$$D = \frac{k_B T}{3\pi\eta d_H} \tag{2.11}$$

Where d_H is the hydrodynamic diameter of the particles, k_B is the Boltzmann constant,

T is the temperature in Kelvin and n is the viscosity of the solvent.

2.3.2. Experimental Methods: It has been seen that particles in dispersion are in a constant, random Brownian motion and this causes the intensity of scattered light to fluctuate as a function of time. The correlator used in a DLS instrument constructs the intensity autocorrelation function G(τ) of the scattered intensity [2],

$$G(\tau) = \langle I(t)I(t+\tau)\rangle \tag{2.12}$$

Where τ is the time difference (the sample time) of the correlator. For a large numberof monodisperse particles in Brownian motion, the correlation function (given thesymbol G) is an exponential decaying function of the correlator time delay τ,

$$G(\tau) = A[1 + Be^{-2\Gamma\tau}] \tag{2.13}$$

Where A is the baseline of the correlation function, B is the intercept of the correlationfunction. Γ is the first cumulant and is related to the translational diffusion coefficientas, Γ=Dq2, where q is the scattering vector and its magnitude is defined as,

$$q = \left(\frac{4\pi n}{\lambda_0}\right)\sin\left(\frac{\theta}{2}\right) \tag{2.14}$$

Where n is the refractive index of dispersant, λ_0 is the wavelength of the laser and θ, the scattering angle. For polydisperse samples, the equation can be written as,

$$G(\tau) = A\left[1 + B|g^{(1)}(\tau)|2\right] \tag{2.15}$$

Where the correlation function $g^{(1)}(\tau)$ is no longer a single exponential decay and can be written as the Laplace transform of a continuous distribution G(Γ) of decay times,

$$g^{(1)}(\tau) = \int_0^\infty G(\Gamma)e^{(-\Gamma\tau)d\Gamma} \tag{2.16}$$

The size distribution of the particles are obtained by fitting, using non-linear least square fitting or CONTIN program, the autocorrelation function to multi-

exponential function. The size distribution obtained is a plot of the relative intensity of light scattered by particles and is therefore known as an intensity size distribution. However, in the intensity distribution graph, the area of the peak for the larger particle appears at least 106 times larger than the peak for the smaller particle. This is because large particles scatter much more light than small particles, as the intensity of light scattering by a particle is proportional to the sixth power of its diameter (Rayleigh's approximation).

2.4. Förster Resonance Energy Transfer (FRET):

FRET is an electrodynamic phenomenon involving the non radiative transfer of the excited state energy from the donor dipole (D) to an acceptor dipole (A) in the ground state (Figure 2.5).Basically, FRET is of two types: (i) homo-molecular FRET and (ii) hetero-molecular FRET. In the former case the same fluorophore acts both as energy donor and acceptor, while in the latter case two different molecules act as donor and acceptor[3].

2.4.1. Theory: Each donor-acceptor (D-A) pair participating in FRET is characterized by a distance known as Förster distance (R_0) i.e., the D-A separation at which energy transfer is 50% efficient. The rate of resonance energy transfer (k_T) from donor to an acceptor is given by

$$k_T = \frac{1}{\tau_D}\left(\frac{R_0}{r}\right)^6 \tag{2.17}$$

where τ_D is the lifetime of the donor in the absence of acceptor and r is the donor toacceptor (D-A) distance. The rate of transfer of donor energy depends upon the extent of overlap of the emission spectrum of the donor with the absorption spectrum of the acceptor (J(λ)), the quantum yield of the donor (Q_D), the relative orientation of the donor and acceptor transition dipoles (k^2) and the distance between the donor and acceptor molecules (r) (Figure 2.5). In order to estimate FRET efficiency of the donor and hence to determine distances between donor acceptor pairs, the methodology described below is followed [4]. R_0 is given by,

$$R_0 = 0.211[k^2 n^{-4} Q_D J(\lambda)]^{1/6} \tag{2.18}$$

where n is the refractive index of the medium, Q_D is the quantum yield of the donorand (J(λ))is the overlap integral. k^2 is defined as,

$$k^2 = (\cos\theta_T - 3\cos\theta_D \cos\theta_A)^2 = (\sin\theta_D \sin\theta_A \cos\varphi - 2\cos\theta_D \cos\theta_A)^2 \quad (2.19)$$

where θ_TT is the angle between the emission transition dipole of the donor and theabsorption transition dipole of the acceptor, θ_D and θ_A are the angles between thesedipoles and the vector joining the donor and acceptor and φ is angle between theplanes of the donor and acceptor .k^2value can vary from 0 to 4. For collinear and parallel transition dipoles, k^2= 4; for parallel dipoles, k^2= 1; and for perpendicularly oriented dipoles, k^2= 0. For donor and acceptors that randomized by rotational diffusion prior to energy transfer, the magnitude of $k^2$is assumed to be 2/3. However, in systems where there is a definite site of attachment of the donor and acceptor molecules, to get physically relevant results, the value of k^2 has to be estimated from the angle between the donor emission and acceptor absorption dipoles (J(λ)), the overlap integral, which expresses the degree of spectral overlap between the donor emission and the acceptor absorption, is given by

$$J(\lambda) = \frac{\int_0^\infty F_D(\lambda)\epsilon_A(\lambda)\lambda^4 d\lambda}{\int_0^\infty F_D(\lambda)d\lambda} \quad (2.20)$$

where FD(λ) is the fluorescence intensity of the donor in the wavelength range of λ to λ +dλ and is dimensionless. εA(λ) is the extinction coefficient (in $M^{-1}cm^{-1}$) of the acceptor at λ . If λ is in nm, then J(λ) is in units of M^{-1} cm^{-1} nm^4.

Once the value of R_0 is known, the efficiency of energy transfer can be calculated. The efficiency of energy transfer (E) is the fraction of photons absorbed by the donor which are transferred to the acceptor and is defined as,

$$E = \frac{k_T(r)}{\tau_D^{-1} + k_T(r)} \quad (2.21)$$

Or

$$E = \frac{R_0^6}{r^6 + R_0^6} \quad (2.22)$$

For D-A systems decaying with multi exponential lifetimes, E is calculated from the amplitude weighted lifetimes of the donor in absence (τ_D) and presence (τ_{DA}) of the acceptor as,

$$E = 1 - \frac{\tau_{DA}}{\tau_D} \quad (2.23)$$

The D-A distances can be measured using Eq. 2.22 and 2.23.

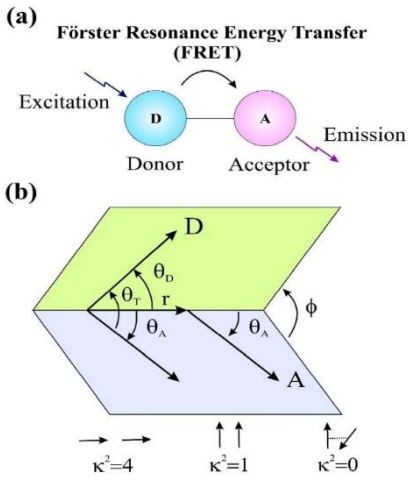

Figure 2.5: *(a) Schematic illustration of the FRET process (b) Dependence of the orientation factor k^2 on the directions of the emission and absorption dipoles of the donor and acceptor, respectively.*

2.5. Linear Sweep Voltammetry (LSV):

Linear Sweep Voltammetry (LSV) is a basic potentiostatic sweep method. It is equivalent to a one-segment cyclic voltammetry experiment. In LSV, working electrode potential is swept linearly between final and initial values and current is measured as a function of time. The most common output from an LSV experiment is current vs. potential, called a voltammogram./alert] At its most basic level, LSV sweeps potential vs. reference electrode in one direction, often through the electroactive species' E^0, which allows for the investigation of the resulting electrochemical species generated at the electrode surface. LSV provides both qualitative and quantitative information about electrochemical systems and has become well-established as a fast and reliable characterization tool. LSV is often used to study the kinetics of electron transfer reactions, including catalysis, and has been expanded for use in organic and inorganic synthesis, sensor and biological system evaluation, and fundamental physical mechanics of electron transfer reactions, such as reversibility, formal potentials, and diffusion coefficient determination. In an LSV experiment, potential is swept linearly from an initial to final potential, sampling current at specified intervals (Figure 2.6). potentiostats have digital waveform generators on board. This means that linear sweeps are approximated by a series of small stair steps, whose step size is defined by the 16-

bit resolution Analog-to-Digital converter (ADC) on the circuit board and current/potential range selected.

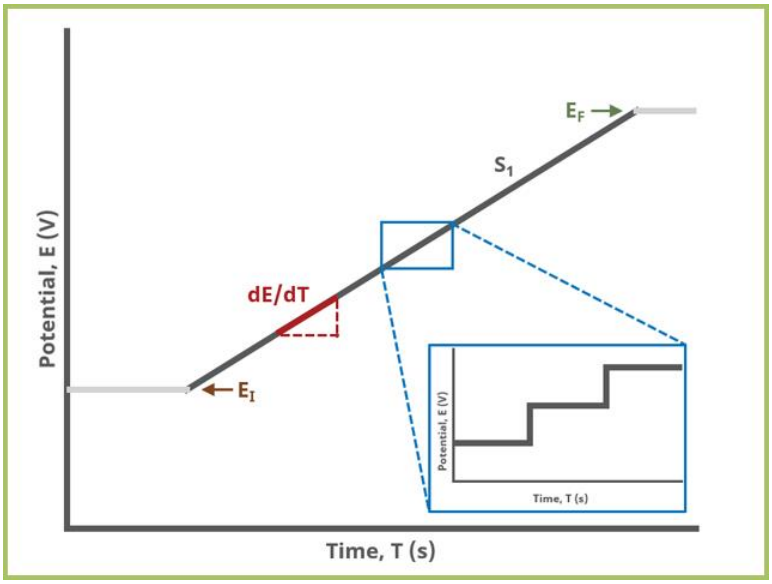

Figure 2.6: *Linear Sweep Voltammetry (LSV) typical waveform.*

For example, on the WaveDriver 100, the current step resolution on the ±100 nA range is

$$\frac{200nA}{2^{16}} = 3.1pA \tag{2.24}$$

2.6. Preclinical Animal Model:

2.6.1. General Handling of Animals: All animal studies and experimental procedures were performed at Central Animal Facility, Dept. of Zoology, Uluberia College, India (Reg. No.: 2057/GO/ReRcBi/S/19/CPCSEA) following the protocol approved by the Institutional Animal Ethics Committee as per standard guideline of Committee for Control and Supervision of Experiments on Animals (CCSEA), Ministry of Fisheries, Animal Husbandry and Dairying, Govt. of India. Healthy non-diabetic BALB/c and Swiss albino mice of both sexes (age: 5-6 weeks, body weight, BW: 20±2.3 g) were used in the current study. All the experimental animals were kept in standard, clean polypropylene cages and maintained normal environmental condition as per guidelines (temperature 21 ± 1 °C; relative humidity 45–55%; 1:1 light and dark cycle). Pathogen free water and standard laboratory pellet diet for mice (Saha Enterprise, Kolkata, India) were available ad libitum throughout the experimental period. All mice were allowed to acclimatize

for 2 weeks before the treatment. Autoclaved nest material and paper houses served as cage enrichment for mice. All the mice were allowed to acclimatize for 2 weeks before beginning of the treatment protocol. Animal cages were always randomly assigned to treatment or control groups.

2.6.2. Dextran Sulfate Sodium (DSS) Induced Ulcerative Colitis Mice Model: In chapter 8 study, we evaluated the potential of Ch-Mn_3O_4 NPs in the treatment of DSS-induced Ulcerative Colitis (UC) in BALB/c mice, a well-known animal model for testing therapeutic interventions against UC [5]. DSS in mice causes human ulcerative colitis-like pathologies due to its toxicity to colonic epithelial cells, which results in compromised mucosal barrier function. It induces intestinal inflammation by most likely damaging the epithelial monolayer lining of the large intestine, which allows proinflammatory intestinal contents to spread into underlying tissue. Treatment with DSS promotes ROS production which leads to activation of inflammatory cascades responsible in the pathogenesis of UC. The weight loss, diarrhoea, and occult blood in stool are common clinical observations found in the DSS-induced colitis mouse model, which is very much similar to the human UC pathologies [6]. Therefore, an efficient reversal of damage in this mouse model is supposed to reflect the possible effects of a compound in higher animals. The purpose of this study was to assess the potential of orally-administrable Chitosan capped Mn_3O_4 NPs (Ch-Mn_3O_4 NPs) as a therapeutic agent for rapid recovery from ulcerative colitis. To define *in vivo* effects of Ch-Mn_3O_4 NPs, we selected BALB/c mice as our preclinical animal model. In brief, the therapeutic potential of Ch-Mn_3O_4 NPs was evaluated along with histopathological changes, inflammatory cytokines level, mitochondrial activity etc. And disease activity index (DAI) was monitored in time dependent manner. The experimental model of UC was established according to the previously stated protocol [5].

Mice were randomly divided into four groups (N=10/group): (1) control; (2) DSS; (3) DSS+Ch-Mn_3O_4NPs; (4) Ch-Mn_3O_4 NPs. Animals of Group 1 served as control and received normal saline (150 µL; oral). Animals of Group 2 served as diseased model and received 5% DSS in drinking water for 12 days. Animals of Group 3 received 5% DSS in drinking water for 12 days. Animals of Group 4 served as NPs control and received single oral dose of Ch-Mn_3O_4 NPs (0.25mg kg^{-1} BW) on a daily basis for 15 days. After development of severe UC on day 13, Group 2

animals left untreated, Group 3 animals received single oral dose of Ch-Mn_3O_4 NPs (0.25mg kg^{-1} BW) on a daily basis for 15 days. All doses were finalized based on reported literature, bio-compatibility study and pilot experimentation. As chitosan treatment did not improve the symptoms of ulcerative colitis, that group was not included in our treatment protocol.

2.6.3. Sub-Chronic Toxicity of Ch-Mn_3O_4 NPs in Experimental Mice: BALB/c mice were randomly divided into four groups (N=10/group). Ch-Mn_3O_4 NPs was administrated through oral gavage at three dose levels i.e. 0.25mg kg^{-1} BW, 0.5 mg kg^{-1} BW and 1 mg kg^{-1} BW correspond to low, intermediate and high dose respectively for 28 days[7]. Normal saline was administrated to the mice of control group. Treatment was done once daily for 28 days. At 29th day all animals were sacrificed after 24 hours of last administration of doses.

2.6.4. Bio-distribution of Ch-Mn_3O_4 NPs in Experimental Mice: For bio-distribution study, Ch-Mn_3O_4 NPs was administrated through oral gavage for 07 days in BALB/c mice. Normal saline was administrated to the mice of control group. Treatment was done once daily for 07 days. At 8th day all animals were sacrificed after 24 hours of last administration of doses.

2.6.5. Evaluation of Potential Use of C-Mn_3O_4NPs as Organ Specific Contrast Agent in Mice Model: In chapter 9, we evaluate the potential use of citrate-functionalized Mn_3O_4 nanoparticles (C-Mn_3O_4NPs) as a targeted X-ray contrast agent for lungs and brain in Swiss albino mice model. New diagnostic strategy for the better management of diseases is the need of the hour. However, in most cases, these new diagnostic techniques are expensive and require trained expertise. To develop a cost effective and easy technique, modification of some of the conventional diagnostic techniques can be useful. Here, we are focusing on the direct observation of the accumulation of reactive oxygen species (ROS) using X-ray induced radiolucency.

In this study, mice were randomly divided into three groups (N=06/group): (1) Control; (2) C-Mn_3O_4 NPs; (3) FA-Mn_3O_4 NPs. Animals of Group 1 served as control and received PBS. Animals of Group 2 received single dose of C-Mn_3O_4NPs (0.25mg kg^{-1} BW). Animals of Group 3 received single dose of FA-Mn_3O_4 NPs (0.25mg kg^{-1} BW). After treatment, all the animals subjected to X-ray imaging. All the treatment was done through tail vein injection.

2.7. Systems and Molecular Probes:

2.7.1. Human Serum Albumin (HSA): Serum albumins are multi-domain proteins forming the major soluble protein constituent (60% of the blood serum) of the circulatory system [8]. Human Serum Albumin (HSA) (molecular weight 66,479 Da) is a heart-shaped tri-domain protein (Figure 2.7) with each domain comprising of two identical subdomains A and B with each domain depicting specific structural and functional characteristics [9]. HSA having 585 amino acid residues assumes solid equilateral triangular shape with sides ~80 Å and depth ~30 Å [10]. Its amino acid sequence comprises of 17 disulfide bridges distributed over all domains, one free thiol (Cys34) in domain-I and a tryptophan residue (Trp214) in domain-IIA. About 67% of HSA is α-helical while the rest of the structure being turns and extended polypeptides [10]. Each domain contains 10 principle helices (h1-h10). Subdomains A and B share a common motif that includes h1, h2, h3 and h4 for subdomain-A, and h7, h8, h9, h10 for subdomain-B. The nonexistence of disulfide linkage connecting h1 and h3 in subdomain-IA is an exception. HSA is engaged with various physiological functions involving maintenance of osmotic blood pressure, transportation of a wide variety of ligands in and out of the physiological system. The protein binds various kinds of ligands [11] including photosensitizing drugs and nanoparticles [12]. The principal binding regions are located in subdomains IIA and IIIA of which IIIA binding cavity is the most active one [10] and binds digitoxin, ibuprofen and tryptophan. Warfarin, however, occupies a single site in domain-IIA. It is known that HSA undergoes reversible conformational transformation with change in pH of the protein solution [11, 13], which is veryessential for picking up and releasing the drugs at sites of differing pH inside the physiological system. At normal pH (pH = 7), HSA assumes the normal form (N) which abruptly changes to fast migrating form (F) at pH values less than 4.3, as this form moves “fast” upon gel electrophoresis [14]. Upon further reduction in pH to less than 2.7 the F-form changes to the fully extended form (E). On the basic side of the normal pH (above pH = 8), the N-form changes to basic form (B) and above pH = 10, the structure changes to the aged form (A). Serum albumin undergoes an ageing process when stored at low ionic strength and alkaline pH. The ageing process is catalyzed by the free sulfhydryl group and

involves sulfhydryl-disulfide interchange that results in the conservation of the sulfhydryl at its original position.

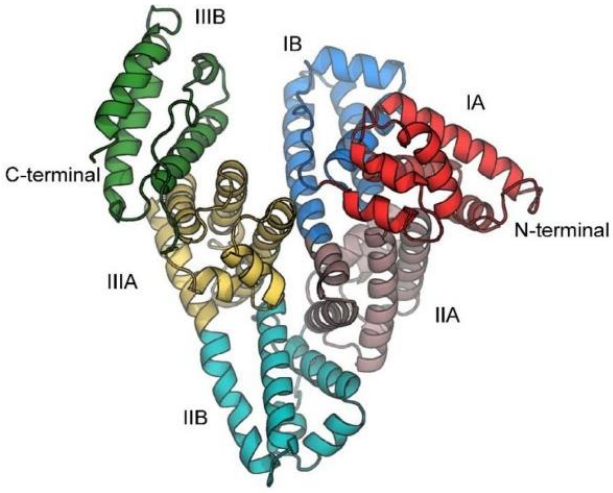

Figure 2.7: *Structure of Human Serum Albumin (HSA). Different domains and subdomains are marked with different colors.*

2.7.2. Bilirubin (BR): Bilirubin (BR), the yellow-orange breakdown product of normal heme catabolism in mammalian systems, introduces great biological and diagnostic values[15]. Both antioxidant and toxic properties have been attributed to BR [16], which is normally conjugated with glucuronic acid and then excreted in the bile. However, when its conjugation with glucuronic acid is inhibited, as in neonatal jaundice and in hereditary forms of congenital jaundice, excess BR bind and deposit to various tissues, giving rise to severe hyperbilirubinemia and neurotoxicity. Phototherapy, the most effective treatment for jaundice to date, decreases the BR levels in the blood by changing the ZZ-BR isomer into water-soluble ZE-BR [17-19]. Because this reaction is readily reversible, equilibrium is established between native BR and the ZE isomer when BR is photoirradiated in a closed system. The second fastest reaction that occurs when BR is exposed to light is the production of lumirubin, a structural isomer of BR[20].

2.7.3. 2,2-Diphenyl-1-picrylhydrazyl (DPPH): 2,2-Diphenyl-1-picrylhydrazyl (DPPH) is a stable nitrogen centered free radical having a strong purple color and is conventionally used to determined free radicalscavenging activities of natural and synthetic antioxidants [21]. Neutralization of this radical by antioxidants can happen through either direct reduction via electron transfers or radical quenching

via hydrogen atom transfer [22]. The strong absorption band centered at 520 nm disappears upon neutralization and the solution becomes colorless. In conventional literature, the change in DPPH absorbance after the addition of a test material is often used as an index of the antioxidant capacity of the material [23-25].

2.7.4. 2'-7'-Dichlorofluorescin diacetate (DCFH-DA): Dichlorofluorescin diacetate (DCFH-DA) is a cell permeable fluorogenic probe widely used in measurement of various reactive oxygen species (ROS). After internalization into the cell, DCFH-DA is readily deacetylated by cellular esterases to non-fluorescent DCFH carboxylate anion (for *in vitro* assays de-esterification is achieved using NaOH)[26-28]. Subsequently, two-electron oxidation of DCFH by intracellular (or extracellular for *in vitro* assays) ROS results in the formation of a fluorescent product, 2'-7'dichlorofluorescein (DCF), which can be monitored by several fluorescence-based techniques (e.g., spectroscopy, confocal microscopy, flow cytometry) [29, 30]. The fluorescence intensity of DCF quantifies the intracellular (or extracellular) ROS and oxidative stress [31, 32].

2.7.5. 3-(4,5-dimethylthiazol-2-yl)-2,5-diphenyl tetrazoliumbromide (MTT): 2'-7'3-(4,5-Dimethylthiazol-2-yl)-2,5-diphenyltetrazolium bromide (MTT) is a water-soluble tetrazolium dye that is converted into an insoluble purple formazan due to the catalytic activity of mitochondrial succinate dehydrogenase in living cells. Hence, the reduction of MTT to formazan crystal is dependent on mitochondrial respiration and reflects to the metabolic activity of a cell [33]. The formazan product is estimated by measuring the absorbance at 550 nm after dissolution in DMSO and widely used to determine cell viability. It has to be noted that, cells with low metabolic activities i.e., thymocytes and splenocytes reduce very low amount of MTT, whereas, rapidly dividing cells reduce more. Moreover, the assay condition can greatly influence the metabolic activity of a cell, subsequently leading to altered tetrazolium dye reduction without affecting cell viability.

2.7.6. Rhodamine-123 (Rh-123): Rhodamine 123 (Rh-123) is a cell-permeable, cationic, green-fluorescent dye (λ_{ex}=503 nm; λ_{em}=527 nm) that is readily sequestered by active mitochondria without any cytotoxic effects. This is widely used as a sensitive and specific probe to monitor mitochondrial membrane potential ($\Delta\Psi m$)asmitochondrial energization induces red shift along with quenching of Rh-123 fluorescence. The rate of fluorescence decay is proportional

to the mitochondrial membrane potential [34]. The measurements can be performed using flow cytometry, fluorescence microscopy and spectroscopy.

2.7.7. Luminol: Luminol (5-Amino-2,3-dihydro-1,4-phthalazinedione) is one of the best knownand most widely used chemiluminescent compounds, which glows with a bright bluelight when activated with an oxidizing agent like hydrogen peroxide (H_2O_2) in analkaline solution in the presence of a catalyst. Reaction of the compound with theoxidant results in replacement of nitrogen and hydrogen with oxygen. As a result, thevibrational energy created by the reaction is transferred to an electron which is pushedup to a higher energy level which is subsequently emitted in the form of a photon(λ_{em}=425 nm) during its return to the stable lower energy ground state. Luminolchemiluminescence is often used as an indicator to detect present of OH radicals in asolution[35].

2.7.8. MitoSOX™ Red: MitoSOXTM Red (Thermo Fisher Scientific, USA) is a non-toxic cell-permeable fluorogenic dye (λ_{ex}=510 nm; λ_{em}=580 nm) that specifically targets mitochondria in living cells. As it produces red fluorescence explicitly in presence of superoxide (not in presence of other reactive oxygen or nitrogen species), it is widely used to probe mitochondrial superoxide content as a marker of oxidative stress [36]. This reagent may be used to distinguish artefacts of isolated mitochondrial preparations from direct measurements of superoxide generated in the mitochondria of live cells. It may also provide a valuable tool in the discovery of agents that modulate mitochondrial redox state in various pathologies.

2.7.9. JC-1: JC-1 is a lipophilic, fluorescent, cationic carbocyanine dye which accumulates in the mitochondria in a concentration-dependent manner. The dye exists as a monomer at low concentrations and yields green fluorescence (λ_{ex}=510 nm; λ_{em}=527). While, at higher concentrations, the dye forms J-aggregates that exhibit a broad excitation spectrum and a red shift in the emission maxima (λ_{ex}=585 nm; λ_{em}=590 nm). Thus, in healthy cells with a normal ($\Delta\Psi m$), the JC-1 dye enters and accumulates in the energized and negatively charged mitochondria and spontaneously forms red fluorescent J-aggregates. By contrast, in unhealthy or apoptotic cells it enters the mitochondria but to a lesser degree since the inside of the mitochondria is less negative because of increased membrane permeability and consequent loss of electrochemical potential. Under this condition, JC-1 does not

reach a sufficient concentration to trigger the formation of J aggregates thus retaining its original green fluorescence.

Based on these premises, the red/green fluorescence ratio of the dye in the mitochondria can be considered as a direct assessment of the state of the mitochondria polarization whereas the higher is the ($\Delta\Psi m$), the more elevated is the red shift of the dye (more J aggregates are formed). Vice-versa; the lower is the ($\Delta\Psi m$) of the mitochondria and the lower is the red to green ratio of the fluorescent marker (few J aggregates are formed). Therefore, mitochondrial depolarization is indicated by a reduction in the red to green fluorescence intensity ratio[37].

2.7.10. 4-(Dicyanomethylene)-2-methyl-6-(4-dimethylaminostyryl)-4*H*-pyran: 4-(Dicyanomethylene)-2-methyl-6-(4-dimethylaminostyryl)-4*H*-pyran (DCM) is a red laser dye that consists of dicyanomethylene as an electron acceptor and dimethylaniline group as an electron donor. It has a π-conjugated 4*H*-pyran-4-ylidiene which bridges both the acceptor/donor groups. It can be used as a dopant and also in organic solid state lasers. It can be used as a laser dye to enhance the emission of distributed feedback (DFB) device by Förster resonance energy transfer (FRET). This also be used as a capping layer that allows the conversion of blue to red colored emission in organic light emitting diodes (OLED) [38]. DCM may also find potential applications in the enhancement of energy transfer of different devices like metal organic frameworks (MOFs), dye sensitized solar cells (DSSCs) and polarity sensors.

Reference

[1] S. R. Phillips, L. J. Wilson, and R. F. Borkman, Acrylamide and iodide fluorescence quenching as a structural probe of tryptophan microenvironment in bovine lens crystallins, *Curr. Ey. Res.,* 5 (1986) 611.

[2] J. Stetefeld, S. A. McKenna, and T. R. Patel, Dynamic light scattering: A practical guide and applications in biomedical sciences, *Biophys. Rev.,* 8 (2016) 427.

[3] L. Stryer, Fluorescence energy transfer as a spectroscopic ruler, *Annu. Rev. Biochem.,* 47 (1978) 819.

[4] D. Banerjee and S. K. Pal, Simultaneous binding of minor groove binder and intercalator to dodecamer DNA: Importance of relative orientation of donor and acceptor in FRET, *J. Phys. Chem. B.,* 111 (2007) 5047.

[5] B. Chassaing, J. D. Aitken, M. Malleshappa, and M. Vijay-Kumar, Dextran sulfate sodium (DSS)-induced colitis in mice, *Curr. Protoc. Immunol.,* 104 (2014) 15.

[6] I. Okayasu, S. Hatakeyama, M. Yamada, T. Ohkusa, Y. Inagaki, and R. Nakaya, A novel method in the induction of reliable experimental acute and chronic ulcerative colitis in mice, *Gastroenterology,* 98 (1990) 694.

[7] A. Shakya, S. K. Chaudhary, H. R. Bhat, and S. K. Ghosh, Acute and sub-chronic toxicity studies of Benincasa hispida (Thunb.) cogniaux fruit extract in rodents, *Regul. Toxicol. Pharmacol.,* 118 (2020) 104785.

[8] G. Franglen, Plasma Albumin, *S*tructure and Function of Plasma Proteins, *Springer*, Berlin, 1974, 265.

[9] M. Dockal, D. C. Carter, and F. Ruker, The three recombinant domains of human serum albumin. Structural characterization and ligand binding properties, *J. Biol. Chem.,* 274 (1999) 29303.

[10] X. M. He and D. C. Carter, Atomic structure and chemistry of human serum albumin, *Nature,* 358 (1992) 209.

[11] J. Ghuman, P. A. Zunszain, I. Petitpas, A. A. Bhattacharya, M. Otagiri, and S. Curry, Structural basis of the drug-binding specificity of human serum albumin, *J. Mol. Biol.,* 353 (2005) 38.

[12] M. Wardell, Z. Wang, J. X. Ho, J. Robert, F. Ruker, J. Ruble*, et al.*, The atomic structure of human methemalbumin at 1.9 A, *Biochem. Biophys. Res. Commun.,* 291 (2002) 813.

[13] G. Piccione, D. Alberghina, S. Marafioti, C. Giannetto, S. Casella, A. Assenza*, et al.*, Electrophoretic serum protein fraction profile during the different physiological phases in Comisana ewes, *Reprod. Domest. Anim.,* 47 (2012) 591.

[14] B. Liu, Y. Pang, R. Bouhenni, E. Duah, S. Paruchuri, and L. McDonald, A step toward simplified detection of serum albumin on SDS-PAGE using an environment-sensitive flavone sensor, *Chem. Commun. (Camb).,* 51 (2015) 11060.

[15] J. T. G. Overbeek, C. Vink, and H. Deenstra, The solubility of bilirubin, *Recueil. des. Travaux. Chimiques. des. Pays-Bas.,* 74 (1955) 81.

[16] R. Stocker, A. N. Glazer, and B. N. Ames, Antioxidant activity of albumin-bound bilirubin, *Proc. Natl. Acad. Sci. U.S.A.,* 84 (1987) 5918.

[17] P. Woodgate and L. A. Jardine, Neonatal jaundice: Phototherapy, *BMJ. Clin. Evid.,* 2015 (2015).

[18] A. A. Lamola, W. E. Blumberg, R. McClead, and A. Fanaroff, Photoisomerized bilirubin in blood from infants receiving phototherapy, *Proc. Natl. Acad. Sci. U.S.A.,* 78 (1981) 1882.

[19] G. Agati and F. Fusi, New trends in photobiology. Recent advances in bilirubin photophysics, *J. Photochem. Photobiol .B.,* 7 (1990) 1.

[20] J. F. Ennever, A. T. Costarino, R. A. Polin, and W. T. Speck, Rapid clearance of a structural isomer of bilirubin during phototherapy, *J. Clin. Invest.,* 79 (1987) 1674.

[21] S. C. Ghagane, S. I. Puranik, V. M. Kumbar, R. B. Nerli, S. S. Jalalpure, M. B. Hiremath*, et al.*, In vitro antioxidant and anticancer activity of Leea indica leaf extracts on human prostate cancer cell lines, *Integr. Med. Res.,* 6 (2017) 79.

[22] E. J. Garcia, T. L. Oldoni, S. M. Alencar, A. Reis, A. D. Loguercio, and R. H. Grande, Antioxidant activity by DPPH assay of potential solutions to be applied on bleached teeth, *Braz. Dent. J.,* 23 (2012) 22.

[23] A. Khan, H. Nazar, S. M. Sabir, M. Irshad, S. I. Awan, R. Abbas, M. Akram, A. Khaliq, J. B. Rocha, S. D. Ahmad, F. Malik, Antioxidant activity and inhibitory effect of some commonly used medicinal plants against lipid per-oxidation in mice brain, *Afr. J. Tradit. Complement. Altern. Med.,* 11 (2014) 83.

[24] A. Tai, T. Sawano, F. Yazama, and H. Ito, Evaluation of antioxidant activity of vanillin by using multiple antioxidant assays, *Biochim. Biophys. Acta.,* 1810 (2011) 170.

[25] E. B. Culhuac, A. Maggiolino, M. Elghandour, P. De Palo, and A. Z. M. Salem, Antioxidant and anti-inflammatory properties of phytochemicals found in the yucca genus, *Antioxidants (Basel),* 12 (2023) 574.

[26] E. Eruslanov and S. Kusmartsev, Identification of ROS using oxidized DCFDA and flow-cytometry, *Methods. Mol. Biol.* 594 (2010) 57.

[27] R. P. Rastogi, S. P. Singh, D. P. Hader, and R. P. Sinha, Detection of reactive oxygen species (ROS) by the oxidant-sensing probe 2',7'-dichlorodihydrofluorescein diacetate in the cyanobacterium Anabaena variabilis PCC 7937, *Biochem. Biophys. Res. Commun.,* 397 (2010) 603.

[28] A. Aranda, L. Sequedo, L. Tolosa, G. Quintas, E. Burello, J. V. Castell, Gombau, L., Dichloro-dihydro-fluorescein diacetate (DCFH-DA) assay: A quantitative method for oxidative stress assessment of nanoparticle-treated cells, *Toxicol. In Vitro,* 27 (2013) 954.

[29] B. Kalyanaraman, V. Darley-Usmar, K. J. Davies, P. A. Dennery, H. J. Forman, M. B. Grisham, G. E. Mann, K. Moore, L. J. Roberts II, H. Ischiropoulos, Measuring reactive oxygen and nitrogen species with fluorescent probes: Challenges and limitations, *Free. Radic. Biol. Med.,* 52 (2012) 1.

[30] L. R. de Haan, M. J. Reiniers, L. F. Reeskamp, A. Belkouz, L. Ao, S. Cheng, B. Ding, R. F. van Golen, M. Heger, Experimental conditions that influence the utility of 2'7'-.dichlorodihydrofluorescein diacetate (DCFH(2)-DA) as a fluorogenic biosensor for mitochondrial redox status, *Antioxidants (Basel).,* 11 (2022) 1424.

[31] X. Wang and M. G. Roper, Measurement of DCF fluorescence as a measure of reactive oxygen species in murine islets of Langerhans, *Anal. Method.,* 6 (2014) 3019.

[32] W. J. Koopman, S. Verkaart, S. E. van Emst-de Vries, S. Grefte, J. A. Smeitink, and P. H. Willems, Simultaneous quantification of oxidative stress and cell spreading using 5-(and-6)-chloromethyl-2',7'-dichlorofluorescein, *Cytometry A.,* 69 (2006) 1184.

[33] J. van Meerloo, G. J. Kaspers, and J. Cloos, Cell sensitivity assays: The MTT assay, *Methods. Mol. Biol.,* 731 (2011) 237.

[34] A. Baracca, G. Sgarbi, G. Solaini, and G. Lenaz, Rhodamine 123 as a probe of mitochondrial membrane potential: Evaluation of proton flux through F_0 during ATP synthesis, *Biochim. Biophys. Acta.,* 1606 (2003) 137.

[35] H. Kobayashi, E. Gil-Guzman, A. M. Mahran, Rakesh, D. R. Nelson, A. J. Thomas, Jr.*, et al.*, Quality control of reactive oxygen species measurement by luminol-dependent chemiluminescence assay, *J. Androl.,* 22 (2001) 568.

[36] B. A. Roelofs, S. X. Ge, P. E. Studlack, and B. M. Polster, Low micromolar concentrations of the superoxide probe MitoSOX uncouple neural mitochondria and inhibit complex IV, *Free. Radic. Biol. Med.,* 86 (2015) 250.

[37] K. Elefantova, B. Lakatos, J. Kubickova, Z. Sulova, A. Breier, Detection of the mitochondrial membrane potential by the cationic dye jc-1 in l1210 cells with massive overexpression of the plasma membrane ABCB1 drug transporter, *Int. J. Mol. Sci.,* 19 (2018) 1985.

[38] G. Somasundaram, V. Rajaraman, V. Mahalingam, K. Rajendran, Electrostatic investigation of 4-dicyanomethylene-2,6-dimethyl-4h-pyran (DDP) dye with amide derivatives in water, *ACS Omega,* 5 (2020) 751.

CHAPTER 3

Instrumentation and Sample Preparation

In this chapter, the details of the instrumental setups, sample preparation techniques, and experimental protocols used for the studies described in this thesis have been described. Furthermore, details about the *in silico* (i.e., computational) studies have been included in this chapter.

3.1. Instrumental Setup:

3.1.1. Steady-State Absorption and Fluorescence Spectroscopy: Steady-state UV-Vis absorption and emission spectra of the molecules of interest were recorded using Shimadzu Model UV-2600 spectrophotometer (Shimadzu Corporation, Kyoto, Japan) and Jobin Yvon Fluoromax-3® spectrofluorimeter (Horiba, Kyoto, Japan), respectively. Schematic ray diagrams of these two instruments are shown in Figures 3.1 and 3.2.

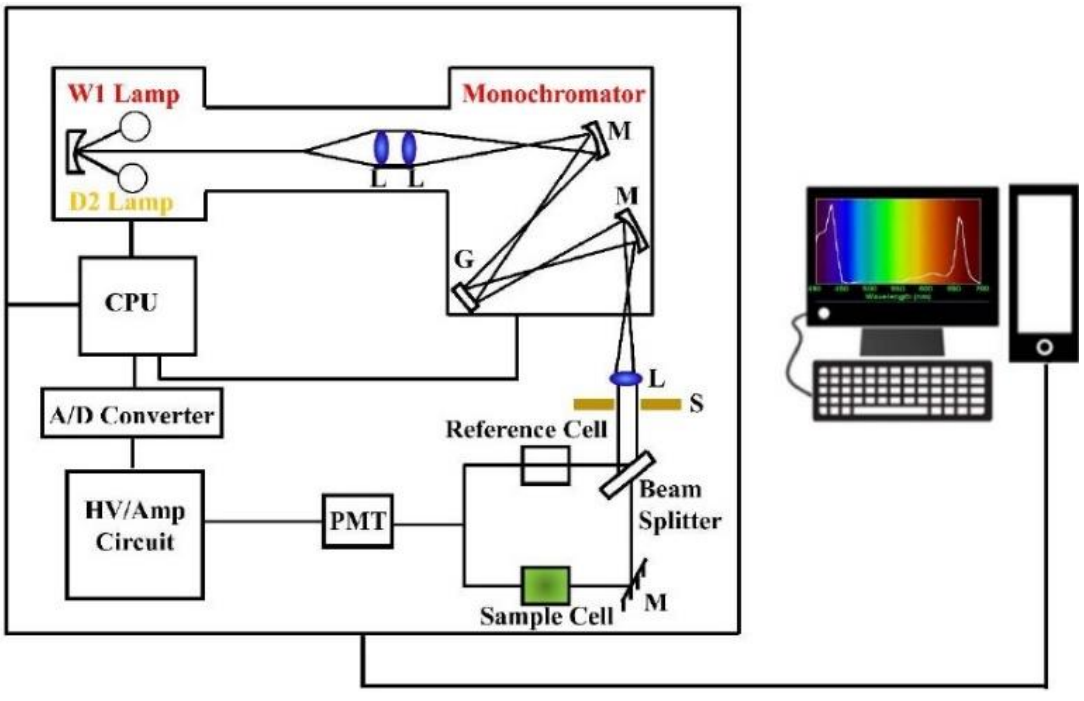

Figure 3.1: *Schematic ray diagram of an absorption spectrophotometer. Tungsten halogen (W1) and deuterium lamps (D2) are used as light sources in the visible and UV regions, respectively. M, G, L, S, PMT designate mirror, grating, lens, shutter and photomultiplier tube, respectively. CPU, A/D converter and HV/amp indicate central processing unit, analog to digital converter and high-voltage/amplifier circuit, respectively.*

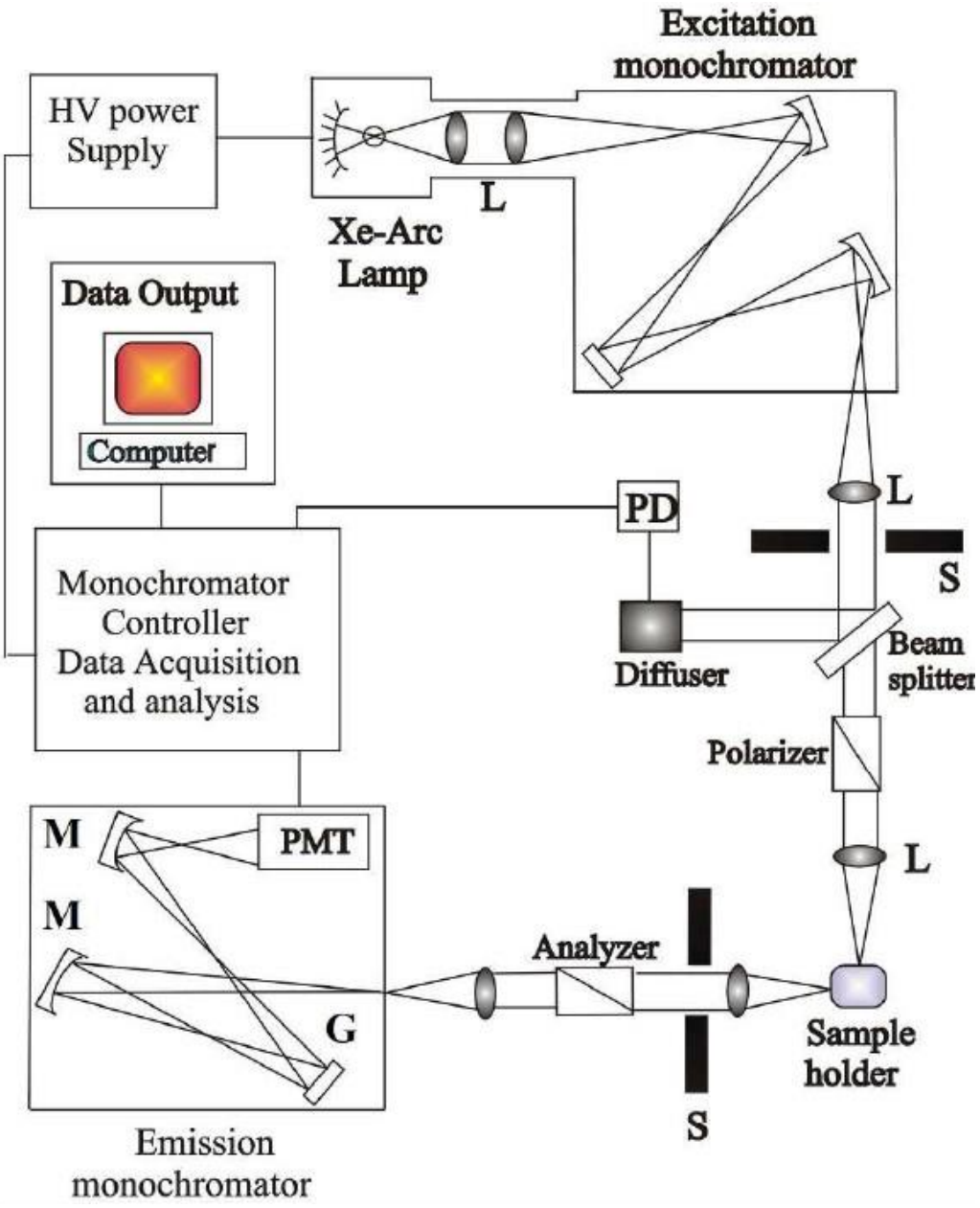

Figure 3.2: *Schematic ray diagram of an emission spectrofluorometer. M, G, L, S, PMT and PD represent mirror, grating, lens, shutter, and photomultiplier tube and reference photodiode, respectively.*

3.1.2. Time-Correlated Single Photon Counting (TCSPC) Technique: All the picosecond-resolved fluorescence transients were recorded using TCSPC technique. The schematic block diagram of a TCSPC system is shown in Figure 3.3. TCSPC setup from Edinburgh instruments, UK, was used during fluorescence decay acquisitions. The instrument response functions (IRFs) of the laser sources at different excitation wavelengths varied between 70 ps to 80 ps. The fluorescence from the sample was detected by a photomultiplier after dispersion through a grating monochromator [1]. For all transients, the polarizer in the emission side was

adjusted to be at 54.7° (magic angle) with respect to the polarization axis of excitation beam.

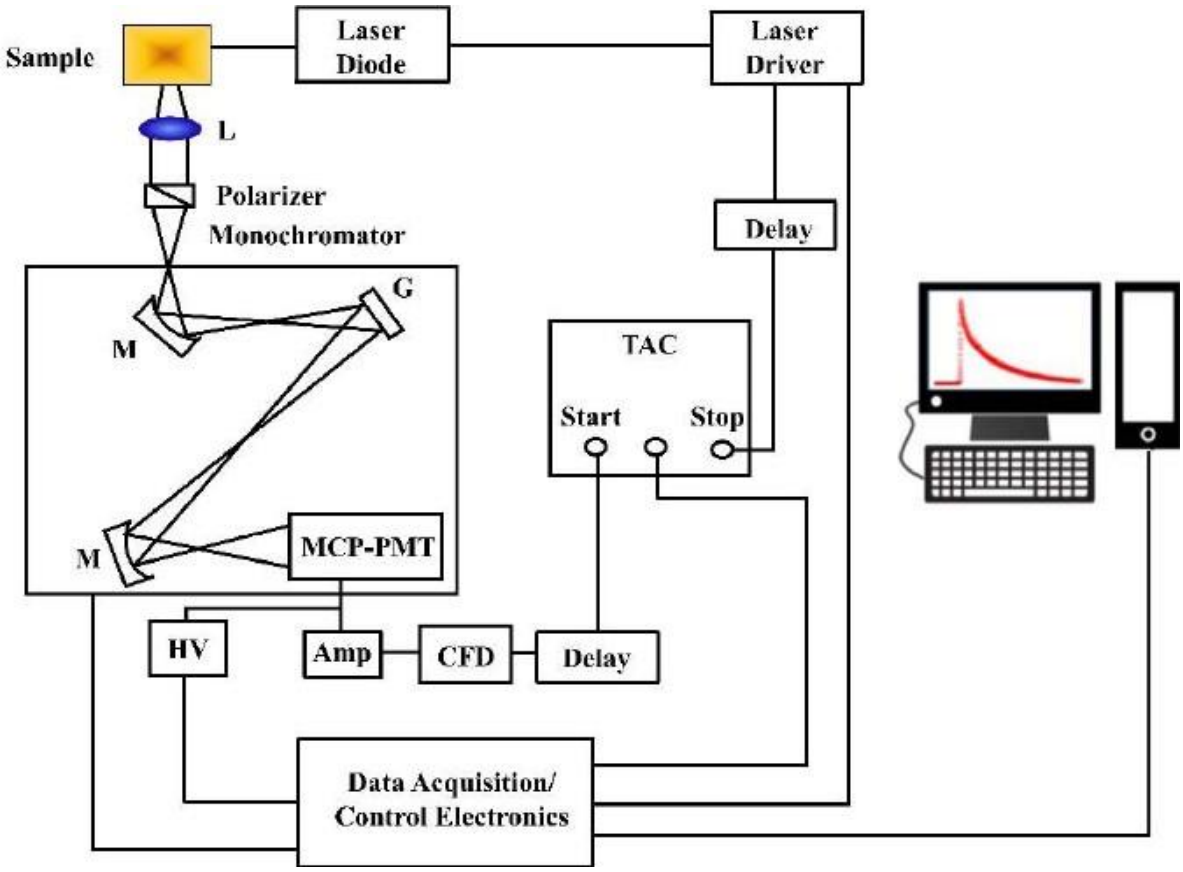

Figure 3.3: *Schematic ray diagram of a time correlated single photon counting (TCSPC) spectrophotometer. A signal from microchannel plate photomultiplier tube (MCP-PMT) is amplified (Amp) and connected to start channel of time to amplitude converter (TAC) via constant fraction discriminator (CFD) and delay. The stop channel of the TAC is connected to the laser driver via a delay line. L, M, G and HV represent lens, mirror, grating and high voltage source, respectively.*

3.1.3. Dynamic Light Scattering (DLS): Dynamic light scattering (DLS), also known as Photon Correlation Spectroscopy (PCS) or Quasi-Elastic Light Scattering (QELS), is one of the most popular techniques used to determine the hydrodynamic size of the particle. DLS measurements were performed on a Nano S Malvern instruments, UK employing a 4 mW He-Ne laser (λ= 632.8 nm) and equipped with a thermostatic sample chamber. The instrument allows DLS measurements in which all the scattered photons are collected at 173˚ scattering angle (Figure 3.4). The instrument measures the time dependent fluctuation in intensity of light scattered from the particles in solution at a fixed scattering angle. The ray diagram of the DLS setup is shown in Figure 3.4.

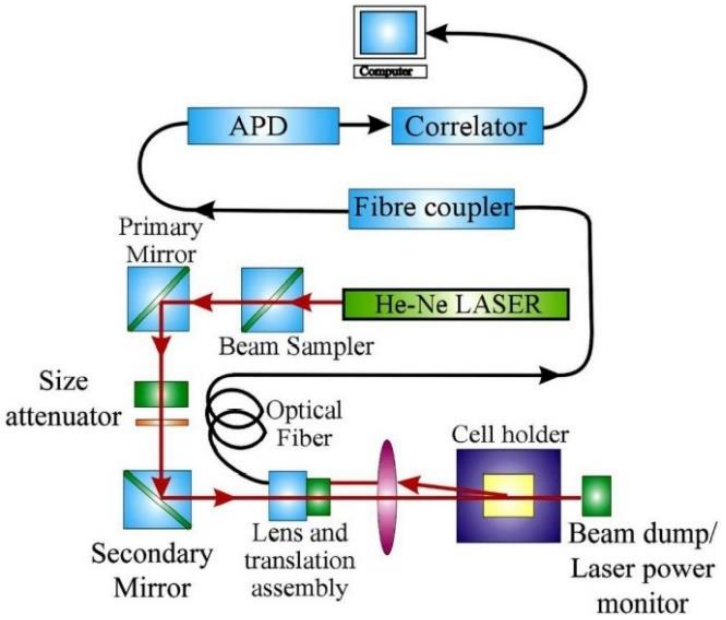

Figure 3.4: *Schematic ray diagram of dynamic light scattering (DLS) instrument. The avalanche photo diode (APD) is connected to preamplifier/amplifier assembly and finally to correlator. It has to be noted that lens and translational assembly, laser power monitor, size attenuator, laser are controlled by the computer.*

3.1.4. X-ray Diffraction (XRD) Measurement: XRD is a popular and a powerful technique for determining crystal structure of crystalline materials. By examining the diffraction pattern, one can identify the crystalline phase of the material. Small angle scattering is useful for evaluating the average interparticle distance while wide-angle diffraction is useful for refining the atomic structure of nanoclusters. The widths of the diffraction lines are closely related to strain and defect size and distribution in nanocrystals. As the size of the nanocrystals decreases, the line width is broadened due to loss of long-range order relative to the bulk. This XRD line width can be used to estimate the size of the particle by using the Debye-Scherrer formula,

$$D = \frac{0.9\lambda}{\beta cos\theta} \tag{3.1}$$

Here, D is the nanocrystal diameter, λ is the wavelength of light, β is the full-width half-maximum (FWHM) of the peak in radians, and θ is the Bragg angle. XRD measurements were performed on a PANalytical XPERT-PRO diffracto-meter (Figure 3.5) equipped with CuKα radiation (λ = 1.5418 Å at 40 mA, 40 kV). XRD patterns were obtained by employing a scanning rate of 0.02° s^{-1} in the 2θ range from 15° to 75°.

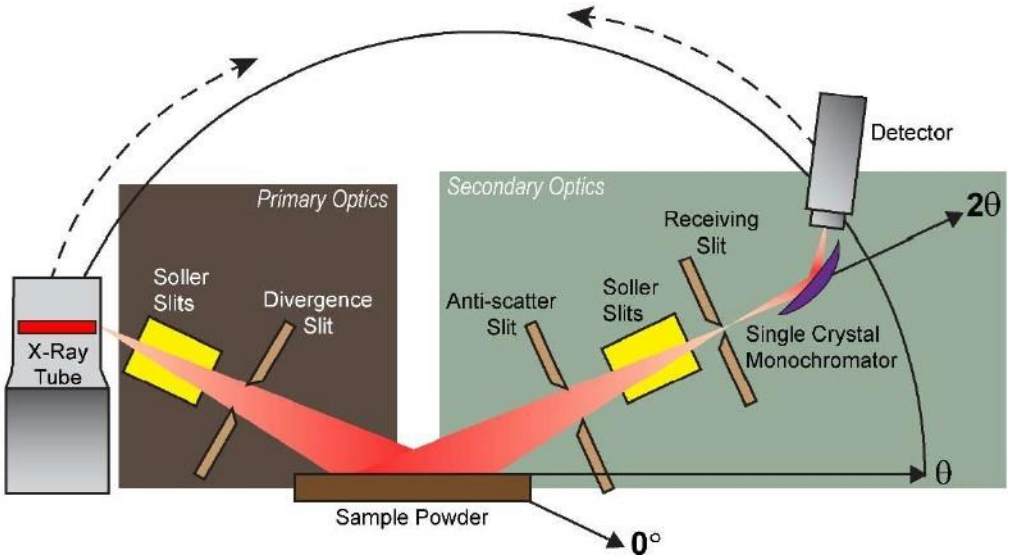

Figure 3.5: *Schematic diagram of X-ray diffraction (XRD) instrument. By varying the angle θ, the Bragg's law conditions, nλ=2dsinθ are satisfied by different d-spacings in polycrystalline materials. Plotting the angular positions and intensities of the resultant diffracted peaks of radiation produces a pattern, which is characteristic of the sample.*

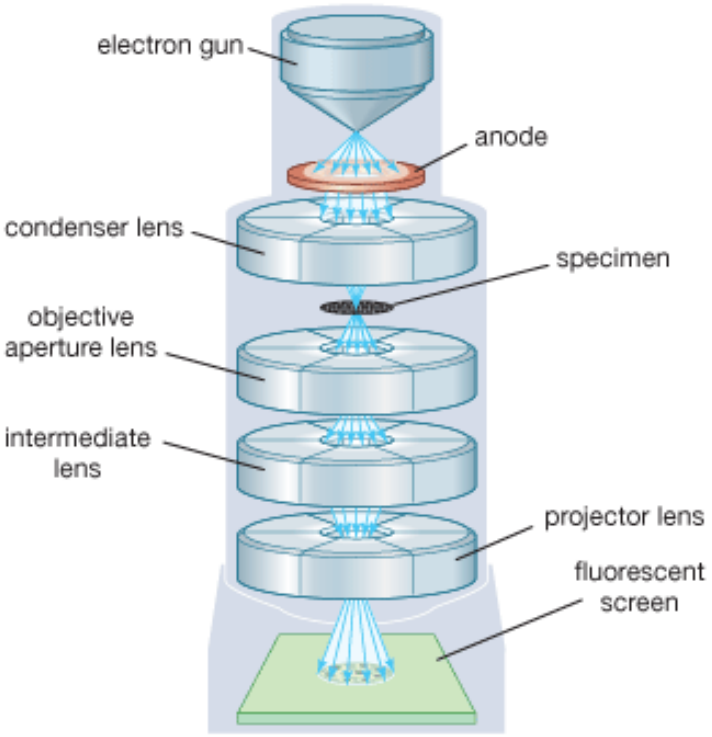

Figure 3.6: *Schematic diagram of a typical transmission electron microscope (TEM). After the transmission of electron beam through a specimen, the magnified image is formed either in the fluorescent screen or can be detected by a CCD camera.*

3.1.5. Transmission Electron Microscope (TEM): A FEI TecnaiTF-20 field-emission high-resolution TEM (Figure 3.6) equipped with an energy dispersive X-ray (EDAX) spectrometer was used to characterize the microscopic structures of samples and to analyze their elemental composition. The sizes of the nanoparticles

were determined from the TEM images obtained at 200 kV acceleration voltage of the microscope. Samples for TEM were prepared by placing a drop of the nanoparticle solution on a 300-mesh carbon-coated copper grid and allowing the film to evaporate overnight at room-temperature.

3.1.6. Scanning Electron Microscope (SEM): Surface characterization of nanomaterials were performed by field emission scanning electron microscopy (FESEM, QuantaTM 250 FEG, FEI Company, Oregon, USA). An electron-gun is attached to SEM and the electrons from filament triggered by 0 KV to 30 KV voltages. These electrons go first through a condenser lens and then through an objective lens, followed by an aperture to finally reach the specimen. The high energy electrons bombard the sample and back again giving secondary electrons. The signal from secondary electrons are detected by detector and amplified. The ray diagram of the SEM setup is shown in Figure 3.7.

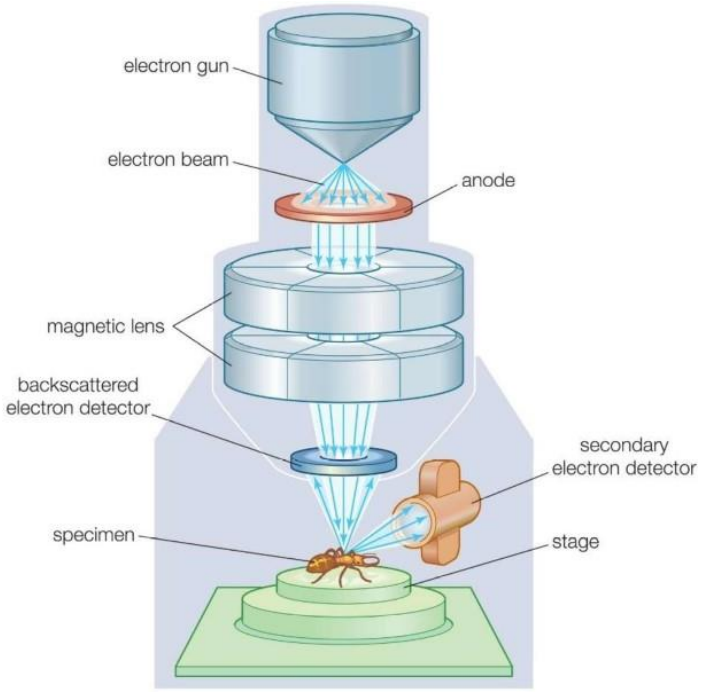

Figure 3.7: *Schematic diagram of typical scanning electron microscope (SEM).*

3.1.7. Fourier Transformed Infrared (FTIR) Measurement: FTIR spectroscopy is a technique that can provide very useful information about functional groups in a sample. An infrared spectrum represents the fingerprint of a sample with absorption peaks which corresponds to the frequencies of vibrations between the bonds of the atoms making up the material. As each different material is a unique combination

of atoms, no two compounds produce the exact same infrared spectrum. Therefore, infrared spectroscopy can result in a positive identification (qualitative analysis) of every different kind of material. In addition, the size of the peaks in the spectrum is a direct indication of the amount of material present.

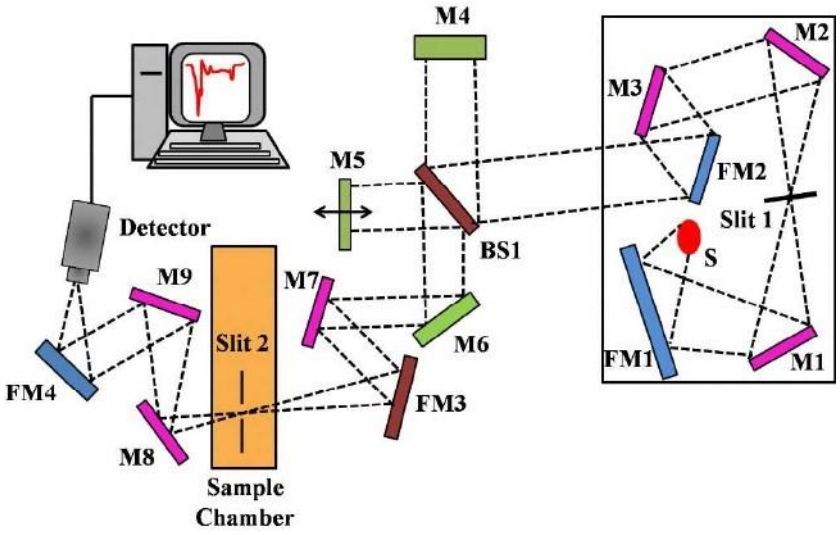

Figure 3.8: *Schematic of Fourier Transform Infrared (FTIR) spectrometer. It is basically a Michelson interferometer in which one of the two fully-reflecting mirrors is movable, allowing a variable delay (in the travel-time of the light) to be included in one of the beams. M, FM and BS1 represent the mirror, focussing mirror and beam splitter, respectively. M5 is a moving mirror.*

The two-beam Michelson interferometer is the heart of FTIR spectrometer. It consists of a fixed mirror (M4), a moving mirror (M5) and a beam-splitter (BS1), as illustrated in Figure 3.8. The beam-splitter is a laminate material that reflects and transmits light equally. The collimated IR beam from the source is partially transmitted to the moving mirror and partially reflected to the fixed mirror by the beam-splitter. The two IR beams are then reflected back to the beam-splitter by the mirrors. The detector then sees the transmitted beam from the fixed mirror and reflected beam from the moving mirror, simultaneously. The two combined beams interfere constructively or destructively depending on the wavelength of the light (or frequency in wavenumbers) and the optical path difference introduced by the moving mirror. The resulting signal is called an interferogram which has the unique property that every data point (a function of the moving mirror position) which makes up the signal has information about every infrared frequency which comes from the source. Because the analyst requires a frequency spectrum (a plot of the intensity at each

individual frequency) in order to make identification, the measured interferogram signal cannot be interpreted directly.

A means of "decoding" the individual frequencies is required. This can be accomplished via a well-known mathematical technique called the Fourier transformation. This transformation is performed by the computer which then presents the user with the desired spectral information for analysis. FTIR measurements were performed on a JASCO FTIR-6300 spectrometer (transmission mode). For the FTIR measurements, powdered sample were mixed with KBr powder and pelletized. The background correction was made using a reference blank of KBr pellet.

3.1.8. Gel Electrophoresis: Electrophoresis is a technique which allows the separations and analysis of charged molecules in an electric field. An electrophoretic set up is composed of two electrodes of opposite charge (anode and cathode), connected by a conducting medium called an 'electrolyte' [2]. The differences in the velocity (v) of the ionic particles determine the separation effect. Velocity is the product of the particle's mobility (m) and the field strength (E):

$$V = mE \tag{3.2}$$

A charged molecule's mobility during an electrophoretic separation is influenced by its size, shape, charge, and temperature of the system. Gel electrophoresis is generally used for separation and purification of proteins and nucleic acids. Agarose gel electrophoresis is suitable for separating DNA fragments composed of a few hundred base pairs to about 20 kb [3]. An agarose gel is a complex network of polymeric molecules whose average pore size depends on the concentration of agarose and buffer composition used. The size of the molecules that can be separated depends on how large the gel's pores are [4]. An agarose gel electrophoresis system consists of electrophoresis chamber and power supply, gel casting trays, sample combs, electrophoresis buffer, loading buffer, ethidium bromide (EtBr), and transilluminator etc. One method of staining DNA is to expose it to the dye EtBr. Under ultraviolet (UV) light, EtBr fluoresces red-orange as it intercalates between the stacking bases of nucleic acids [5]. When electric field is applied across the agarose gel, DNA migrates toward the anode (Figure 3.9). After completion of the

running process, the separated bands on agarose gel are visualized with the help of gel documentation system.

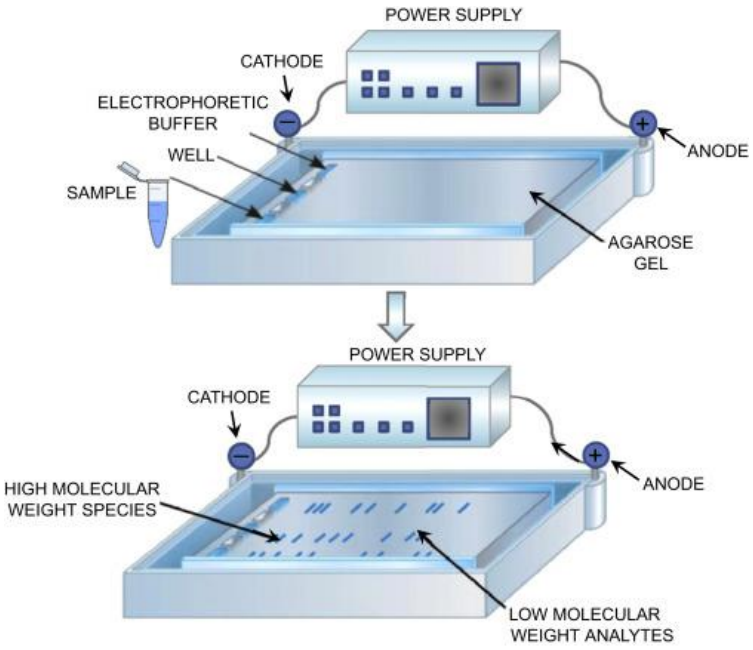

Figure 3.9: *Agarose electrophoresis system.*

3.1.9. Automated Hematology Analyzer: Complete blood count (CBC) and other important hematological parameters of experimental mice were performed by automated hematology analyzer (Sysmex-K1000 Automated Hematology Analyzer). It is composed of hydraulic, pneumatic and electronic systems. The hydraulic system performs the sample dilution, mixing and hemolysis for CBC test. The electronic system analyzes and computes the signals processed by the detector circuit. The pneumatic system produces the constant air pressure and the vacuum for operating master valves and sample transfer in the hydraulic system. The analyzer counts and sizes blood cells using the electric resistance detection method.

The blood samples are aspirated and diluted by the device and then sent through the transducer aperture. A constant DC current flows between an internal electrode and an external electrode in the aperture unit. As blood cells pass through the aperture, they produce the change in the resistance of conductive diluent (Figure 3.10). These alterations are quantified as an increase in the voltage between the electrodes, which is proportional to the size of each cell. Thus blood cells are counted and sized by detecting the conductivity (or resistance) differential between the particle and the diluent in which they are suspended to compute the final estimation.

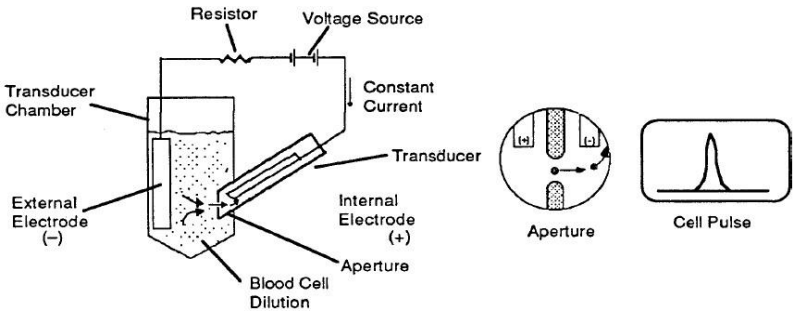

Figure 3.10: *Schematic of electric resistance detection of automated hematology analyzer.*

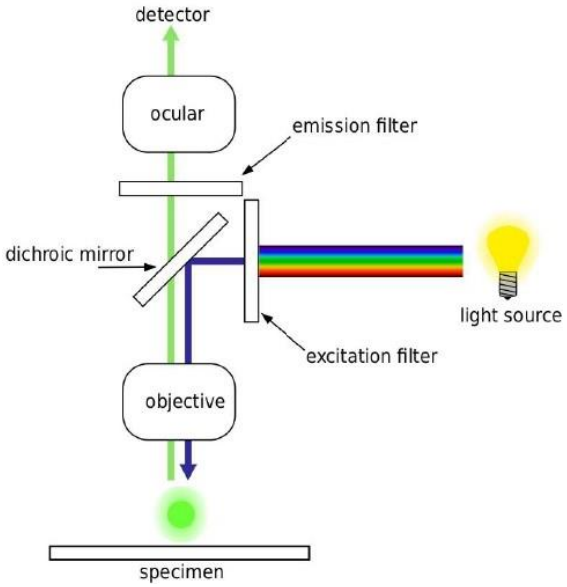

Figure 3.11: *Schematic presentation of the fluorescence microscope.*

3.1.10. Fluorescence Microscope: Commercially available fluorescence microscope (Leica DM6B microscope, Germany) was used in our study to observe the histopathological slides. The light source is usually a mercury-vapor lamp. For bright field, Tungsten-halogen lamp was used. In particular, an inverted setup with a mercury-vapor lamp as light source is shown. The dichroic mirror, excitation and emission filter are joined together within the filter cube (Figure 3.11). Since mercuryvapor lamps emit light over the whole optical spectrum as well as in the ultraviolet range, an optical excitation filter is used to isolate one specific wavelength [6].

Due to the Stokes shift, it is possible to separate excitation and emission light in the same light path optically via a dichroic mirror. This way, only the emission light is

collected by the objective. An emission filter helps to suppress unwanted background light.

3.1.11. Linear Sweep Voltammetry (LSV) Measurements: Linear Sweep Voltammetry (LSV) measurements were carried out at electrochemical workstation (Model CHI1110 C, CH Instruments, TX, USA) in a three-electrode cell at a scan rate of 100 mVs^{-1}. Ag/AgCl in saturated KCl was used as a reference electrode. Platinum wire and Platinum rod were used a counter and working electrode, respectively. 1 M KCl was used as an electrolyte and the sample under study was dissolved in this solution for LSV measurements.

3.1.12. Chronoamperometry Measurements: For chronoamperometry measurements we used a three-electrode cell. Here also, Ag/AgCl in saturated KCl was used as a reference electrode. Platinum wire and Platinum rod were used as counter and working electrode, respectively. Similar to LSV, 1 M KCl was used as electrolyte and the sample under study was dissolved in this solution for LSV measurements. Here the step potential is applied through a potentiostat (Model RPS-3005, METRAVI, India) across the working electrode. Overall, three-cell system was behaving as a RC circuit, and after applying the constant potential of 0.9 V for a definite time, we measured the current decay profile between counter and working electrode with a digital oscilloscope (Model VDS1022, OWON, India).

3.1.13. X-ray Technique:

3.1.13.1. Conventional X-ray System: A radiological examination is one of the most important diagnostic aids available in the medical practice. It is based on the fact that various anatomical structures of the body have different densities for the X-rays. When X-rays from a point source penetrate a section of the body, the internal body structures absorb varying amounts of the radiation. The radiation that leaves the body has a spatial intensity variation, i.e. an image of the internal structure of the body. X-rays are electromagnetic radiation located at the low wavelength end of the electromagnetic spectrum. The X-rays in the medical diagnostic region have wavelength of the order of 10^{-10} m. They propagate with a speed of 3×10^{10} cm s^{-1} and are unaffected by electric and magnetic fields. According to the quantum theory, electromagnetic radiation consists of photons, which are conceived as 'packets' of energy. Their interaction with matter involves an energy exchange and the relation between the wavelength and the photon is given by

$$E = h\nu = h\frac{c}{\lambda} \quad (3.3)$$

Where, h = Planck's constant = 6.32×10^{-34} J s.

c = velocity of propagation of photons (3×10^{10} cm/s).

ν = frequency of radiation

λ = wavelength

A vibration can be characterized either by its frequency or by its wavelength. In the case of X-rays, the wavelength is directly dependent on the voltage with which the radiation is produced. It is, therefore, common to characterize X-rays by the voltage, which is a measure of the energy of the radiation. X-rays are produced whenever electrons collide at very high speed with matter and are thus suddenly stopped. The energy possessed by the electrons appears from the site of the collision as a parcel of energy in the form of highly penetrating electromagnetic waves (X-rays) of many different wavelengths, which together form a continuous spectrum. X-rays are produced in a specially constructed glass tube, which basically comprises (i) a source for the production of electrons, (ii) an energy source to accelerate the electrons, (iii) a free electron path, (iv) a mean of focusing the electron beam and (v) a device to stop the electrons. Stationary mode tubes and rotating anode tubes are the two main types of X-ray tubes.

Figure 3.12. shows a block diagram of basic X-ray machine sub-systems. Basically, there are two parts of the circuit. One of them is for producing high voltage, which is applied to the tube's anode and comprises a high voltage step-up transformer followed by rectification. The current through the tube follows the HT pathway and is measured by a mA metre. A kV selector switch facilitates change in voltage between exposures. The voltage is measured with the help of a kV metre. The exposure switch controls the timer and thus the duration of the application of kV. To compensate for mains supply voltage (230 V) variations, a voltage compensator is included in the circuit. The second part of the circuit concerns the control of heating X-ray tube filament. The filament is heated with 6–12 V of AC supply at a current of 3–5 amperes. The filament temperature determines the tube current or mA, and, therefore, the filament temperature control has an attached mA selector. The filament current is controlled by using, in the primary side of the filament

transformer, a variable choke or a rheostat. The rheostat provides a stepwise control of mA and is most commonly used in modern machines. The kV meter is connected across the primary of the HT transformer. It actually measures volts, whereas it is calibrated in kV, by using an appropriate multiplication factor of the turns-ratio of the transformer. In the older types of diagnostic X-ray generators, the kV meters indicated only noload voltage. In order to obtain the load voltage, which varies with the tube current, a suitable kV metre compensation is provided in the circuit. The kV meter compensator is ganged to the mA selector mechanically. Therefore, the mA is selected first and the kV setting is made afterwards during the operation of the machine. Moving coil meters are used for making current (mA) measurements, while for shorter exposures, an mAs meter, which measures the product of mA and time in seconds is used by moving meters. Block diagram of an X-ray machine have now been generally replaced by digital mA and mAs meters.

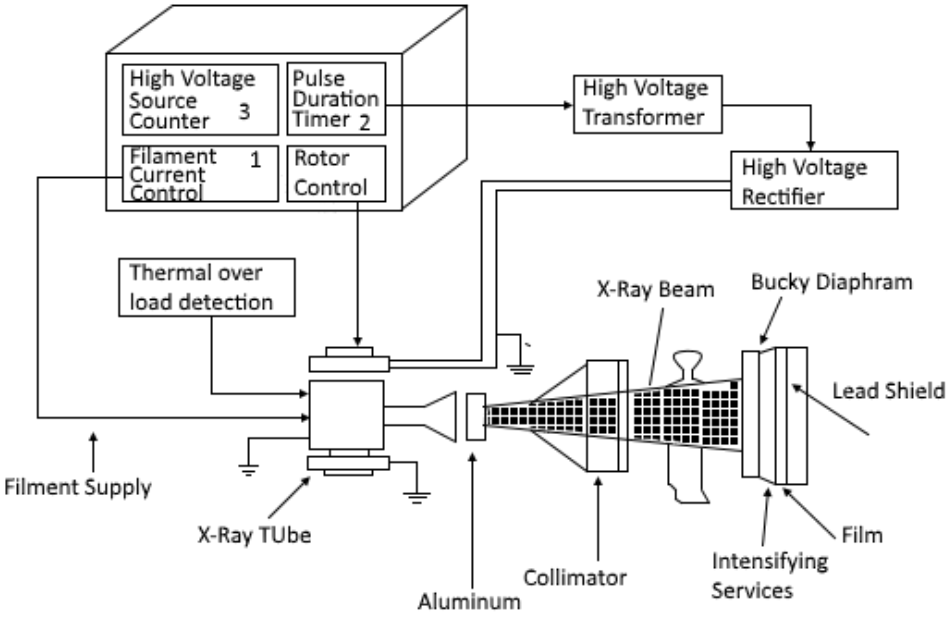

Figure 3.12: *Block diagram of an X-ray machine.*

X-rays normally cannot be detected or visualized directly by the human senses. Therefore, indirect methods need to be utilized to produce an image of the intensity distribution of X-rays that have passed through the body of a patient. X-rays which have a much shorter wavelength than visible light, react with photographic emulsions in a similar fashion as that of light. After having been processed in

developing solution, a film that has been exposed to X-rays shows an image of the X-ray intensity.

3.1.13.2. Digital X-ray System: Figure 3.13 shows a block diagram of digital X-ray system. Electrical charges proportional to X-ray intensity seen by the pixel are stored in the thin film transistor (TFT) storage cap. A number of such pixels form the flat detector panel (FDP). The charges are deciphered by read-out electronics from the FDP and transformed into digital data. The circuit has two chains: the acquisition and the biasing chain. At the beginning of the acquisition chain, an analog front-end is capable of multiplexing the charges on different FDP (channels) storage caps and converting those charges into voltage. The biasing chain generates bias voltages for the TFT array through intermediate bias-and-gate control circuitry. Digital control and data conditioning are controlled by a DSP (Digital Signal Processor), an FPGA (Field Programmable Gate Array), an ASIC (Applications Specific Integrated Circuit) or a combination of these. These processors also manage high-speed serial communications with the external image processing unit through a highspeed interface. (Texas Instruments, 2010).

Temperature sensors, DACs (Digital to Analog Converter), amplifiers and high-input voltage-capable switching regulators are other key system blocks. Each block must synchronize frequenc ies to avoid crosstalk with other blocks in the acquisition chain. The number of FDP pixels determines the number of ADC (Analog to Digital Converter) channels versus ADC speed. Static or dynamic acquisition also determines the ADC speed. While static acquisition means a single image in less than 1 s, dynamic means an image is refreshed at 30 Hz for more specific cardiovascular, fluoroscopic or related applications that require much faster data conversion with the same number of channels. The image signal levels are converted to digital data by an analog front end (AFE). The AFE's sampling speed is determined by the number of pixels in the CCD array and the frame rate. In addition, the AFE corrects sensor errors such as dark current correction, offset voltages and defective pixels. Depending on the signal level, the presence of programmable gain amplifiers (PGAs), the linearity of the PGAs and the range of gains available may also be important. During digitization, the number of bits determines image contrast. Typically, digitizing the initial data with two to four bits more precision than desired in the final image is recommended. For example, if 8 bits of final image data are

required, initially digitize to 10 bits to allow for rounding errors during image processing. The main metric for image quality is detection quantum efficiency (DQE), a combination of contrast and SNR (Signal to Noise Ratio) expressed in percentage. The higher the contrast and lower the noise, the higher the DQE. Contrast is the number of shades of gray determined by the ADC's output resolution. Generally, 14 or 16 bits are suitable for the application. SNR indicates not only SNR from the ADC, but system SNR impact from X-ray dose, pixel size and all electronic components. SNR can be improved by increasing X-ray dose and photodiode spacing and decreasing electronics noise. Increasing the X-ray dose is not suitable for patients or operators. Increasing photodiode spacing may not be suitable because this decreases spatial resolution. Decreasing the noise from the system's electronics is the main challenge. Finally, several image enhancement techniques are used for noise reduction, contrast improvement and edge enhancement. For viewing radiological images, high performance CRT monitors have been commonly used. However, recently active matrix LCD monitors have become popular as they have ergonomic advantages because of shorter depth, lower weight, power consumption and heat output. Their technical properties are very close to the most advanced CRT monitors and no differences of diagnostic performance have been observed with appropriately chosen LCD monitors.

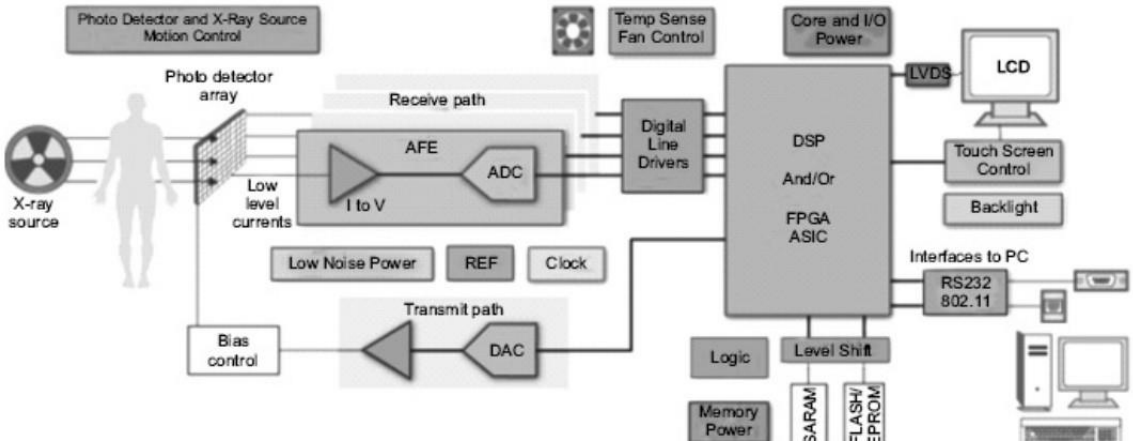

Figure 3.13. *Block diagram of a digital X-ray system.*

3.1.14. Laser Raman Spectroscopy: Raman spectroscopy is a useful technique for the identification of a wide range of substances− solids, liquids, and gases. It is a straightforward, non-destructive technique requiring no sample preparation. Raman

spectroscopy involves illuminating a sample with monochromatic light and using a spectrometer to examine light scattered by the sample.

At the molecular level photons can interact with matter by absorption or scattering processes. Scattering may occur either elastically, or inelastically. The elastic process is termed Rayleigh scattering, whilst the inelastic process is termed Raman scattering. The electric field component of the scattering photon perturbs the electron cloud of the molecule and may be regarded as exciting the system to a 'virtual' state. Raman scattering occurs when the system exchanges energy with the photon and the system subsequently decays to vibrational energy levels above or below that of the initial state. The frequency shift corresponding to the energy difference between the incident and scattered photon is termed the Raman shift. Depending on whether the system has lost or gained vibrational energy, the Raman shift occurs either as an up or down-shift of the scattered photon frequency relative to that of the incident photon. The down-shifted and up-shifted components are called, respectively, the Stokes and anti-Stokes lines. A plot of detected number of photons versus Raman shift from the incident laser energy gives a Raman spectrum. Different materials have different vibrational modes, and therefore characteristic Raman spectra. This makes Raman spectroscopy a useful technique for material identification. There is one important distinction to make between the Raman spectra of gases and liquids, and those taken from solids− in particular, crystals. For gases and liquids it is meaningful to speak of the vibrational energy levels of the individual molecules which make up the material. Crystals do not behave as if composed of molecules with specific vibrational energy levels; instead the crystal lattice undergoes vibration. These macroscopic vibrational modes are called phonons.

In modern Raman spectrometers (Horiba LabRAM set up), lasers are used as a photon source due to their highly monochromatic nature, and high beam fluxes (Figure 3.14). This is necessary as the Raman effect is weak, typically the Stokes lines are ~105 times weaker than the Rayleigh scattered component. In the visible spectral range, Raman spectrometers use notch filters to cut out the signal from a very narrow range centred on the frequency corresponding to the laser radiation. Most Raman spectrometers for material characterization use a microscope to focus the laser beam to a small spot (<1−100 □ m diameter). Light from the sample passes back through the microscope optics into the spectrometer. Raman shifted radiation is detected

with a charge-coupled device (CCD) detector, and a computer is used for data acquisition and curve fitting. These factors have helped Raman spectroscopy to become a very sensitive and accurate technique.

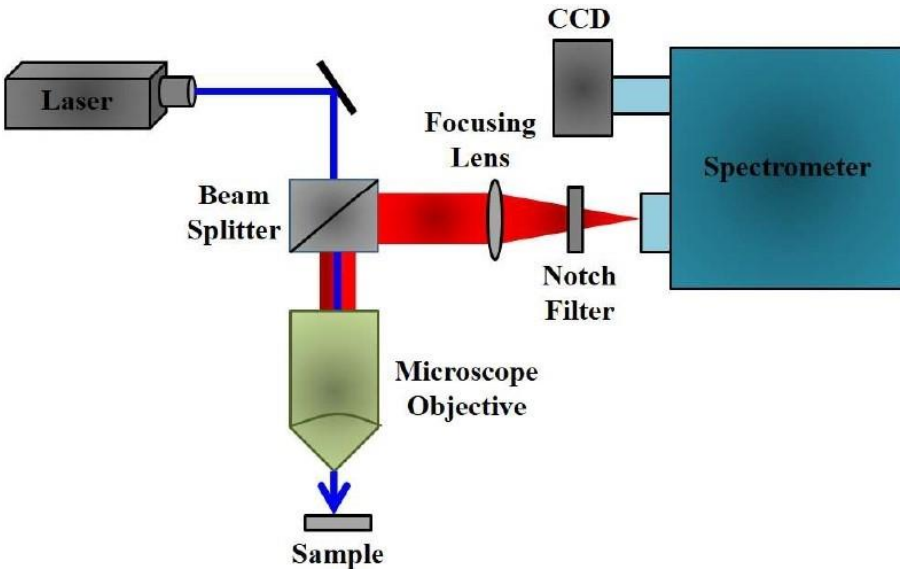

Figure 3.14: *Schematic diagram of a Raman spectrometer is shown.*

3.2. Sample Preparation:

3.2.1. Chemicals Used: Manganese chloride tetrahydrate, 4′,6-diamidino-2-phenylindole (DAPI), ethanol amine (EA), folic acid (FA), thiourea, sodium citrate tribasic, chitosan, lead nitrate, bilirubin, human serum albumin (HSA), 2′,7′ -dichlorofluorescindiacetate (DCFH-DA) and ethidium bromide (EtBr) were obtained from Sigma Aldrich (St Louis, MO, USA). 30% (w/v) Hydrogen peroxide (H_2O_2) was obtained from Merck (NJ, USA). We bought A549 (adenocarcinomic human alveolar basal epithelial cells) cell line from National Centre for Cell Science (NCCS, Pune, India). 3-(4,5-Dimethylthiazol-2-yl)-2,5- diphenyltetrazolium bromide (MTT) and Dulbecco's Modified Eagle's Medium (DMEM), were obtained from Hi-Media (Mumbai, India). Penicillin/streptomycin/neomycin (PSN) anti-biotic, trypsin and fetal bovine serum (FBS), were procured from Gibco-Life Technologies (Gaithersburg, MD, USA). Antibodies were purchased from Santa Cruz Biotechnology, Inc. (USA). We used Millipore water whenever required. All reagents were of analytical grade and used without further purification. All other chemicals were purchased from Sigma Aldrich (St Louis, MO, USA) unless otherwise stated.

3.2.2. Synthesis of the Folate Functionalized Mn_3O_4 (FA-Mn_3O_4) Nanoparticles: Firstly, 207 g of $MnCl_2.4H_2O$ was dissolved in 5 mL of ethanol amine and continuously stirred for 30 minutes (solution I). In the intervening period 27.5 g of folic acid (12.5 mM, pH 8) was dissolved into 5 mL of Milli-Q water (solution II). Then solution II was added dropwise to the solution I. The mixture was then again stirred for 30 minutes. After that required amount of NaOH (0.1 M) was added to the mixture to maintain the solution pH at 7. Then the whole mixture was moved into a Teflon-lined stainless-steel autoclave. It was then kept in a sealed condition at 150 C for 18 hours. After 18 hours the mixture was permitted to cool down to normal temperature. Then we isolated the product with the help of centrifugation. Washing was carried out for four times first with water and ethanol subsequently. The resultant product then dehydrated on water bath until dark orange power was formed.

3.2.3. Synthesis of the Zinc Oxide Nanoflowers (ZnO NF) Functionalized Cotton Cloth: Zinc nitrate hexahydrate [$Zn(NO_3)_2$, $6H_2O$; Sigma-Aldrich] and hexamethylenetetramine ($C_6H_{12}N_4$; Aldrich) were used as the starting materials for a low-temperature hydrothermal synthesis of ZnO NFs on the cotton fiber matrix.

For the synthesis of the ZnO-functionalized cotton cloth, at first, seed layer ZnO nanoparticles of ~5 nm in size were prepared in ethanol. In a typical synthesis process, to a 2 mM zinc acetate [$Zn(CH_3COO)_2{\cdot}2H_2O$; 20 mL in ethanol] solution heated at 55°C, 4 mM sodium hydroxide (NaOH) solution (20 mL of ethanol) was dropwise added under continuous stirring conditions. The glass beaker was then covered tightly with aluminum foil and heated at 65°C for 2 h with continuous stirring. After 2 h, the resultant transparent ZnO nanoparticle colloidal solution (seeding material) was allowed to cool down to room temperature and stored in a refrigerator for further use.

For seeding of the 5 nm ZnO particles on the cotton cloth, the cloths (3 cm × 3 cm) were dipped into the seeding solution for 10 min and then dried into a hot oven operating at 95 °C for 10 min. The procedure was repeated 11 times. Then, the cloth was transferred to an autoclave vessel. An aqueous solution of zinc nitrate (20 mM) and hexamethylenetetramine (20 mM) was used as the precursor solution for the ZnO NF growth, which was carried out at 102 °C for 15 h. This led to the growth of ZnO NFs with a length of ~600−850 nm and a diameter of ~150−300 nm. To

maintain a constant growth rate of the ZnO NFs during the hydrothermal process, the old precursor solution was replaced with a fresh solution every 5 h. The as-obtained ZnO NF samples were then taken out of the reaction vessel and rinsed thoroughly with DI water to remove unreacted residues. Finally, the samples were annealed in air at ~110 °C for 3 h prior to the study.

3.2.4. Synthesis of the Graphitic Carbon Nitride Nanosheets (g-C_3N_4 NS): Initially the bulk phase of g-C_3N_4 was prepared using a pyrolysis technique as reported in previous literature.4 In this context, ~10 g of thiourea was heated in a muffle furnace at ~620 °C for 3 h. After normal cooling, the resultant yellowish white g-C_3N_4 powder (~5 mg) was subjected to ultrasonication in 15 mL of deionized water (for ~6 h). After the completion of the desired time, the exfoliated nanosheets were obtained as a whitish solution.

3.2.5. Synthesis of the Carbon Nitride Nanodots (C-C_3N_4 NDs): 0.1 mg of g- C_3N_4 Ns were dispensed in 10 mL of Millipore water, and the aqueous solution of g- C_3N_4 powder was subjected to ultrasonication for 3 h at room temperature. Then the solution was added to a 1 M solution of sodium citrate tribasic in a 1/1 ratio (v/v). This resultant mixture was stirred for 12 h using a cyclomixer. After 12 h the solution was subjected to centrifugation to eliminate the larger uncapped insoluble particles and water-soluble C- C_3N_4 NDs were collected.

3.2.6. Synthesis of the Chitosan Functionalized Mn_3O_4 (Ch-Mn_3O_4) Nanoparticles: A reported method was followed for the template-free syn-thesis of Mn_3O_4 nanoparticles (NPs) in ambient temperature and pressure [7]. For the capping of nanomaterials, chitosan solution (5 mg/ml) was prepared in 1% acetic acid. Then the pH was adjusted to 6 and as prepared Mn3O4 nanoparticle (50 mg) was added to the 5 ml of chitosan solution. The mixture was then kept for stirring for 24 h in a cyclomixer. After 24 h, using a syringe flter (diameter 0.22 μm) successfully capped NP was separated from non-functionalized bigger nanoparticles.

3.2.7. Synthesis of the Citrate Functionalized Mn_3O_4 (C-Mn_3O_4) Nanoparticles: For synthesis of bulk Mn_3O_4 nanoparticles at standard temperature and pressure we followed a bottom up approach [8]. In a typical procedure, 598 g of $MnCl_2$, $4H_2O$ (3 mmol) was added to 30 ml of ethanol amine (EA) in a beaker, and ultrasonicated at 56 kHz operating frequency for 15 mins. This dissolves $MnCl_2$ to form a clear brown solution. Then equal amount of Mili-Q (from Millipore) water (30 ml) was added

and the resultant mixture was stirred at room temperature for 6 hrs. Then the suspension was centrifuged at 3000 rpm for 15 minutes, and the black precipitate was subsequently washed three times using ethanol in order to remove excess EA. After that it was dried in an incubator at 60°C to get a glossy black powder, the as prepared Mn_3O_4 NPs.

To functionalize the as-prepared Mn_3O_4 NPs with ligand citrate, at first, 0.5 M citrate solution (pH 7.0) was prepared in Milli-Q water. In the ligand solution, as prepared Mn_3O_4 NPs (~150 mg of powder Mn_3O_4 NPs in 6 ml ligand solution) were added and extensively mixed for 10 hrs in a cyclomixer. Finally, we filtered out the nonfunctionalized large NPs using a syringe filter (0.22 μm diameter). The resulting filtrated solution (after proper dilution) was used in further experiments.

3.2.8. Measurement of Photo-Induced ROS Using DCFH: *In vitro* ROS generation ability of the NPs were evaluated using DCFH-DA following a reported method without any modification [9]. In short, DCFH was prepared by the de-esterification reaction of DCFHDA at room temperature. At first, we mixed 0.5 mL of 1.0 mM DCFH-DA in methanol in presence of 2.0 mL of 0.01 (N) NaOH for 30 min at room temperature. The resultant mixture was neutralized with 10 mL of 25 mM NaH_2PO_4 at pH 7.4. The resultant solution was kept at 4°C in the dark until use. To this solution NPs were added and ROS generation capacity was accessed through monitoring of fluorescence emission at 520 nm upon excitation at 488 nm. ROS generation ability at different wavelength of light irradiation after adding the nanoparticle (dispersed in DMSO, water mixture) into reaction media containing DCFH was measured and the change in fluorescence was reported.

3.2.9. Cell Culture: Cells were maintained at 37ºC in 5% CO_2 in Dulbecco's Modified Eagle Medium (DMEM) or RPMI 1640 growth medium (Himedia, India) that contained 10% foetal bovine serum (Invitrogen, USA), L glutamine (2 mM), penicillin (100 units mL^{-1}), and streptomycin (100 ng mL^{-1}) (Sigma, USA). Before experimentation, the cells were washed twice with PBS and incubated with Dulbecco's Modified Eagle Medium (DMEM) or RPMI 1640 medium (FBS, 0.5%) for 1 h and then treated as described in respective figure legends.

3.2.10. Measurement of cell viability: To determine the cell viability MTT assay was performed. After achieving 75–80% confluence, cells were harvested in phosphate buffered saline (PBS) with 0.52 mM EDTA and 0.25% trypsin. The

treatments were performed as described in the figure legends. During the initial screening, cells were incubated with nanoparticles and DMSO water mixture for 6 hours. After 6 hours of incubation, we rinsed the cells with PBS. Then MTT solution was added to each well and kept for 4 h in an incubator to form purple formazan salt. In the next step DMSO was used to solubilize the formazan salt and the absorbance was recorded using an ELISA reader (BioTek Instruments, Inc., Vermont, USA) at specified wavelength. Cell viability was determined as follows:

$$\text{Cell Viability (\%)} = \frac{\text{Abs}_{\text{control}} - \text{Abs}_{\text{sample}}}{\text{Abs}_{\text{control}}} \times 100 \qquad (3.4)$$

ere, $\text{Abs}_{\text{sample}}$ denotes the absorbance values of treated cell and $\text{Abs}_{\text{control}}$ is denoting the same for untreated cells.

3.2.11. *In-cellulo* Photodynamic Therapy (PDT): Based on the initial screening result, a specific concentration was chosen for the *in vitro* PDT assay. A549 cells were incubated in a time-dependent manner (5, 10, 15, 20, 25 and 30 min) with 0.31 mg mL^{-1} of FA-Mn_3O_4 NPs under blue light irradiation following the MTT assay for determination of effective dose of photodynamic therapy.

3.2.12. Measurement of Intracellular ROS Generation: Intracellular ROS production was examined using DCFH-DA, which is a well-known ROS generator. A549 cells were cultured at 37°C in a humidified atmosphere under CO_2 (5%) in DMEM with appropriate supplementation. Firstly, after the treatment with FA-Mn_3O_4 NPs, A549 cells were incubated at 37ºC for 25 min with 10 mM of DCFH-DA. Upon excitation at 488 nm fluorescence intensity was recorded at 522 nm. The intracellular ROS was also measured using fluorescence microscopic technique (Olympus BX51 fluuorescence microscope, Olympus Optical Co. Ltd, Sibuya-ku, Tokyo, Japan) and ImageJ software was used to analyse the photographs.

Secondly, A549 cells were seeded in 6 well plate and were treated with PBS, chitosan (3.4 μgml^{-1}), and Ch-Mn_3O_4 NPs (3.4 μgml^{-1}) for 3 h. Then the incubated cells were then washed with PBS and treated with DCFH-DA probe for 30 min. At the end of this period, the excess amount of DCFH-DA was thoroughly cleaned with PBS. Then cells were scraped and suspended in PBS. The cell suspensions were subjected to the measurement of DCF fluorescence intensity using fluorolog, Model LFI-3751 (Horiba-Jobin Yvon, Edison, NJ) spectrofluorimeter. All spectroscopic experiments were performed using quartz cuvette of path length 1 cm.

3.2.13. Determination of Nuclear Condensation and Fragmentation Using Fluorescence Microscopy: To assess chromatin condensation or nuclear damage, A549 cells were incubated with or without FA-Mn_3O_4 NPs (0.31 mg mL^{-1}) along with light exposure (15 min). Then both groups of cells were stained using DAPI (50 mg mL^{-1}) for 10 min. With a fluorescence microscope (Olympus BX51, Olympus Optical Co. Ltd, Sibuya-ku, Tokyo, Japan) the images were obtained and ImageJ software was used to analyse the images.

3.2.14. Western Blotting Analysis: After protein isolation, mitochondrial and cytosolic content of Bax, Bcl-2 and GAPDH were analyzed using Western blotting. In brief, 25 mM HEPES buffer, pH 7.5, containing 5 mM EDTA, 2 mM dithiothreitol, 1% CHAPS, and 1 mg mL^{-1} pepstatin, leupeptin, and aprotinin were used to homogenize tissue sample. Centrifugation of homogenates were done at 14000g for 20 min at 4ºC. Then the pellet was discarded and supernatants were stored. Protein concentrations in the extracts were evaluated using the bicinchoninic acid kit (Autospan Liquid Gold, Span Diagnostics Ltd., Surat). Then western blotting analysis was done with 10 mg of proteins aliquots. The proteins were transferred electrophoretically (Trans-Blot Turbo Transfer System, Biorad Laboratories Inc., CA, USA) onto poly screen polyvinylidene difluoride (PVDF) membranes (Biorad Laboratories Inc., CA, USA) after subjected to electrophoresis on 15% polyacrylamide gels containing 0.1% SDS, 5% non-fat dried milk dissolved in Tris-buffered saline containing 0.1% Tween 20 (TBST) was used to block the membranes for 1 h at RT. After washing three times with the same, the membrane was incubated with TBST containing 5% dried milk and anti-Bcl-2, anti- Bax and anti-GAPDH monoclonal antibody (Cell Signaling Technology Inc., MA, USA) for 2 h at RT. After repeated washing with TBST, the membrane was incubated with horseradish peroxidase (HRP) conjugated anti-rabbit IgG antibody (Santa Cruz Biotechnology, CA, USA) for 1 h at RT. Protein bands were visualized by using an enhanced chemiluminescence kit and an image analyser. Optical densities of the bands were measured using ImageJ software (http://rsb.info.nih.gov/ij/) and normalized against GAPDH.

3.2.15. Determination of DNA Fragmentation Using Agarose Gel Electrophoresis: Total hepatic DNA was isolated following a standard procedure described earlier [10]. Aliquots of DNA solution were prepared and stored at 4ºC.

From absorption at 260 nm DNA concentration was assessed. Hepatic DNA (5.0 mg) stained with ethidium bromide was loaded on 1.5% agarose gels for observing the DNA fragmentation. We performed electrophoresis for 2 h at 90 V, and gels were photographed under UV transillumination (InGenius3 gel documentation system, Syngene, MD, USA).

3.2.16. Computational Study:

3.2.16.1. Binding Study: The optimized ortho-rhombic ZnO wurtzite unit cell (a = 5.63, b = 3.25, and c = 5.21) with eight atoms was taken to build a large supercell. For binding calculations on the ⟨002⟩, ⟨100⟩, and ⟨101⟩ facets, slabs of atoms with the exposed ⟨002⟩, ⟨100⟩, and ⟨101⟩ phases, respectively, were cut out of the bulk (supercell). For the calculation with a nanosphere, a sphere of a radius of 15 Å was cut out from the bulk and then appropriate surface atoms were removed to make it stoichiometrically neutral. The ACE2-bound SARS-CoV-2 spike protein structure (PDB ID: 6LZG) was obtained from the Protein Data Bank (PDB). ACE2 protein was removed before docking with the nanostructures. The structure of the lectin protein (PDB ID: 4YWA) of P. aeruginosa was also obtained from PDB. Molecular docking was performed using AutoDock Vina following a previously published protocol [11]. The docked structures were energy-minimized under OPLS using the Desmond molecular dynamics program [12] as implemented in Schrodinger Maestro (academic release 2018-4), followed by rescoring with AutoDock Vina. Changes in the atomic positions of the protein backbone after minimization were computed in terms of rmsd.

3.2.16.2. Sequence Analysis: The sequence of the cell surface adhesion lectin protein lecA of *P. aeruginosa* was obtained from the PDB (PDB ID: 4YWA). The structure and sequence of the RBD of SARS-CoV-2 were also obtained from the PDB (ID: 6LZG). Sequence alignment was performed using Clustal Omega [13] with no end gap penalty. Local alignments were performed with LALIGN . Similar amino acids in the binding sites of the two proteins are mapped using PyMOL molecular graphics software.

3.2.16.3. Multiphysics Simulation: Particle (i.e., microbe) flow through the cotton mesh was simulated using laminar flow and particle tracing modules of COMSOL. A two-dimensional periodic model of the mesh was constructed. The fiber diameter

in the model is 10 μm, and the separation between fibers is also kept at 10 μm. The velocity of exhaled air for laminar flow was 5.66 m s^{-1}. Considering the size of bacteria, viruses, and respiratory droplets (e.g., the SARS-CoV-2 diameter was 0.05−0.2 μm, the bacterium diameter was typically 0.5−5.0 μm; the respiratory droplet size during normal breathing was ~1 μm), the particle size and density used were 1 μm and 1.1 g cm3, respectively [14]. Particles move in the air velocity field. On collision with a fiber, a particle either sticks to it or gets scattered. The probability of the particle sticking to the fibrils was set according to the binding energies with ZnO facets and cellulose fibrils. The simulation time was 0.1 s. The increase in the thickness of cellulose fibers due to ZnO deposition was ignored in the simulation.

3.2.16.4. Molecular Docking: Citrate and folate structures were obtained from PubChem database (PubChem CIDs: 135398658 and 31348, respectively). The Mn_3O_4 unit cell was obtained from the Crystallography Open Database with accession ID 1514120. A slab geometry was generated from the bulk Mn_3O_4. The citrate and folate were docked on the nano surface of the Mn_3O_4 slab followed by geometry optimization using previously published protocol [15]. Charge density differences and Bader charge analysis was performed on the optimized geometries. The citrate and folate bound structures were further subjected to molecular dynamics (MD) simulation in explicit solvent (simple point charge water model) under OPLS (optimized potential for liquid simulations) at three different temperatures (7 °C, 37°C and 77°C) following previously published protocol [16].

3.2.17. Antibacterial Tests: The bacterial strains of Gram-negative *P. aeruginosa* and Gram-positive *S. aureus* and *S. hominis* as used in this study were obtained from Dey's Medical Stores Mfg. Ltd., Kolkata, India((they have procuredthe strain from ATCC)). The glassware, suction nozzles, and culture medium were sterilized in an autoclave at a high pressure of 0.1 MPa and a temperature of 120 °C for 30 min before experiments. Bacteria cultures were cultivated in a sterilized Luria-Bertani (LB) broth (Himedia, India), and incubation was done at 37 °C with a shaking incubator for 24 h.

The colony count method was used to estimate antibacterial properties through the concentration of the survival colony bacteria in co-cultured solution. First, original bacterial suspensions were washed three times with phosphate-buffered saline (PBS; pH 7.4) solution to a concentration of 10^8 CFU/mL. Then, they were incubated with

respective nanoparticlesfor 1 hr and sometimes poured onto the ZnO NF-functionalized cotton fabric and incubated for 1 h. Third, the incubated bacterial solution was diluted five times to a certain concentration. The resulting bacterial PBS suspensions (100 μL) were spread on gelatinous LB agar plates, culturing at 37 °C for 24 h. The number of survival colonies was counted manually. For growth curve analysis, the bacterial solution which was diluted five times was added to LB and kept at 37 °C. 600 nm absorbance (or optical density; OD_{600}) was monitored at regular intervals (1 h) to assess the growth kinetics.

The bacteria cells after proper incubation were stained with DAPI and PI. The DAPI stains all cells, while PI only stains the membrane-disrupted cells. The $(1 - \frac{\text{Red}}{\text{Blue}})$ ratio was obtained to assess the survivability of specific bacteria strain. All tests were repeated at least six times. In case of ZnO NF-functionalized cotton fabric, to rule out the role of charge−charge interactions in the antimicrobial effect, we coated the cotton fabric with positively charged poly-L-lysine and performed the plate count experiment with *P. aeruginosa*, following the procedure described above.

3.2.18. Quantification and Characterization of ROS Generated by Nanoparticles: DCFH a very popular chemical for quantification of ROS generation was prepared from DCFH-DA via de-esterification reaction at room temperature following a standardized protocol described in earlier studies [9],[17, 18] ROS generated in the reaction medium reacted with DCFH and convert it to DCF which has a characteristic fluorescence emission maxima at 520 nm when excited at 488 nm. DCFH was allowed to react with increasing concentration of NPs in aqueous medium and fluorescence was recorded using fluorolog, Model LFI-3751 (Horiba-Jobin Yvon, Edison, NJ) spectrofluorimeter. Chemiluminescence produced by oxidized luminol was recorded using fluorolog, Model LFI-3751 (Horiba-Jobin Yvon, Edison, NJ).

3.2.19. Measurement of ROS Via Fenton-Like Reaction Using Luminol: *In vitro*, the ROS generation ability of the NPs via Fenton like reaction were evaluated using the chemiluminescence assay of Luminol following reported methods with slight modification [19, 20]. In short, we use a reaction between $CoCl_2$ and H_2O_2 to produce OH radicals (OH.). Then luminol was added to quantify the ROS generated in this reaction. For C-Mn_3O_4 NPs and $CoCl_2$ complex we did a similar assay to quantify the ROS produced.

3.2.20. Synthesis of Lipid vesicles: The lipid vesicles were synthesized using standard injection methods [21]. Typically the phospholipid were dissolved in chloroform and were injected rapidly in PBS buffer (pH 7.4) followed by vigorous stirring for half an hour. Finally, the chloroform and a part of buffer in the whole mixture were removed by rotary evaporator under reduced pressure. This injection method of liposome preparation is advantageous because of its simplicity, fast implementation and offers the possibility of producing small-sized liposomes with minimal technical requirements.

3.2.21. Förster Resonance Energy Transfer (FRET) Experiment: For a given donor-acceptor (D-A) pair, the efficiency (E) of energy transfer depends critically on the donor-acceptor distance (r) as follows (Equation 3.5) [22]

$$E = \frac{R_0^6}{R_0^6 + r^6} \tag{3.5}$$

The efficiency of energy transfer from a donor (D) to an acceptor (A) is calculated from Equation [22]

$$E = 1 - \frac{\tau_{DA}}{\tau_D} \tag{3.6}$$

Here, τ_{DA} and τ_D denote the fluorescence lifetimes of the donor in presence and absence of the acceptor (DCM), respectively.

3.2.22. Bilirubin Degradation Measurement: The degradation kinetics of bilirubin by C-Mn_3O_4 NPs was recorded at 460 nm wavelength using Shimadzu UV-Vis 2600 spectrometer.

3.2.23. Hemolysis Assay: Human venous blood samples were collected in a heparinized blood collection tube (Ethical Permission No/NMC/ 26, dated 3/1/2018, NRSMH, Kolkata). The whole blood was then divided into four groups and was treated with lead nitrate, lead nitrate with C-C_3N_4 NDs, C-C_3N_4 NDs, and PBS, respectively. After 30 min of incubation, the samples were subjected to centrifugation. Next, the absorbance of the centrifuged samples was determined. The samples were stained with Leishman's stain to observe the microscopic structure of red blood cells (RBCs) using a Leica microscope.

3.2.24. The ABTS Radical Scavenging Assay: The assay was performed using the standard kit purchased from Sigma-Aldrich. We have used 0.5 $\mu g ml^{-1}$ NPs for the experiment. The kit provided trolox solutions as standard. A standard curve for trolox solution was done using the provided solutions. After 5 mins of incubation,

we have observed the absorbance at 405 nm using Shimadzu UV-Vis 2600 spectrometer. The anti-oxidant potential was calculated using the following equation:

$$\text{Anti-oxidant-potential (mM)} = \frac{Absorbance\ at\ 405 - intercept}{Slope} \text{ X Dilution factor} \quad (3.7)$$

3.2.25. Evaluation of Disease Activity Index (DAI) Score: Body weights, hemoccult, gross blood, and stool consistencywere analysed on a daily basis. Disease activity index (DAI) was calculated byscoring percentage of weight loss, intestinal bleeding [no blood, occult blood (haemoccult +), or gross blood], and stool consistency (normal stool, loosestool, or diarrhea), as previously described [23]. The clinical features werescored separately and then correlated with a histological score: DAI = (body weight loss score)+(diarrhea score)+(rectal bleeding score).

3.2.26. Blood Collection: At the end of the experimental period, the animals were euthanized and decapitated after being fasted. Blood was collected from retro orbital plexus just before sacrifice, kept in sterile non-heparinized tubes for further analysis.

3.2.27. Serum Isolation: After collection of blood, kept in sterile non-heparinized tubes in slanting position at 45° angle for 45 min and centrifuged at 3500×g for 20 min. The clear serum (straw colour) was obtained and used in subsequent biochemical analysis.

3.2.28. Measurement of Inflammatory Cytokines Level: All serum samples were sterile, hemolysis-free and were stored at -20°C before determination of the biochemical parameters. The concentration of inflammatory cytokines (IL-1β, and IL-12) was measured according to the respective protocol provided by kit manufacturers (G-Biosciences, St Louis, MO, USA).

3.2.29. Assessment of Hematological Parameters: For hematological studies, the blood was collected in heparinized tubes. Blood-cell count was done using blood smears in Sysmax-K1000 Cell Counter. Parameters studied were hemoglobin, total red blood cells, hematocrit, packed cell volume (PCV), mean corpuscularvolume (MCV), mean corpuscular hemoglobin (MCH), mean corpuscular haemoglobin concentration (MCHC), platelets, total white blood cells etc.

3.2.30. Occult Blood Test: For collection of stool samples, individual mouse was placed in an empty autoclaved cage without bedding. Then mouse was allowed to defecate normally. Once the mouse has defecated 2-3 faecal pellets, mouse was removed from the collection cage. Now the faecal pellets were collected in a

sterilized centrifuge tube using sterile toothpick. And the samples were stored in -80°C freezer. The two field occult blood test in stool sample was performed using commercially available kits (HEMOSPOT; Coral Clinical Systems, Goa, India) following the protocol described by respective manufacturers.

3.2.31. Histopathological Examination: At the end of the experimental period, the animals were sacrificed and different organs along with colons were collected for histological examination [9, 24]. For microscopic evaluation, a conventional technique of paraffin wax sectioning and differential staining was used. Tissues were fixed with 4% paraformaldehyde, embedded in paraffin, and cut into a 5μm thick section. After de-waxing and gradual hydration with ethanol (Merck, USA), the sections were stained with hematoxylin and eosin (SRL, India). The sections were then observed under an optical microscope (Olympus, Tokyo, Japan). It is noteworthy to mention here that the histopathologist was blinded to the treatment groups while scoring and evaluating the samples. For immunohistochemistry, colon sections were incubated for 60 mins with rat anti-mouse caspase-1, NF-κβ p-65antibodies (Santa Cruz Biotechnology) followed by a 30mins incubation with 10 $mgml^{-1}$ FITC conjugated mouse $IgGF_c$ binding antibody (Santa Cruz Biotechnology). To check CD-68 expression, colon sections were incubated for 60 min with rat anti-mouse CD68 antibody (Santa Cruz Biotechnology, India) followed by a 30 min incubation with $10mgml^{-1}$ HRP conjugated rabbit anti-rat secondary antibody (Santa Cruz Biotechnology, India). After detection of peroxidase activity with 3-amino-9-ethylcarbazole (Sigma, USA), sections were counterstained with Mayer's hematoxylin (SRL, India). After that the tissues were viewed by Leica DM6B microscope.

3.2.32. Histology Scoring: The Geobes score has been used for histopathological analysis to evaluate all aspects of mucosal injury in ulcerative colitis. Scoring system is divided in 6 grades: architectural changes [grade 0], chronic inflammatory infiltrate [grade 1], lamina propria neutrophils and eosinophils [grade 2], neutrophils in epithelium [grade 3], crypt destruction[grade 4] and erosions or ulcerations [grade 5], and each grade of the score is divided in 4 subcategories [25]. It is noteworthy to mention here that the histopathologist was blinded to the treatment groups while scoring.

3.2.33. Mitochondria Isolation And Mitochondrial Function Determination: Mitochondria were isolated from mouse colon following the method reported earlier with slight modification [26]. In brief, colon was excised and homogenized in a tissue homogenization medium containing 225mMD-mannitol, 75mM sucrose, 0.05mM EDTA, 10mM KCl, and 10mM HEPES (pH 7.4). The homogenates were centrifuged at 600 ×g for 15min and the resulting supernatants were centrifuged at 8500 ×g for 10min. The pellets were washed thrice and resuspended in the same buffer. All procedures were performed at 4°C. Mitochondrial function was evaluated by determining $\Delta\Psi_m$ using JC-1 (Sigma, MO, USA), ATP production (Abcam, Germany). And then mPTP opening was evaluated in terms of mitochondrial swelling by monitoring the decrease in absorbance at 540 nm after the addition of $CaCl_2$ (100mM).

3.2.34. Bio-Distribution: For bio-distribution study, all the organs of the experimental mice were collected after 7 days of daily single dose treatment with Ch-Mn_3O_4 NPs. After collection, all the tissue samples were dried immediately using liquid nitrogen and weighed. The detection and quantification of Manganese (Mn) content in tissue samples was carried out using Inductively coupled plasma optical emission spectroscopy (ICP-OES) (Agilent Technologies, USA). The tissue samples were digested following the USEPA methods 200.2 revision 2.8 with slight modifications for performing ICP-OES method. After proper filtration, the digested solution was diluted with deionized water to a final volume of 10 mL.

3.2.35. Quantification and Statistical Analysis: All quantitative data are expressed as Mean ± Standard Deviation (SD), unless otherwise stated. One-way analysis of variance (ANOVA) followed by correction of false discovery rate (post hoc FDR: two stage step up method of Benjamini, Krieger and Yekutieli) for multiple comparisons was performed for comparison between multiple groups [27]. Beforehand, the normality of each parameter was checked by normal quantile–quantile plots. Sample size in our animal studies were determined following the standard sample sizes previously been used in similar experiments as per relevant literature. Designated sample size (in figure legends) always refers to biological replicates (independent animals). GraphPad Prism v8.0 (GraphPad Software), and Sigmaplot v14.0 (Systat Software, Inc.) were used for statistical analysis. For all comparisons, a *P* value <0.05 was considered to be statistically significant.

Reference

[1] D. O'Connor, Time-correlated single photon counting, *Academic press*, Cambridge, 2012.

[2] S. Surzycki, Agarose gel electrophoresis of DNA, *Springer, Berlin*, 2000.

[3] D. Voytas, Agarose gel electrophoresis, *Curr. Protoc. Mol. Biol.*, 51 (2000) 2.

[4] P.Y. Lee, J. Costumbrado, C.-Y. Hsu, Y.H. Kim, Agarose gel electrophoresis for the separation of DNA fragments, *J. Vis. Exp.*, (2012) e3923.

[5] J. Sigmon, L.L. Larcom, The effect of ethidium bromide on mobility of DNA fragments in agarose gel electrophoresis, *Electrophor.*, 17 (1996) 1524.

[6] F. Rost, Fluorescence microscopy, applications, *Elsevier,* Amsterdam, 2017.

[7] S. Lei, K. Tang, Z. Fang, H. Zheng, Ultrasonic-assisted synthesis of colloidal Mn_3O_4 nanoparticles at normal temperature and pressure, *Cryst. Growth Des.*, 6 (2006) 1757.

[8] A. Adhikari, N. Polley, S. Darbar, D. Bagchi, S. Pal, Citrate functionalized Mn_3O_4 in nanotherapy of hepatic fibrosis by oral administration, *Future Sci. OA*, 2 (2016) FSO146.

[9] N. Polley, S. Saha, A. Adhikari, S. Banerjee, S. Darbar, S. Das, S.K. Pal, Safe and symptomatic medicinal use of surface-functionalized Mn_3O_4 nanoparticles for hyperbilirubinemia treatment in mice, *Nanomedicine (Lond).* 10 (2015) 2349.

[10] B. Uhal, I. Joshi, A.L. True, S. Mundle, A. Raza, A. Pardo, M. Selman, Fibroblasts isolated after fibrotic lung injury induce apoptosis of alveolar epithelial cells in vitro, *Am. J. Physiol. - Lung Cell. Mol. Physiol.*, 269 (1995) L819.

[11] W. Li, M. Moore, Angiotensin-converting enzyme 2 is a functional receptor for the SARS coronavirus, *Nature*, 2 (2003) 450.

[12] R.N. Kirchdoerfer, C.A. Cottrell, N. Wang, J. Pallesen, H.M. Yassine, H.L. Turner, K.S. Corbett, B.S. Graham, J.S. McLellan, A.B. Ward, Pre-fusion structure of a human coronavirus spike protein, *Nature*, 531 (2016) 118.

[13] F. Sievers, D.G. Higgins, Clustal Omega for making accurate alignments of many protein sequences, *Protein Sci.*, 27 (2018) 135.

[14] M. Loferer-Krossbacher, J. Klima, R. Psenner, Determination of bacterial cell dry mass by transmission electron microscopy and densitometric image analysis, *Appl. Environ. Microbiol.*, 64 (1998) 688.

[15] M.N. Hasan, T.K. Maji, U. Pal, A. Bera, D. Bagchi, A. Halder, S.A. Ahmed, J.H. Al-Fahemi, T.M. Bawazeer, T. Saha-Dasgupta, S.K. Pal, Wide bandgap semiconductor-based novel nanohybrid for potential antibacterial activity: Ultrafast spectroscopy and computational studies, *RSC Adv.*, 10 (2020) 38890.

[16] P. Biswas, A. Adhikari, U. Pal, P. Singh, M. Das, T. Saha-Dasgupta, S.S. Choudhury, R. Das, S.K. Pal, Flexibility modulates the catalytic activity of a thermostable enzyme: Key information from optical spectroscopy and molecular dynamics simulation, *Soft Matter*, 16 (2020) 3050.

[17] C.P. LeBel, H. Ischiropoulos, S.C. Bondy, Evaluation of the probe 2', 7'-dichlorofluorescin as an indicator of reactive oxygen species formation and oxidative stress, *Chem. Res. Toxicol.*, 5 (1992) 227.

[18] R. Cathcart, E. Schwiers, B.N. Ames, Detection of picomole levels of hydroperoxides using a fluorescent dichlorofluorescein assay, *Anal. Biochem.*, 134 (1983) 111.

[19] I.P. Ivanova, S.V. Trofimova, I.M. Piskarev, N.A. Aristova, O.E. Burhina, O.O. Soshnikova, Mechanism of chemiluminescence in Fenton reaction, *J. Biophys. Chem.*, 3 (2012) 88.

[20] Z. Cheng, G. Yan, Y. Li, W. Chang, Determination of antioxidant activity of phenolic antioxidants in a Fenton-type reaction system by chemiluminescence assay, *Anal. Bioanal. Chem. Res.*, 375 (2003) 376.

[21] P. KUMARS, Solvation dynamics of DCM in lipid, *J. Phys. Chem. B*, 104 (2000) 4529.

[22] J. Lakowicz, Principles of fluorescence spectroscopy (ed. Lakowicz, JR), in, *Springer,* Berlin, 2013.

[23] D. Friedman, B. Künzli, A-Rahim YI, Sevigny J, Berberat PO, Enjyoji K, et al. From the Cover: CD39 deletion exacerbates experimental murine colitis and human polymorphisms increase susceptibility to inflammatory bowel disease, *Proc. Natl. Acad. Sci. U.S.A.*, 106 (2009) 16788.

[24] A. Adhikari, S. Darbar, T. Chatterjee, M. Das, N. Polley, M. Bhattacharyya, S. Bhattacharya, D. Pal, S.K. Pal, Spectroscopic studies on dual role of natural flavonoids in detoxification of lead poisoning: Bench-to-bedside preclinical trial, *ACS Omega*, 3 (2018) 15975.

[25] A. Jauregui-Amezaga, A. Geerits, Y. Das, B. Lemmens, X. Sagaert, T. Bessissow, T. Lobatón, M. Ferrante, G. Van Assche, R. Bisschops, A simplified Geboes score for ulcerative colitis, *J. Crohns Colitis.*, 11 (2017) 305.
[26] T. Lampl, J.A. Crum, T.A. Davis, C. Milligan, V.D.G. Moore, Isolation and functional analysis of mitochondria from cultured cells and mouse tissue, *J. Vis. Exp.*, (2015) e52076.
[27] Y. Benjamini, A.M. Krieger, D. Yekutieli, Adaptive linear step-up procedures that control the false discovery rate, *Biometrika*, 93 (2006) 491.

CHAPTER 4

Synthesis and Characterization of a Nanomaterial with Industrial Scaling-up Possibility for Photodynamic Therapeutic Application

4.1. Introduction:

Cancer has become one of the major threats to life expectancy of the global population during the last few decades. According to the Global Cancer Observatory (GLOBOCAN) database and World Health Organization (WHO), approximately 9.6 million deaths occurred from cancer in 2017 [1, 2], among which lung cancer caused the highest rate of mortality compared to other cancer types. The available curatives for cancer e.g., chemotherapy, immunotherapies and surgeries are painful, troublesome and extremely costly. Besides the high cost and side effects, the available curatives have failed to reduce the mortality rate due to cancer, hence, new alternative treatment strategies are extremely necessary.

From its discovery the photodynamic therapy (PDT) is gradually becoming an efficacious alternative [3]. PDT requires minimal invasion for complete destruction of malignant cells, and has less side effects. In most of the cases PDT activates the ROS mediated apoptosis pathway in cancer cells that results in the annihilation of carcinoma [4]. PDT involves administration of photosensitizing agent, which may require some modulation after internalization in specific cells followed by activation of the agent by radiation of a specific wavelength. As a result, some irreversible photo induced damage takes place in targeted cells [3]. Although, proved effective, several limitations (i.e., poor water solubility, aggregate formation, high dermal toxicity and low clearance) [5, 6] of the conventional organic PDT agents hinder widespread application of it in the clinical settings. In recent studies, inorganic nanoparticles emerged as an effective alternative because of its biocompatibility, high retention time in circulation, target specificity (by attaching ligand) and low toxicity [4, 7]. Another problem that confines the use of PDT is the absence of a mechanism that can ensure target specific delivery (sometimes the normal cells become as vulnerable

as cancer cells). In this regard, folic acid (FA) could be used as an inexpensive and stable ligand for targeting folate receptors (FR), a tumour-associated protein over-expressed in cancer cells having high binding affinity towards folic acid ($K_d \approx 10^{-10}$ M) [8]. The strategy of targeting cancer cells through FRs is a well- recognized strategy due to overexpression of FR in a variety of cancer cells including those in breast, kidney, colon, ovaries, cervix and renal cell carcinomas [8].

Recent advances in nanotherapy have created scopes of specific targeting strategies for increasing drug concentrations within tumours while restricting the undesired toxicity to its surrounding healthy cells [9-12]. Some of the nanoparticles are photosensitive agent i.e. those are only active in presence of specific wavelength of light. By tagging folate with photosensitized nanoparticle precise treatment of cancer via PDT is possible. But synthesis of folic acid capped nanomaterial is a multistep and complicated process.

Previously, for synthesis of folic acid capped NPs for biomedical application, various approaches have been utilized, such as use of different organic linkers like 2,3-dibromopropionyl chloride (DBPC), N-hydroxysuccinimide (NHS), 1-ethyl-3-(3-dimethylaminopropyl)-carbodiimide (EDC), polyethylene glycol and polylactic-coglycolic acid based attachment [13-18]. However, the use of organic linkers to functionalize nanoparticles can increase production cost as well as can reduce the efficacy of the nanosystem. So, an alternative facile strategy is extremely needed.

Recently, many studies have used folic acid on nanocarriers for the specific targeting of over-expressing FRs on cancer cells, but information on the capping of folic acid to manganese oxide nanoparticles (Mn_3O_4 NPs) and exploration of its toxic effect have not yet been reported. In the recent years, manganese oxide nanoparticle showed promising results in the field of nanotherapy. By modulating the surface functionalization of this nanoparticle one can modulate its physicochemical, magnetic and optical properties [19]. Its ROS generation ability with different capping ligands [19-21] makes it a potential agent against cancer and associated disorders. In this study we demonstrate a one-step method for the preparation of folic

acid-functionalised manganese oxide nanoparticles (FA-Mn_3O_4 NPs) which have enhanced uptake and toxicity in cancer cells upon blue light irradiation.

4.2. Results and Discussion:

4.2.1. Novel One Pot Synthesis And Spectroscopic Characterization of Folate-Mn_3O_4 Nanohybrid for Potential Photodynamic Therapeutic Application [22]: Functionalization of manganese oxide nanoparticles with organic ligands like folate can significantly alter their surface electronic structures [19]. So, at first we have observed the UV-Vis electronic absorption pattern of as prepared Mn_3O_4 NPs (thin film on quartz plate) (Figure 4.1), folic acid and FA-Mn_3O_4 NPs (~pH 7.0). The as prepared Mn_3O_4 NPs exhibited no distinct signature in the UV-Visible region.

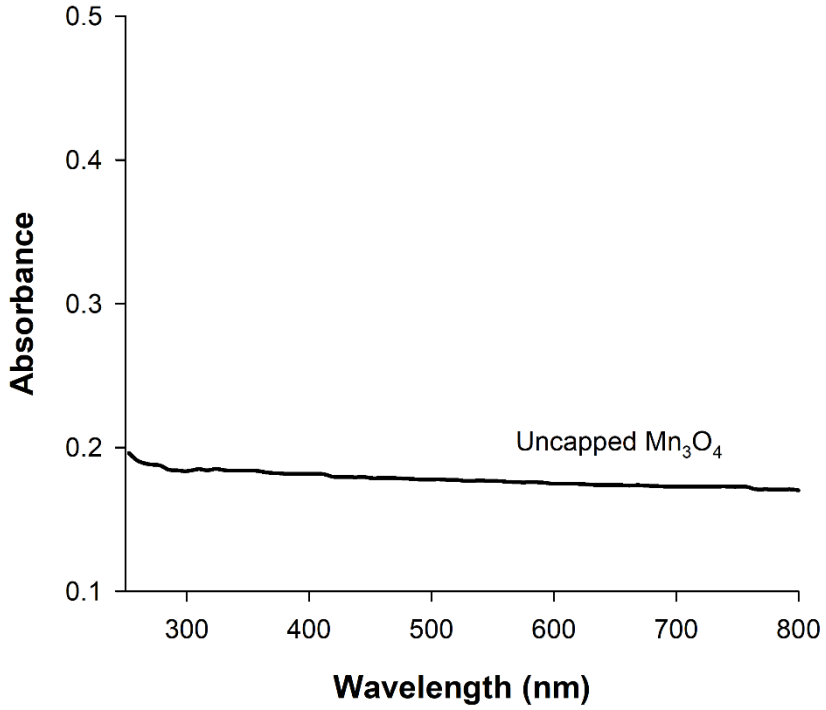

Figure 4.1: *Absorbance of as-prepared Mn_3O_4 nanoparticles thin film on quartz plate. No visible absorbance band is present.*

Folic acid has displayed characteristic absorption pattern with peaks 260 nm and 340 nm (Figure 4.2.a) which can be attributed to π–π* (for both alkyl and aromatic group) and n–π* (due to presence of COOH, –NH, NH_2 and C=O groups) intraligand transitions [23]. In the case of FA-Mn_3O_4 NPs, the characteristic absorption pattern of the folic acid disappeared (shifted by ~40 nm and ~20 nm). Instead, it shows one high energy peak at 300 nm and a shoulder around 360 nm (Figure 4.2.a), along with

a low energy peak at 410 nm (Figure 4.2.a-inset). The peak at 300 nm could be possibly due to ligand-to metal charge transfer (LMCT) processes involving folate–$Mn^{3+}/^{4+}$ interaction, one of the high energy charge transfer process [24]. The other expected LMCT band at around 385 nm has not been appeared in the absorption spectrum presumably because of the more intense absorption at 300 nm that has obscured it. However the band at 385 nm is distinctly visible in the excitation spectrum at around 385 nm (Figure 4.2.b).

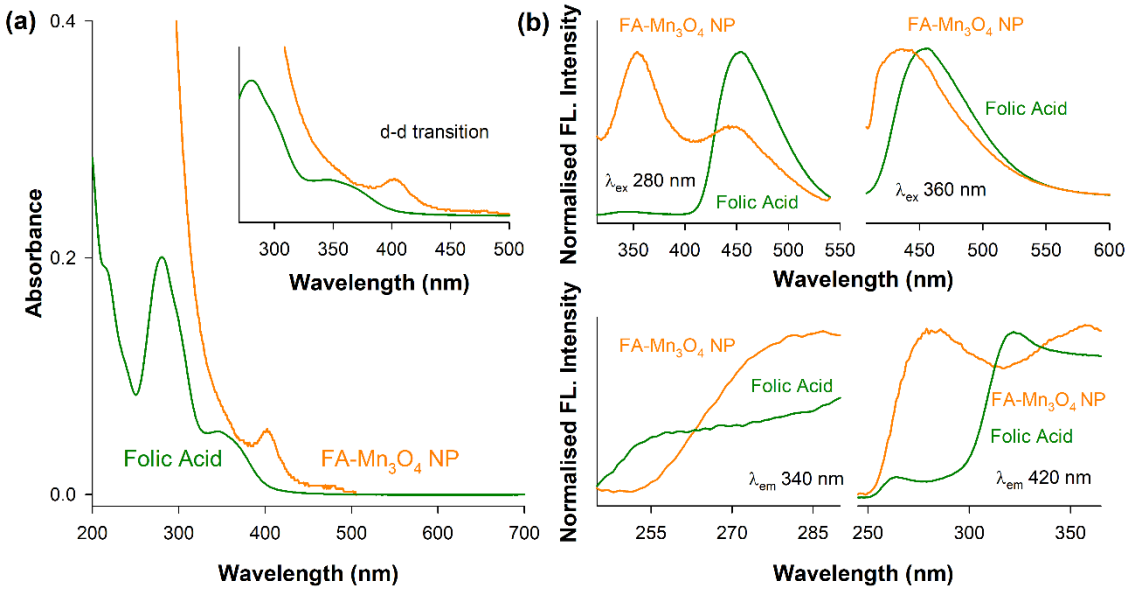

Figure 4.2: *(a) The absorption spectra of folate-capped NPs (FA-Mn_3O_4 NPs) used as PDT agent in the present study and the capping agent folate (FA) are shown in panel. A magnified version of the absorption spectrum of the NPs in the rage of 300–500 nm is shown in the inset. The absorption peaks due to ligand to metal charge transfer (LMCT) and d–d transition (see text) are evident. (b) The corresponding emission and excitation spectra of FA and FA-Mn_3O_4 NPs.*

The other band at 410 nm is reasonably attributed to d–d transitions of Mn^{3+} in FA-Mn_3O_4 NPs, as the degeneracy of ^5E_g ground state term of d^4 (Mn^{3+}) high-spin octahedral environment, has been lifted by the Jahn–Teller effect, that ultimately leads to a tentative assignment of the observed band to the transitions $^5B_{1g} \longrightarrow {}^5E_g$. The other possible low energy transitions e.g., $^5B_{1g} \longrightarrow {}^5B_{2g}$, and $^5B_{1g} \longrightarrow {}^5A_{1g}$ are not evident because previous studies have shown this transition happens in presence of ligands with alpha hydroxy carboxylate groups. In summary, the absorbance studies confirms the functionalization of the NPs with folate. Fluorescence emission spectrum upon excitation at 280 nm for FA and FA-Mn_3O_4 NP (Figure 4.2.b) gave a precise insight of the nanohybrid. The relatively low quantum yield emission peak

of FA at 340 nm arises from p-aminobenzoyl-L-glutamic acid [19, 24, 25]. Upon functionalization, this 340 nm peak becomes prominent along with significant quenching of the emission peak of FA at 460 nm which originates from 6-formyl pterin residue [26]. These changes in characteristic peaks of folic acid provide essential information about attachment of folic acid with Mn_3O_4 nanoparticle. From the change in emission peak at 460 nm we can conclude that the Mn_3O_4 is attached with FA via 6-formyl pterin residue as electrons density responsible for this peak has shifted to nanoparticle. The emission peak at 340 nm which is present in both species help us to prove the presence of p-aminobenzoyl-L-glutamic residue of FA in the synthesized nanomaterial. Hence from absorbance and fluorescence spectra we can conclude that the FA has successfully capped with the Mn_3O_4 nanoparticle.

A transmission electron microscopy (TEM) study has been performed to characterize the water soluble FA-Mn_3O_4 NPs in detail and also to confirm the functionalization process. As illustrated in Figure 4.3.a, TEM analysis revealed the spherical shape of the FA-Mn_3O_4 NPs with average diameter of around 4.86 ± 0.24 nm (Figure 4.3.b). Corresponding high resolution TEM (HRTEM) image (Figure 4.3.c) of single particle confirms the crystalline nature of the NPs having interplanar distance of ~3.15 Å which corresponds to the spacing between the (112) planes of Mn_3O_4 tetragonal crystal lattice [21, 27]. All X-ray diffraction (XRD) peaks corresponding to (101), (112), (200), (103), (211), (004), (220), (204), (105), (312), (303), (321), (224) and (400) planes of FA-Mn_3O_4 NPs (Figure 4.3.d) exactly reflects the tetragonal hausmannite structure of Mn_3O_4 with a lattice constant of a = 5.76 Å and c = 9.47 Å and space group of $I4_1/amd$ described in literature (JCPDS no. 24-0734) [20, 21, 27].

Absence of any additional peaks from other phases, indicated high purity and good crystallinity of the synthesized material. From the aforementioned findings we can conclude that the hydrothermal method was able to synthesize highly crystalline Mn_3O_4 capped with folate. In our synthesis process the first step involved the mixing of $MnCl_2$ with EA (see chapter 3, 3.2.2), this mixing lead to the formation of $MnCl_2(EA)_2$ After this complex was formed introduction of distilled water to the mixture through folic acid solution induced the formation of Mn_3O_4. Now, the pH adjustment is required for the stability of the metal oxide. So in this process colloidal nanoparticles were formed without any additional nucleation, i.e. $MnCl_2$

contributed to the nucleation process whereas the growth was due to the creation of *in situ* $MnCl_2(EA)_2$ complex [27]. In the second phase the carboxy group of glutamate moiety of 6-formyl pterin residue in folic acid was attached to the nanoparticle due to higher temperature and functioned as reducing agent to decrease the size of the NPs.

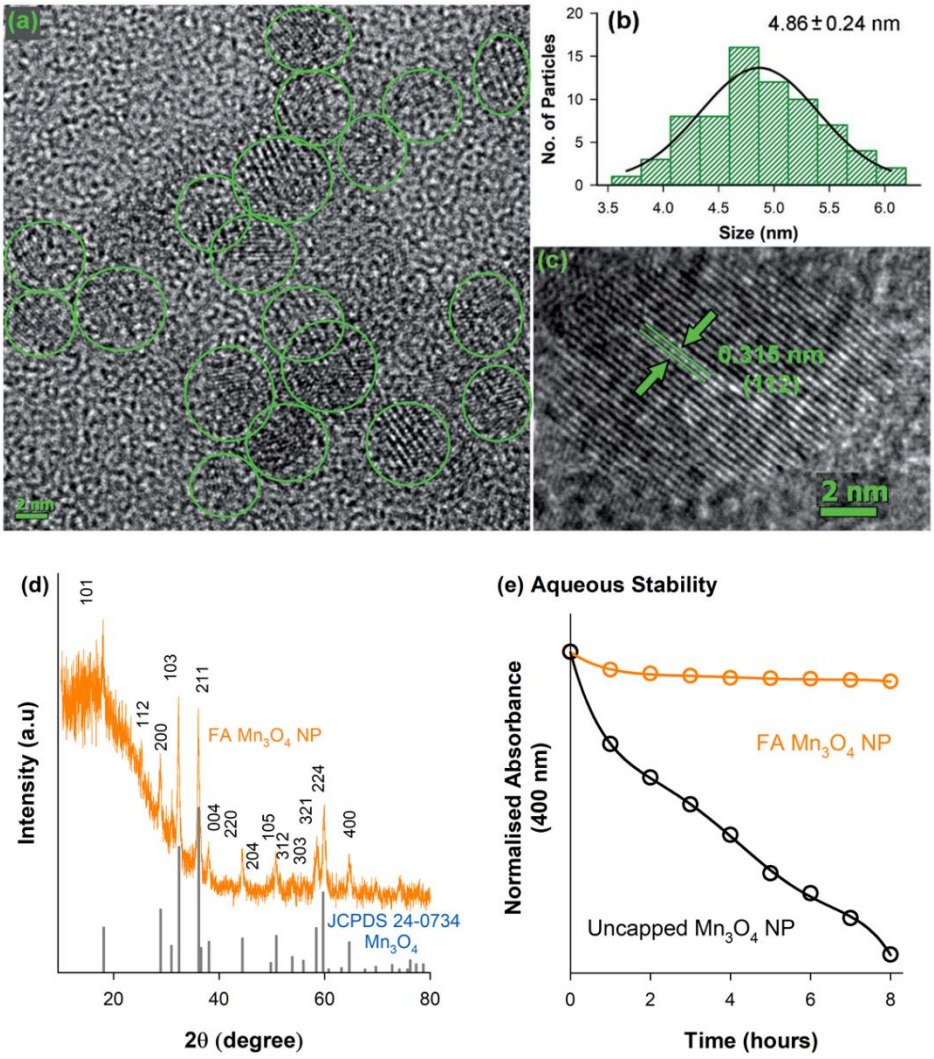

Figure 4.3: *(a) The particle distribution of the nanoparticles (NPs) recorded under transmission electron microscopy (TEM). (b) The particle size distribution is shown with average size of 4.86±0.24 nm and (c) high-resolution electron micrograph (HRTEM) of the NPs with a clear interplanar distance of 0.315 nm for (112) planes in the Mn_3O_4 NPs is evident. (d) XRD pattern of synthesized FAMn_3O_4 NPs which exactly matches to that of library spectra. (e) Capping with folate increases the colloidal stability of the NPs as illustrated in time dependent absorbance studies (solid lines are guide to the eye).*

So, by increasing temperature we have successfully bypassed the need of organic linker to tag folic acid with nanoparticle. From the above mentioned experiments we can conclude that Mn_3O_4 has been successfully formed by hydro- thermal process

and capping of FA has not affected the crystal structure of the nanoparticle. The colloidal stability was also analysed for FA-Mn_3O_4 and Mn_3O_4 dispersed in DMSO–water mixture, which shows the FA capping drastically increased the solubility of the Mn_3O_4 NPs (otherwise insoluble) in aqueous media (Figure 4.3.e).

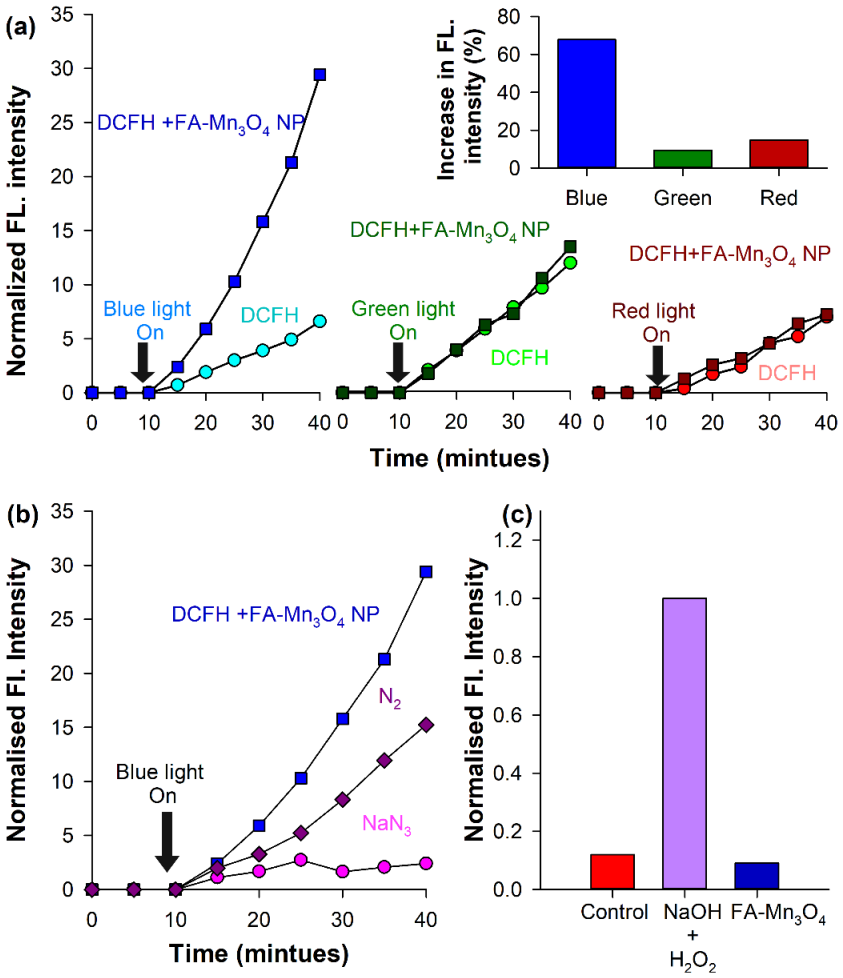

Figure 4.4: *In vitro ROS generation ability of the nanoparticles in different light illumination. (a) DCFH oxidation with respect to time in addition of FAMn_3O_4 NPs and control in the dark and with subsequent light (red, green and blue) irradiation. (b) DCFH oxidation with respect to time with FAMn_3O_4 NPs addition in an atmosphere of purged nitrogen (violet), sodium azide (pink), and a control (blue) under darkwith subsequent blue-light irradiation. (c) Chemiluminescence of luminol prior to blue-light illumination for 15 min for the control, NaOH+H_2O_2 and FA-Mn_3O_4 NPs.*

After detailed photophysical characterization, ROS generation ability of the nanohybrid (FA-Mn_3O_4 NP) was evaluated vitro by monitoring the conversion of DCFH, a widely used marker for detection of ROS, to dichlorofluorescein (DCF) in aqueous medium [28]. In presence of ROS, non-fluorescent DCFH undergoes oxidation to produce florescent DCF (λ_{ex}= 488 nm; λ_{em}= 520 nm). We monitored the fluorescence intensity of DCF at 520 nm (λ_{ex}= 488 nm) with respect to time (Figure

4.4.a). FA-Mn_3O_4 NPs showed negligible ROS generation in absence of light. Then evaluated photo induced ROS generation capability of FA-Mn_3O_4 NPs upon a wide range of visible light irradiation (blue: 430±15 nm, green: 540±15 nm, and red: 640±15 nm). From Figure 4.4.a, it is evident that the maximum increment of fluorescence intensity was obtained under blue light excitation in FA-Mn_3O_4 NPs; almost six fold increase compared to free folic acid. This enhancement in ROS generation ability in presence of blue light may be attributed to the absorption band (i.e., d–d transition band) of FA-Mn_3O_4 NPs at ~410 nm, which was triggered after folic acid sensitization. Thus, exposure to the blue light facilitates the excitation followed by relocation of valence band electrons to conduction band of the metal, which in turn creates an electron–hole pair in the metal [29-31]. The excited state electrons may either migrate towards the dissolved oxygen present in the solution to reduce it to superoxide radical anion ($O_2^{\bullet-}$), or generate singlet oxygen ($^1O_2$) during their return to the ground state. Similarly, the holes can oxidize hydroxyl ion or water molecules and generate hydrogen peroxide (H_2O_2) or hydroxyl radical ($OH^{\bullet}$) [29-31]. Although, the high amount of ROS generated due to photo-irradiation makes the nanohybrid suitable for PDT, it is important to identify the nature of ROS. However, DCFH oxidation is a non-specific marker of ROS, i.e., they show similar response to superoxide anions or singlet oxygen radicals. On the other hand, luminol specifically oxidizes in presence of superoxide to generate chemiluminescence [32]. As depicted in Figure 4.4.c, no chemiluminescence was observed in the presence of FA-Mn_3O_4 NPs after blue-light irradiation for 15 min, which rules out the likelihood of superoxide production by the nanohybrid. To investigate the participation of singlet oxygen radicals, we carried out the DCFH oxidation assay in the presence of a well-known singlet oxygen quencher, sodium azide [21, 32]. The rate of DCFH oxidation (i.e., increase in fluorescence intensity) was decreased significantly in presence of sodium azide (Figure 4.4.b). The aforementioned results clearly indicates the nature of the ROS predominantly to be singlet oxygen rather than superoxide anion, which is consistent with the previously reported mechanistic pathways of ROS generation by surface functionalized manganese oxide nanoparticles [20, 21, 33]. To elucidate the role of dissolved oxygen in the aforementioned ROS generation pathway, we carried out DCFH oxidation assay after nitrogen purging

for one hour. The reduction in DCFH oxidation implies that the dissolved oxygen in the medium is involved in the generation of singlet oxygen.

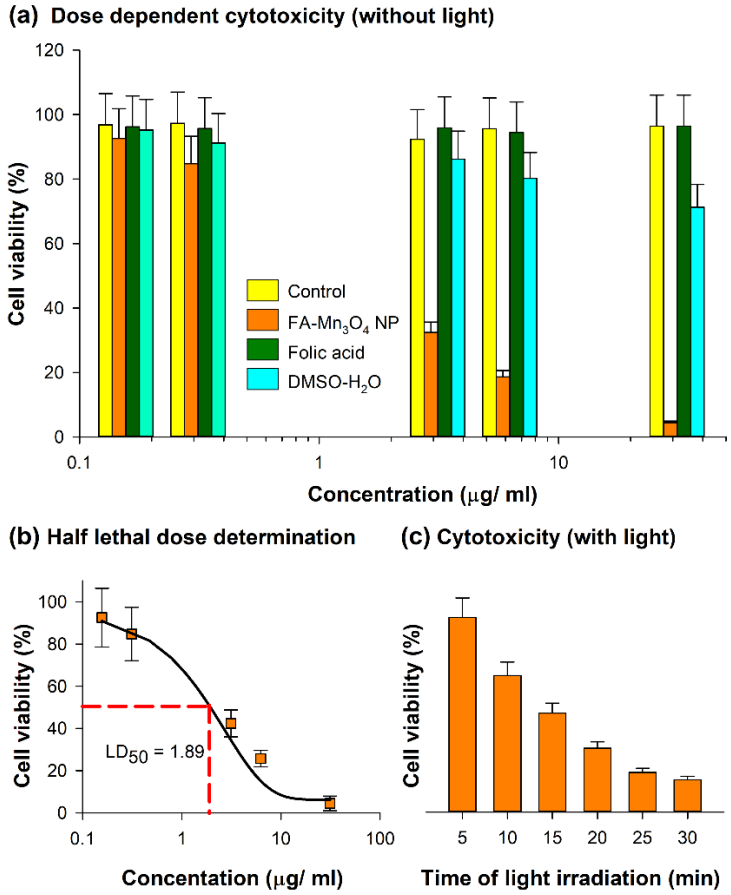

Figure 4.5: *(a) MTT assay quantified cell viability with different concentrations of FA, DMSO–H_2O mixture (the solvent) and FA-Mn_3O_4 NPs in the absence of blue light. (b) The LD_{50} dose found to be 1.89 mgmL^{-1} (6h of incubation with NPs). (c) Light induced cytotoxicity after treatment with 0.31 mgmL^{-1} of FA-Mn_3O_4 NPs followed by blue light irradiation for different time durations (0–30 mins).*

The comprehensive characterization studies and analysis of photo-induced dynamics in FA-Mn_3O_4 NPs were followed by the use of the nanohybrid as an effective PDT agent. So, we evaluated the cytotoxicity of FA-Mn_3O_4 NPs to A549 cells (human alveolar basal epithelial cells) in both the absence and presence of 430±15 nm light irradiation using MTT assay. Bio-reduction of MTT leads to production of formazan [34], which is related to mitochondrial activity (Figure 4.5.a) and thereby cell viability which can be estimated by measuring the absorption at 570 nm. In absence of light, the half lethal dose (LD_{50}) of FA-Mn_3O_4 NPs was found to be ~2 µgmL^{-1} (Figure 4.5.b) at an incubation period of 6 h. For folic acid, a well-known cell nutrient, minimal cytotoxic (~5%) effect was observed at the aforementioned concentration. Hence we have excluded folic acid from the next part

of our cellular study. For DMSO–water mixture, no significant reduction in cell viability (~15%) was found up to concentration ~2 μgmL^{-1}. As low dark and high light induced cytotoxicity are the two most essential properties of the NPs for their application in PDT [35], we used the apparently non-toxic (cell viability ~84.8% in absence of light) concentration of 0.31 μgmL^{-1} FA-Mn_3O_4 NPs for the photo-induced cytotoxicity experiments (described in later part of the study). Next, we incubated the A549 cells with 0.31 μgmL^{-1} FA-Mn_3O_4 NPs under different time of blue light exposure. A gradual reduction in the cell viability was observed with increase in blue light irradiation time (in 5, 10, 15, 20, 25 and 30 min of light exposure cell viability was 75.5%, 52.9%, 38.4%, 24.8%, 15.4% and 12.6%, respectively) as compared to the FA-Mn_3O_4 NP treated cells without light exposure (Figure 4.5.c). A light dose of 20 min shows optimum effect on cell death (cell viability 24.8%) and after that the effect is minimal, suggesting a rapid ROS activity of FA-Mn_3O_4 NPs in A549 cells, consistent with extracellular ROS generation. These *in vitro* PDT experiments illustrates the photodynamic effect of FA-Mn_3O_4 NPs in destruction of lung cancer cells (A549) under blue light irradiation which may further be evaluated in animal models (which is beyond the purview of this study).

To elucidate the role of ROS in the FA-Mn_3O_4 NP-mediated PDT against cancer, the FA-Mn_3O_4 NP-loaded A549 cells were stained with DCFH-DA, an intracellular ROS probe. DCFH-DA is non-fluorescent, which is oxidized by ROS to DCF that emits at green. As depicted in Figure 4.6.a and Figure 4.6.b, FA-Mn_3O_4 NPs (0.31 $mgmL^{-1}$) showed insignificant ROS generation activity without light irradiation. After irradiation with blue light for 20 min, the intracellular ROS level reached saturation, which is consistent with both extracellular ROS generation and photo-induced cytotoxicity assay. The considerable light induced enhanced intracellular ROS activity and optimum dark toxicity of 0.31 μgmL^{-1} dose of FA-Mn_3O_4 NPs indicates its potential in PDT.

Next, to understand the mode of cell death we performed microscopic studies. In bright field microscopic analysis apoptotic changes like reduction in cell size, clear cytoplasm etc. become evident in case of light irradiated cells treated with FA-Mn_3O_4 NPs, whereas, the cells without light illumination showed normal morphology [36, 37]. The extent of apoptosis was further evaluated using nuclear staining dye DAPI (Figure 4.6.a).

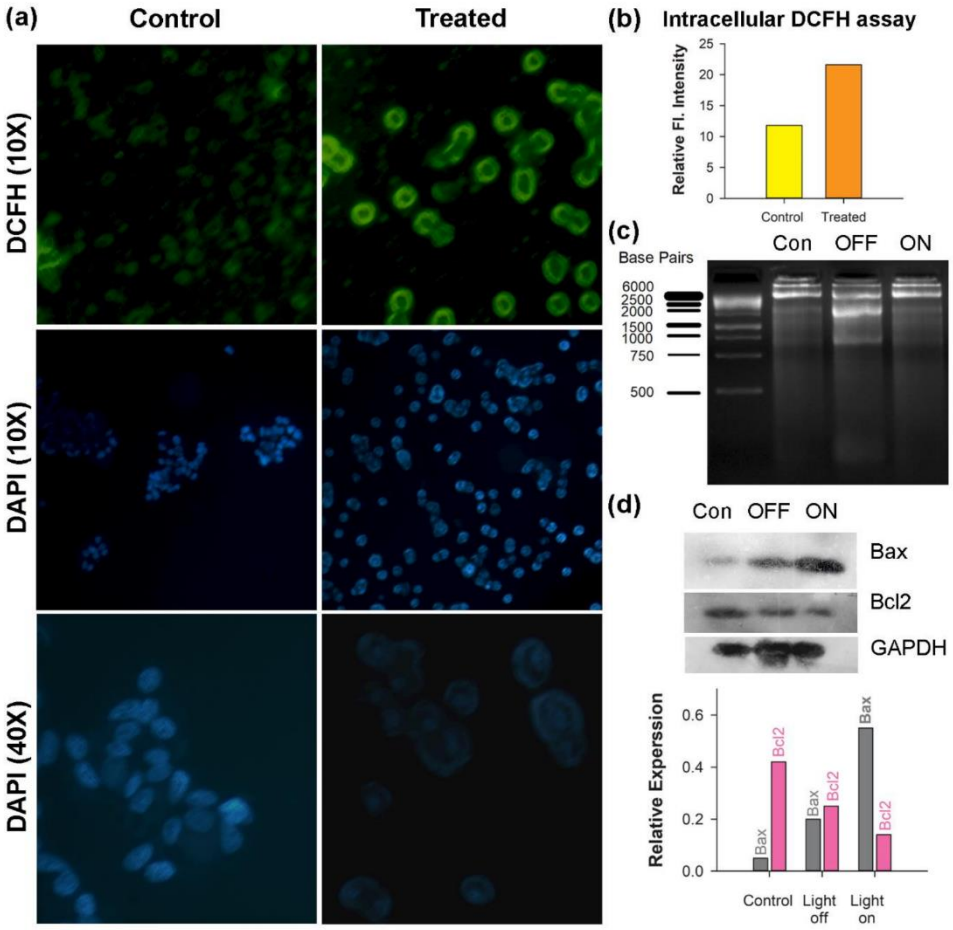

Figure 4.6: *(a) Fluorescence microscopic images of A549 cells stained with DCFH shows increased DCF fluorescence upon photo irradiation (blue light). DAPI stained cells showed apoptotic body upon PDT using FA-Mn_3O_4NPs. The white arrows indicate apoptotic bodies. (b) Quantification of intracellular ROS. (c) DNA fragmentation assay using gel electrophoresis technique. (d) Western blot analysis for relative change in expression levels of Bax and Bcl2 proteins, to major controller of apoptosis.*

DAPI can bind specifically to nuclear DNA and emit a blue light visible with a fluorescence microscope [38, 39]. When the nuclei of A549 cells were studied by DAPI staining, we found that normal nuclei had a homogeneous pattern of staining (Figure 4.6.a). In contrast, FA- Mn_3O_4 NP treated (with photo irradiation) nuclei were smaller and brighter than normal cells, nuclear fragmentation and condensation (apoptotic bodies) were evident (Figure 4.6.a). These findings suggest that the photo-induced FA-Mn_3O_4 NPs demonstrated changes consistent with apoptosis [40].

The damage of nuclear DNA as observed in DAPI staining was further accessed by DNA fragmentation assay using gel electrophoresis. DNA was extracted from the nanoparticle treated cells (both in presence and in absence of blue light) and run on

1.5% agarose gel. Figure 4.6.c shows that in presence of blue light there was a significant damage of nuclear DNA in terms of ladder formation, a biochemical hallmark of apoptosis [41], compared to both control and FA-Mn_3O_4 NP treated ones in the absence of light. Various studies suggest that the balance between proapoptotic (Bax/Bad) and antiapoptotic (Bcl-2/Bcl-xL) members of the Bcl-2 protein family determine the fate of a cell in physiological milieu [38, 41]. Figure 4.6.d displays the expression of Bax which was increased in the cells that were incubated with FA-Mn_3O_4 in presence of light whereas, the expression of Bcl2 protein was drastically decreased in these group of cells. It is well know that Bcl2 protein family acts as an anti-apoptotic actor by inhibiting Bax.

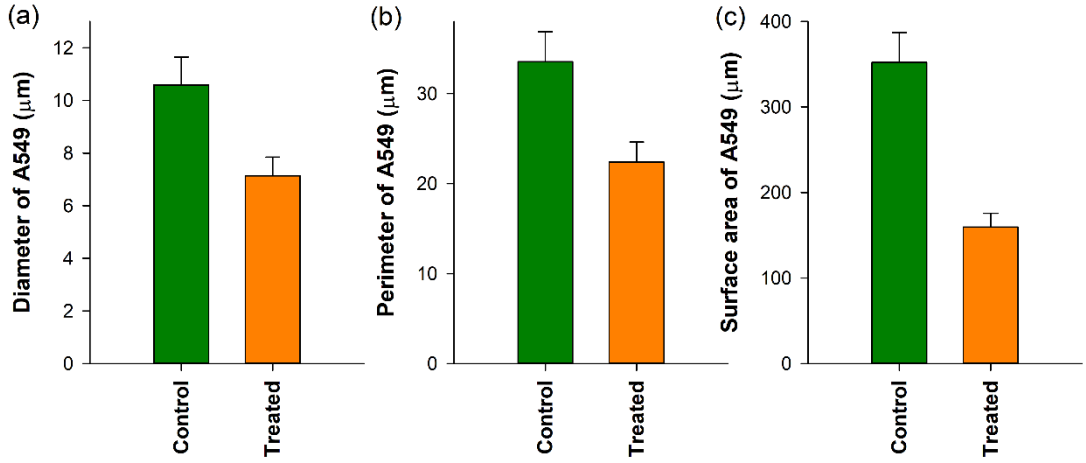

Figure 4.7: *Comparison between various morphometric parameters of control and FA-Mn_3O_4 NP treated A549 cells.*

Thus in summary, FA-Mn_3O_4 NPs in presence of blue light increases the cellular ROS level, which triggers the Bax expression in cells. On the other hand, FA-Mn_3O_4 NPs down regulate the Bcl2 expression, in turn reduces the inhibition on Bax. As a result, increased Bax can induce the nuclear DNA fragmentation thereby dictating the cells to undergo apoptosis. The morphometric data of cells are shown in Figure 4.7.

4.3. Conclusion:

From this study we can conclude that we have developed a facile and cost effective method for synthesis of folic acid capped Mn_3O_4 nanoparticles without using any additional organic linker (confirmed by spectroscopic studies). This folic acid capped

nanoparticle can generate ROS in the presence of blue light (as depicted in both intracellular and extracellular DCFH assay) and can be used as an efficacious PDT agent against adenocarcinomic human alveolar basal epithelial cells (lung cancer cells). Nuclear DNA fragmentation, apoptotic body formation overexpression of Bax and down regulation of Bcl2 proteins suggest the underlying mechanism to be apoptosis. Although, we have described the photo induced cytotoxicity of FA-Mn_3O_4 NPs in lung cancer cells as a model, the similar effects can be observed in other carcinomas too. Hence, blue light induced PDT can be effectively used to treat carcinomic tissues (e.g. lung cancer, colorectal cancer, stomach cancer, throat cancer etc.) by introduction of blue light using optical fibers. Finally, this work elicits a new approach towards the synthesis of effective, low cost nanohybrids for diagnosis and therapy of alveolar adenocarcinoma.

Reference

[1] F. Bray, J. Ferlay, I. Soerjomataram, R.L. Siegel, L.A. Torre, A. Jemal, Global cancer statistics 2018: GLOBOCAN estimates of incidence and mortality worldwide for 36 cancers in 185 countries, *CA: Cancer J. Clin.*, 68 (2018) 394.

[2] J. Ferlay, M. Colombet, I. Soerjomataram, C. Mathers, D.M. Parkin, M. Piñeros, A. Znaor, F. Bray, Estimating the global cancer incidence and mortality in 2018: GLOBOCAN sources and methods, *Int. J. Cancer.*, 144 (2019) 1941.

[3] T.J. Dougherty, C.J. Gomer, B.W. Henderson, G. Jori, D. Kessel, M. Korbelik, J. Moan, Q. Peng, Photodynamic therapy, *J. Natl. Cancer Inst.*, 90 (1998) 889.

[4] R. Lv, Y. Wang, J. Liu, M. Feng, F. Yang, X. Jiang, J. Tian, When a semiconductor utilized as an NIR laser-responsive photodynamic/photothermal theranostic agent integrates with upconversion nanoparticles, *ACS Biomater. Sci. Eng.*, 5 (2019) 3100.

[5] F. Wang, D. Banerjee, Y. Liu, X. Chen, X. Liu, Upconversion nanoparticles in biological labeling, imaging, and therapy, *Analyst*, 135 (2010) 1839.

[6] S. Zeng, H. Wang, W. Lu, Z. Yi, L. Rao, H. Liu, J. Hao, Dual-modal upconversion fluorescent/X-ray imaging using ligand-free hexagonal phase $NaLuF_4$: Gd/Yb/Er nanorods for blood vessel visualization, *Biomater.*, 35 (2014) 2934.

[7] R. Lv, C. Zhong, R. Li, P. Yang, F. He, S. Gai, Z. Hou, G. Yang, J. Lin, Multifunctional anticancer platform for multimodal imaging and visible light driven photodynamic/photothermal therapy, *Chem. Mater.* , 27 (2015) 1751.

[8] C. Xing, L. Liu, H. Tang, X. Feng, Q. Yang, S. Wang, G.C. Bazan, Design guidelines for conjugated polymers with light-activated anticancer activity, *Adv. Funct. Mater.*, 21 (2011) 4058.

[9] M.K. Yu, J. Park, S. Jon, Targeting strategies for multifunctional nanoparticles in cancer imaging and therapy, *Theranostics*, 2 (2012) 3.

[10] H. Maeda, The enhanced permeability and retention (EPR) effect in tumor vasculature: The key role of tumor-selective macromolecular drug targeting, *Adv. enzym res.*, 41 (2001) 189.

[11] T.M. Allen, Ligand-targeted therapeutics in anticancer therapy, *Nat. Rev. Cancer.*, 2 (2002) 750.

[12] V.P. Torchilin, Nanoparticulates as drug carriers, *Imperial college press, London*, 2006.

[13] R. Nandi, S. Mishra, T.K. Maji, K. Manna, P. Kar, S. Banerjee, S. Dutta, S. Sharma, P. Lemmens, K.D. Saha, A novel nanohybrid for cancer theranostics: Folate sensitized Fe_2O_3 nanoparticles for colorectal cancer diagnosis and photodynamic therapy, *J. Mater. Chem. B*, 5 (2017) 3927.

[14] F. Sonvico, S. Mornet, S. Vasseur, C. Dubernet, D. Jaillard, J. Degrouard, J. Hoebeke, E. Duguet, P. Colombo, P. Couvreur, Folate-conjugated iron oxide nanoparticles for solid tumor targeting as potential specific magnetic hyperthermia mediators: synthesis, physicochemical characterization, and in vitro experiments, *Bioconjug. Chem.*, 16 (2005) 1181.

[15] J.-J. Lin, J.-S. Chen, S.-J. Huang, J.-H. Ko, Y.-M. Wang, T.-L. Chen, L.-F. Wang, Folic acid–Pluronic F127 magnetic nanoparticle clusters for combined targeting, diagnosis, and therapy applications, *Biomater.*, 30 (2009) 5114.

[16] K. Hayashi, M. Moriya, W. Sakamoto, T. Yogo, Chemoselective synthesis of folic acid−functionalized magnetite nanoparticles via click chemistry for magnetic hyperthermia, *Chem. Mater.*, 21 (2009) 1318.

[17] A.J. Ditto, K.N. Shah, N.K. Robishaw, M.J. Panzner, W.J. Youngs, Y.H. Yun, The interactions between L-tyrosine based nanoparticles decorated with folic acid and cervical cancer cells under physiological flow, *Mol. Pharmaceutics.*, 9 (2012) 3089.

[18] S. Mohapatra, S. Mallick, T. Maiti, S. Ghosh, P. Pramanik, Synthesis of highly stable folic acid conjugated magnetite nanoparticles for targeting cancer cells, *Nanotechnology*, 18 (2007) 385102.

[19] A. Giri, N. Goswami, M. Pal, M.T.Z. Myint, S. Al-Harthi, A. Singha, B. Ghosh, J. Dutta, S.K. Pal, Rational surface modification of Mn_3O_4 nanoparticles to induce multiple photoluminescence and room temperature ferromagnetism, *J. Mater. Chem. C*, 1 (2013) 1885.

[20] N. Polley, S. Saha, A. Adhikari, S. Banerjee, S. Darbar, S. Das, S.K. Pal, Safe and symptomatic medicinal use of surface-functionalized Mn_3O_4 nanoparticles for hyperbilirubinemia treatment in mice, *Nanomed.*, 10 (2015) 2349.

[21] A. Adhikari, N. Polley, S. Darbar, D. Bagchi, S.K. Pal, Citrate functionalized Mn_3O_4 in nanotherapy of hepatic fibrosis by oral administration, *Future Sci. OA*, 2 (2016) FSO146.

[22] S. Mondal, A. Adhikari, M. Das, S. Darbar, A. Alharbi, S.A. Ahmed, S.S. Bhattacharya, D. Pal, S.K. Pal, Novel one pot synthesis and spectroscopic characterization of a folate-Mn_3O_4 nanohybrid for potential photodynamic therapeutic application, *RSC Adv.*, 9 (2019) 30216.

[23] M. Abd El-Wahed, M. Refat, S. El-Megharbel, Synthesis, spectroscopic and thermal characterization of some transition metal complexes of folic acid, *Spectrochim. Acta A Mol.: Biomol. Spectrosc.*, 70 (2008) 916.

[24] M.E. Bodini, L.A. Willis, T.L. Riechel, D.T. Sawyer, Electrochemical and spectroscopic studies of manganese (II),-(III), and-(IV) gluconate complexes. 1. Formulas and oxidation-reduction stoichiometry, *Inorg. Chem.*, 15 (1976) 1538.

[25] Y.-F. Han, F. Chen, Z. Zhong, K. Ramesh, L. Chen, E. Widjaja, Controlled synthesis, characterization, and catalytic properties of Mn_2O_3 and Mn_3O_4 nanoparticles supported on mesoporous silica SBA-15, *J. Phys. Chem. B*, 110 (2006) 24450.

[26] M.K. Off, A.E. Steindal, A.C. Porojnicu, A. Juzeniene, A. Vorobey, A. Johnsson, J. Moan, Ultraviolet photodegradation of folic acid, *J. Photochem. Photobiol. B: Biol.*, 80 (2005) 47.

[27] S. Lei, K. Tang, Z. Fang, H. Zheng, Ultrasonic-assisted synthesis of colloidal Mn_3O_4 nanoparticles at normal temperature and pressure, *Cryst. Growth Des.*, 6 (2006) 1757.

[28] S. Chaudhuri, S. Sardar, D. Bagchi, S. Dutta, S. Debnath, P. Saha, P. Lemmens, S.K. Pal, Photoinduced dynamics and toxicity of a cancer drug in proximity of inorganic nanoparticles under visible light, *ChemPhysChem*, 17 (2016) 270.

[29] J. Bogdan, J. Pławińska-Czarnak, J. Zarzyńska, Nanoparticles of titanium and zinc oxides as novel agents in tumor treatment: A review, *Nanoscale Res. Lett.*, 12 (2017) 1.

[30] I. Grčić, D. Vujević, K. Žižek, N. Koprivanac, Treatment of organic pollutants in water using TiO_2 powders: photocatalysis versus sonocatalysis, *React. Kinet. Mech. Catal.*, 109 (2013) 335.

[31] A. Mills, S. Le Hunte, An overview of semiconductor photocatalysis, *J. Photochem. Photobiol. A, Chem.*, 108 (1997) 1.

[32] S. Sardar, S. Chaudhuri, P. Kar, S. Sarkar, P. Lemmens, S.K. Pal, Direct observation of key photoinduced dynamics in a potential nano-delivery vehicle of cancer drugs, *Phys. Chem. Chem. Phys.*, 17 (2015) 166.

[33] A. Giri, N. Goswami, C. Sasmal, N. Polley, D. Majumdar, S. Sarkar, S.N. Bandyopadhyay, A. Singha, S.K. Pal, Unprecedented catalytic activity of Mn_3O_4 nanoparticles: potential lead of a sustainable therapeutic agent for hyperbilirubinemia, *RSC Adv.*, 4 (2014) 5075.

[34] M. Ishiyama, H. Tominaga, M. Shiga, K. Sasamoto, Y. Ohkura, K. Ueno, A combined assay of cell vability and *in vitro* cytotoxicity with a highly water-soluble tetrazolium salt, neutral red and crystal violet, *Biol. Pharm. Bull.*, 19 (1996) 1518.

[35] J. Tian, L. Ding, H.-J. Xu, Z. Shen, H. Ju, L. Jia, L. Bao, J.-S. Yu, Cell-specific and pH-activatable rubyrin-loaded nanoparticles for highly selective near-infrared photodynamic therapy against cancer, *J. Am. Chem. Soc.*, 135 (2013) 18850.

[36] S. Elmore, Apoptosis: a review of programmed cell death, *Toxicol. Pathol.*, 35 (2007) 495.

[37] F. Lang, E. Gulbins, I. Szabo, A. Lepple-Wienhues, S.M. Huber, C. Duranton, K.S. Lang, P.A. Lang, T. Wieder, Cell volume and the regulation of apoptotic cell death, *J. Mol. Recognit.*, 17 (2004) 473.

[38] F. Lian, Y. Li, M. Bhuiyan, F.H. Sarkar, p53-independent apoptosis induced by genistein in lung cancer cells, *Nutr. Cancer*, 33 (1999) 125.

[39] Y. Teow, S. Valiyaveettil, Active targeting of cancer cells using folic acid-conjugated platinum nanoparticles, *Nanoscale*, 2 (2010) 2607.

[40] F.J. Blanco, R. Guitian, E. Vázquez-Martul, F.J. de Toro, F. Galdo, Osteoarthritis chondrocytes die by apoptosis: A possible pathway for osteoarthritis pathology, *Arthritis Rheumatol.*, 41 (1998) 284.

[41] P.B. Pal, K. Sinha, P.C. Sil, Mangiferin, a natural xanthone, protects murine liver in Pb (II) induced hepatic damage and cell death via MAP kinase, NF-κB and mitochondria dependent pathways, *PloS One*, 8 (2013) e56894.

CHAPTER 5

Synthesis and Characterization of a Nanomaterial for its Potential application as a Nanoceutical Fabric Against Airborne Diseases

5.1. Introduction:

The emerging coronavirus disease 2019 (COVID-19) pandemic, caused by severe acute respiratory syndrome-related coronavirus 2 (SARS-CoV-2), has imposed a global socioeconomic burden, particularly to the public and private healthcare systems due to unprecedented morbidity, mortality, and economic disruption [1]. At the time of writing, over 81.27 million patients have been infected by SARS-CoV-2, with over 1.77 million deaths worldwide [2]. Recently, some of the vaccine candidates have received conditional approval from various authorities around the world despite suffering from numerous issues like dose, interval between two shots, and so forth. Even after that, it will take several months to reach the common people due to challenges like regulatory issues, large-scale production, and mass distribution to the public [3]. Therefore, the sole line of defence recommended by almost all the apex medical bodies throughout the world is "non-pharmacological interventions" like the use of personal protective equipment (PPE) (e.g., face mask, face shield, gloves, and so forth) and personal hygiene (e.g., handwashing and cough and sneeze etiquette) [4-6]. As the world is ready to reopen and most of the countries are waiting for a second or third wave of virus outbreak, PPE, particularly face masks, has become an integral part of day-to-day life. Although face masks are commonly used to provide protection to the wearer (e.g., first responders), they were originally introduced to protect surrounding persons [7]. Generally, the term "face mask" covers a broad range of PPE that reduces the transmission of respiratory particles or droplets [7].

Recently, Centres for Disease Control and Prevention (CDC) warned against the use of one-way valves or vents in face masks for potential threat of spreading COVID-19 through expelled respiratory droplets [8]. However, the face masks without valves or vents can cause several health problems and severe discomfort to the wearer [9,

10]. Some pieces of evidence suggest that commonly available N95 face masks can lead to changes in blood oxygen (O_2) and carbon dioxide (CO_2) levels when used for long periods, especially by people who are elderly or obese or have chronic obstructive pulmonary disease [9-11]. Other adverse health effects range from increased blood pressures, increased heart rates, chest pain, and hypercapnia [12, 13]. One of the feasible solutions to this problem is by covering the valve or vent with a porous filter that can either trap or kill the microorganisms including viruses, alongside allowing the air to flow across. Unfortunately, no study has been performed up to date to design such filters or to address the problem by other means. In this regard, filters made up of natural fabrics (e.g., cotton) functionalized with antimicrobial agents could be an effective solution.

Although a vast diversity of organic compounds with recognized antimicrobial activity have been incorporated into polymers in order to develop antimicrobial fibers, they exhibit several drawbacks related to their thermal and chemical instability, which could lead to difficulties throughout the functionalization process and also produce fibrous mats with limited antimicrobial activity due to partial decomposition of the antimicrobial agent [14]. Moreover, the massive use of antibiotics has led to another global problem, the origination of antibiotic-resistant bacteria [15, 16]. Thus, there is a growing need to explore novel antimicrobial agents to functionalize the natural or synthetic fabrics not only to prevent COVID-19 spread but also for other applications like clothing materials for patients to stop hospital-acquired infections, which is also a global challenge.

Consequently, nanoscale materials with unique and tuneable physicochemical properties (i.e., higher chemical, mechanical, and thermal stability) are interesting elements for preparation of hygienic surfaces. For example, silver ions and silver-based nano compounds are highly toxic to microorganisms, showing strong biocidal effects on various species of bacteria [17-19]. Gold nanoparticles [20, 21], bimetallic nanomaterials (e.g., Ag/Au, Ag/Pt, and so forth) [22, 23], graphene-based materials[24], and metal oxide nanoparticles [e.g., titanium dioxide (TiO_2), copper oxide (CuO), silica (SiO_2), and so forth] [25-27] are other examples. However, they all suffer from the problem of inherent toxicity of the nanomaterials, limiting their human use [28-32]. Recently, several ultrasmall metal nanoclusters particularly of gold (Au) and silver (Ag) have shown wide spectrum antimicrobial activity [33-36].

Even these ultrasmall metal nanoclusters have been impregnated into biocompatible hydrogels to eradicate bacterial biofilms [34]. The nanoclusters induce metabolic imbalance in the microorganism, leading to enhanced reactive oxygen species generation, which in turn kills the microbe [33]. One of the advantages of these nanoclusters is the possibility of atomic-level control of the size, structure, composition, and surface functionalization leading to a more personalized treatment strategy [37]. Moreover, they do not pose the problem of antibiotic resistance. However, biocompatibility and cytotoxicity of these materials remain a key concern. Therefore, it is of considerable interest to design a nanoparticle-functionalized fabric (i.e., nanoceutical fabric) that can efficiently kill or trap microorganisms without any harmful side effect to the user.

In this study, we have rationally designed a nanoceutical cotton fabric duly sensitized with the non-toxic zinc oxide (ZnO) nanomaterial for potential use as a membrane filter in the one-way valve or vent of the face mask for the ease of breathing without the risk of COVID-19 spread. A comprehensive computer-assisted simulation study revealed the unique potential of ZnO nanoflowers (ZnO NFs) having nearly two-dimensional nanopetals in entrapment and denaturation of coronavirus spike protein (resulting into eradication of the virus), which mediates the viral pathogenesis through attachment to angiotensin converting enzyme-2 (ACE-2) receptors in the human respiratory tract. Subsequently, we have synthesized ZnO NF on a natural cotton fiber matrix using a one-pot hydrothermal-assisted approach. In-depth electron-microscopic, steady-state, and picosecond resolved spectroscopic studies confirm the attachment of ZnO NF to the cellulose matrix of cotton at the atomic level to develop the nanoceutical fabric filter. An exhaustive antimicrobial study using a capsule containing virulent *Pseudomonas aeruginosa* as a mimic of coronavirus (as the lectins in *P. aeruginosa* share similar homology to coronavirus spike protein) reveals excellent antimicrobial (bactericidal) efficiency of the developed nanoceutical fabric filter. To our understanding, the novel nanoceutical fabric used in the one-way valve of a face mask would be the choice to assure breathing comfort along with source control of COVID-19 infection. The developed nanosensitized cloth can further be used as an antibacterial (as well as anti SARS CoV-2) dress material in general to stop hospital-acquired infections.

5.2. Results and Discussion:

5.2.1. Nanoceutical Fabric Prevents COVID-19 Spread through Expelled Respiratory Droplets: A Combined Computational, Spectroscopic and Anti-Microbial Study [38]:

5.2.1.1. Prediction of the Potential Antiviral Nanostructure and Model Experimental Organism: SARS-CoV-2 (Figure 5.1.a,b), generally initiates its infection process by binding to functional receptors on the membrane of a host cell [39]. In the case of humans, membrane-bound ACE-2 (the functional host receptor) plays a crucial role in pathogenesis of COVID-19 providing viral entry to human cells (Figure 5.1.c, d) [40, 41]. The spike (S) protein present in the outer surface of SARS-CoV-2 binds to human ACE-2 with a very strong affinity and subsequently mediates membrane fusion leading to host cell entry of the virus (Figure 5.1.c,d) [40, 42, 43]. The computed binding energy for human ACE-2 and SARS-CoV-2 S-protein from the crystal structure (PDB ID: 6LZG; Figure 5.1.d) of the complex was found to be −20.28 kcal mol^{-1}. Following minimization of the complex under the optimized potentials for liquid simulations [44] (OPLS) force field, the binding energy drops to −29.83 kcal mol^{-1}. This strong binding energy can be attributed to the large surface area at the protein−protein interface and several favorable intermolecular interactions including hydrogen bonding, ionic, and hydrophobic interactions. Hence, it is difficult to develop small-molecule competitive inhibitors that can disrupt such an elaborate molecular recognition. Therefore, we looked into the prospective nanomaterials having a similar magnitude to ACE-2 protein along with the ability to compete for the viral S-protein binding. In this regard, our primary choice was ZnO considering its biocompatibility and known antimicrobial and antiviral effect [45-47]. In a computer simulation, a spherical ZnO nanoparticle (~30 nm diameter, similar dimensions of ACE-2) was constructed and its interaction with the viral S-protein was studied (Figure 5.1.e). The spherical nanoparticle provided a convex surface for interactions similar to the ACE-2 receptor protein. Since the geometry of the nanosurface at the binding region is known to affect the protein−nanomaterial interaction [48, 49], we further simulated the interaction of S-protein with the flat sheet-like ZnO surface having various exposed crystal facets (⟨100⟩, ⟨101⟩, and ⟨002⟩) as observed in the Xray diffraction (XRD) pattern (*vide infra*).

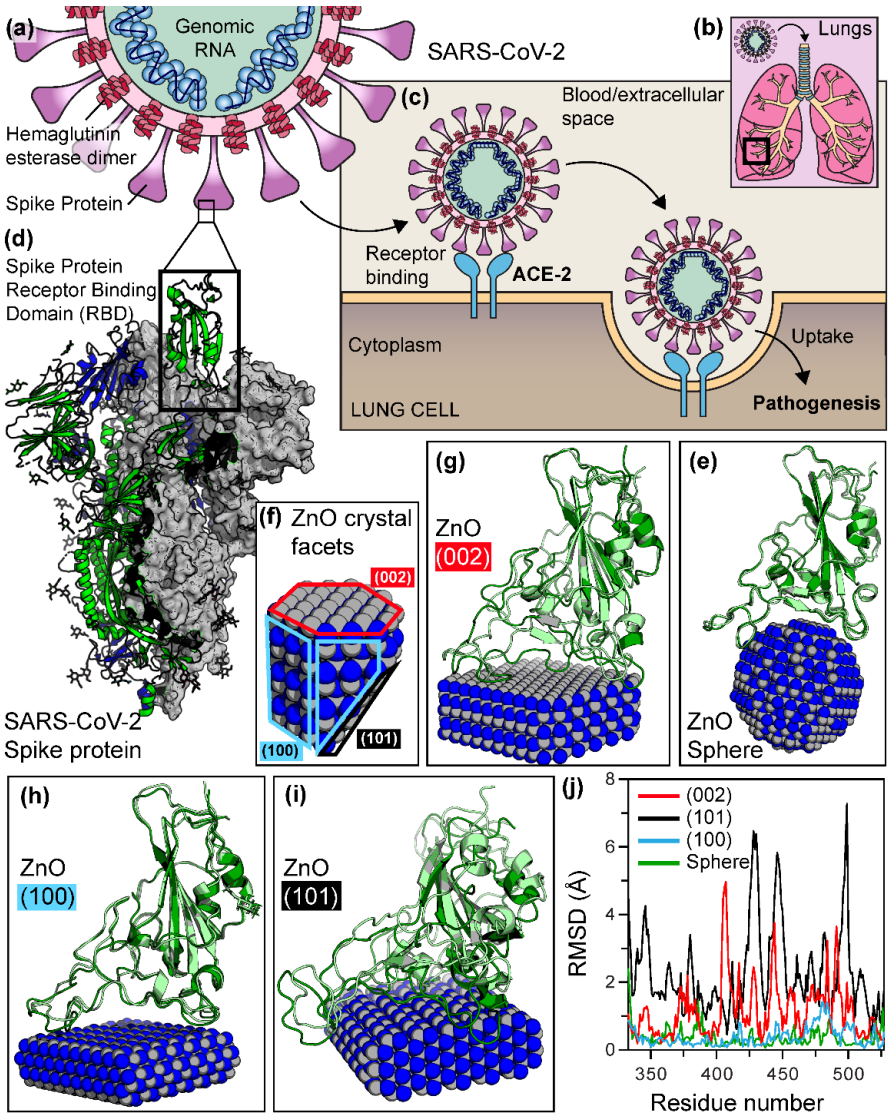

Figure 5.1: *(a) SARS-CoV-2 structure. (b) Infection through respiratory tract. (c) Spike RBD binds to ACE-2 of host lung cell causing internalization of the virus. (e) Binding of spike RBD with spherical ZnO nanoparticle. (f) ZnO crystal facets used for calculation. (g), (h) & (i) binding of spike RBD to the (101), (100), and (002) crystal facet of ZnO, respectively. Light colored are native structures. Dark colored are denatured structure after energy minimization. (j) RMSD values after energy minimization.*

As evident from the molecular docking study, the SARSCoV-2 S-protein can bind favorably with both the ZnO nanosphere and the flat facets (⟨100⟩, ⟨101⟩, and ⟨002⟩) of the ZnO nanostructure with binding energies of −17, −11, −21, and −16 kcal mol^{-1}, respectively. Binding on the ⟨101⟩ ZnO nanosurface was very much comparable with that of ACE-2. After the energy minimization of the docked complexes, the binding energies were found to be −21, −13, −40, and −22 kcal mol^{-1}, respectively.

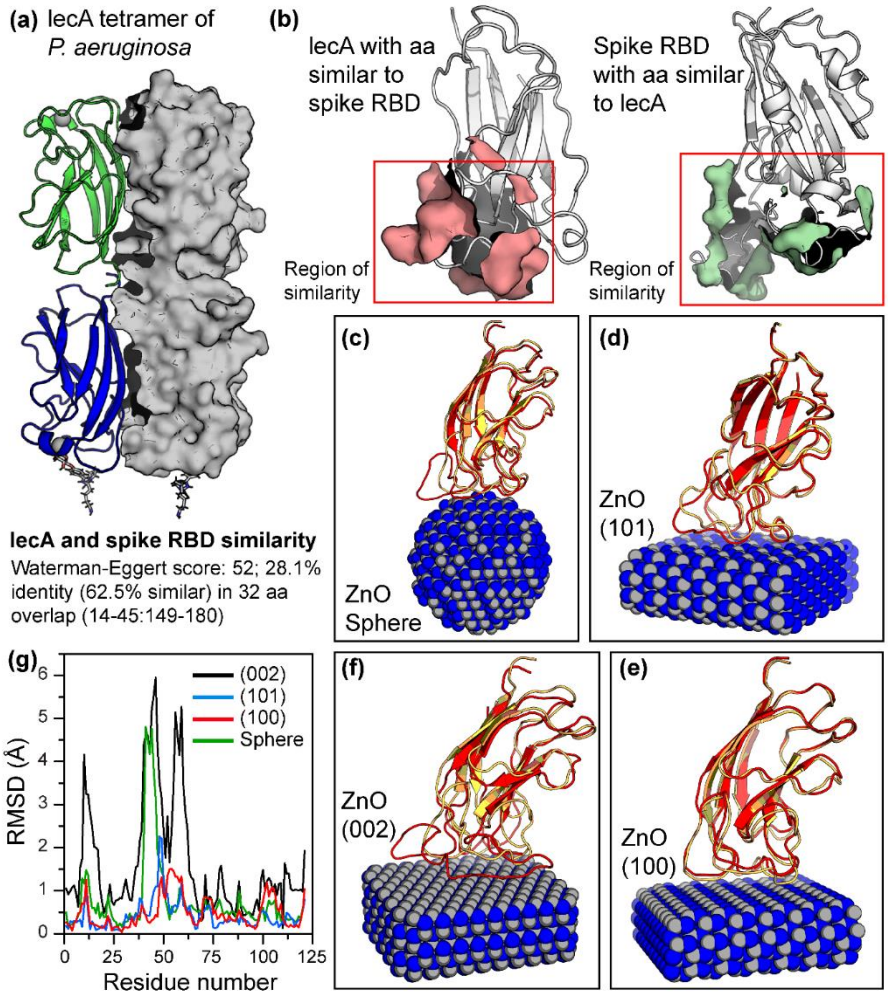

Figure 5.2: *(a) Tetrameric structure of lecA. (b) Similarity between lecA and spike RBD. (c) Binding of spike RBD with spherical ZnO nanoparticle. (d), (e) & (f) binding of lecA to the (101), (100), and (002) crystal facet of ZnO, respectively. Light colored are native structures. Dark colored are denatured structure after energy minimization. (i) RMSD values after energy minimization.*

Figure 5.1.e–i shows the bound conformations of spike protein with the ZnO nanosphere and various facets on ZnO nanosurfaces. Interestingly, when structural deviations (in terms of root-mean-square deviation, rmsd) were studied and compared between the docked and energy-minimized conformations of the spike receptor binding domain (RBD) (Figure 5.1.j), large structural perturbations become evident in the binding regions of SARS-CoV-2 Sprotein due to binding on ZnO nanofacets. Least change was observed in the case of the nanosphere, whereas most change occurred on the ⟨101⟩ facet of ZnO. Since the structure and function of proteins are highly correlated, infliction of a large structural perturbation in the protein structure by an inhibitor or ligand is generally associated with its loss of function [44]. The observed *in silico* structural changes, therefore, indicate that the

viral S-protein may lose its pathological function if it comes in contact with the ZnO nanosurface. Bearing in mind the transmissibility and pathogenicity of SARS-CoV-2 as well as unavailability of the SARS-CoV-2 strain and biosafety requirements for experimental studies, we looked for similar organisms as an alternative model preferably of the bacterial origin having adhesion proteins analogous to viral S-protein. Lectin-A (LecA) protein of *P. aeruginosa* (Figure 5.2.a) was found to show a high degree of similarity in the binding site residues as evident from the amino acid sequence alignment depicted in Figure 5.2.a,b. In the largest 32 amino acid overlap region (14−45:149−180), the two proteins showed 28.1% identity and 62.5% similarity with a Waterman−Eggert score of 52. Detailed sequence alignments of the Spike RBD and LecA protein are given in the Supporting Information. Apart from the structural similarity, LecA resembles the function of viral S-protein and mediates bacterium-host cell recognition and adhesion, which are the critical steps in initiating *P. aeruginosa* pathogenesis. Interestingly, for both SARS-CoV-2 and *P. aeruginosa*, lungs are the primary target organs, and both of them cause similar acute and chronic lung infection [50-52]. Therefore, considering the structural and functional resemblances in a possible example of molecular mimicry, *P. aeruginosa* LecA was chosen as an alternative to SARS-CoV-2 S-protein for subsequent computational and experimental binding studies with the ZnO nanostructures.

The molecular docking study illustrates that the *P. aeruginosa* LecA protein can bind favorably with the ZnO ⟨100⟩, ⟨101⟩, and ⟨002⟩ nanofacets as well as on the ZnO nanosphere with comparable binding energies of −9, −11, −12, and −11 kcal mol^{-1}, respectively. After the energy minimization of the docked complexes, the binding energies were found to be −11, −14, −26, and −17 kcal mol^{-1}, respectively. Figure 5.2.c−f shows the bound conformations of LecA protein with the ZnO nanosphere and nanofacets, respectively. Structural deviations in terms of rmsds were studied and compared between the docked and minimized complexes and graphically represented in Figure 5.2.g. It is evident from Figure 5.2.g that large structural perturbation, similar to the viral S-protein, takes place in the binding regions of LecA protein on the ZnO nanofacets. Thus, the computational binding study shows that the ZnO nanosurface can trap the adhesion proteins of SARS-Cov-2 as well as that of *P. aeruginosa*. The sheet-like flat ZnO nanostructures not only bind these adhesion proteins (i.e., viral S-protein and LecA) but also impart large-scale structural

perturbation in the bound protein (i.e., denaturation), leading to functional impairment and disinfectant effects. Therefore, based on the computational findings, *P. aeruginosa* (having LecA) was chosen as a model SARS-CoV-2 mimic, and the ZnO sheet-like nanostructure was selected as an antimicrobial agent for subsequent experimental validation.

5.2.1.2. Design of the Natural Cotton Fabric Functionalized with ZnO NF Featuring Flat Sheet-like Petals: Encouraged by the *in silico* studies, we intended to decorate the natural cotton fabric with flat ZnO sheet-like structures, which eventually self-assembled into more complex rose-like ZnO NF during the hydrothermal-assisted low-temperature one-pot synthesis process.

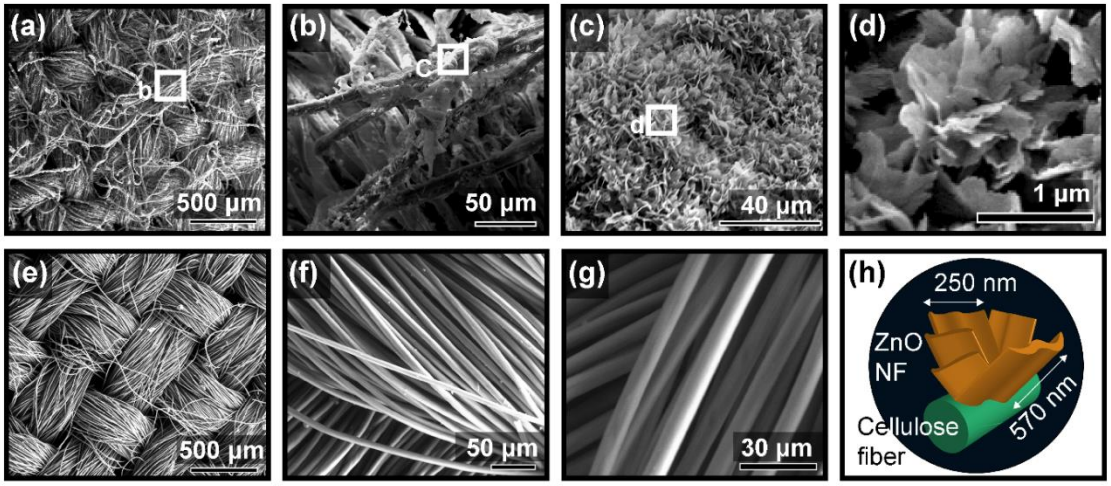

Figure 5.3: *(a-d) SEM of ZnO NF decorated cotton cloth. (e-g) SEM of bare cotton cloth. (h) Schematic of the ZnO NF as observed under SEM.*

The scanning electron micrographs confirm the formation of the flower-like morphology of ZnO on the surface of the cotton fiber (Figure 5.3.a−5.3.d).Figure 5.3.e−5.3.g shows the scanning electron micrographs of the bare cloth. The flat sheet like petals of the flower have a length of~600−850 nm and a diameter of ~150−300 nm with an aspect ratio of ~3 (schematically represented in Figure 5.3.h). It should be noted that the surface of the petals is not smooth, rather coated with small granules of nanoparticles. Energy-dispersive X-ray analysis confirms the presence of ZnO in the nanostructure (Figure 5.4.a). Elemental mapping confirmed the uniform distribution of ZnO NF on the surface of the cotton matrix (Figure 5.4.b). Thermal gravimetric (TG)−differential thermal analysis shows~9% (w/w) loading of ZnO NF to cellulose fibers (Figure 5.4.c).

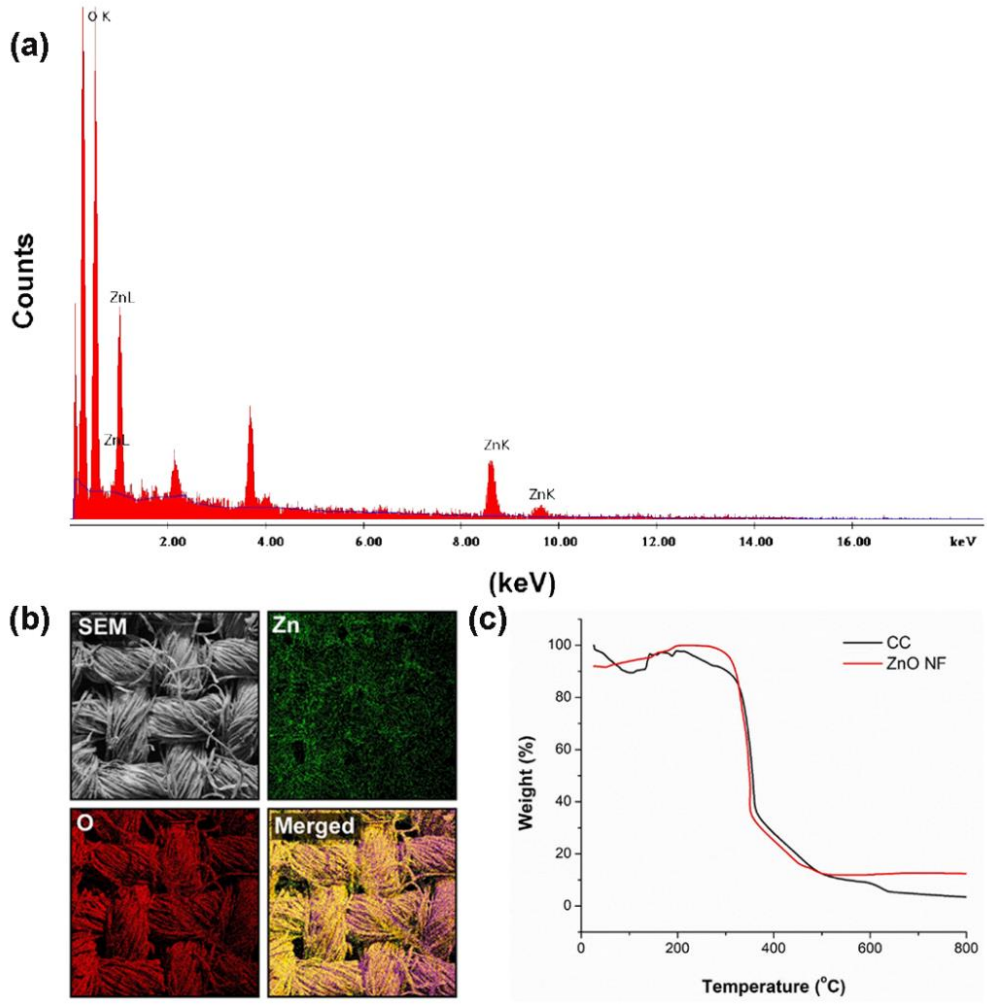

Figure 5.4: *(a) Energy Dispersive X-tay Analysis (EDX) of ZnO NF decorated cotton cloth. (b) Elemental mapping showing the uniform distribution of ZnO NF over the cotton matrix. The merged image was obtained by overlaying the other three images. In the merged image the purple regions indicate overlap between SEM and O; the yellow regions indicate overlap of Zn, O and SEM. (c) TG data of ZnO NF decorated cotton cloth and bare cotton cloth.*

At the outset, we investigated the growth of the ZnO phase on the cotton clothes using the XRD technique. With 5 h of intermediate growth time, the ZnO phase is not distinguishable properly as the prominent XRD peaks are suppressed by the broad hump of cellulose within the Bragg angle (2θ) range between 31 and 38°in Figure 5.5.a. Nevertheless, the signature of the ⟨101⟩ plane of ZnO at~36.2°can be traced from the XRD pattern. The growth of ZnO becomes quite dominant when the growth time is increased to 15 h. In this case, the diffraction peaks appearing at 2θof 31.8, 34.4, 36.1, 47.4, 56.6, 63.0, 68.0, and 69.2°represent the⟨100⟩, ⟨002⟩, ⟨101⟩, ⟨102⟩, ⟨110⟩, ⟨103⟩, ⟨112⟩, and ⟨201⟩ planes of ZnO nanocrystals, respectively.

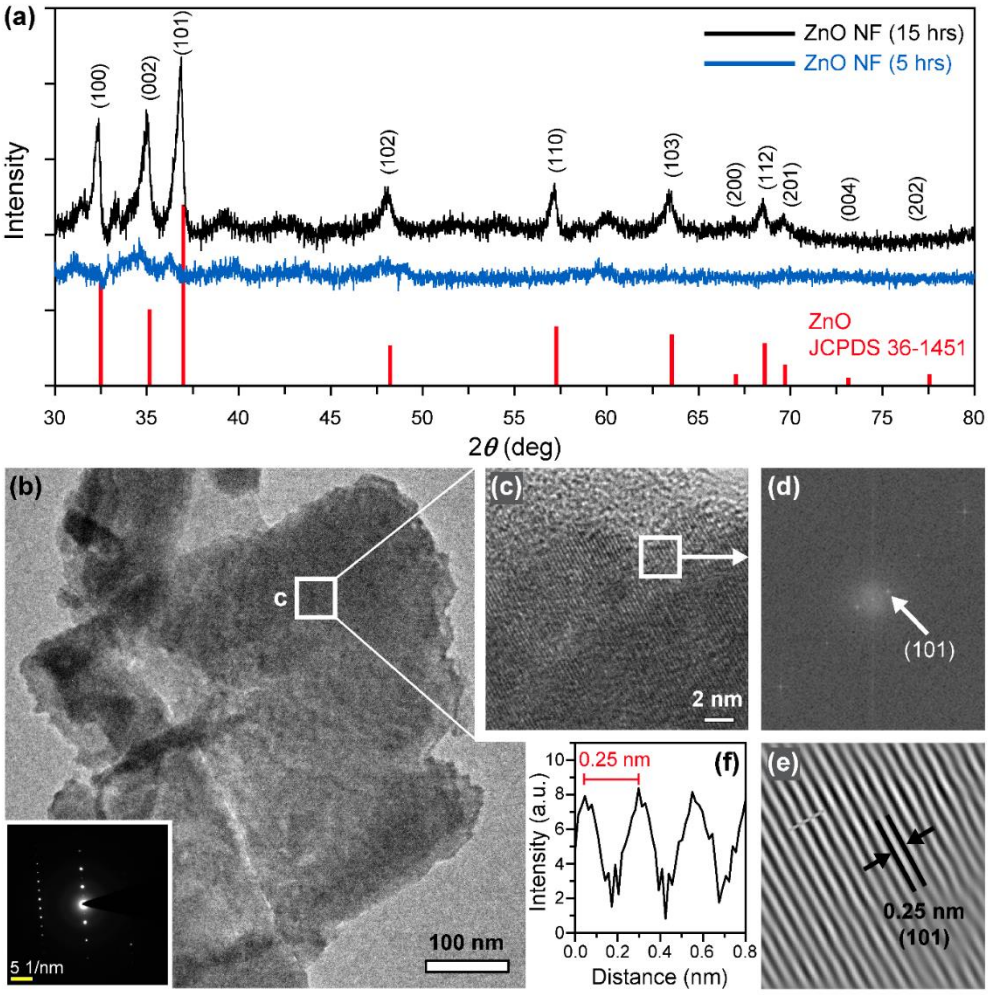

Figure 5.5: *(a) XRD of the ZnO NF decorated cotton cloth at different synthesis phase. (b) TEM of a single fully grown petal. Inset shows the SAED pattern. (c) HRTEM of the petal. (d) Electron diffraction pattern of the petal. (e) FFT shows the fringe pattern. (f) Fringe distance as calculated from FFT.*

The observed peaks are in good agreement with those for hexagonal closed-packed ZnO having the wurtzite structure [lattice constants a= 3.249,c= 5.206 Å; space group P63mc(186)] as reported earlier (JCPDS 36-1451) [53]. Sharp diffraction peaks indicate good crystalline quality of the synthesized NFs, and the absence of any additional peak directs toward the high purity of the material. The highly intensified peak at 36.1°indicates the dominance of the ⟨101⟩ plane in the material. The transmission electron microscopy (TEM) image (Figure 5.5.b) shows the size of a single ZnO NF petal to be ~600×300 nm. The high-resolution TEM (HRTEM) image taken at the centre of the petal indicates the presence of the ⟨101⟩ plane (Figure 5.5.c). The presence of distinct bright spots in the selected area electron diffraction (SAED) pattern (Figure 5.5.d) corresponds to the crystalline nature of the petals.

Fast Fourier transformation (FFT) shows that the crystallite is dominated by the⟨101⟩ plane of ZnO, with a lattice fringe spacing of 0.25 nm (Figure 5.5.e,f).

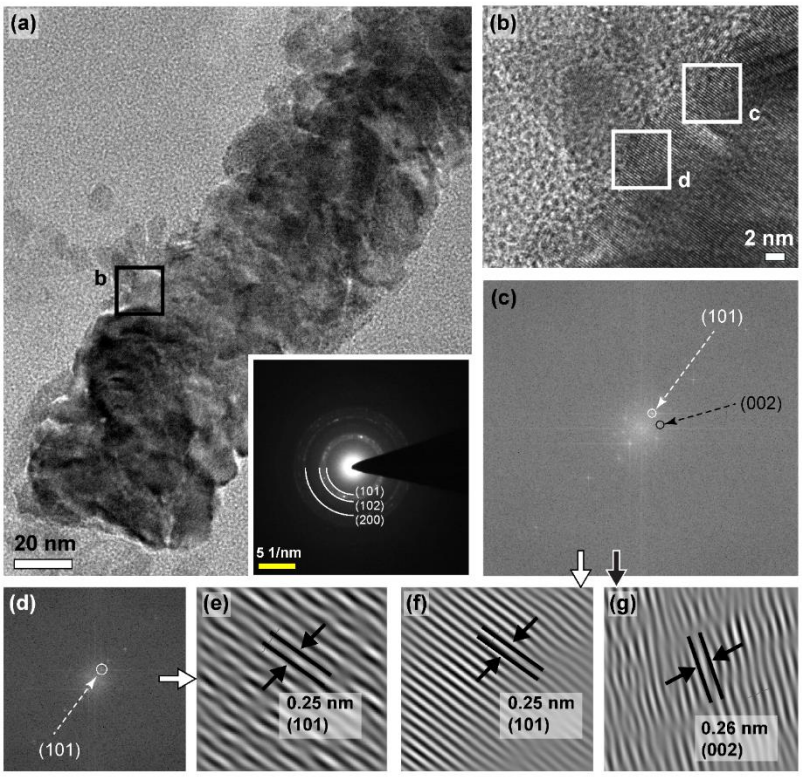

Figure 5.6: *(a) TEM of a single growing petal (5 h). Inset shows the SAED pattern. (b) HRTEM of the petal. (c) & (d) Electron diffraction pattern of the petal from different areas. (e-g) FFT shows the fringe pattern.*

Further, as shown in Figure 5.6.a, the formation of the nanorod-like morphology can be observed when the reaction time is reduced (i.e., 5 h). The surface of the nanorods appears to be rough and can be originated from the presence of a large number of crystallites. The SAED pattern shows small spots within the diffused ring and reveals the polycrystallinity of the nanorods as each spot arises from the Bragg reflection from individual crystallites (Figure 5.6.a inset). The rings can be indexed as⟨101⟩, ⟨102⟩, and ⟨200⟩ of the wurtzite phase of ZnO, which exactly correlates with the XRD pattern (Figure 5.5.a). Next, a close look of the nanorod at different locations (marked as c,d in Figure 5.6.b) reveals the presence of the⟨101⟩and⟨002⟩planes of ZnO with interplanar spacings of~0.25 and 0.26 nm, respectively (Figure 5.6.c−5.6.g). The exhibition of polycrystalline nature of the nanorods with various crystallites is different from nanorods grown on crystalline surfaces (e.g., Si). Thus, it can be anticipated that the use of the cotton substrate in the synthesis process plays a big role in forming nanorods with exposed crystallites

on the surface (Figure 5.6). In fact, the functional groups present in the cellulose fibers act as nucleation sites for the growth of nanorods (step 1 in Figure 5.7). It can be noted that in HMT-based hydrothermal synthesis, $Zn(OH)_2$ acts as the nucleation agent according to the following equations [54]:

$$\left.\begin{aligned} &C_6H_{12}N_4+4H_2O \rightarrow C_6H_{12}N_4H_4^{+}+4OH^{-} \\ &[Zn(C_6H_{12}N_4)]^{2+} + 4OH \rightarrow Zn(OH)_4^{\,2+}+C_6H_{12}N_4 \\ &Zn(OH)_4^{\,2+} \rightarrow Zn^{2+} + 4OH \\ &Zn^{2+} + 2OH \rightarrow ZnO+ H_2O \\ &\text{Or} \\ &Zn^{2+} + 2OH \rightarrow Zn(OH)_2 \rightarrow ZnO+ H_2O \end{aligned}\right\} \quad (5.1)$$

In the present investigation, the abundant and random distribution of these functional groups based nucleation sites on the cellulose fiber surface provides a continuous platform for ZnO growth along the direction of fibers (step 1 in Figure 5.7). Now, the random distribution of the functional groups leads to the randomly oriented nucleation sites, and consequently, the growth is evident to be different in different directions. The observation of the rough surface with different crystallites of the⟨101⟩ and ⟨002⟩ planes is the consequence of such a growth process. It is worth mentioning here that the method used to functionalize the cotton fibers is widely applicable to other substrates. Similar strategies were used to functionalize glass and nylon fishing nets previously [55, 56]. However, in both the cases, distinct nanorods were formed instead of NF, which may be due to the more oriented distribution of the surface functional groups. Also, from our understanding, the size of the cotton fibers will not impact the fabrication results. However, the type of functional groups may have an impact on the fabrication process, which needs to be explored in future with greater detail.

Now, it is well established that in ZnO crystals, the surface energy (per mole) varies with the direction as $\gamma_{[0001]} < \gamma_{[11-20]} < \gamma_{[10-10]}$ [57]. Hence, the growth of the ⟨002⟩ plane along the [0001] direction is highly favorable from a thermodynamic point of view. Thus, the nanorods with exposed ⟨002⟩ planes offer chances for further growth. As a result, with increased reaction time, the nanorods suffer two-dimensional growth,

that is, along horizontal as well as vertical directions to the surface of the fiber, leading to the development of petal-like features (step 4 in Figure 5.7).

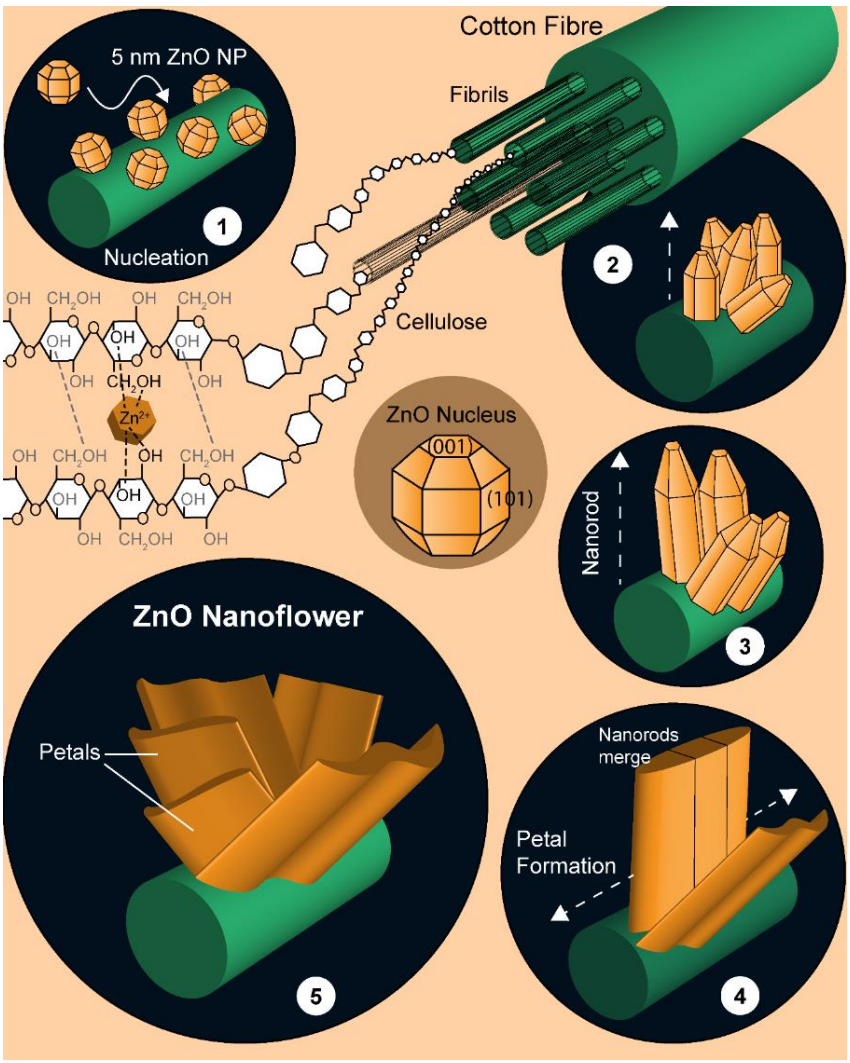

Figure 5.7: *Schematic representation of the different phases of ZnO nanoflower growth on cellulose membrane. Step 1: The nucleation, Step 2: Nanorod formation, Step 3: Elongation of nanorod, Step 4: Merging of nanorod, formation of petals. Step 5: Formation of ZnO Nanoflower.*

To ensure this fact, TEM analysis has been performed on four different edges of the fully grown petal. In none of these areas, any signature of the⟨002⟩ plane has been found. It is well known that a plane with a higher growth rate disappears quickly [58]. Thus, the disappearance of the ⟨002⟩ plane confirms the speculated lateral growth of the nanorods to form the petals. Subsequent self-assembly of such petal-like features leads to the formation of a flower-like morphology of ZnO at a higher reaction time (step 5 in Figure 5.7). Figure 5.8.a shows the absorbance spectrum recorded from bare cotton cloths and ZnO NF decorated cotton cloths. As the constituent of the cotton fiber is cellulose, the observed absorption bands at 200–220

and 270−290 nm could be assigned to oxidized xylans and monocarboxyl celluloses due to the presence of carboxyl and carbonyl groups, respectively [59].

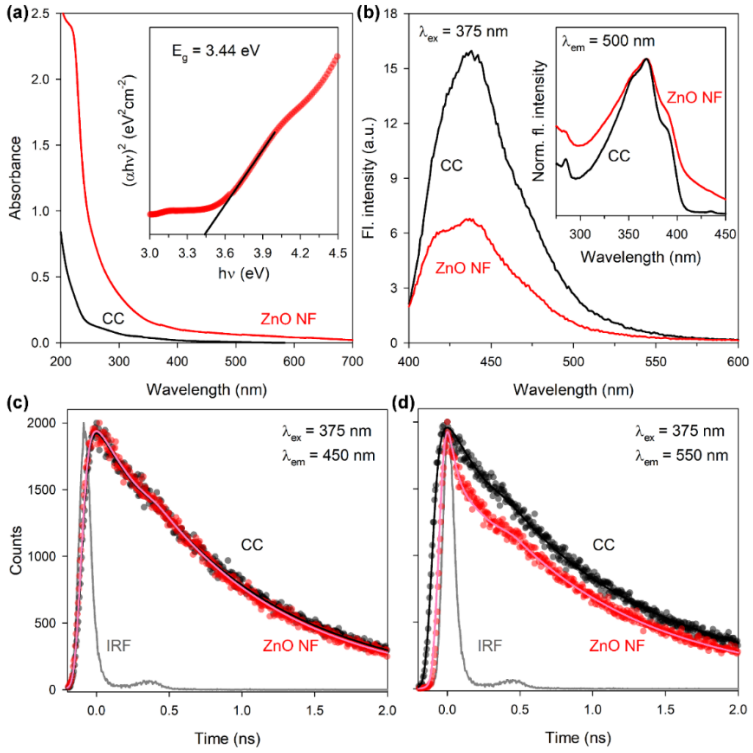

Figure 5.8: *(a) Absorbance of ZnO NF grown on cellulose fibers of cotton cloth. (b) Fluorescence emission spectra. Inset shows the fluorescence excitation spectra ZnO NF grown on cellulose fibers of cotton cloth. (c) & (d) Fluorescence lifetime spectra at different wavelength ZnO NF grown on cellulose fibers of cotton cloth.*

Furthermore, the absorption bands at 230−250 and 290−320 nm could be assigned to heteroaromatics of the furan and pyron types, respectively, and the low-intensity absorption shoulder above 300 nm to conjugated heteroaromatics [59]. Functionalization with ZnO NF leads to the appearance of the characteristic ZnO absorption edge at 365 nm which is blueshifted by 8 nm relative to the bulk exciton absorption (373 nm). Correspondingly, ZnO NF exhibited a slightly higher optical energy gap (Eg) of 3.44 eV with respect to bulk ZnO (3.37 eV) (Figure 5.8.a inset). The slight change in the absorption edge and Eg can be well explained by the oriented attachment of multiple ZnO nanorods in the flower-like morphology [60, 61]. The fluorescence emission spectra of the cotton cloth in the solid state (Figure 5.8.b) show an intense peak around 430 nm and a broad shoulder ranging from 470 to 560 nm when excited at 375 nm. The observed emission pattern of the cotton cloth exactly matches to the previously reported photoluminescence characteristics of

cellulose fibers [59, 62]. Gavrilov and Ermolenko (1966) [63], who studied photoluminescence of cellulose in great detail, have suggested that the broad emission band of cellulose originates from three different types of excitation centres. The presence of multiple excitation maxima (i.e., 265, 350, and 390 nm) in the excitation spectra of the bare cotton cloth (Figure 5.8.b inset) further supports their findings. Functionalization with ZnO NF significantly quenched the emission of the cellulose constituent (Figure 5.8.b), which indicates possible interactions between ZnO NF and cellulose fibers. The observed increase in the λ_{em} 410 nm/λ_{em} 450 nm ratio could be due to a possible interaction between the Zn-vacancy state of ZnO NF and the OH groups of cellulose fibers (O=C−O−Zn) as previous studies suggest that the presence of carboxylic groups in the anhydro glucose units shifts the emission maxima of cellulose to shorter wavelengths (blue shift) [59, 62, 64]. A detailed computational study (i.e., molecular docking) further supports the strong binding of ZnO NF with the cellulose fiber, mostly through hydrogen bonding. The calculated binding energies per unit area of the cellulose fiber with different facets of the ZnO nanostructure were found to be −21 kcal $mol^{-1}nm^{-2}$ (sphere), −43 kcal $mol^{-1}nm^{-2}$ [⟨002⟩ facet], −41 kcal $mol^{-1}nm^{-2}$ [⟨100⟩ and ⟨110⟩ facets], and −39 kcal $mol^{-1}nm^{-2}$ [⟨101⟩ facet]. The highly negative binding energies indicate stronger attachment between the cellulose fiber and ZnO NF.

To get further insight into the quenching mechanism, we studied the excited-statefluorescence lifetime of cellulose (i.e., cotton cloth) and ZnO NF-decorated cellulose. Interestingly, the fluorescence lifetime of both the samples remained unchanged at 450 nm (λ_{ex} 375 nm) (Figure 5.8.c), while a decrease was observed at 550 nm (λ_{ex}375 nm) upon ZnO NF decoration (Figure 5.8.d). This could well be interpreted by the existence of several luminescent centers (originating from the presence of conjugated chromophores of various origins) in the cellulose [63]. One possible mechanism behind the observed decrease in the fluorescence lifetime of ZnO NF-decorated cellulose could be due to the photoinduced electron transfer from the lowest unoccupied molecular orbital level of the lowenergy excitation centers (near the red end) of cellulose to the conduction band of ZnO, resulting in the luminescence quenching of cellulose [65]. The presence of a very fast component (i.e., 25 ps) in the excited-state lifetime decay of ZnO NF-decorated cellulose further supports our conjecture. In contrast, due to the mismatch in the energy levels, the

highenergy excitation centers (near the blue end) of cellulose cannot undergo such electron or energy transfers. The quenching in this region is static in nature and may be originated due to ground-state interactions between ZnO NF and cellulose which we explained in the earlier section. In summary, the results of our optical studies confirm the attachment of ZnO NF to the cellulose fibers of the cotton cloth.

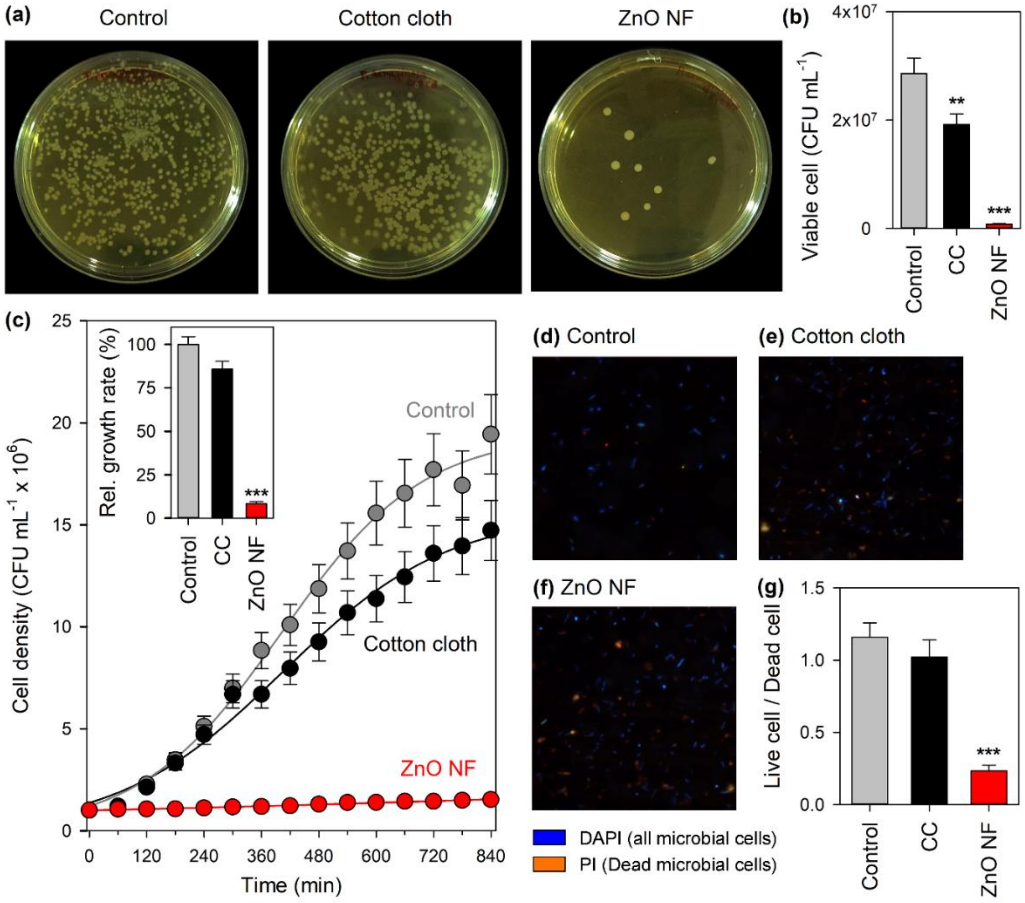

Figure 5.9: *(a) Agar plate assay. (b) Cell viability as observed in agar plate assay. (c) Growth curve analysis. Inset shows relative growth rates. (d-f) DAPI-PI differential staining. (g) Ratio of live vs dead cells as observed under microscope.*

5.2.1.3. Antimicrobial Activity of the ZnO NF-Functionalized Cotton Fabric: The antimicrobial activity of the ZnO NFdecorated cotton fabric was evaluated against the SARS-CoV-2 mimic pathogenic capsule containing (having LecA, the mimic of viral spike protein) Gram-negative model bacteria *P. aeruginosa*. To directly assess the antimicrobial effect, after 1 h of incubation (in the dark, 37°C) over the ZnO NF-decorated cotton cloth and bare cotton cloth, *P. aeruginosa* was transferred and cultured on a Luria−Bertani (LB) agar medium (i.e., the platecount assay) for 12 h (at 37 °C).

The original bacterial inoculum, which was employed over the fabrics for initial incubation, served as a control. As shown in the photographs of the agar plates after 12 h (Figure 5.9.a), a clear killing activity was observed in the case of the ZnO NF-functionalized cotton fabric resulting into very few colonies. Colony count shows (Figure 5.9.b) that in the ZnO NF-functionalized cotton fabric, the bacterial growth was~79% lower compared to the control [$P< 0.0001$; $F(2,15) = 303.2$, one-way analysis of variance (ANOVA)] and ~54% lower compared to the bare cotton fabric [$P< 0.0001$; $F(2,15) = 303.2$, one-way ANOVA].

Further, the antibacterial effect of the ZnO NF-decorated cotton cloth on the *P. aeruginosa* growth kinetics was evaluated in liquid LB media. The bacterial growth was monitored by the measurement of the optical density at 600 nm (OD600) as a reflection of the bacterial concentration in the culture. After 1h of incubation over the respective fabrics (inoculation at 1×10^6 CFU/mL), we started monitoring the growth kinetics. The original bacterial inoculum, which was employed over the fabrics for initial incubation, served as a control. Figure 5.9.c clearly indicates that the ZnO NF-decorated cotton cloth caused complete inhibition of growth and this was even continued for 14 h. The bare cotton cloth also showed a weaker growth inhibition. The growth rate was~10 times lower in the case of the ZnO NF-functionalized cotton fabric compared to both the control [$P< 0.0001$;$F(2,15) = 1062$, one-way ANOVA] and bare cotton fabric [$P< 0.0001$;$F(2,15) = 1062$, one-way ANOVA] (Figure 5.9.c inset).

Our computational studies have suggested that ZnO NF can simultaneously bind and denature *P. aeruginosa* LecA (SARSCoV-2 spike protein mimic), resulting into disruption of the bacterial cell membrane, which eventually is responsible for the observed antimicrobial activity. In order to confirm that ZnO NF disrupts the bacterial membrane, *P. aeruginosa* cells were treated with PI after incubation with the ZnO NF-decorated cotton fabric. It is worth mentioning here that PI is a small molecule dye that upon binding to double-stranded DNA fluoresces red upon excitation, and it cannot cross an intact cytoplasmic membrane [66, 67]. We expected that ZnO NF induced membrane disruption would lead to an increase in nucleic acid staining by PI compared to that of the control or bare cotton cloth-treated ones. As shown in Figure 5.9.d,e, control bacteria as well as bacteria incubated with the bare cotton fabric remained unstained to PI. In comparison,

intracellular PI staining was clearly visible in cultures exposed to the ZnO NF-decorated cotton fabric (Figure 5.9.f). We further evaluated the number of viable cells using differential staining with DAPI and PI. As discussed earlier, PI generally stains the membrane-disrupted cells, whereas DAPI stains all nuclear materials irrespective of their viability. The differentially stained images of control and cotton fabric-inoculated bacteria show more number of viable cells than dead cells (ratio~1.2) (Figure 5.9.g). In contrast, the number of living cells was significantly reduced in the case of the ZnO NF-functionalized cotton fabric (~0.45) (Figure 5.9.g).

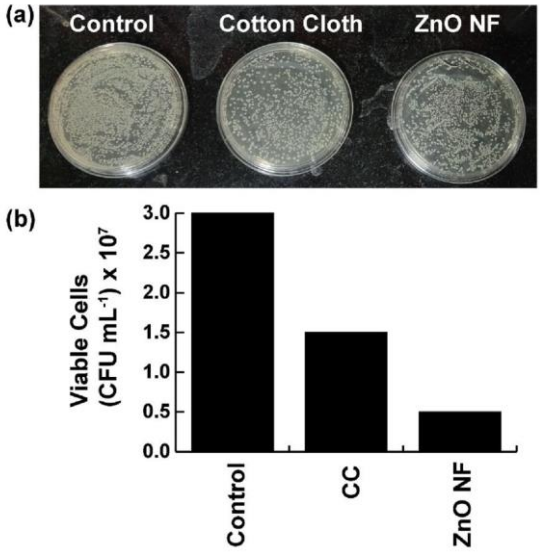

Figure 5.10: *(a) Digital photographs of S. aureus colonies on agar plate after treatment with ZnO NF decorated cotton cloth and bare cotton cloth. (b) Bacterial cell count after 12 hrs. of incubation.*

Next, we investigated the antimicrobial ability of the ZnO NF-decorated cotton fabric toward Gram-positive bacteria *Staphylococcus aureus*. The results of the plate count assay showed the antimicrobial activity to be significant but lower compared to *P. aeruginosa* (Figure 5.10), which may be due to the absence of the S-protein mimic in *S. aureus*. In one of the recent studies, it was observed that the nanoparticles having an anionic surface showed lower antialgal and antiyeast activity compared to those having a cationic surface [68]. The probable explanation could be the poor adhesion of anionic particles to the microbial cell membranes (anionic in nature) due to electrostatic repulsion. However, the particle−cell membrane electrostatic adhesion in the case of cationic nanoparticles leads to enhanced antiyeast and antialgal action. As hydrothermally produced ZnO has a positive surface charge and

P. aeruginosa has a negative surface charge, there is a possibility that the bacteria bind to NF predominantly through electrostatic interactions between bacterial glycolipids and NF. Therefore, in order to understand the role of charge−charge interactions in the antimicrobial activity, we have decorated the cellulosefiber of the cloth with positively charged poly-L-lysine and repeated the antimicrobial experiment (i.e., the plate count assay). The results show a marginal decrease (~12%) in the bacterial count in the poly-Llysine coated cloth compared to the control (Figure 5.11).

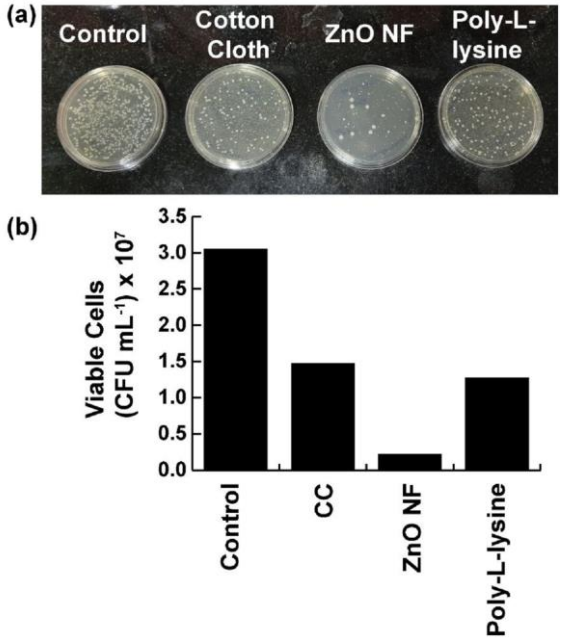

Figure 5.11: *(a) Digital photographs of P. aeruginosa colonies on agar plate after treatment with ZnO NF decorated cotton cloth, Poly-L-lysine coated cotton cloth and bare cotton cloth. (b) Bacterial cell count after 12 hrs. of incubation.*

Thus, although the charge−charge interaction may play a role in the binding of *P. aeruginosa* to ZnO nanocrystals, the antimicrobial activity is predominantly due to the binding and subsequent denaturation of SARS-CoV-2 spike protein-mimicking protein of *P. aeruginosa*. Next, we performed a computer simulation study to understand whether the filtration effect is due to the RBD mimic adsorbing to the ZnO crystals or due to some other blockade by the protrusions of thefibers and their new ZnO decoration. Particle (i.e., the microbe) flow through the cellulose fiber mesh was simulated using laminar flow and particle tracing algorithms as implemented in COMSOL multiphysics software. A simplified two-dimensional model of the cellulose fiber mesh (with~10μm pores) was built as depicted in Figure 5.12.a, and the particle flow was studied through this mesh under normal exhalation

conditions Figure 5.12.b). ZnO deposition on the cellulose fiber slightly increased the diameters of such fibers (Figure 5.3.a, b, e, f), which was ignored in the simulation. In this regard, it has to be noted that the sizes of the microbes are much smaller (~0.05−0.5μm) compared to the pores. Particle penetration ability up to 100 μm of the cellulose fiber mesh was studied varying the sticking probability (i.e., the affinity) from 0.1 to 1 (per collision), and it was found that penetration ability decreases exponentially with the increase in sticking probability (Figure 5.12.e).

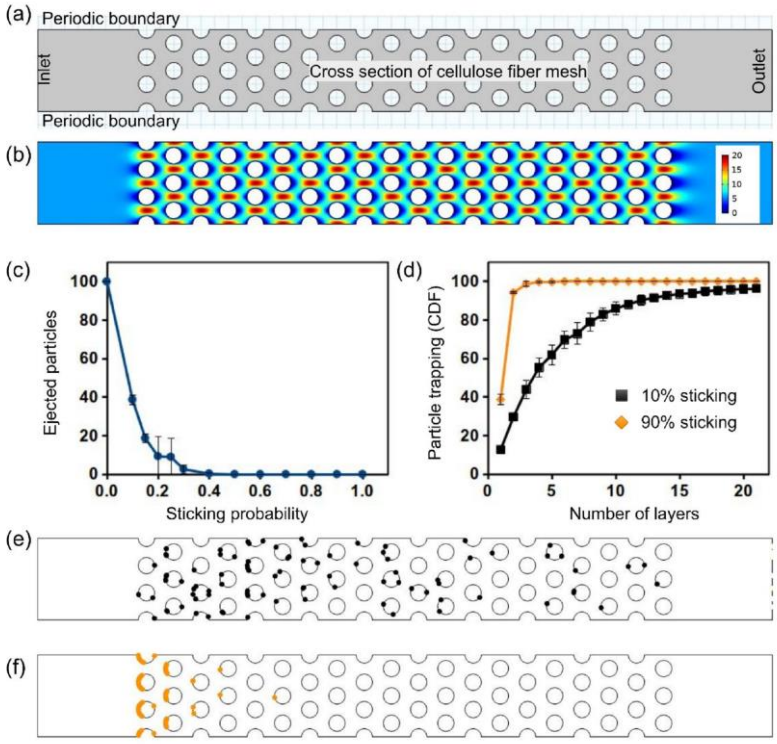

Figure 5.12: *(a) Two dimensional periodic model of the system. The grid lines are 10 μm apart. (b) Laminar air flow through the mesh. Velocity of the air (ms-1) is depicted by the color bar. (c) Exponential decay of penetration ability of the particles (in percentage) upto 100 μm with increase in sticking probability of the fibers. (d) Cumulative distribution function (CDF) of trapped particles along with the cellulose fiber layers. The 10% sticking indicates the bare fibers. 90% sticking indicates ZnO NF decorated fibers (e) Trapped particles at 0.1 sticking probability (the bare fibers). (f) Trapped particles at 0.9 sticking probability (the ZnO NF decorated fibers).*

As evident from our microbial experiments, the sticking probability of the bare cotton cloth is very low (~10% or ~0.1). The simulation results show that with a sticking probability of 0.1, 20 layers of the fabric are required to trap ~98% of the particles. However, Figure 5.3 shows the alterations are of only 1−2 layers. On the contrary, molecular docking showed that binding free energy of SARS-CoV-2 RBD on the ⟨101⟩ facet of ZnO is −29 kcal/mol, indicating a very high binding affinity

with a large equilibrium constant [1.82×10^{21} as obtained from $\Delta G=-R\times T\times\ln(k_{eq})$ equation]. Such a large k_{eq} suggests that almost all the particles remain bound and the sticking probability is close to 1. The simulation results demonstrate that even with a 90% sticking probability, all the particles got trapped within the first few layers of the cellulose fiber mesh (Figure 5.12.e,f). Thus, the bare fibers or fiber protrusions alone cannot stop the spread of the microbe, while the ZnO-covered regions can instantly trap them due to their high binding affinity. Moreover, the bare fibers have not shown significant antimicrobial activity in our experiments. Therefore, the antimicrobial activity as depicted by the ZnO NF-fabricated cotton cloths is predominantly due to the attachment and subsequent denaturation of the spikeprotein mimic by the ZnO surface.

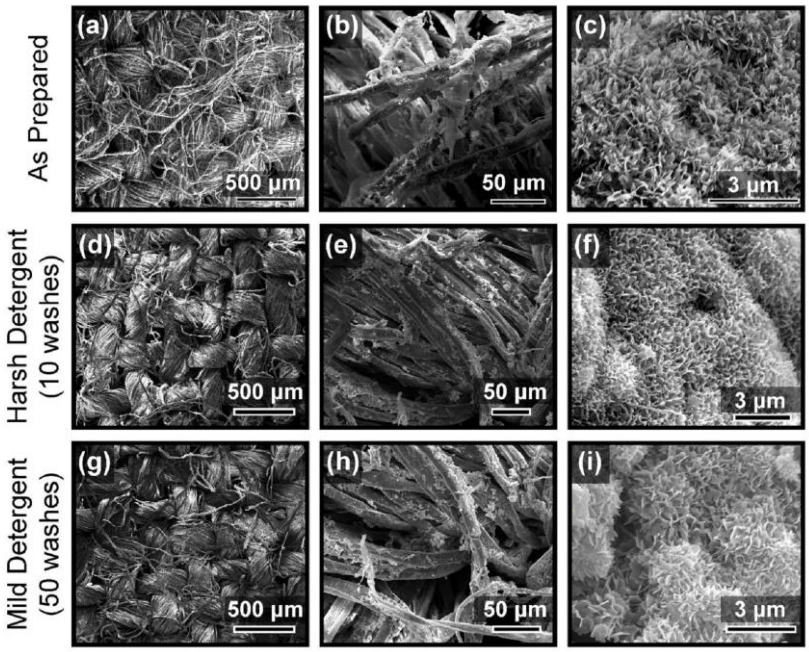

Figure 5.13: *(a-c) SEM images of the as prepared ZnO NF functionalized cotton fabric without any wash. (d-f) SEM images of the ZnO NF functionalized cotton fabric after 10 washes with harsh detergent. (g-i) SEM images of the ZnO NF functionalized cotton fabric after 50 washes with mild detergent.*

Thus, our antimicrobial studies experimentally provide evidence that ZnO NF can induce membrane damage, resulting into a loss of membrane potential leading to inhibition of PI staining. It further depicts that ZnO NF is an effective antimicrobial agent particularly against SARS-CoV-2-mimicking microorganisms. Washability and Reusability of the ZnO NF-Functionalized Cotton Fabric.For regular use as an

antimicrobial hospital dress material (or PPE), washability and reusability of the fabric are the two major factors.

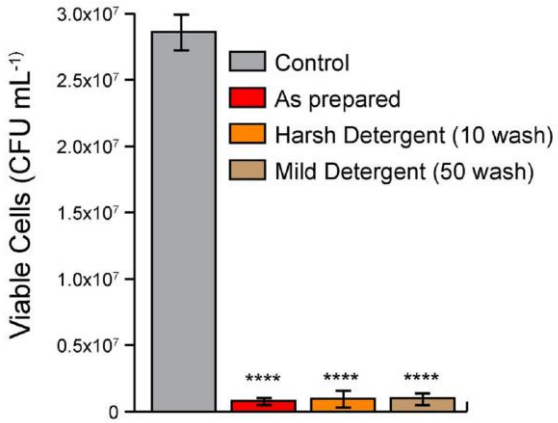

Figure 5.14: *Role of washing with detergent on the antimicrobial activity (P. aeruginosa) of the ZnO NF functionalized cotton fabric.*

To address this issue, we have washed the fabric material with a mild detergent as well as with a harsh detergent in tap water. Even after 50 washes with the mild detergent and 10 washes with the harsh detergent, the ZnO NF coating of the cottonfibers remained almost intact as observed under SEM (Figure 5.13). The antibacterial activity was also sustained in both the cases as compared to the original ZnO NF-functionalized fabric (Figure 5.14). Therefore, the ZnO NF-functionalized cotton fabric was found to be highly reusable with sufficient washability.

5.3. Conclusion:

In conclusion, we successfully functionalized the commonly available cotton fabrics with ZnO NFs. The ZnO NF functionalized cotton fabrics showed significant antimicrobial activities against the SARS-Cov-2 mimic model pathogenic microorganism as depicted in our detailed antimicrobial assays. The ZnO NFs were able to destroy the microbial membrane leading to inhibition of infection. A detailed computational study along with *in vitro* studies using viral spike protein mimicking protein and bacteria showed the trapping ability of the fabric. As a proof of concept, we designed a laboratory grade prototype respirator for using in common N95 masks using the ZnO NF-functionalized cotton fabrics. The porous respirator helped to solve the problem of CO_2 rebreathing and prevented spread of microbes through the

pores. The ZnO NF-functionalized cotton fabrics can further be used to design comfortable, washable antimicrobial PPE, which is an urgent need of today.

Reference

[1] M.E. Deming, N.L. Michael, M. Robb, M.S. Cohen, K.M. Neuzil, Accelerating development of sars-cov-2 vaccines — The role for controlled human infection models, *N. Engl. J. Med.*, 383 (2020) e63.

[2] COVID-19 Dashboard, in *Johns Hopkins University & Medicine* (2020).

[3] S. Talebian, G.G. Wallace, A. Schroeder, F. Stellacci, J. Conde, Nanotechnology-based disinfectants and sensors for SARS-CoV-2, *Nat. Nanotechnol.*, 15 (2020) 618.

[4] J. Haushofer, C.J.E. Metcalf, Which interventions work best in a pandemic?, *Science*, 368 (2020) 1063.

[5] Q.X. Ma, H. Shan, H.L. Zhang, G.M. Li, R.M. Yang, J.M. Chen, Potential utilities of mask-wearing and instant hand hygiene for fighting SARS-CoV-2, *J. Med. Virol.*, 92 (2020) 1567.

[6] N.H.L. Leung, D.K.W. Chu, E.Y.C. Shiu, K.-H. Chan, J.J. McDevitt, B.J.P. Hau, H.-L. Yen, Y. Li, D.K.M. Ip, J.S.M. Peiris, W.-H. Seto, G.M. Leung, D.K. Milton, B.J. Cowling, Respiratory virus shedding in exhaled breath and efficacy of face masks, *Nat. Med.*, 26 (2020) 676.

[7] E.P. Fischer, M.C. Fischer, D. Grass, I. Henrion, W.S. Warren, E. Westman, Low-cost measurement of face mask efficacy for filtering expelled droplets during speech, *Sci. Adv.*, 6 (2020) eabd3083.

[8] Considerations for Wearing Masks., in *Centers for Disease Control and Prevention (USA)* (2020).

[9] M. Morishima, T. Mitsuno, K. Kishida, Problems related to mask use in hay fever sufferers by repeated surveys, *Int. J. Cloth. Sci.*, 29 (2017) 123.

[10] H.P. Lee, D.Y. Wang, Objective assessment of increase in breathing resistance of N95 respirators on human subjects, *Ann Occup Hyg.*, 55 (2011) 917.

[11] R.J. Roberge, A. Coca, W.J. Williams, J.B. Powell, A.J. Palmiero, Physiological impact of the N95 filtering facepiece respirator on healthcare workers, *Respir. Care*, 55 (2010) 569.

[12] S.Y. Kyung, Y. Kim, H. Hwang, J.-W. Park, S.H. Jeong, Risks of N95 face mask use in subjects with COPD, *Respir. Care*, 65 (2020) 658.

[13] Y. Li, H. Tokura, Y.P. Guo, A.S.W. Wong, T. Wong, J. Chung, E. Newton, Effects of wearing N95 and surgical facemasks on heart rate, thermal stress and subjective sensations, *Int. Arch. Occup. Environ. Health*, 78 (2005) 501.

[14] H. Rodríguez-Tobías, G. Morales, D. Grande, Comprehensive review on electrospinning techniques as versatile approaches toward antimicrobial biopolymeric composite fibers, *Mater. Sci. Eng. C,* 101 (2019) 306.

[15] G.P.C. Salmond, M. Welch, Antibiotic resistance: adaptive evolution, *Lancet*, 372 (2008) S97.

[16] B. Spellberg, J.G. Bartlett, D.N. Gilbert, The future of antibiotics and resistance, *N. Engl. J. Med.*, 368 (2013) 299.

[17] Z.-m. Xiu, Q.-b. Zhang, H.L. Puppala, V.L. Colvin, P.J.J. Alvarez, Negligible particle-specific antibacterial activity of silver nanoparticles, *Nano Lett.*, 12 (2012) 4271.

[18] S. Shrivastava, T. Bera, A. Roy, G. Singh, P. Ramachandrarao, D. Dash, Retracted: Characterization of enhanced antibacterial effects of novel silver nanoparticles, *Nanotechnology*, 18 (2007) 225103.

[19] Z. Shi, J. Tang, L. Chen, C. Yan, S. Tanvir, W.A. Anderson, R.M. Berry, K.C. Tam, Enhanced colloidal stability and antibacterial performance of silver nanoparticles/cellulose nanocrystal hybrids, *J. Mater. Chem. B*, 3 (2015) 603.

[20] D. MubarakAli, N. Thajuddin, K. Jeganathan, M. Gunasekaran, Plant extract mediated synthesis of silver and gold nanoparticles and its antibacterial activity against clinically isolated pathogens, *Colloids Surf. B: Biointerfaces*, 85 (2011) 360.

[21] Y. Zhao, Y. Tian, Y. Cui, W. Liu, W. Ma, X. Jiang, Small molecule-capped gold nanoparticles as potent antibacterial agents that target gram-negative bacteria, *J. Am. Chem. Soc.*, 132 (2010) 12349.

[22] Y. Zhao, C. Ye, W. Liu, R. Chen, X. Jiang, Tuning the composition of AuPt bimetallic nanoparticles for antibacterial application, *Angew. Chem. Int. Ed.*, 53 (2014) 8127.

[23] K. Gopinath, S. Kumaraguru, K. Bhakyaraj, S. Mohan, K.S. Venkatesh, M. Esakkirajan, P. Kaleeswarran, N.S. Alharbi, S. Kadaikunnan, M. Govindarajan, G. Benelli, A. Arumugam, Green synthesis of silver, gold and silver/gold bimetallic nanoparticles using the Gloriosa superba leaf extract and their antibacterial and antibiofilm activities, *Microb. Pathog.*, 101 (2016) 1.

[24] S. Szunerits, R. Boukherroub, Antibacterial activity of graphene-based materials, *J. Mater. Chem. B*, 4 (2016) 6892.
[25] F.R. Marciano, D.A. Lima-Oliveira, N.S. Da-Silva, A.V. Diniz, E.J. Corat, V.J. Trava-Airoldi, Antibacterial activity of DLC films containing TiO_2 nanoparticles, *J. Colloid Interface Sci.*, 340 (2009) 87.
[26] Y. Li, W. Zhang, J. Niu, Y. Chen, Mechanism of photogenerated reactive oxygen species and correlation with the antibacterial properties of engineered metal-oxide nanoparticles, *ACS Nano*, 6 (2012) 5164.
[27] G.S. Alvarez, C. Hélary, A.M. Mebert, X. Wang, T. Coradin, M.F. Desimone, Antibiotic-loaded silica nanoparticle–collagen composite hydrogels with prolonged antimicrobial activity for wound infection prevention, *J. Mater. Chem. B*, 2 (2014) 4660.
[28] Y.S. Kim, M.Y. Song, J.D. Park, K.S. Song, H.R. Ryu, Y.H. Chung, H.K. Chang, J.H. Lee, K.H. Oh, B.J. Kelman, I.K. Hwang, I.J. Yu, Subchronic oral toxicity of silver nanoparticles, *Part. Fibre Toxicol.*, 7 (2010) 20.
[29] C. Beer, R. Foldbjerg, Y. Hayashi, D.S. Sutherland, H. Autrup, Toxicity of silver nanoparticles—Nanoparticle or silver ion?, *Toxicol. Lett.*, 208 (2012) 286.
[30] S. Kittler, C. Greulich, J. Diendorf, M. Köller, M. Epple, Toxicity of silver nanoparticles increases during storage because of slow dissolution under release of silver ions, *Chem. Mater.*, 22 (2010) 4548.
[31] H.A. Jeng, J. Swanson, Toxicity of metal oxide nanoparticles in mammalian cells, *J. Environ. Sci. Part A*, 41 (2006) 2699.
[32] A.B. Djurišić, Y.H. Leung, A.M. Ng, X.Y. Xu, P.K. Lee, N. Degger, R. Wu, Toxicity of metal oxide nanoparticles: Mechanisms, characterization, and avoiding experimental artefacts, *Small*, 11 (2015) 26.
[33] K. Zheng, M.I. Setyawati, D.T. Leong, J. Xie, Antimicrobial gold nanoclusters, *ACS Nano*, 11 (2017) 6904.
[34] H. Haidari, Z. Kopecki, R. Bright, A.J. Cowin, S. Garg, N. Goswami, K. Vasilev, Ultrasmall agnp-impregnated biocompatible hydrogel with highly effective biofilm elimination properties, *ACS Appl. Mater. Interfaces*, 12 (2020) 41011.
[35] K. Zheng, M.I. Setyawati, D.T. Leong, J. Xie, Observing antimicrobial process with traceable gold nanoclusters, *Nano Res.*, 14 (2021) 1026.

[36] K. Zheng, J. Xie, Composition-dependent antimicrobial ability of full-spectrum Au_xAg_{25-x} alloy nanoclusters, *ACS Nano*, 14 (2020) 11533.
[37] K. Zheng, J. Xie, Engineering ultrasmall metal nanoclusters as promising theranostic agents, *Trends Chem.*, 2 (2020) 665.
[38] A. Adhikari, S. Mondal, T. Chatterjee, M. Das, P. Biswas, R. Ghosh, S. Darbar, H. Alessa, J.T. Althakafy, A. Sayqal, Redox nanomedicine ameliorates chronic kidney disease (CKD) by mitochondrial reconditioning in mice, *Commn. Biol.*, 4 (2021) 1.
[39] J. Bian, Z. Li, Angiotensin-converting enzyme 2 (ACE2): SARS-CoV-2 receptor and RAS modulator, *Acta Pharm. Sin. B*, 11 (2021) 1.
[40] A.R. Bourgonje, A.E. Abdulle, W. Timens, J.L. Hillebrands, G.J. Navis, S.J. Gordijn, M.C. Bolling, G. Dijkstra, A.A. Voors, A.D. Osterhaus, Angiotensin-converting enzyme 2 (ACE2), SARS-CoV-2 and the pathophysiology of coronavirus disease 2019 (COVID-19), *J. Pathol.*, 251 (2020) 228.
[41] W. Li, M.J. Moore, N. Vasilieva, J. Sui, S.K. Wong, M.A. Berne, M. Somasundaran, J.L. Sullivan, K. Luzuriaga, T.C. Greenough, H. Choe, M. Farzan, Angiotensin-converting enzyme 2 is a functional receptor for the SARS coronavirus, *Nature*, 426 (2003) 450.
[42] R.N. Kirchdoerfer, C.A. Cottrell, N. Wang, J. Pallesen, H.M. Yassine, H.L. Turner, K.S. Corbett, B.S. Graham, J.S. McLellan, A.B. Ward, Pre-fusion structure of a human coronavirus spike protein, *Nature*, 531 (2016) 118.
[43] M. Hoffmann, H. Kleine-Weber, S. Schroeder, N. Krüger, T. Herrler, S. Erichsen, T.S. Schiergens, G. Herrler, N.-H. Wu, A. Nitsche, M.A. Müller, C. Drosten, S. Pöhlmann, Sars-cov-2 cell entry depends on ACE2 and TMPRSS2 and is blocked by a clinically proven protease inhibitor, *Cell*, 181 (2020) 271.
[44] P. Biswas, A. Adhikari, U. Pal, P. Singh, M. Das, T. Saha-Dasgupta, S.S. Choudhury, R. Das, S.K. Pal, Flexibility modulates the catalytic activity of a thermostable enzyme: Key information from optical spectroscopy and molecular dynamics simulation, *Soft Matter*, 16 (2020) 3050.
[45] R.K. Dutta, B.P. Nenavathu, M.K. Gangishetty, A.V.R. Reddy, Studies on antibacterial activity of ZnO nanoparticles by ROS induced lipid peroxidation, *Colloids Surf. B: Biointerfaces*, 94 (2012) 143.

[46] A. Tavakoli, A. Ataei-Pirkooh, G. Mm Sadeghi, F. Bokharaei-Salim, P. Sahrapour, S.J. Kiani, M. Moghoofei, M. Farahmand, D. Javanmard, S.H. Monavari, Polyethylene glycol-coated zinc oxide nanoparticle: an efficient nanoweapon to fight against herpes simplex virus type 1, *Nanomedicine (Lond.),* 13 (2018) 2675.

[47] Z. Li, R. Yang, M. Yu, F. Bai, C. Li, Z.L. Wang, Cellular level biocompatibility and biosafety of ZnO nanowires, *J. Phys. Chem. C*, 112 (2008) 20114.

[48] R. Madathiparambil Visalakshan, L.E. González García, M.R. Benzigar, A. Ghazaryan, J. Simon, A. Mierczynska-Vasilev, T.D. Michl, A. Vinu, V. Mailänder, S. Morsbach, The influence of nanoparticle shape on protein corona formation, *Small*, 16 (2020) 2000285.

[49] P. Roach, D. Farrar, C.C. Perry, Surface Tailoring for Controlled Protein Adsorption: Effect of Topography at the Nanometer Scale and Chemistry, *J. Am. Chem. Soc.*, 128 (2006) 3939.

[50] C. Chemani, A. Imberty, S.d. Bentzmann, M. Pierre, M. Wimmerová, B.P. Guery, K. Faure, Role of leca and lecb lectins in *Pseudomonas aeruginosa* induced lung injury and effect of carbohydrate ligands, *Infect. Immun.*, 77 (2009) 2065.

[51] J.B. Lyczak, C.L. Cannon, G.B. Pier, Lung infections associated with cystic fibrosis, *Clin. Microbiol. Rev.*, 15 (2002) 194.

[52] J.-Y. Fagon, J. Chastre, Y. Domart, J.-L. Trouillet, C. Gibert, Mortality Due to Ventilator-Associated Pneumonia or Colonization with Pseudomonas or Acinetobacter Species: Assessment by Quantitative Culture of Samples Obtained by a Protected Specimen Brush, *Clin. Infect. Dis.*, 23 (1996) 538.

[53] B. Weng, M.-Q. Yang, N. Zhang, Y.-J. Xu, Toward the enhanced photoactivity and photostability of ZnO nanospheres via intimate surface coating with reduced graphene oxide, *J. Mater. Chem. A*, 2 (2014) 9380.

[54] M.H. Mamat, Z. Khusaimi, M.M. Zahidi, S.A. Bakar, Y.M. Siran, S.A.M. Rejab, A.J. Asis, S. Tahiruddin, S. Abdullah, M.R. Mahmood, Controllable growth of vertically aligned aluminum-doped zinc oxide nanorod arrays by sonicated sol–gel immersion method depending on precursor solution volumes, *Jpn. J. Appl. Phys.*, 50 (2011) 06GH04.

[55] P. Sathe, K. Laxman, M.T.Z. Myint, S. Dobretsov, J. Richter, J. Dutta, Bioinspired nanocoatings for biofouling prevention by photocatalytic redox reactions, *Sci. Rep.*, 7 (2017) 3624.

[56] Z.S. Seddigi, S.A. Ahmed, S. Sardar, Samir K. Pal, Ultrafast dynamics at the zinc phthalocyanine/zinc oxide nanohybrid interface for efficient solar light harvesting in the near red region, *Sol. Energy Mater. Sol.*, 143 (2015) 63.

[57] S. Bayan, D. Mohanta, Directed growth characteristics and optoelectronic properties of Eu-doped ZnO nanorods and urchins, *J. Appl. Phys.*, 108 (2010).

[58] H. Zhang, D. Yang, Y. Ji, X. Ma, J. Xu, D. Que, Low temperature synthesis of flowerlike ZnO nanostructures by cetyltrimethylammonium bromide-assisted hydrothermal process, *J. Phys. Chem. B*, 108 (2004) 3955.

[59] A. Castellan, R. Ruggiero, E. Frollini, L.A. Ramos, C. Chirat, Studies on fluorescence of cellulosics, *Holzforschung*, 61 (2007) 504.

[60] R. Vinod, P. Sajan, S.R. Achary, C.M. Tomas, V. Munoz-Sanjosé, M.J. Bushiri, Enhanced UV emission from ZnO nanoflowers synthesized by the hydrothermal process, *J. Phys. D: Appl. Phys.*, 45 (2012) 425103.

[61] W. Yang, Q. Li, S. Gao, J.K. Shang, NH_{4+} directed assembly of zinc oxide micro-tubes from nanoflakes, *Nanoscale Res. Lett.*, 6 (2011) 491.

[62] P. Grönroos, M. Bessonoff, K. Salminen, J. Paltakari, S. Kulmala, Phosphorescence and fluorescence of fibrillar cellulose films, *Nord. Pulp Pap. Res. J.*, 33 (2018) 246.

[63] M.Z. Gavrilov, I.N. Ermolenko, A study of cellulose luminescence, *J. Appl. Spectrosc.*, 5 (1966) 542.

[64] T. Kitaoka, A. Isogai, F. Onabe, Chemical modification of pulp fibers by TEMPO-mediated oxidation, *Nord. Pulp Pap. Res. J.*, 14 (1999) 279.

[65] H. Ma, W. Ma, J.-F. Chen, X.-Y. Liu, Y.-Y. Peng, Z.-Y. Yang, H. Tian, Y.-T. Long, Quantifying visible-light-induced electron transfer properties of single dye-sensitized ZnO entity for water splitting, *J. Am. Chem. Soc.*, 140 (2018) 5272.

[66] M. Eschbach, K. Schreiber, K. Trunk, J. Buer, D. Jahn, M. Schobert, Long-term anaerobic survival of the opportunistic pathogen *Pseudomonas aeruginosa* via pyruvate fermentation, *J. Bacteriol.*, 186 (2004) 4596.

[67] A.J. Kora, J. Arunachalam, Assessment of antibacterial activity of silver nanoparticles on *Pseudomonas aeruginosa* and its mechanism of action, *World J. Microbiol. Biotechnol.*, 27 (2011) 1209.
[68] A.F. Halbus, T.S. Horozov, V.N. Paunov, Surface-modified zinc oxide nanoparticles for antialgal and antiyeast applications, *ACS Appl. Nano Mater.*, 3 (2020) 440.

CHAPTER 6

Characterization of Oxidative Stress-induced Disorders and Modulation Reactive Oxygen Species in Biologically Relevant System for Potential Therapeutic Applications

6.1. Introduction:

In the last two decades, reactive oxygen species (ROS) have attracted tremendous attention from the scientific community because of their ever-expanding physiological roles. The infamous identity of ROS for their potential to destroy cellular macromolecules, often termed as oxidative stress [1, 2], has been changed with discoveries about their novel beneficial actions in physiological systems, particularly cell signaling [3, 4]. The presence of both noxious and beneficial functions of ROS in physiological milieu led to introduction of the terms 'oxidative distress' (i.e., enhanced level of intracellular ROS and subsequent damage to bio-macromolecules) and 'oxidative eustress' (i.e., controlled levels of ROS that helps in redox signaling), instead of 'oxidative stress' which only indicates the harmful effects [5-7]. The oxidative eustress condition is required to maintain redox homeostasis and normal cell functions. Alterations in the homeostatic redox state (either increase or decrease in ROS level) potentially lead to harmful pathophysiological conditions including neurodegenerative, cardio-vascular, chronic kidney, and gastro-intestinal diseases. A crucial balance between ROS production and elimination is vital for maintenance of cellular redox homeostasis. This balancing phenomena is referred to as 'redox buffering'. Therefore, developing an exogenous agent that can scavenge excessive cellular ROS while preserve the oxidative eustress condition could be an unprecedented strategy against several unmet disorders caused by redox imbalance. In this regard, multivalent transition metal-oxide nanoparticles (e.g., Fe_2O_3, Mn_3O_4, etc.) with redox modulatory properties can be the material of choice [8-11]. Recently, they have showed promising results for the treatment of several chronic diseases. However, concerns over toxicity, biocompatibility and stability in the gastro-

intestinal (GI) tract limited their therapeutic application. Previously, we have shown that functionalization of these nanomaterials with bio-compatible ligands could overcome the problem of biocompatibility [10, 12-14].

Damages in oxidative state of cells can be occurred because of some exogenous agents called exotoxins. These exotoxins invades human body through exposome. Cobalt (Co), an abundant transition metal found in earth's crust, is one of the major exotoxins. Though it is required as a trace element by the living organisms for proper functioning of vitamin-B12 (cyanocobalamine)[15], excessive exposure to Co from environmental, occupational, medical, and dietary sources can lead to progression of toxicity in humans giving rise to several health hazards particularly neuro-degenerative disorders like Alzheimer's disease, Parkinson's disease etc. [16-18]. Exposure of cobalt to the human system usually occurs via the respiratory and gastrointestinal route. Occupational exposure to cobalt in glass, pottery, jewellery and hard metal production industries is also a major cause of cobalt poisoning in humans. In addition, extensive exposure to environmental pollutants, medicines and dietary supplements containing Co^{2+} has also lead to the pathogenesis of Co-toxicity [15]. Another major source of Co-toxicity is metal-on-metal (MOM) hip-implantation. Individuals who received the implantation suffered from numerous organ disorders due to elevated level of Co^{2+} in blood [19-22]. Excessive exposure to cobalt can affect almost every organ systems of the body including hepatic, renal, hematopoietic, respiratory systems [23]. Most dangerously, Co^{2+} can pass the blood-brain barrier and affect brain functions. In brain cells, Co^{2+} initiate the generation of ROS via Fenton like reaction in presence of H_2O_2 [24-26]. Excessive generation of ROS then triggers DNA damage and other changes in gene expression resulting in apoptosis and premature death of neural cells [17, 27-31]. Despite the above mentioned severe physiological consequences, the detoxification techniques of Co^{2+} are sparse. Although some chelators like EDTA, DMSA, N-acetylcysteine, DTPA are suggested to treat Co-toxicity, only a few evidences are available [19, 20, 32, 33]. The constant rise in the manifestation and severity of Co-toxicity among humans, demands an antidote that not only removes the Co^{2+} from the physiological milieu but also protect the organs from oxidative damages. The reported chelators although can inefficiently remove the metal ion from the body, are unable to protect the organs from oxidative damages. In this regard, the development of an agent that can

efficiently chelate Co^{2+} out of the body as well as prevent the excessive oxidative stress generated by the ions can prove to be a promising therapeutic strategy against cobalt poisoning, which is the sole motive of our work.

First, we have developed a novel chitosan-functionalized Mn_3O_4 nanoparticle (Ch-Mn_3O_4 NPs) and explored its ability to maintain cellular redox homeostasis in terms of redox buffering capacity using both *in vitro* and *in vivo* cellular model (A549 cells) [34]. Functionalization of the nanomaterial with chitosan (composed of randomly arranged β-linked D-glucosamine and N-acetyl-D-glucosamine) [35] can be specifically targeted to the intestinal cells, in case of oral administration due to its stability in the low pH of the upper GI tract, owing to the swelling behaviour and the electrostatic repulsion between the adjacent protonated amino groups in the lower pH [36]. Chitosan and chitosan derivatives also have the ability to interact with the tight junctions of the intestinal cells, thereby leading to an expansion of the paracellular routes and increasing the intestinal absorption of the functionalized nanomaterials [37-42] facilitating to treat otherwise untreatable GI tract diseases like ulcerative colitis, Crohn's disease etc. where pathogenesis involves redox imbalance [43]. Organ specific delivery of nano-therapeutic agent and obvious remediation of the malfunctioning organ may be an indication for the theranostic application of the agent [44, 45].

In the next section, the use of nanoscience can discover a path to achieve a sustainable solution against cobalt toxicity in humans. Numerous in-vitro studies have described the ability of metallic nanoparticles to bind and/or detect heavy metals. For example, silver and gold nanoparticles can efficiently bind bivalent metal ions like mercury(Hg^{2+}), copper(Cu^{2+}), lead(Pb^{2+}), cobalt(Co^{2+}) etc [46-48]. However, their low bio-availability and several other complications limit their use in the medicinal field. In our previous studies, it has been shown that C-Mn_3O_4 NPs are bio-compatible and have antioxidant activity. It can interact with positively charged materials like bilirubin, methylene blue etc. [49-51]. Hence, it can be hypothesized that these NPs can be a potential solution against diseases related to Co-toxicity in humans. In this work, through *in vitro* spectroscopic studies we explored the possible Co (II)-chelating activity of C-Mn_3O_4 NPs. Transmission electron microscopy, UV-Vis and fluorescence spectroscopic techniques were used to confirm the Co-chelating efficacy of the NPs. We also investigated whether the

NPs were able to decrease the Fenton like reaction thereby, reducing the oxidative stress that plays the major role in pathogenesis of neuronal damage. Thus, the use of the C-Mn_3O_4 NPs as a nanomedicine for cobalt chelation and remediation associated with oxidative stress may uncover an unexplored route in the elimination of cobalt toxicity.

6.2. Results and Discussion:

6.2.1. Synthesis and Spectroscopic Characterization of a Target Specific Nano-Hybrid for Redox-Buffering in Cellular Milieu [52]: Transmission electron micrographs (TEM) and SAED patterns indicate that Ch- Mn_3O_4 NPs are spherical in shape and crystalline in nature (Figure 6.1.a).

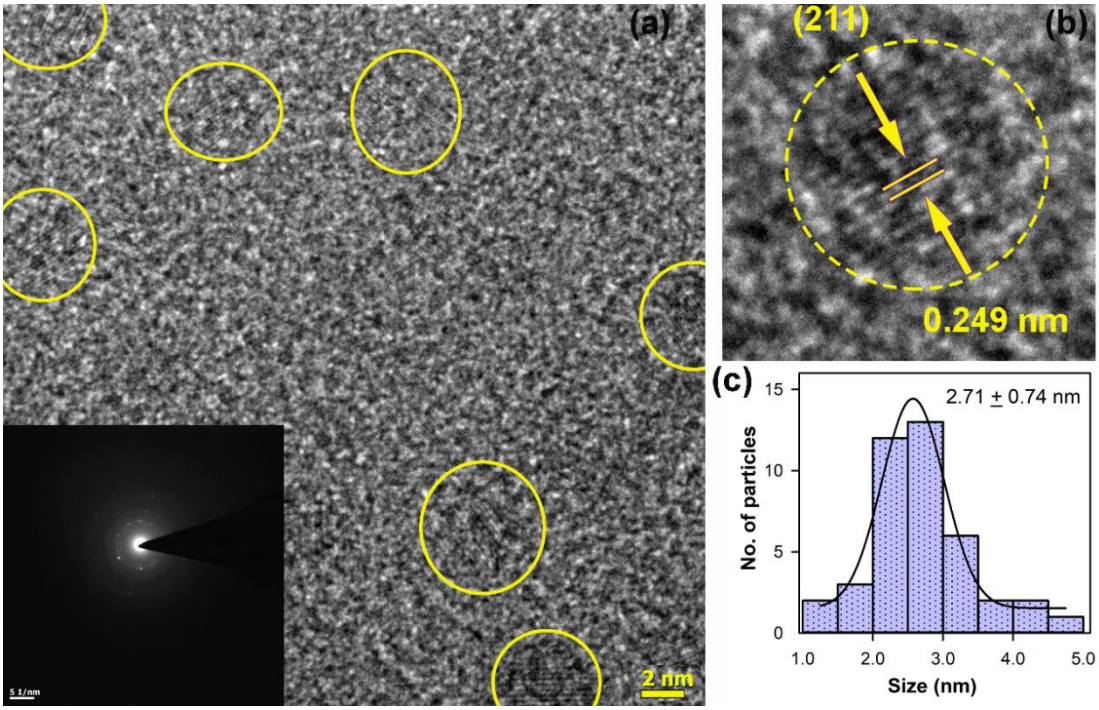

Figure 6.1: *(a) The particle distribution of the nanoparticles (NPs) recorded under transmission electron microscopy (TEM). Inset SAED pattern. (b) High-resolution electron micrograph (HRTEM) of the NPs with a clear interplanar distance of 0.249 nm for (211) planes in the Mn_3O_4 NPs is evident. (c) The particle size distribution is shown with average size of 2.71±0.74 nm.*

HR-TEM of single nanoparticle (Figure 6.1.b) reveals the interfringe distance of 2.49 Å corresponding to (211) planes of Mn_3O_4 spinel lattice [53]. The size of Ch-Mn_3O_4 NPs ranges from 1.5 nm –4.5 nm having an average diameter of 2.71 ± 0.74 nm (Figure 6.1.c). The X-ray diffraction (XRD) pattern (Figure 6.2.a) indicates the tetragonal hausmannite structure (JCPDS 24-0734) of the NPs [53, 54]. The average

hydrodynamic diameter of the Ch-Mn_3O_4 NPs is ~7.4 nm as depicted in dynamic light scattering. Thus, the functionalized nanomaterial comprised of a ~3 nm NP core surrounded by ~2 nm of chitosan layer (Figure 6.2.b).

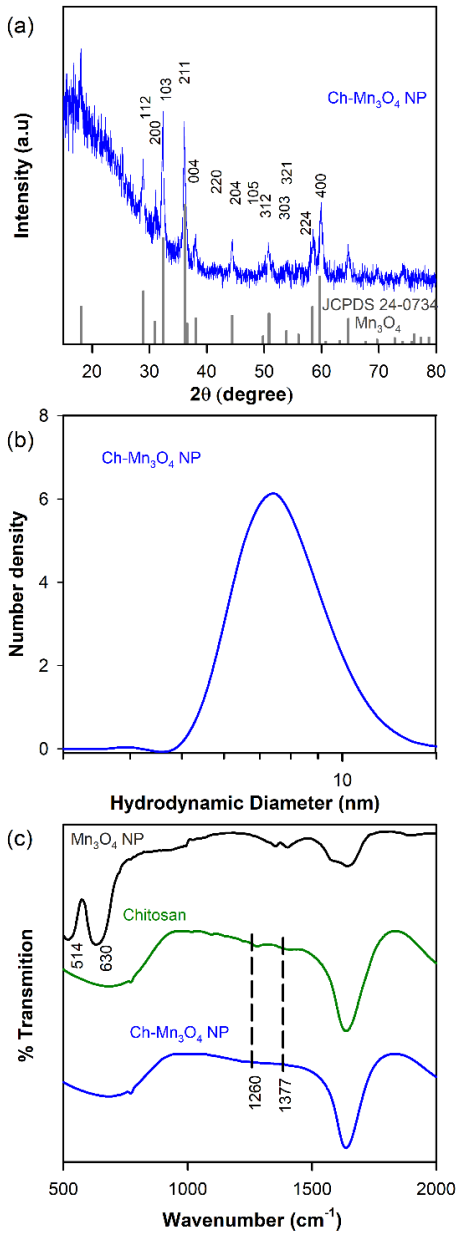

Figure 6.2: *(a) XRD pattern of synthesized Ch-Mn_3O_4NPs which exactly matches to that of library spectra. (b) Hydrodynamic diameter of Ch-Mn_3O_4 NPs measured by Dynamic light scattering. (c) FTIR spectra shows covalent binding of ligand chitosan to as prepared Mn_3O_4 NPs.*

FTIR studies (Figure 6.2.c) revealed covalent binding between C-N groups of chitosan and surface OH groups of the NPs as indicated by the perturbation of corresponding stretching bands around 1260 cm^{-1} and 1377 cm^{-1}, respectively [51, 55].

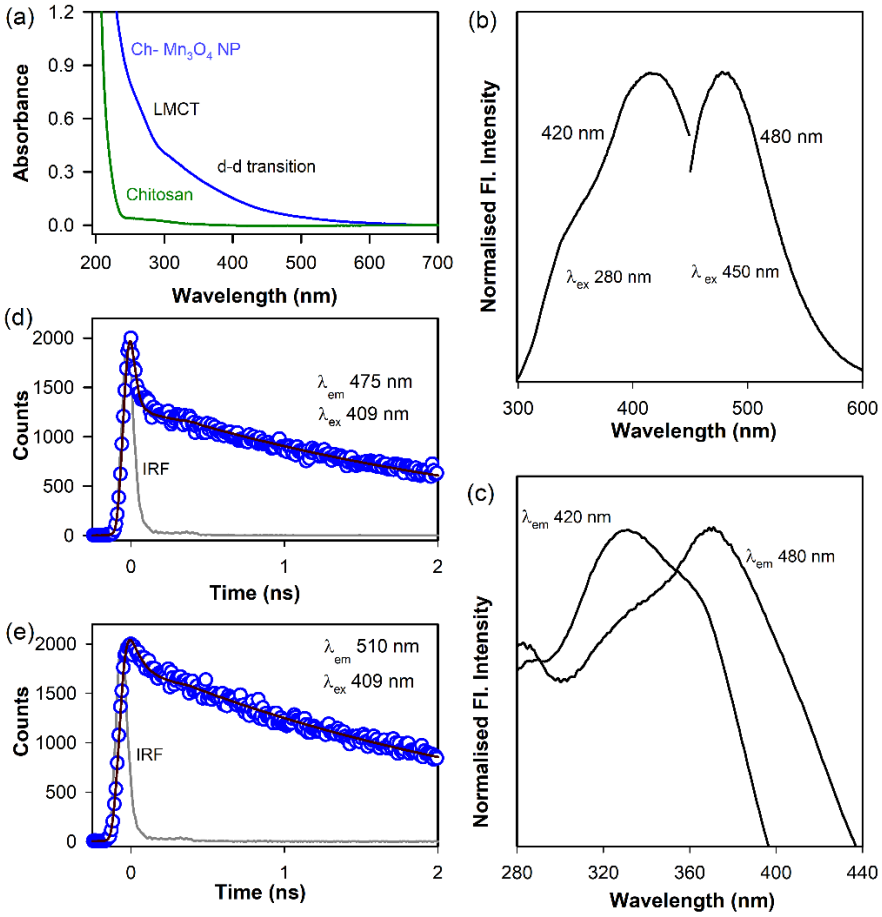

Figure 6.3: *Spectroscopic characterization of the nanohybrid. (a) The absorption spectra of chitosan-capped NPs (Ch-Mn_3O_4NPs) and the capping agent chitosan (Ch). The absorption peaks due to ligand to metal charge transfer (LMCT) and d–d transition (see text) are shown. (b) and (c) Fluorescence emission and excitation spectra of Ch-Mn_3O_4NPs respectively. (d) and (e) are the picosecond-resolved fluorescence transient spectra of Ch-Mn_3O_4 recorded at 475 nm and 510 nm upon excitation at 409 nm, respectively.*

Functionalization with chitosan led to appearance of several optical characteristics to the otherwise featureless Mn_3O_4 NPs. Figure 6.3.a shows the UV-Vis absorbance spectra of Ch-Mn_3O_4 NPs. The observed high energy bands around 280 nm and 320 nm could be the ligand-to-metal charge transfer (LMCT) bands originated due to the interaction between functional groups of chitosan and Mn^{2+}/Mn^{3+} on the NP surface. The 410 nm band possibly resulted from the forbidden d-d transition ($^5B_{1g} \rightarrow {}^5E_g$) of Mn^{3+}, as the degeneracy of the ^5E_g ground state term of d4 has been lifted in a high-spin octahedral environment by the Jahn-Teller effect. The absence of other possible lower energy transitions e.g., $^5B_{1g} \rightarrow {}^5B_{2g}$ and $^5B_{1g} \rightarrow {}^5A_{1g}$ may be due to the lack of α-hydroxy carboxylate group in functionalizing ligand, chitosan. Steady state fluorescence spectra reveals presence of two emission peaks at 420 nm (blue) and

480 nm (green) when excited at absorption bands (Figure 6.3.b). Corresponding excitation spectra (Figure 6.3.c) confirms the origin of the emission peaks as a result of observed LMCT and d-d transitions, respectively. Figure 6.3.d and 6.3.e show the picosecond-resolved fluorescent transients of Ch-Mn_3O_4 NPs at emission wavelength of 475 nm and 510 nm (excitation source: 409 nm). The obtained lifetimes indicate that the emission at 475 nm contains both radiative and non-radiative transitions resulting in a lower average lifetime (τ_{avg} 6.8 ns) compared to the emission at 510 nm (τ_{avg} 20.74 ns), which contains only a single radiative state (Table 6.1.). The significant reduction in average lifetime is due to the reciprocal relationship between average lifetime and rate-constants (Equation 6.1) [56].

$$k_r + k_{nr} = \tau_a^{-1} \tag{6.1}$$

Here τ_{avg}, k_r and k_{nr} denote average lifetime, radiative and non-radiative rate-constants, respectively.

Table 6.1: *Pico-second Resolved Fluorescence Lifetime of Ch-Mn_3O_4 NPs (Values in Parentheses Represent the Relative Weight Percentage of the Time Components.)*

System	**Excitation wavelength (λ_{ex})**	**Emission wavelength (λ_{em})**	**τ_1(ps)**	**τ_2(ps)**	**τ_3(ps)**	**τ_{avg}(ns)**
Ch-Mn_3O_4 NPs	409 nm	475 nm	24 (73)	190 (50)	3045 (21)	6.8
		510 nm	-	190.19 (32)	3178 (67)	20.74

In order to be effective in maintenance of redox homeostasis, the buffering agent should be able to generate as well as scavenge ROS in physiological milieu. Hence, we evaluated the ROS generation ability of Ch-Mn_3O_4 NPs using DCFH. The conversion of non-fluorescent DCFH to fluorescent DCF (λ_{ex} 488 nm; λ_{em} 520 nm) in presence of Ch-Mn_3O_4 NPs was monitored to quantify the ROS generation [57]. It is evident from Figure 6.4.a that Ch-Mn_3O_4 NPs have the potential to generate ROS in dark. The nature of the ROS was found to be singlet oxygen as addition of sodium azide (NaN_3), a singlet oxygen quencher, reduced ROS generation (Figure 6.4.a) [57]. Involvement of dissolved oxygen in the process of ROS generation was

confirmed from nitrogen purging assay (Figure 6.4.a). Inability of Ch-Mn_3O_4 NPs to oxidize luminol (i.e., absence of chemiluminescence) excluded the likelihood of superoxide production (Figure 6.4.b). To explore the anti-oxidant ability of Ch-Mn_3O_4 NPs, we used luminol oxidation assay in presence of H_2O_2 (i.e., ROS generator) [54]. Luminol exhibited chemiluminescence in presence of superoxide generated by H_2O_2 (Figure 6.4.c, 6.4.d). Addition of Ch-Mn_3O_4 NPs into the system led to disappearance of chemiluminescence signal (Figure 6.4.c, 6.4.d), signifying the anti-oxidant activity of the functionalized NPs in elimination of the superoxide generated by H_2O_2. Addition of chitosan resulted in insignificant change in chemiluminescence of oxidized luminol (Figure 6.4.c, 6.4.d). We evaluated the *in vitro* redox buffering capacity of the synthesized Ch-Mn_3O_4 NPs using H_2O_2, a potent intracellular ROS, as the oxidant in DCFH assay. Figure 6.5.a illustrates that the oxidation of DCFH increased significantly with increasing concentrations of H_2O_2. When Ch-Mn_3O_4 NPs were present in the mixture the DCFH oxidation rate remains almost unaltered even after addition of 2.5 mM H_2O_2 (Figure 6.5.b). The results indicate the effective quenching of ROS generated from H_2O_2 by Ch-Mn_3O_4 NPs. It should be noted that Ch-Mn_3O_4 NPs always maintained a baseline level of ROS concentration in the medium instead of eliminating all of them which is particularly important in the context of sustaining the oxidative eustress in physiological milieu. Figure 6.5.c shows the relation between DCFH oxidation rate (V_f) and oxidant (i.e., [H_2O_2]) concentration. It is evident from Figure 6.5.c that DCFH oxidation by H_2O_2 followed a sigmoidal kinetics, and presence of Ch-Mn_3O_4 NPs significantly reduced the oxidation rate.

The redox buffer capacity of a system is numerically equal to the change of concentration of an oxidant (or reductant) added to a solution, which is reduced or oxidized, to change the effective reduction potential by 1 unit (1V). Therefore, the redox buffer capacity (β) can be represented as:

$$\beta = \frac{\delta c_{ox}}{\delta E^{eff}} \tag{6.2}$$

Where, c_{ox} denoted the concentration of oxidant added.

The redox buffering capacity and effective reduction potential of Mili-Q water and Ch-Mn_3O_4 NPs was experimentally determined by analyzing the dependence

between $1/V_f$ and $1/c_{ox}$ [7] Ch-Mn_3O_4 NPs showed significantly high redox buffering capacity in comparison with Mili-Q water.

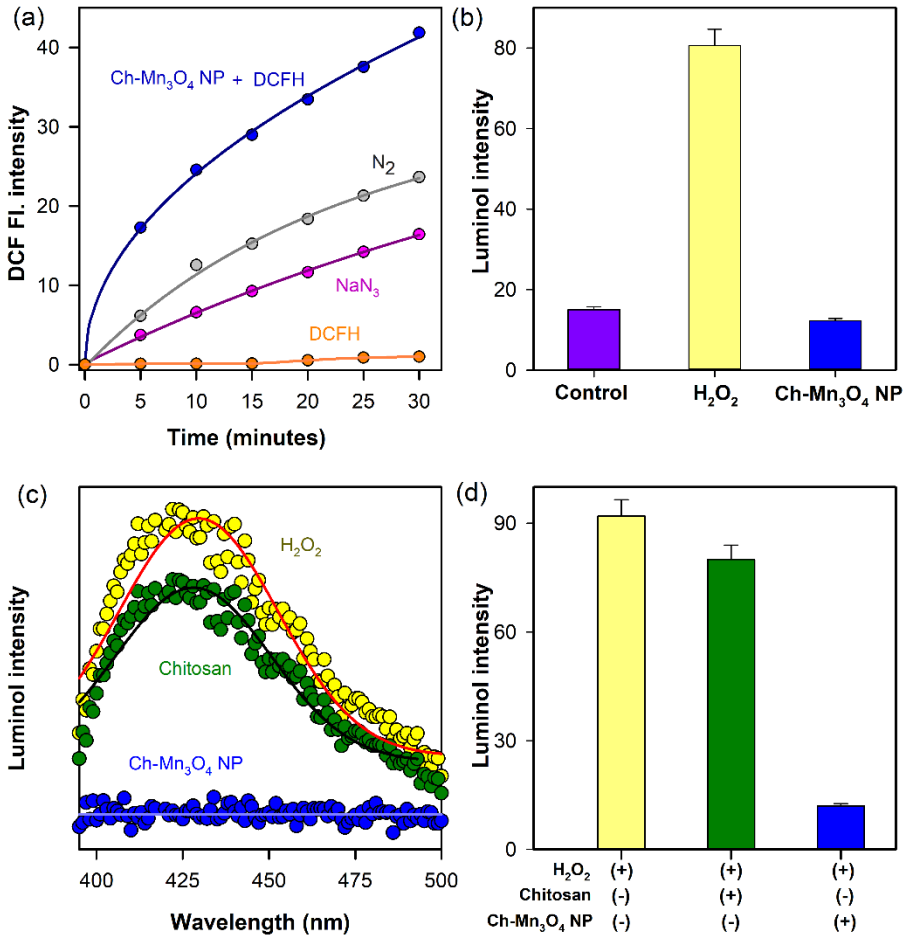

Figure 6.4: *(a) DCFH oxidation with respect to time in addition of Ch-Mn_3O_4NPs (blue), addition in an atmosphere of purged nitrogen (gray), sodium azide (purple) and control (saffron) in the dark. (b) Chemiluminescence of luminol for the control, NaOH + H_2O_2 and Ch-Mn_3O_4NPs. (c) Chemiluminescence intensity of Luminol in the presence of H_2O_2 (control) and after addition of Chitosan, Ch-Mn_3O_4NPs. (d) Representation of level of ROS in the presence of H_2O_2, Chitosan and Ch-Mn_3O_4 NPs.*

Further comparison of buffering capacities among different concentrations of Ch-Mn_3O_4 NPs revealed that higher concentrations of NPs negatively affected the buffering capacity (Figure 6.5.d, Table 6.2.). This is probably due to the higher rate of ROS generation by the NPs at high concentrations. Thus, the *in vitro* findings divulge the fact that Ch-Mn_3O_4 NPs can effectively maintain the desired redox state of a system by balancing the ROS generation and elimination, and the modulation of the redox state can be achieved by simply changing the concentrations of the NPs.

To evaluate the redox buffering capacity of Ch-Mn_3O_4 NPs in cellular milieu, we used human adenocarcinomic alveolar basal epithelial (A549) cells, whose redox state is naturally perturbed due to presence of huge oxidative distress [34]. The fluorescence intensity of intracellular DCF was very high for the untreated and chitosan-treated cells (Figure 6.5.e, 6.5.f) indicating presence of high concentrations of ROS. While the cells treated with Ch-Mn_3O_4 NPs showed much lower fluorescence of DCF.

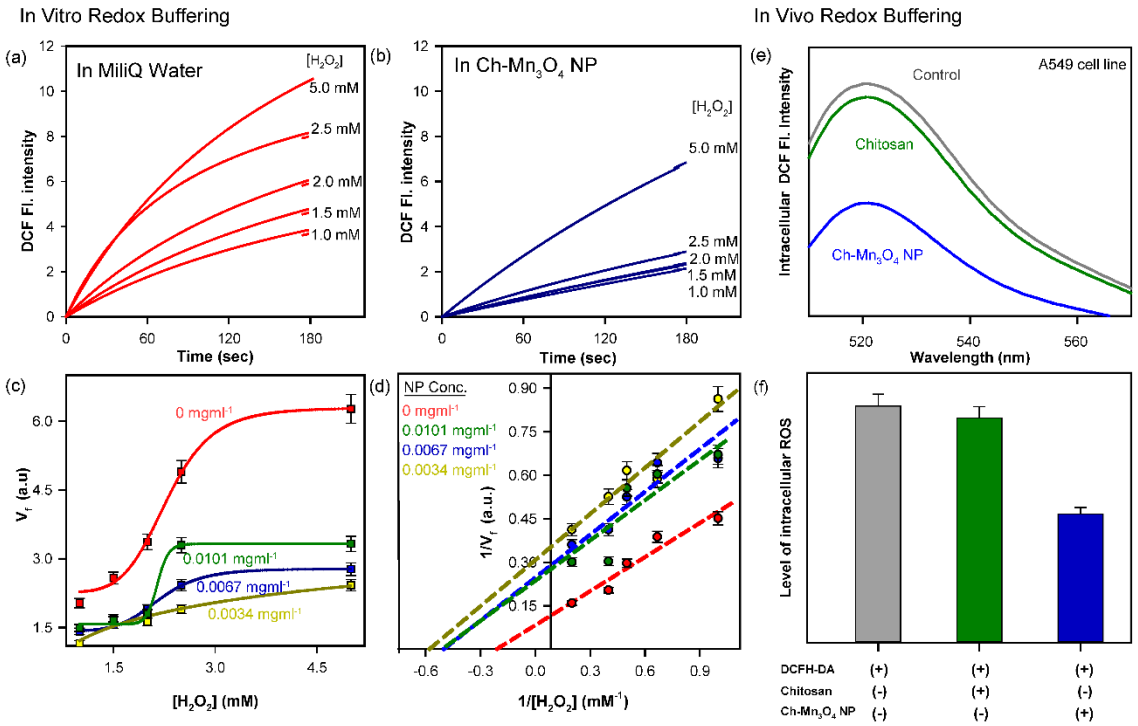

Figure 6.5: *(a) The effects of H_2O_2 on the DCF fluorescence intensity in H_2DCF-mixed MiliQ water. (b) The effects of H_2O_2 on the DCF fluorescence intensity in H_2DCF added to Ch-Mn_3O_4 NP solution. (c) The dependence of H_2DCF oxidation rate in MiliQ water & Ch-Mn_3O_4 NP solution on the oxidant concentration. (d) Determination of the redox parameters on the basis of the experimental values. In vivo assessment of buffering activity of Ch-Mn_3O_4NPs in A549 cell line. (e) Intracellular DCF Fl. intensity of control cells and cells treated with chitosan and Ch-Mn_3O_4NPs for 30 minutes. (f) Representation of intracellular ROS in different treatment groups.*

Thus, it can be concluded that treatment with Ch-Mn_3O_4 NPs helped the cells to achieve oxidative eustress condition and they are efficient redox buffers even in physiological milieu. The cytotoxicity study in 3T3L cells (having eustress condition) shows the non-toxicity of Ch-Mn_3O_4 NPs even at 100 times higher dose than that is required for buffering. Redox buffering requires sensing and rapid

adjustment in the cellular redox environment to maintain the oxidative eustress condition.

Table 6.2: *Concentration Depended Redox Buffering Capacity of Ch-Mn_3O_4 NPs.*

Concentration of Ch-Mn_3O_4 ($mgml^{-1}$)	**Buffering Capacity (a.u.)**
0	0.391
0.0034	0.529
0.0067	0.493
0.0101	0.462

Our experimental findings suggest that Ch-Mn_3O_4 NPs can sense and swiftly shift the redox balance in favour of oxidative eustress. This behaviour of Ch-Mn_3O_4 NPs as a redox modulator is analogous to pH buffers as they adjust the pH of a solution by sensing the concentration of H^+ ions present in the medium.

Previous studies have shown that after functionalization of Mn_3O_4 NPs with ligand the Mn^{3+} oxidation state predominates over Mn^{+2} oxidation state . Also it has been shown that at a neutral or at a slightly basic pH (~8) Mn^{3+} tends to disproportionate to Mn^{4+} oxidation state. In addition, the low amount of Mn^{2+} ions present in the system is also converted to Mn^{3+} which subsequently generate Mn^{4+} [50, 58]. These spontaneous conversion in the oxidation states of Mn ($Mn^{2+}\rightarrow Mn^{3+} \rightarrow Mn^{4+}$) on the surface of the functionalized nanomaterial generate electrons which react with dissolved O_2 of the medium and produce ROS. Some amount of the ROS produced by the above mentioned process is simultaneously neutralized by the reverse conversions thereby, maintaining a steady state of ROS. Thus, at oxidative eustress condition of cells, a dynamic equilibrium exists between the generation and elimination of ROS by Ch-Mn_3O_4 NPs, which takes part in redox signaling and helps in maintenance of normal cell functions. At oxidative distress condition, other than the discussed mechanism of ROS neutralization, the Ch-Mn_3O_4 NPs takes into account other free radical scavenging mechanisms like mitoprotection, strengthening of cellular antioxidant enzyme network etc. which have previously been described for manganese containing nanoparticles [13, 50]. Besides the buffering activity, Ch-Mn_3O_4 NPs can be specifically targeted to the intestine. The specific intestine targeting potential can be achieved because of chitosan, which is a

known intestinal targeting agent as it absorbed by the intestinal epithelia without its own degradation [37-39, 41, 59]. Hence, Ch-Mn_3O_4 NPs can be effectively used against several intestinal disorders in which pathogenesis is originated from the redox imbalance.

6.2.2. Spectroscopic Study on the Interaction of Co^{2+} With Citrate- Mn_3O_4: Towards the Development of Nanotherapy Against Cobalt Toxicity [60]: Here we used Mn_3O_4 nanoparticles functionalized with a biocompatible carboxyl rich ligand, citrate, for potential use in detoxification of cobalt, a well-known neurotoxic agent. The transmission electron micrographs image (Figure 6.6.a), clearly shows that the C-Mn_3O_4 NPs are nearly spherical.

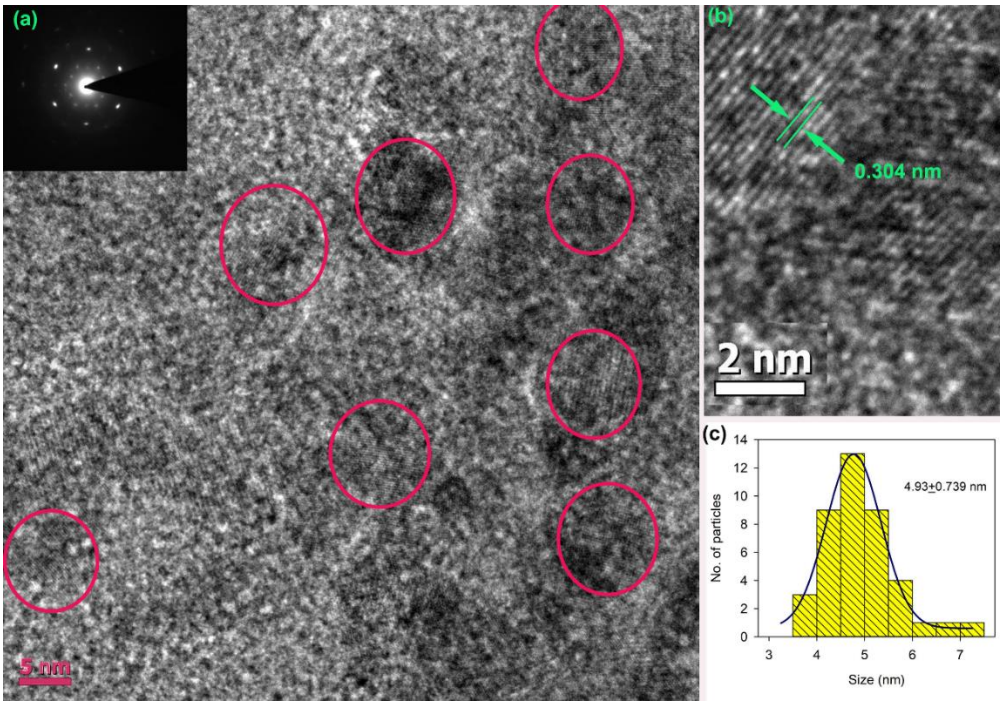

Figure 6.6: *(a) Particle distribution of C-Mn_3O_4 NPs recorded under transmission electron microscopy (TEM). (b) HR-TEM of C-Mn_3O_4 NPs with a clear interplanar distance of 0.304 nm which corresponds to (112) plane in the Mn_3O_4 nanoparticle (NP). (c) Size distribution of the NP with average size shown to be 4.93 ± 0.739 nm.*

The spherical shape of Mn_3O_4 NPs arises due to the involvement of an ultrasonic pretreatment step during the formation of Mn_3O_4 nanocrystals. This ultrasonic irradiation creates an acoustic cavitation that includes the formation, growth, pulsation, and collapse of tiny bubbles in liquids. These tiny bubbles work as transient nucleation centre (template) for the crystal growth [53] resulting in spherical shaped nanoparticles. Selected area electron diffraction (SAED) pattern

(Figure 6.6.a-inset) along with HRTEM image (Figure 6.6.b) confirmed the crystalline nature of the NPs having interfringe distance of ~0.304 nm corresponding to the (112) planes of Mn_3O_4 (hausmannite) tetragonal crystal lattice [10, 50, 51, 53, 54]. Figure 6.6.c indicates the size distribution of the NPs obtained from TEM images. This histogram reveals that the average size of the NPs is 4.93±0.739 nm.

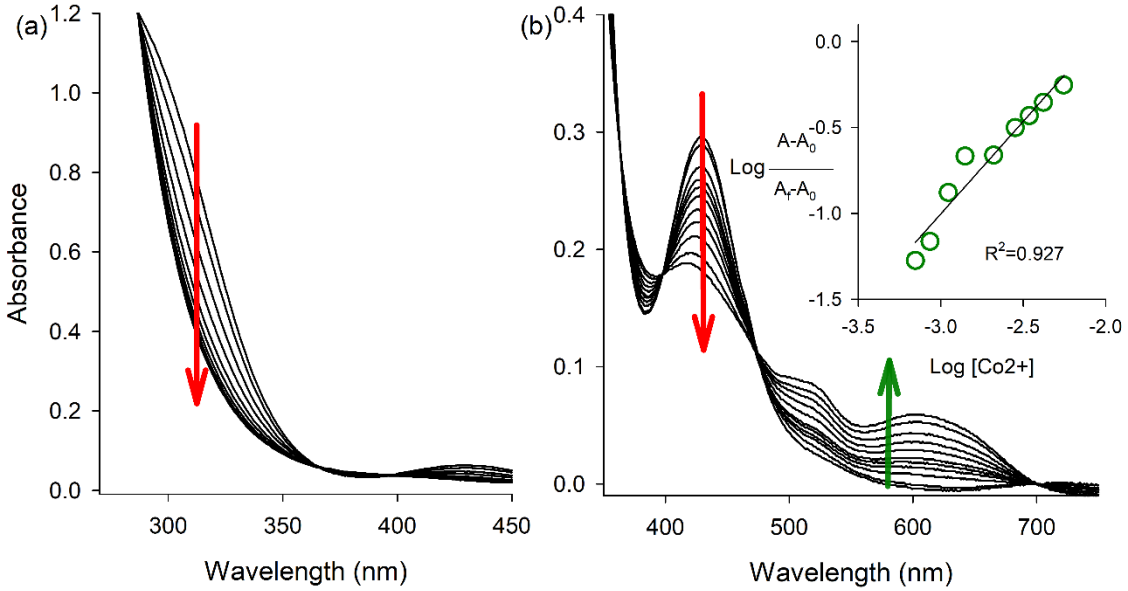

Figure 6.7: *(a&b) Absorption spectra of C-Mn_3O_4 NPs (after correction of Raleigh scattering) in presence of varying concentrations (0 to 1.12 × 10^{-2} M) of $CoCl_2$. Arrows indicate the increase in the concentration of Co^{2+}. Inset shows the Benesi-Hildebrand plot for the determination of binding constant.*

Previous studies show that Mn_3O_4 NPs upon functionalization with α-hydroxy carboxylate containing ligands can display interesting optical properties. The UV-Vis absorption spectra of C-Mn_3O_4 NPs (Figure 6.7.a and 6.7.b) illustrated three well defined regions i.e., 250-320 nm (region 1), 320-550 nm (region 2) and 550-700 nm (region 3). The high energy absorption band (region 1) having peak at ~300 nm could have been arisen due to high energy ligand-to metal charge transfer (LMCT) process involving citrate–$Mn^{3+/4+}$ interaction at NP surface [10, 49, 51]. The other band around 430 nm (region 2) may reasonably be attributed to d–d transitions of Mn^{3+} in C-Mn_3O_4 NPs, as the degeneracy of ^5E_g ground state term of d^4 (Mn^{3+}) high-spin octahedral environment is lifted by the Jahn–Teller effect leading to $^5B_{1g} \rightarrow {}^5E_g$ transition.

The other possible low energy transitions e.g., $^5B_{1g} \rightarrow {}^5B_{2g}$, and $^5B_{1g} \rightarrow {}^5A_{1g}$ were not prominent (region 3) as a result of masking effect of the more intense absorption at

430 nm. Figure 6.7.a revealed that addition of $CoCl_2$ caused disappearance of the charge transfer band observed at ~300 nm. The disappearance of this band can be due to the chemical bonding or electron transfer to the Co^{2+}ions, as a result of strong metal support interaction [61, 62]. From Figure 6.7.b it is eminent that with subsequent addition of Co^{2+}, the band around 430 nm was decreasing while the other two low energy d-d transition (around 510 nm and 620 nm) bands were becoming more prominent. The apparent changes in d-d transitions bands could be interpreted as an effect of the interaction of many small Co^{2+} ions at nanoscale interparticle distances within a single Mn_3O_4 nanocluster [62]. The three isosbestic points observed around 360 nm, 400 nm, 480 nm described the processes to be in equilibrium. The binding constant (K_b= 1.69×10^2 M) of Co^{2+}-NP complex is calculated using the Benesi–Hildebrand equation (Equation (1); R^2=0.927);

$$log\frac{A-A_0}{A_f-A_0} = \log[Co^{2+}] + logK_b \quad (6.3)$$

Where, A_0, A, and A_f are the initial (without Co^{2+}), intermediate (with Co^{2+}) and final absorbance (with saturated amount of Co^{2+}) at 300 nm respectively. The binding constant (K_b) is calculated by linear fitting of absorption titration curve (Figure 6.7.b-inset).

Figure 6.8.a described the fluorescence pattern of C-Mn_3O_4 NPs. Upon excitation at 410 nm the C-Mn_3O_4 NPs showed a sharp emission peak at 480 nm which was quenched upon subsequent addition of $CoCl_2$. It is evident from Figure 6.8.a (inset) that there was no change in the pattern of excitation spectra of C-Mn_3O_4 NPs after addition of $CoCl_2$. The quenching of fluorescence can be attributed to various mechanisms taking place such as ground state complex formation, excited state reaction, energy transfer, collisional quenching, molecular rearrangement etc. [63]. In this case no visible shift in fluorescence maxima or any kind of change in the pattern of fluorescence spectrum. In addition the quenching behavior is following the classical Stern-Volmer (SV) equation (Equation 6.4);

$$\frac{F_0}{F} - 1 = K_{sv}[Q] = K_q\tau_0[Q] = \frac{\tau_0}{\tau} - 1 \quad (6.4)$$

Where, F and F_0 indicate the fluorescence intensity in presence and in the absence of quencher molecule respectively.

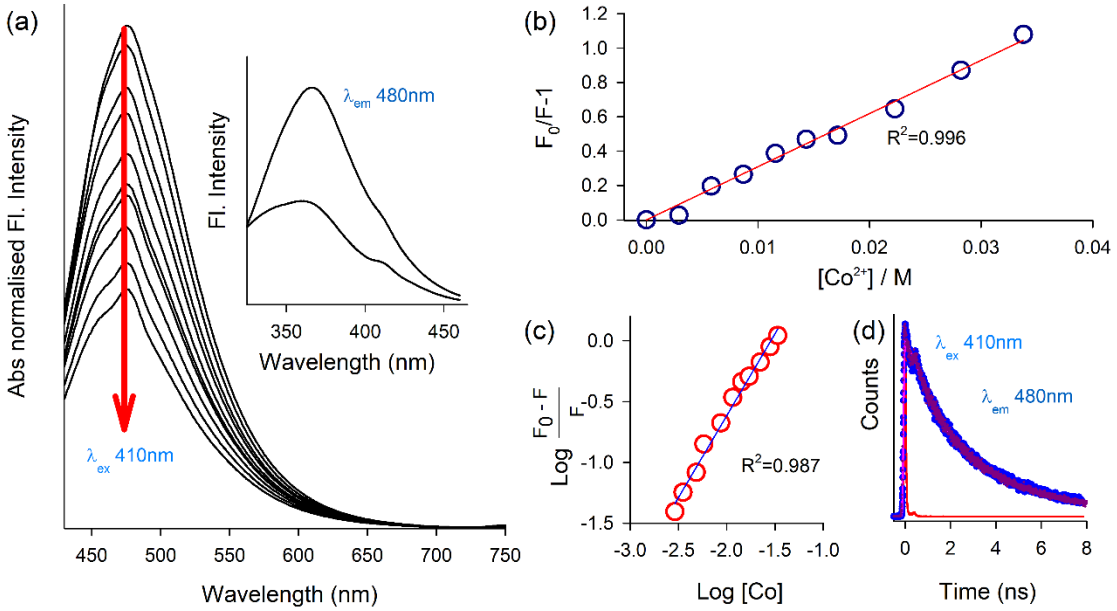

Figure 6.8: *(a) Fluorescence spectra of C-Mn_3O_4 NPs in the presence of different concentrations of $CoCl_2$ (0 to 2.8 X 10^{-2} M of $CoCl_2$) (λ_{ex} = 410 nm). Inset shows the respective excitation spectra. (b) Stern-Volmer plot. (c) Modified Stern-Volmer plot. (d) Excited life time decay of NP and NP-Co^{2+} complex.*

[Q] is the quencher concentration, K_{SV} designates the SV quenching constant, k_q the bimolecular quenching rate constant, τ_0 is the fluorescence lifetime of fluorophore in the absence of quencher while τ is the fluorescence lifetime of fluorophore in the presence of quencher molecule [63]. The linear pattern in the SV plot (Figure 6.8.b) denoted a single type of quenching, either dynamic or static [12, 63, 64]. Figure 6.8.c revealed the double logarithmic plot and determined association constant from the plot is 1.17 × 10^2 M (K_a, similar to that found from the absorbance) and number of binding sites (n=1.34) using Equation (6.5)

$$log\frac{F_0-F}{F} = logk_a + nlog[Q] \qquad (6.5)$$

We have further investigate about the excited state lifetime of the NP and Co^{2+}-NP complex (Figure 6.8.d) which showed no change in lifetime. The K_q (K_{sv}/τ_0) value was determined to be 0.43×10^{11} $M^{-1}S^{-1}$ which was higher than diffusion control rate (10^{10} $M^{-1}S^{-1}$). The value of K_q along with lifetime data indicated the nature of the quenching to be static (association constant K_a=K_{SV}=1.17 × 10^2 M) [53]. Thus, the cumulative outcomes from spectroscopic experiments suggested a strong binding between Co^{2+} and NP. There are two possible ways Co^{2+} can interact with the NPs, either through replacement of the Mn^{2+} ions in the spinel hausmannite structure (such that the overall size remains the same) or through binding to the surface of the

NPs (where the overall size of the cluster increases and forms agglomerate). In order to investigate the possible way of interaction of the Co^{2+} ions with the NPs TEM studies were performed. Figure 6.9. shows that upon binding with Co^{2+} the size of the NPs increases slightly. However, the crystallinity increased as indicated by better contrast in the TEM images as well as by the clearer interfringe pattern in HRTEM (Figure 6.9.a & 6.9.b). However, it has to be noted that the contrast of C-Mn_3O_4 NPs in TEM and HRTEM is lower than other metals (e.g., gold, silver etc.). Previous studies have also stated the low contrast of manganese oxide nanoparticles when synthesized at ambient temperature [53]. Thus, the change, in contrast, may be attributed to the binding of Co^{2+} to the C-Mn_3O_4 NPs. The results of EDAX analysis (Figure 6.9.a-inset) further confirm the binding of Co^{2+} in the nanostructure. The absence of agglomeration rules out the possibility of interaction of Co^{2+} ions with the surface of the NPs.

Figure 6.9.c shows the histogram of the size distribution of NPs after interacting with Co^{2+} ions. The slight increase in the overall size of the NPs (Figure 6.9.b) supports the conclusion that Co^{2+} ions were become the integrated part of the hausmannite structure by replacing the Mn^{2+} ions. It is well known that H_2O_2 at the physiological pH generates $OH^{\cdot}$ which can potentially damage the cellular biomolecules. The conversion from H_2O_2 to $OH^{\cdot}$ requires the presence of transition metal ions. Though iron ions are the principal catalyst in this regard, other transition metal ions like Co^{2+} can initiate the Fenton like reaction *in vivo* [25, 65, 66]. It has been already reported that Co^{2+} has higher catalytic efficiency than Fe^{2+} for the degradation of H_2O_2 via Fenton like reaction [67]. The reaction mechanism is as followed

$$Co^{2+} + H_2O_2 = Co\ (III) + OH^{\cdot} + OH^{-}$$

So, excessive Co^{2+} present in physiological milieu efficiently produced $OH^{\cdot}$ radical from H_2O_2 that damage cell membrane by initiating lipid peroxidation in addition to that it also damage the DNA [65, 68]. Besides DNA damage the produced ROS initiate the degradation of various cellular proteins and damage the mitochondria [1, 69]. These events cumulatively prelude apoptosis in cells that result in damage to the brain [13, 68, 70, 71]. So to quantify the generated ROS by $CoCl_2$ in physiological pH we further investigated its ability for Fenton like reaction. Here we used luminol to quantify the ROS produced by this Fenton like reaction. In Figure 6.10.a

quantification of $OH^{\cdot}$ radical produced by Co^{2+} and Co^{2+}-NP in the presence of H_2O_2 is shown.

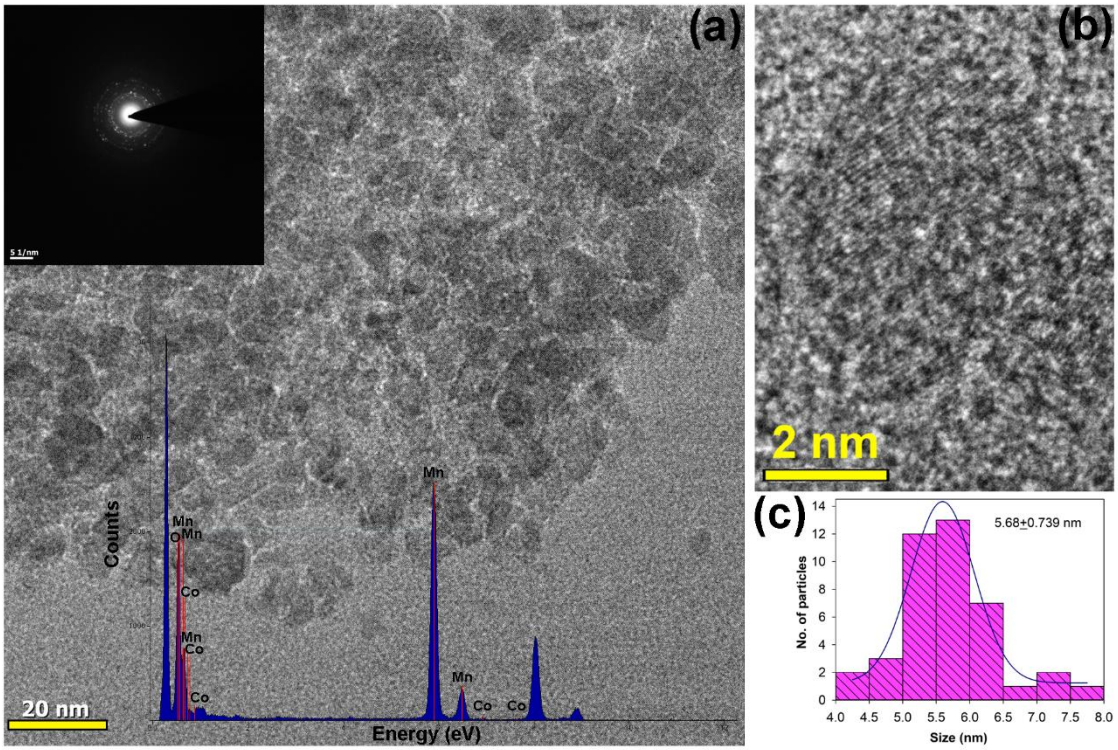

Figure 6.9: *(a) Distribution of Co^{2+} bound C-Mn_3O_4 NPs recorded under transmission electron microscopy (TEM). Energy dispersive X-ray analysis (E-DAX) analysis (inset) (b) HRTEM of Co^{2+} bound C-Mn_3O_4 NPs and the inter planer distance is shown to be 0.306 nm which corresponds to (112) plane of the Mn_3O_4 nanoparticle (NP). (c) Size distribution of the NP with average size shown to be 5.68 ± 0.739 nm.*

This figure suggested a drastic reduction in capability of Co^{2+} to catalysis Fenton like reaction in the complex form with NP. Figure 6.10.b indicated the actual chemiluminescence intensity of luminol for all cases. It is eminent that after complex formation with C-Mn_3O_4 NPs Co^{2+}completely loss its ability to carry out the Fenton like reaction. So C-Mn_3O_4 NPs inhibit the catalytic efficiency of Co^{2+} for H_2O_2 degradation via Fenton like reaction and the simultaneous generation of $OH^{\cdot}$ radical through the complex formation with Co^{2+}. As it successfully ceases the ROS production by Co^{2+} ions we could conclude that C-Mn_3O_4 NPs detoxify Co^{2+} from the physiological milieu. From the experimental data, it is convenient that C-Mn_3O_4 NPs can effectively quench the excess Co^{2+} ions. The NPs have citrate on its outer surface and the zeta potential of the NPs confirmed that the NPs are negatively charged. Thus, when it comes to the close proximity of positively charged ions like Co^{2+}, it captures the positively charged ions and incorporates it in its structure.

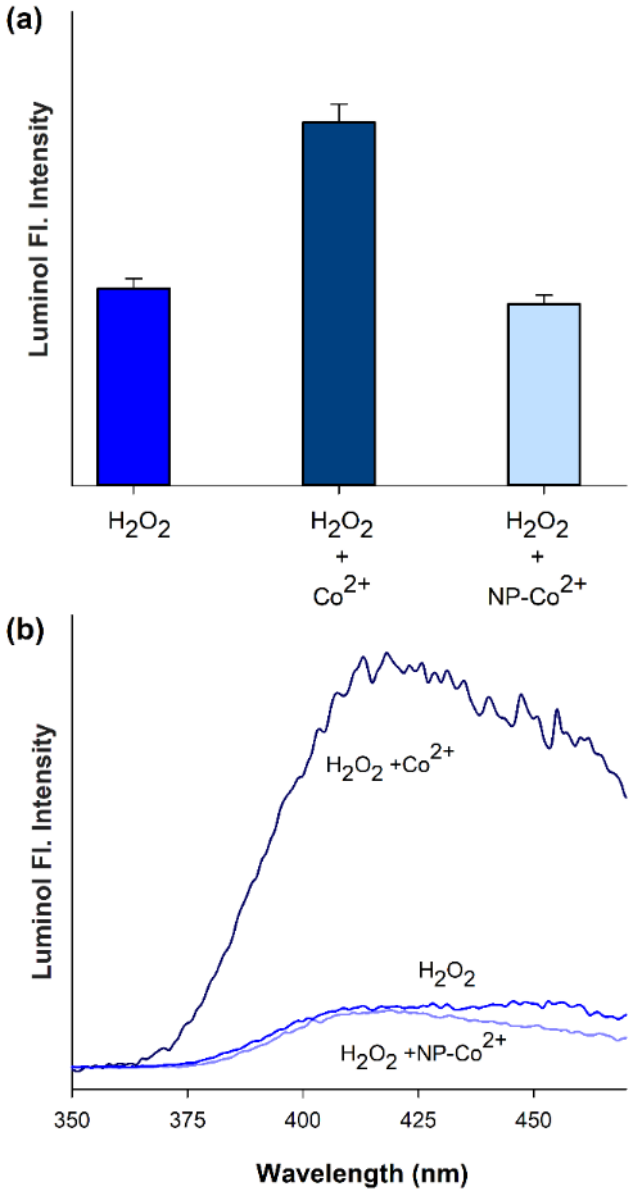

Figure 6.10: *(a) Bar diagram of chemiluminescence of luminol in the presence of H_2O_2, H_2O_2 + Co^{2+}, H_2O_2 + NP-Co^{2+}. (b) Actual Fl. intensity of chemiluminescence of luminol in the presence of H_2O_2, H_2O_2 + Co^{2+}, H_2O_2 + NP-Co^{2+}.*

By this mechanism, C-Mn_3O_4 NPs can effectively remove the Co^{2+} ions from the physiological milieu, which causes several disorders. The NPs not only mobilizes the toxic metal from the organs but also fight against the oxidative damages caused by the ions via ROS generation, i.e. it can act as an antioxidant [12, 64]. The antioxidant ability can arise from various ways, such as quenching ROS through the conversion of $Mn^{2+} \rightarrow Mn^{3+} \rightarrow Mn^{4+}$ [50, 58, 72] or the NPs may act as a radical scavenger, as it is reported that Mn^{2+} ion can act as a free radical scavenger through

various methods [13, 50]. All these evidences strongly suggest that C-Mn_3O_4 NPs can effectively reverse the cobalt induced causality.

6.3. Conclusion:

In summary, the present study intends to highlight the efficient redox buffering capacity of novel Ch-Mn_3O_4 NPs to control oxidative stress in physiological milieu. As chitosan molecule is stable in the GI tract, and has an affinity towards intestinal cells, the Ch-Mn_3O_4 NPs could be a potential therapeutic solution to several GI tract diseases that share the common pathogenesis of redox imbalance. The potentiality of the nanomaterial as theranostic agent following distinct remediation of GI-anomaly in preclinical model is under process in our group.

Next, we report synthesis of a manganese based nano-hybrid (C-Mn_3O_4 NP) that can potentially detoxify the effect of Co^{2+} from the physiological systems. Co^{2+} in physiological pH undergoes reaction with H_2O_2 that leads to the production of OH• radical. The generated radical then damage the nucleic acid, proteins, membranes and subsequently actives MAPK, caspase-3, p38 and other apoptotic machineries in cells that results in cell death. C-Mn_3O_4 NPs not only detoxify Co^{2+} from physiological system via forming a stable complex with it also seizes its ability to produce ROS. Hence, neural death through oxidative stress can be prevented using the C-Mn_3O_4 NPs, which can eventually help to protect from neurodegenerative disorder. Thus C-Mn_3O_4 NPs is paving a new road to detoxify the effect of toxic effects of Co^{2+} and neutralization of its adverse health effects in human subjects.

Reference

[1] A.J. Kowaltowski, A.E. Vercesi, Mitochondrial damage induced by conditions of oxidative stress, *Free Radic. Biol. Med.*, 26 (1999) 463.

[2] C. Li, R.M. Jackson, Reactive species mechanisms of cellular hypoxia-reoxygenation injury, *Am. J. Physiol. Cell Physiol.*, 282 (2002) C227.

[3] K. Brieger, S. Schiavone, F.J. Miller Jr, K.-H. Krause, Reactive oxygen species: From health to disease, *Swiss Med. Wkly*, 142 (2012) w13659.

[4] B. D'Autréaux, M.B. Toledano, ROS as signalling molecules: mechanisms that generate specificity in ROS homeostasis, *Nat. Rev. Mol. Cell Biol.*, 8 (2007) 813.

[5] D.P. Jones, Redefining oxidative stress, *Antioxid. Redox Signal.*, 8 (2006) 1865.

[6] H. Sies, D.P. Jones, Reactive oxygen species (ROS) as pleiotropic physiological signalling agents, *Nat. Rev. Mol. Cell Biol.*, 21 (2020) 363.

[7] G.G. Martinovich, I.V. Martinovich, S.N. Cherenkevich, H. Sauer, Redox buffer capacity of the cell: Theoretical and experimental approach, *Cell Biochem. Biophys.*, 58 (2010) 75.

[8] S. Yan, D. Zhang, N. Gu, J. Zheng, A. Ding, Z. Wang, B. Xing, M. Ma, Y. Zhang, Therapeutic effect of Fe_2O_3 nanoparticles combined with magnetic fluid hyperthermia on cultured liver cancer cells and xenograft liver cancers, *J. Nanosci. Nanotechnol.*, 5 (2005) 1185.

[9] D. Bagchi, V.S.S. Rathnam, P. Lemmens, I. Banerjee, S.K. Pal, NIR-light-active ZnO-based nanohybrids for bacterial biofilm treatment, *ACS omega*, 3 (2018) 10877.

[10] N. Polley, S. Saha, A. Adhikari, S. Banerjee, S. Darbar, S. Das, S.K. Pal, Safe and symptomatic medicinal use of surface-functionalized Mn_3O_4 nanoparticles for hyperbilirubinemia treatment in mice, *Nanomed.*, 10 (2015) 2349.

[11] A. O'Shea, A. Parakh, R.M. Lahoud, S. Hedgire, M.G. Harisinghani, The evolution of iron oxide nanoparticles as MRI contrast agents, *MRS Adv.*, 5 (2020) 2157.

[12] A. Adhikari, P. Biswas, S. Mondal, M. Das, S. Darbar, A.M. Hameed, A. Alharbi, S.A. Ahmed, S. Sankar Bhattacharya, D. Pal, S.K. Pal, A smart nanotherapeutic agent for in vitro and in vivo reversal of heavy-metal-induced causality: Key information from optical spectroscopy, *ChemMedChem*, 15 (2020) 420.

[13] A. Adhikari, M. Das, S. Mondal, S. Darbar, A.K. Das, S.S. Bhattacharya, D. Pal, S.K. Pal, Manganese neurotoxicity: Nano-oxide compensates for ion-damage in mammals, *Biomater. Sci.*, 7 (2019) 4491.
[14] W. Wang, X. Ji, A. Kapur, H. Mattoussi, Surface-functionalizing metal, metal oxide and semiconductor nanocrystals with a multi-coordinating polymer platform, *MRS Adv.*, 1 (2016) 3741.
[15] L. Leyssens, B. Vinck, C. Van Der Straeten, F. Wuyts, L. Maes, Cobalt toxicity in humans—A review of the potential sources and systemic health effects, *Toxicol.*, 387 (2017) 43.
[16] G. Olivieri, C. Hess, E. Savaskan, C. Ly, F. Meier, G. Baysang, M. Brockhaus, F. Müller-Spahn, Melatonin protects SHSY5Y neuroblastoma cells from cobalt-induced oxidative stress, neurotoxicity and increased β-amyloid secretion, *J. Pineal Res.*, 31 (2001) 320.
[17] A.P. Lan, J. Chen, Z.F. Chai, Y. Hu, The neurotoxicity of iron, copper and cobalt in Parkinson's disease through ROS-mediated mechanisms, BioMetals, 29 (2016) 665.
[18] S. Catalani, M. Rizzetti, A. Padovani, P. Apostoli, Neurotoxicity of cobalt, *Hum. Exp. Toxicol.*, 31 (2012) 421.
[19] A. Giampreti, D. Lonati, B. Ragghianti, A. Ronchi, V.M. Petrolini, S. Vecchio, C.A. Locatelli, N-acetyl-cysteine as effective and safe chelating agent in metal-on-metal hip-implanted patients: Two cases, *Case Rep. Orthop.*, 2016 (2016) 8682737.
[20] J.J. Devlin, A.C. Pomerleau, J. Brent, B.W. Morgan, S. Deitchman, M. Schwartz, Clinical features, testing, and management of patients with suspected prosthetic hip-associated cobalt toxicity: A systematic review of cases, *J. Med. Toxicol.*, 9 (2013) 405.
[21] W. Steens, G. Von Foerster, A. Katzer, Severe cobalt poisoning with loss of sight after ceramic-metal pairing in a hip—A case report, *Acta Orthop.*, 77 (2006) 830.
[22] X. Mao, A.A. Wong, R.W. Crawford, Cobalt toxicity—An emerging clinical problem in patients with metal-on-metal hip prostheses, *Med. J. Aust.*, 194 (2011) 649.
[23] J.L. Domingo, Cobalt in the environment and its toxicological implications, *Rev. Environ. Contam. Toxicol.*, 108 (1989) 105.

[24] M. Goebeler, R. Gillitzer, K. Kilian, K. Utzel, E.-B. Bröcker, U.R. Rapp, S. Ludwig, Multiple signaling pathways regulate NF-κB–dependent transcription of the monocyte chemoattractant protein-1 gene in primary endothelial cells, *Blood*, 97 (2001) 46.

[25] C.P. Moorhouse, B. Halliwell, M. Grootveld, J.M.C. Gutteridge, Cobalt(II) ion as a promoter of hydroxyl radical and possible 'crypto-hydroxyl' radical formation under physiological conditions. Differential effects of hydroxyl radical scavengers, *Biochim. Biophys. Acta. Bioenerg.*, 843 (1985) 261.

[26] X. Shi, N.S. Dalal, K.S. Kasprzak, Generation of free radicals from model lipid hydroperoxides and hydrogen peroxide by Co(II) in the presence of cysteinyl and histidyl chelators, *Chem. Res. Toxicol.*, 6 (1993) 277.

[27] G. Wang, T.K. Hazra, S. Mitra, H.-M. Lee, E.W. Englander, Mitochondrial DNA damage and a hypoxic response are induced by $CoCl_2$ in rat neuronal PC12 cells, *Nucleic Acids Res.*, 28 (2000) 2135.

[28] J. Chen, C.E. Mathews, Susceptibility to free radical-mediated and autoimmune diabetes is controlled by retrogenetic interactions of the nuclear and mitochondrial genomes, *Mitochondrion*, 9 (2009) 67.

[29] A. Lan, X. Liao, L. Mo, C. Yang, Z. Yang, X. Wang, F. Hu, P. Chen, J. Feng, D. Zheng, L. Xiao, Hydrogen sulfide protects against chemical hypoxia-induced injury by inhibiting ROS-activated ERK1/2 and p38MAPK signaling pathways in PC12 cells, *PLoS One*, 6 (2011) e25921.

[30] L. Xiao, A. Lan, L. Mo, W. Xu, N. Jiang, F. Hu, J. Feng, C. Zhang, Hydrogen sulfide protects PC12 cells against reactive oxygen species and extracellular signal-regulated kinase 1/2-mediated downregulation of glutamate transporter-1 expression induced by chemical hypoxia, *Int. J. Mol. Med.*, 30 (2012) 1126.

[31] Q. Zhou, C. Liu, W. Liu, H. Zhang, R. Zhang, J. Liu, J. Zhang, C. Xu, L. Liu, S. Huang, L. Chen, Rotenone induction of hydrogen peroxide inhibits mTOR-mediated S6K1 and 4E-BP1/EIF4E pathways, leading to neuronal apoptosis, *Toxicol. Sci.*, 143 (2015) 81.

[32] S.W. Smith, The role of chelation in the treatment of other metal poisonings, *J. Med. Toxicol.*, 9 (2013) 355.

[33] S.M. Bradberry, Metals (cobalt, copper, lead, mercury), *Medicine*, 44 (2016) 182.

[34] C.R. Reczek, N.S. Chandel, ROS promotes cancer cell survival through calcium signaling, *Cancer cell*, 33 (2018) 949.

[35] D.K. Singh, A.R. Ray, Biomedical applications of chitin, chitosan, and their derivatives, *J. macromol. Sci., Polym. Rev.*, 40 (2000) 69.

[36] X. Qu, A. Wirse´n, A.-C. Albertsson, Novel pH-sensitive chitosan hydrogels: Swelling behavior and states of water, *Polymer*, 41 (2000) 4589.

[37] J.-Y. Je, S.-K. Kim, Chitosan as potential marine nutraceutical, *Adv. Food Nutr. Res.*, 65 (2012) 121.

[38] C. Muanprasat, P. Wongkrasant, S. Satitsri, A. Moonwiriyakit, P. Pongkorpsakol, T. Mattaveewong, R. Pichyangkura, V. Chatsudthipong, Activation of AMPK by chitosan oligosaccharide in intestinal epithelial cells: Mechanism of action and potential applications in intestinal disorders, *Biochem. Pharmacol.*, 96 (2015) 225.

[39] B. Huang, D. Xiao, B. Tan, H. Xiao, J. Wang, J. Yin, J. Duan, R. Huang, C. Yang, Y. Yin, Chitosan oligosaccharide reduces intestinal inflammation that involves calcium-sensing receptor (CaSR) activation in lipopolysaccharide (LPS)-challenged piglets, *J. Agric. Food Chem.*, 64 (2016) 245.

[40] M. Thanou, J.C. Verhoef, H.E. Junginger, Chitosan and its derivatives as intestinal absorption enhancers, *Adv. Drug Deliv. Rev.*, 50 (2001) S91.

[41] H. Hyun, S. Hashimoto-Hill, M. Kim, M.D. Tsifansky, C.H. Kim, Y. Yeo, Succinylated chitosan derivative has local protective effects on intestinal inflammation, *ACS Biomater. Sci. Eng.*, 3 (2017) 1853.

[42] S.-J. Yang, F.-H. Lin, H.-M. Tsai, C.-F. Lin, H.-C. Chin, J.-M. Wong, M.-J. Shieh, Alginate-folic acid-modified chitosan nanoparticles for photodynamic detection of intestinal neoplasms, *Biomat.*, 32 (2011) 2174.

[43] C.F. Babbs, Oxygen radicals in ulcerative colitis, *Free Radic. Biol. Med.*, 13 (1992) 169.

[44] A. Zinger, S. Soriano, G. Baudo, E. De Rosa, F. Taraballi, S. Villapol, Biomimetic nanoparticles as a theranostic tool for traumatic brain injury, *Adv. Funct. Mater.*, 31 (2021) 2100722.

[45] C. Wang, S. Ravi, U.S. Garapati, M. Das, M. Howell, J. Mallela, S. Alwarappan, S.S. Mohapatra, S. Mohapatra, Multifunctional chitosan magnetic-

graphene (CMG) nanoparticles: a theranostic platform for tumor-targeted co-delivery of drugs, genes and MRI contrast agents, *J. Mater. Chem. B*, 1 (2013) 4396.

[46] Y. Wang, F. Yang, X. Yang, Colorimetric detection of mercury(II) ion using unmodified silver nanoparticles and mercury-specific oligonucleotides, *ACS Appl. Mater. Interfaces*, 2 (2010) 339.

[47] F. Li, J. Wang, Y. Lai, C. Wu, S. Sun, Y. He, H. Ma, Ultrasensitive and selective detection of copper (II) and mercury (II) ions by dye-coded silver nanoparticle-based SERS probes, *Biosens. Bioelectron.*, 39 (2013) 82.

[48] X. Xue, F. Wang, X. Liu, One-step, room temperature, colorimetric detection of mercury (Hg^{2+}) using DNA/nanoparticle conjugates, *J. Am. Chem. Soc.*, 130 (2008) 3244.

[49] A. Giri, N. Goswami, C. Sasmal, N. Polley, D. Majumdar, S. Sarkar, S.N. Bandyopadhyay, A. Singha, S.K. Pal, Unprecedented catalytic activity of mn_3o_4 nanoparticles: Potential lead of a sustainable therapeutic agent for hyperbilirubinemia, *RSC Adv.*, 4 (2014) 5075.

[50] A. Adhikari, N. Polley, S. Darbar, D. Bagchi, S.K. Pal, Citrate functionalized Mn_3O_4 in nanotherapy of hepatic fibrosis by oral administration, *Future Sci. OA*, 2 (2016) FSO146.

[51] A. Giri, N. Goswami, M. Pal, M.T. Zar Myint, S. Al-Harthi, A. Singha, B. Ghosh, J. Dutta, S.K. Pal, Rational surface modification of Mn_3O_4 nanoparticles to induce multiple photoluminescence and room temperature ferromagnetism, *J. Mater. Chem. C*, 1 (2013) 1885.

[52] S. Mondal, A. Adhikari, R. Ghosh, M. Singh, M. Das, S. Darbar, S.S. Bhattacharya, D. Pal, S.K. Pal, Synthesis and spectroscopic characterization of a target-specific nanohybrid for redox buffering in cellular milieu, *MRS Adv.*, 6 (2021) 427.

[53] S. Lei, K. Tang, Z. Fang, H. Zheng, Ultrasonic-assisted synthesis of colloidal Mn_3O_4 nanoparticles at normal temperature and pressure, *Cryst. Growth Des.*, 6 (2006) 1757.

[54] S. Mondal, A. Adhikari, M. Das, S. Darbar, A. Alharbi, S.A. Ahmed, S.S. Bhattacharya, D. Pal, S.K. Pal, Novel one pot synthesis and spectroscopic characterization of a folate-Mn_3O_4 nanohybrid for potential photodynamic therapeutic application, *RSC Adv.*, 9 (2019) 30216.

[55] C. Song, H. Yu, M. Zhang, Y. Yang, G. Zhang, Physicochemical properties and antioxidant activity of chitosan from the blowfly Chrysomya megacephala larvae, *Int. J. Biol. Macromol.*, 60 (2013) 347.

[56] A. Datta, D. Mandal, S.K. Pal, K. Bhattacharyya, Intramolecular charge transfer processes in confined systems. Nile red in reverse micelles, *J. Phys. Chem. B*, 101 (1997) 10221.

[57] S. Sardar, S. Chaudhuri, P. Kar, S. Sarkar, P. Lemmens, S.K. Pal, Direct observation of key photoinduced dynamics in a potential nano-delivery vehicle of cancer drugs, *Phys. Chem. Chem. Phys.*, 17 (2015) 166.

[58] A.A. Khorobrykh, V.V. Terentyev, S.K. Zharmukhamedov, V.V. Klimov, Redox interaction of Mn–bicarbonate complexes with reaction centres of purple bacteria, Philos. Trans. R. Soc. B: Biol. Sci., 363 (2008) 1245.

[59] M. Thanou, J. Verhoef, H. Junginger, Chitosan and its derivatives as intestinal absorption enhancers, *Adv. Drug Deliv. Rev.*, 50 (2001) S91.

[60] S. Mondal, A. Adhikari, M. Singh, R. Ghosh, M. Goswami, P. Biswas, S.K. Pal, Spectroscopic study on the interaction of Co^{2+} with citrate-Mn_3O_4: Towards the development of nanotherapy against cobalt toxicity, *Mater. Today: Proc.*, 43 (2021) 3692.

[61] K.S. Kim, N. Winograd, X-ray photoelectron spectroscopic binding energy shifts due to matrix in alloys and small supported metal particles, *Chem. Phys. Lett.*, 30 (1975) 91.

[62] S.K. Ghosh, J. Kang, M. Inokuchi, N. Toshima, Solvent-mediated synthesis, characterization and electrocatalytic activity of hydrophilic and dispersive Au–Mn_3O_4 nanocomposites, *Appl. Catal. A-Gen.*, 464 (2013) 225.

[63] J.R. Lakowicz, Principles of Fluorescence Spectroscopy, *Springer,* Berlin,, 2006.

[64] A. Adhikari, S. Darbar, T. Chatterjee, M. Das, N. Polley, M. Bhattacharyya, S. Bhattacharya, D. Pal, S.K. Pal, Spectroscopic studies on dual role of natural flavonoids in detoxification of lead poisoning: Bench-to-bedside preclinical trial, *ACS Omega*, 3 (2018) 15975.

[65] X. Shi, N.S. Dalal, K.S. Kasprzak, Generation of free radicals from model lipid hydroperoxides and hydrogen peroxide by cobalt(II) in the presence of cysteinyl and histidyl chelators, *Chem. Res. Toxicol.*, 6 (1993) 277.

[66] B. Halliwell, J.M.C. Gutteridge, Oxygen toxicity, oxygen radicals, transition metals and disease, *Biochem. J.*, (1984) 1.

[67] M. Strlic, J. Kolar, V.-S. Selih, D. Kocar, B. Pihlar, A comparative study of several transition metals in Fenton-like reaction systems at circum-neutral pH, *Acta Chim Slov.*, 50 (2003) 619.

[68] M.H. Moustafa, R.K. Sharma, J. Thornton, E. Mascha, M.A. Abdel-Hafez, A.J. Thomas, A. Agarwal, Relationship between ROS production, apoptosis and DNA denaturation in spermatozoa from patients examined for infertility, *Hum. Reprod.*, 19 (2004) 129.

[69] M.I. Khan, A. Mohammad, G. Patil, S.A.H. Naqvi, L.K.S. Chauhan, I. Ahmad, Induction of ROS, mitochondrial damage and autophagy in lung epithelial cancer cells by iron oxide nanoparticles, *Biomat.*, 33 (2012) 1477.

[70] C. Guo, L. Sun, X. Chen, D. Zhang, Oxidative stress, mitochondrial damage and neurodegenerative diseases, *Neural Regen. Res.*, 8 (2013) 2003.

[71] H.U. Simon, A. Haj-Yehia, F. Levi-Schaffer, Role of reactive oxygen species (ROS) in apoptosis induction, *Apoptosis*, 5 (2000) 415.

[72] M.J. Horsburgh, S.J. Wharton, M. Karavolos, S.J. Foster, Manganese: Elemental defence for a life with oxygen, *Trends Microbiol.*, 10 (2002) 496.

CHAPTER 7

Synthesis and Characterization of Nanomaterial for Therapeutic and Diagnostic Biological Applications

7.1. Introduction:

Among innumerable nanoscale materials, nanoparticles received considerable attention from contemporary researchers and eventually became one of the most explored scientific fields in the last decade. The introduction of nanoparticles with novel and unique physico-chemical properties resulted into a paradigm shift in the biomedical research field. Particularly, a new type of nanoparticle that integrates diagnostics and therapeutics within a single system (i.e., theranostics) is emerging as the future magic bullet for integrated disease management [1, 2]. Recent developments in imaging techniques revolutionized the potential use of nanomaterials for disease diagnosis as they can be used as fluorescent probe, magnetic resonance imaging (MRI), or X-ray contrast agent. An important property of the nanoparticles is their tenability. One can easily modify the surface functionalizing ligand (i.e., the organic moiety) and thereby alter the target organ specificity, biocompatibility including several other characteristics [3-5]. Among the nanoparticles, surface coated iron oxide nanoparticle has been established as a potent MRI contrast agent owing to its superparamagnetic property [6-9]. The therapeutic activities of iron oxide nanoparticles in diseases like iron deficiency, carcinoma, cardiac disorder etc. have also been studied exhaustively [10-14]. Nanoparticles containing another member of the transition metal family, manganese (Mn) have also displayed huge potential as theranostic agents against several chronic diseases [5, 15, 16]. Redox buffering capability (to function as both pro- and anti-oxidant system), target specificity, and enzyme mimicking activities are the key mechanisms behind the therapeutic potential of Mn based nanoparticle [15, 17]. On the other hand, room temperature ferromagnetic properties, and X-ray opacity allow them to be used as a diagnostic tool [18-20]. However, these diagnostic techniques are expensive and require highly skilled manpower which is limited in developing and under developed countries. Therefore, cost effective and easy to use alternative

diagnostic tools and techniques are obligatory. In this regard, easy to use electrochemistry-based techniques could be a facile alternative considering the unique electrochemical properties of the nanomaterials which remain mostly unexplored in the contemporary field of theranostics.

Bilirubin is a yellow pigmented molecule generated from the breakdown of hemeproteins (i.e., hemoglobin and myoglobin) during the catabolism of red blood cells (RBC) [21]. Although, bilirubin at micromolar concentration act as an antioxidant and protects cells from reactive oxygen species (ROS) mediated damages but at higher concentration it is harmful and toxic to the cells [22-25]. There are two types of bilirubin present in the physiological milieu, i.e., conjugated and unconjugated bilirubin. The conjugation of bilirubin with sugar moiety is performed by the liver and is an important phenomenon to excrete the bilirubin from the body. Some portion of the bilirubin also forms a complex with human serum albumin protein (known as delta bilirubin, a form of conjugated bilirubin) and is transported across the body as a part of the serum [26]. The elevated level of total serum bilirubin particularly in newborn babies is associated with several chronic diseases like neonatal hyperbilirubinemia (>10 $mgdl^{-1}$), Gilbert syndrome (with BR level reaching >6 $mgdl^{-1}$), Crigler–Najjar type I disease (>30 $mgdl^{-1}$) and bilirubin encephalopathy [27-29]. Neonatal jaundice occurs in >80% of neonates in the first week of life and if unmonitored can cause severe damage in the brain (Kernicterus) [25, 29]. On the other hand, the occurrence of the conjugated hyperbilirubinemia is uncommon (1 case per 2500 children) but the detection of conjugated bilirubin specially delta bilirubin is important in some clinical evaluation (like cholestasis, condition of liver, bile flow etc.) [26]. In some cases, where the presence of delta bilirubin prolongs direct hyperbilirubinemia while other liver parameters are normalizing, the amount of delta bilirubin serves as a vital parameter for the clinician [26]. In addition, the regular treatment options for neonatal hyperbilirubinemia (i.e., phototherapy, exchange blood transfusion etc.) require long term hospitalization and have several drawbacks in terms of efficacy and cost. Moreover, no therapeutic drug is available till date that can specifically reduce the bilirubin levels [25, 30]. Therefore, a strategy for continuous monitoring of bilirubin level in blood and its remediation is urgently needed [29, 31-33].

Another threating problem for global mortality rate is the emergence of multiple drug resistant bacterial strains. Massive and random use of antibiotics in various sectors like medicine, agriculture and food industries triggered the generation of the drug-resistant bacterial strains [34, 35]. Drug-resistant infections are causing significant increase in patient mortality and morbidity [36]. Also in Covid-19 affected patient the occurrence of hospital acquired secondary bacterial infection (HAIs) is proving fatal in major cases [37, 38]. So developing a contemporary anti-microbial strategy other than antibiotics is a pressing need to combat the drug-resistant infection. In this case, nanotherapy has set forth a very promising future [39-41]. Many nanomaterials have been appeared as more effective anti-microbial agent than the conventional antibiotics [42, 43]. Apart from the therapy, sometimes an early stage detection of bacterial infection can prevent mortality. So the use of theranostic NPs will provide a solution for the increased mortality rate due to the drug-resistance bacterial infection.

Despite having such advantages, concerns about their behavior in biological system have limited their rapid translation in medicinal field [2, 44]. The unique behavior of NPs at the 'Nano-bio' interface (e.g., membrane, protein, nucleic acids, organelles, biological fluids etc.) critically dictate the bioadversity or biocompatibility of a nanomaterial [2, 45, 46]. Chemical composition, size, shape, crystallinity, surface charge, roughness, porosity, heterogeneity, hydrophilicity or hydrophobicity are the key nanomaterial characteristics that determine the nature of bio-compatibility of the NPs [44, 47-50]. Another fascinating, but mostly unexplored property that plays a defining role in bio-compatibility is surface coatings as the surface ligand guide the molecule to the specific site and also determine its uptake. So critical engineering of the surface ligand can improve the bio-compatibility and refine its theranostic effect.

First, we have investigated the efficacy of a theranostic nanoparticle, citrate functionalized Mn_3O_4 nanoparticles (C-Mn_3O_4 NPs), against hyperbilirubinemia. Previously, we have reported efficient decomposition of bilirubin by C-Mn_3O_4 NPs in both *in-vitro* and *in-vivo* systems along with its potential to reduce bilirubin levels in preclinical model of hyperbilirubinemia [25, 51, 52]. However, its efficacy in the diagnosis of hyperbilirubinemia is yet to be explored. Here, we introduced a compact electrochemical tool for detection of bilirubin in a sample by using the interesting

electrochemical properties of C-Mn_3O_4 NPs. We have also shown the degradation of unconjugated bilirubin as well as delta bilirubin by C-Mn_3O_4 NPs. We have characterized the C-Mn_3O_4 NPs using high-resolution transmission electron microscopy (HRTEM), absorbance and fluorescence spectroscopy. The extent of bilirubin degradation and the mechanism behind it were explored using Langmuir-Hinshelwood study and pico-second resolved lifetime study. Using linear sweep voltammetry we measured the amount of current generated by the NPs with varying the voltage and monitored the change in current when the solution contained bilirubin. Next, the interference of human serum albumin (HSA) in the efficacy of detection and degradation of bilirubin by C-Mn_3O_4 NPs was also explored. We have also tested the recyclability of bilirubin degradation by C-Mn_3O_4 NPs using chronoamperometry measurements and optical methods. It is eminent from the aforementioned studies that C-Mn_3O_4 NPs can efficiently detect the presence of bilirubin in a solution and can also degrade the elevated bilirubin in blood, thereby, remediating hyperbilirubinemia. Thus, C-Mn_3O_4 NPs can undoubtedly be a potent theranostic agent against hyperbilirubinemia and related diseases.

In another study, using Mn_3O_4 as a model nanomaterial with folate and citrate as two surface coating ligands having different physico-chemical properties we thoroughly investigated the effect of surface functionalization in the alteration on biocompatibility, therapeutic effect and diagnostic activity of the NPs. Spectroscopic studies revealed the changes in charge-transfer interactions due to variation in the ligand composition. Computational studies further supported the experimental observations and revealed the underlying mechanism involved. Then we evaluate the diagnostics potential of the two NPs using X-ray imaging technique. The therapeutic effect of the two differently functionalized NPs were investigated by using a model bacteria *Staphylococcus hominis*. This is a Gram positive bacteria, usually present as a commensal on the skin of humans and is responsible for body odor [53]. Recently some of the sub-species of *S. hominis* have been recognized to cause drug-resistant sepsis in neonatal intensive care unit [38, 54]. The two surface functionalized (citrate and folate) nanoparticles though share the same core (Mn_3O_4) exhibited contrasting antimicrobial effects. Next, using a bacterial mimic we further explored the reason behind this differential toxicity against same bacterial strain. We have also explored the theranostic ability of both the functionalized NPs. From the

above study it is eminent that surface functionalized Mn_3O_4 NPs are potent anti-microbial agents against bacterial infection and also can be used as an X-ray contrast agent in disease diagnosis.

Not only, inorganic nanoparticles are able to exhibit the theranostic potential. Some recent studies have shown that organic nanoparticles such as carbon containing nanomaterials can be used in healthcare sectors. In this regard, the two dimensional (2D) materials including graphene and its derivative, are becoming more attractive to the scientific communities due to their unique physical and electronic properties along with their vast scope of application [55-58]. Graphitic carbon nitride (g-C_3N_4, a metal free semiconductor) is one of those 2D materials. Due to its thermal and chemical stability and non-toxicity, it has been considered as a very efficient photocatalytic agent for environmental pollution remediation, energy conversion, and detection of various important chemical substancez [56, 57, 59, 60]. Additionally, the g-C_3N_4 has been shown to be a highly fluorescent material (emits within violet to blue regions) with a low quantum yield [61, 62]. This emitting property is due to the presence of high band gap (2.7 eV) [63]. This fluorescent property makes it a competent agent in biomedical field. Despite these benefits, the use of g-C_3N_4 in the field of medicine is scarce. With the progress in nanotechnology, the field of medicine has also been flooded with potential metal-based nanoparticle [64-68]. Despite of unique target specificity and high reactivity in a low amount, most of these metal nanoparticles have failed in clinical trials owing to huge toxicity [69-72]. In this case, the use of polymeric graphitic nanomaterial as a medicine can be a suitable alternative owing to their excellent thermal and chemical stability, inexpensive, non-toxic nature, earth-abundant, cost-effective and easy synthesis process [59, 60, 73].

Heavy metals are naturally found in the earth's crust but have relatively high density and are toxic even in low concentrations [74, 75]. Their uncontrolled usage in the various industries make them widely distributed in the environment that potentially led to concern regarding their effect on humans. Due to their extreme toxic effect, the World Health Organisation (WHO) and Environmental Protection Agency (EPA) have precisely indicated the level of these metals in drinking water [76]. These heavy metals accumulated in the tissues or certain compartments of the body and induce reactive oxygen species (ROS) to damage the specific organ or tissue that led

to disorders like anemia, Parkinson's, Alzheimer's, Wilson's disease [77-81]. Among these heavy metals, lead (Pb) has been considered as an essential inorganic toxin by the CDC, USA (Centers for Disease Control and Prevention), because it is widely presented in automobile exhaust, industrial wastewater, and decorating materials and effect almost every organ of human body both in children and adults [75, 82-85]. Acute or chronic intake of Pb result in neurasthenia, cardiovascular disease, kidney disease and also seriously affect the reproductive health of both the genders [81, 84]. The available treatment for Pb toxicity are the administration of chelator (i.e., 2, 3-dimercaptosuccinic acid, (DMSA) or edetate calcium disodium, (EDTA)) or haemodialysis [86, 87]. Both therapies involve the elimination of internal Pb and suffer from some major disadvantages like inevitable non-selection, strong side effects, re-distribution of the metal to the brain, and high expenses [88-90]. To date, there is no medication to eliminate Pb from an organ as well as to protect the organ from Pb induced ROS mediated damages. Not only that, the available detection methods for Pb(II) (e.g., atomic absorption spectrometry, inductively coupled plasma mass spectrometry) have their shortcoming [91, 92]. These methods are extremely costly and require extensive sample preparation [92, 93]. So, the invention of a cost beneficiary, simple technique for lead detection is very much important to detect the Pb(II) in food, drinking water, environment and human body.

In this regard, the non-toxic 2D polymeric graphitic nanomaterials can be a cost-beneficial alternative to the available therapies and detection methods without having any additional side-effect. In this study, we have synthesized 2D citrate capped polymeric carbon nitride nanodots (C-C_3N_4 NDs) from a polymeric graphite carbon nitride nanosheet (g-C_3N_4 Ns). We characterized the C-C_3N_4 nanodots using spectroscopic and electron microscopy techniques. These developed nanodots has the potential to generate room temperature ROS. The C-C_3N_4 NDs then were examined for Pb(II) chelation activity and its potential to maintain the cellular oxidative eustress [94, 95]. The spectroscopic studies indicated that the C-C_3N_4 NDs effectively bind to the accumulated Pb(II). The significant change in absorbance and fluorescence spectrum after the formation of Pb(II)-NDs complex serves as cost-effective and simple method for detection of lead. The formed complex is soluble in water and via this formed complex the accumulated Pb(II) can be mobilised from the reaction site. Next, a hemolysis assay demonstrated its ability to chelate the

Pb(II) in the physiological milieu and also to reverse its ROS induced damage and maintain the cellular eustress condition. In conclusion this newly developed 2D, biocompatible C-C_3N_4 NDs is an effective dual acting agent against the lead pollution.

7.2. Results and Discussion:

7.2.1. Interaction of a Jaundice Marker Molecule With Redox Modulatory Nano Hybrid: A Combined Electrochemical and Spectroscopic Study Towards the Development of a Theranostic Tool [96]: In order to characterize the water-soluble C-Mn_3O_4 NPs, transmission electron microscopic (TEM) study was employed. As shown in Figure 7.1.a, the C-Mn_3O_4 NPs are spherical in shape and exhibit unimodal distribution. HRTEM image (Figure 7.1.b) revealed the interplanar distance between fringes is 3.12 Å which corresponds to (112) plane of Mn_3O_4 spinel lattice [97, 98].

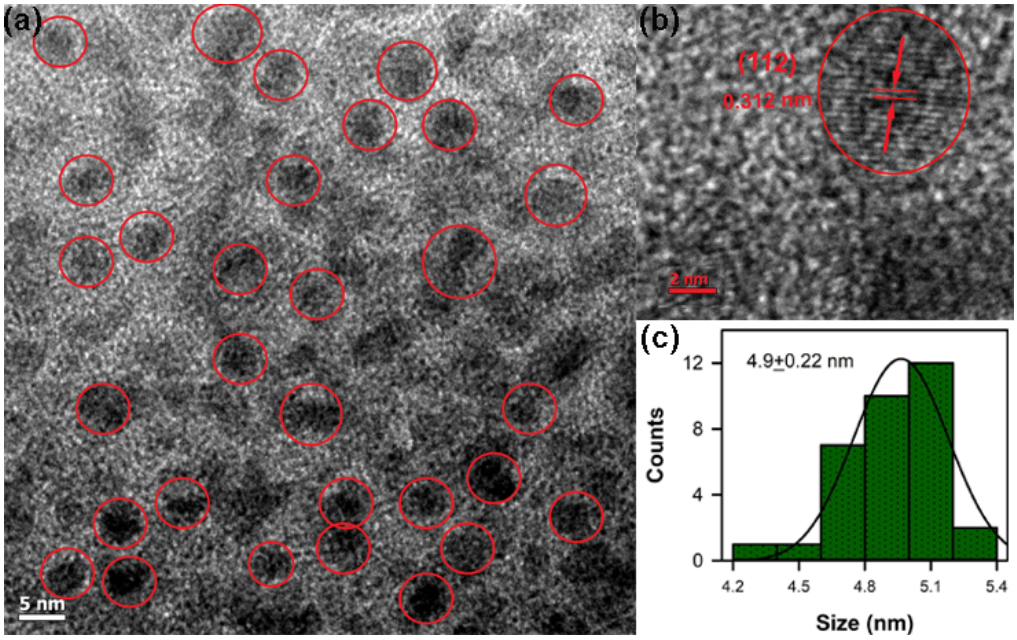

Figure 7.1: *Characterization of C-Mn_3O_4 NPs. (a) TEM image of C-Mn_3O_4 NPs distribution. (b) HR-TEM of C-Mn_3O_4 NPs. (c) Size distribution of C-Mn_3O_4 NPs.*

C-Mn_3O_4 NPs have an average size of 4.9± 0.22 nm (Figure 7.1.c) with a narrow size distribution (4.0 nm - 6.0 nm). Capping with citrate generated exciting optical properties in C-Mn_3O_4 NPs. C-Mn_3O_4 NPs showed a high energy absorption band around 290 nm (Figure 7.2), which could be assigned to ligand-to-metal charge transfer (LMCT) due to the interaction between Mn^{2+}/Mn^{3+} present at the surface of NPs and the ligand [51, 98]. The other bands around 430 nm, 526 nm are due to the

Jahn–Teller (J–T) distorted d–d transitions centred over Mn^{3+} ions in C-Mn_3O_4 NPs (Figure 7.2. inset).

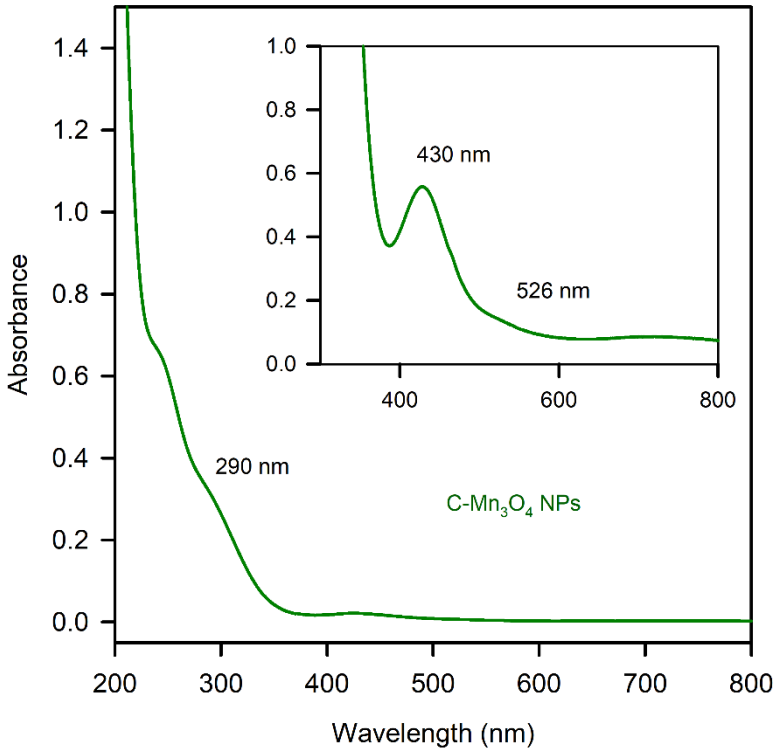

Figure 7.2: *Absorbance of C-Mn_3O_4 NPs. LMCT band is visible at 290 nm. The presence of d-d band is visible at 430 nm and 526 nm (Inset).*

Next, we have explored the bilirubin degradation ability of C-Mn_3O_4 NPs in the presence and absence of HSA. Addition of NPs in the bilirubin solution resulted in a decrease in absorbance of bilirubin at 460 nm with time, which indicates the bilirubin degradation efficiency of C-Mn_3O_4 NPs (Figure 7.3.a). However, the presence of HSA in the reaction medium hindered the degradation rate of bilirubin by NPs to a great extent. The probable cause behind the slow kinetics of degradation of bilirubin in the presence of HSA could be the conjugation of bilirubin with protein, which is a well-studied interaction [99]. Next, we explored the mechanism behind the bilirubin degradation by NPs. Figure 7.3.b showed the Langmuir-Hinshelwood (L-H) plot of bilirubin degradation by C-Mn_3O_4 NPs. The L-H plot confirms that the reaction between the surface of NPs and bilirubin is not the primary mechanism behind bilirubin degradation efficacy of NPs [51, 100]. To explore the main mechanism of bilirubin degradation, we have performed pico-second resolved time

dependent study. Figure 7.3.c shows the charge transfer from NPs to bilirubin as the lifetime of excited state electrons of the NP decreased in the presence of bilirubin.

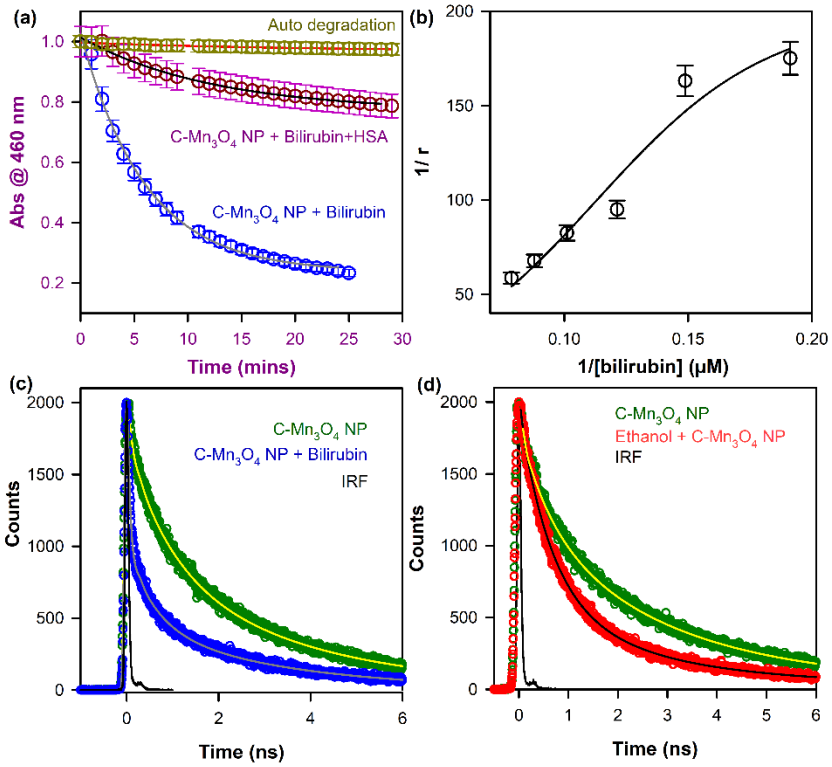

Figure 7.3: *Mechanism of bilirubin degradation. (a)Bilirubin degradation kinetics. (b) Langmuir-Hinshelwood plot of bilirubin degradation by C-Mn_3O_4 NPs. (c) and (d) Life-time of C-Mn_3O_4 NPs and life-time after addition of bilirubin and ethanol.*

This confers two possibilities, one is surface mediated (i.e., direct charge transfer to bilirubin) and the other is ROS mediated (charge transfer mediated by the medium). It is well known that C-Mn_3O_4 NPs generates ROS at room temperature by recruiting the dissolved oxygen of the medium [51, 52, 100]. To explore the second possibility, we have used ethanol, a well-known ROS quencher. Similar type of quenching in the lifetime was observed after addition of ethanol to the NPs solution (Figure 7.3.d, Table 7.1). These results indicate the decrease in the lifetime of the excited state electrons of NPs is not due to direct charge transfer from the surface of NPs to bilirubin, but due to charge transfer from NPs to the substrate (i.e., ethanol or bilirubin) via ROS generation. Thus, C-Mn_3O_4 NPs degrade bilirubin predominantly by charge transfer mechanism through ROS generation. Figure 7.4.a shows the linear sweep voltammograms of C-Mn_3O_4 NPs, bilirubin and C-Mn_3O_4 NPs-bilirubin complex obtained in 1 (M) KCl solution. When the current for bilirubin

was measured, it exhibited a peak around 0.86 V. The peak around 0.86 V was obtained for bilirubin due to its oxidation to methylvinylmaleimide (MVM) [51, 101, 102]. For C-Mn_3O_4 NPs, a peak was observed around 0.95 V and there was a significant decrease in the current peak when bilirubin was added to the medium.

Table 7.1: *Fluorescence Lifetime of Different systems.*

System	τ_1(ns)	τ_2 (ns)	τ_3 (ns)	A_1(%)	A_2 (%)	A_3 (%)
C-Mn_3O_4 NPs	103	897	3469	34.7	31.8	33.3
C-Mn_3O_4 NPs + Bilirubin	48	582	3170	77.7	11.9	10.2
C-Mn_3O_4 NPs + Ethanol	95	673	3310	33.3	35.7	31

When C-Mn_3O_4 NPs are present in the system at neutral pH, the Mn^{3+} charge states rapidly converts to Mn^{4+} state due to the instability of Mn^{3+} charge state at the mentioned pH [51, 103]. This conversion at the surface of NPs results in subsequent generation of reactive oxygen species [51, 104]. The current observed in this case of C-Mn_3O_4 NPs is a resultant of subsequent neutralisation of the ROS in the electrode. However, when bilirubin is present in the medium, the ROS generated by C-Mn_3O_4 NPs degrade it via oxidising it to MVM. So, the effective concentration of ROS present in the system is quenched by bilirubin that ultimately results in the decrease of current. From Figure 7.4.b it is evident that the presence of HSA perturbs the degradation of bilirubin as there is no significant change in the amount of current after the addition of HSA-bilirubin complex to the NP solution. Then we have explored another electrochemical technique, chronoamperometry, which can also be a facile and point-of-care detection method of unconjugated bilirubin. We have applied a constant potential for a fixed time and observed the current decay pattern for C-Mn_3O_4 NPs (before and after the addition of bilirubin) and bilirubin alone. A clear difference in the current decay pattern and in the amount of current were observed for C-Mn_3O_4 NPs after adding bilirubin (Figure 7.4.c). From the decay parameters mentioned in Table 7.2, it can be inferred that the electrochemical strategy using C-Mn_3O_4 NPs selectively detect the unconjugated bilirubin present in the medium. Hence, it is an effective diagnostic tool for hyperbilirubinemia and

associated disorders. Next, we studied the recyclability of the C-Mn_3O_4 NPs for the bilirubin degradation.

Figure 7.5.a shows the recyclability of C-Mn_3O_4 NPs for bilirubin degradation for three consecutive cycles.

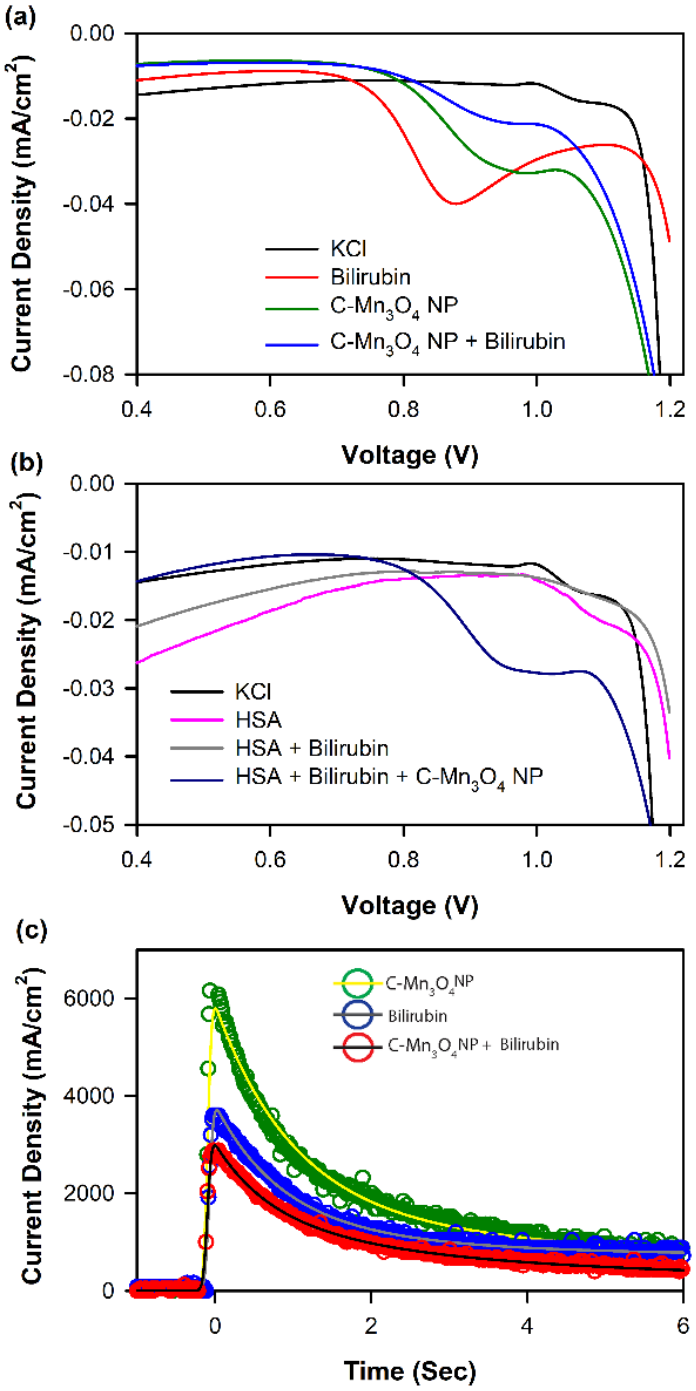

Figure 7.4: *Electrochemical detection of bilirubin. (a and b)Linear sweep voltammetry of C-Mn_3O_4 NPs and after addition of bilirubin, HSA in C-Mn_3O_4 NPs. (c) Decay of current as measured through chronoamperometry at an applied potential of 0.9 V.*

Table 7.2: *Lifetime of the current decay of different species.*

System	τ_1 (Sec/%)	τ_2 (Sec/%)	τ_{AVG} (Sec/%)
C-Mn_3O_4 NHs	0.080 (34%)	11.16 (66%)	7.39
C-Mn_3O_4 NHs + Bilirubin	0.072 (22%)	6.01 (78%)	4.70
Bilirubin	0.080 (28%)	6.01 (72%)	4.34

This indicates C-Mn_3O_4 NPs return to its original state after every cycle of degradation and no significant change in required time for regeneration of NPs was observed. The recyclability in the presence of HSA was lower than the previous one (Figure 7.5.b).

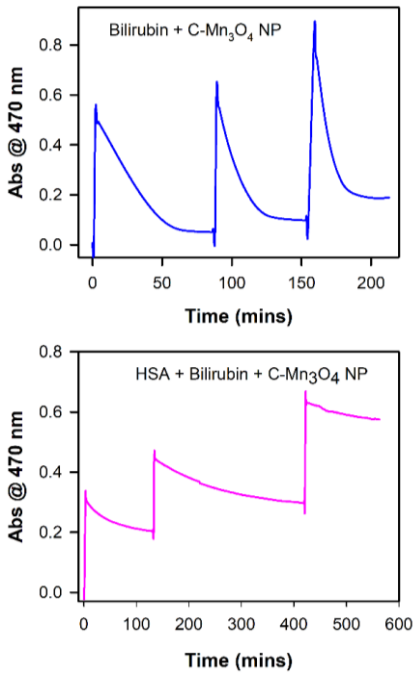

Figure 7.5: *Recyclability of bilirubin degradation by C-Mn_3O_4 NPs. (a) Three consecutive cycles of bilirubin degradation by C-Mn_3O_4 NPs. (b) Three consecutive cycles of bilirubin degradation by C-Mn_3O_4 NPs in the presence of human serum albumin.*

7.2.2. In-vitro and Microbiological Assay of Functionalized Hybrid-Nanomaterials to Validate Their Efficacy In Nano-Theranostics: A Combined Spectroscopic and Computational Study [3]:

7.2.2.1. Alteration of the Capping Material Effect the Structural and Optical Properties of Mn_3O_4 NPs: Figure 7.6.a and Figure 7.7.a show the transmission

electron micrographs (TEM) of Mn_3O_4 NPs functionalized with different surface ligands, folate and citrate.

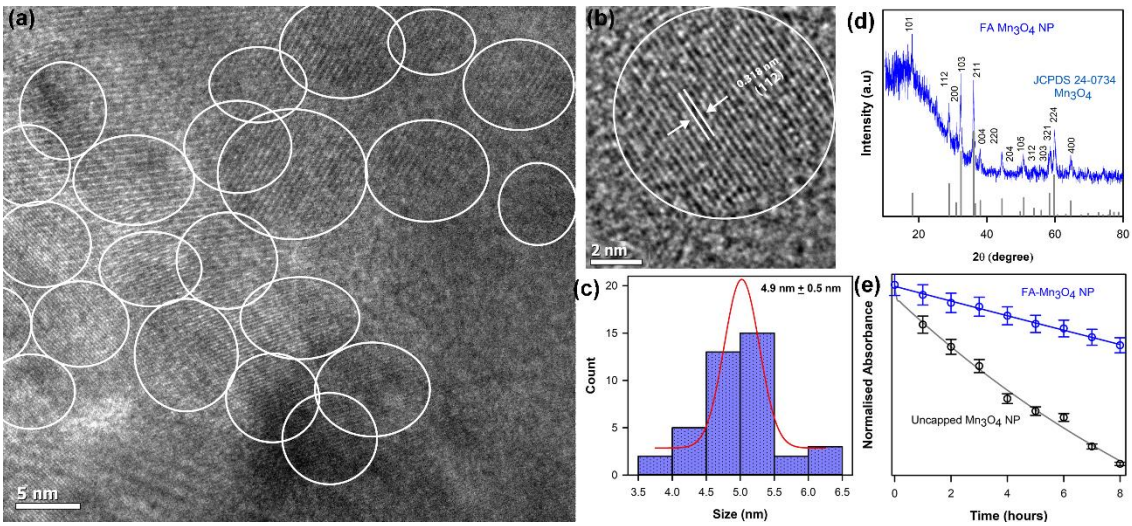

Figure 7.6: *Characterization of FA-Mn_3O_4 nanoparticles. (a) The particle distribution of the nanoparticles (NPs) recorded under transmission electron microscopy (TEM). (b) The particle size distribution is shown with average size of 4.945 ± 0.533 nm and (c) Highresolution electron micrograph (HRTEM) of the NPs with a clear interplaner distance of 0.318 nm for (112) planes in the Mn_3O_4 NPs is evident. (d) XRD pattern of synthesized FA-Mn_3O_4 NPs which exactly matches to that of library spectra. (e) Capping with folate increases the colloidal stability of the NPs as illustrated in time dependent absorbance studies.*

Both FA-Mn_3O_4 NPs and C-Mn_3O_4 NPs are spherical in shape with comparable average diameters of 4.9±0.5 nm (Figure 7.6.c) and 5.1±0.6 nm (Figure 7.7.c), respectively. The high resolution TEM (HRTEM) images of both FA-Mn_3O_4 NPs (Figure 7.6.b) and C-Mn_3O_4 NPs (Figure 7.7.b) show exposed (112) facet of Mn_3O_4 tetragonal crystal lattice with interfringe distance of 0.312 nm. The contrast of TEM images are comparatively poor as it has to be noted that the contrast of Mn based NPs in TEM and HRTEM are found to be lower than metallic form of Mn and the other metals (e.g., gold, silver etc.) [5, 98, 105]. All X-ray diffraction (XRD) peaks for both ligand functionalized NPs (Figure 7.6.d and 7.7.d) exactly matched with the hausmannite structure of manganese oxide (JCPDS no. 24-0734) [105, 106]. The aforementioned results confirmed the successful synthesis of Mn_3O_4 NPs and also indicate that functionalization with either hydrophobic or hydrophilic ligand has no impact on the inherent chemical composition, crystallinity, structure, size, or shape of the nanomaterial [98]. However, the nature of functionalizing ligand greatly affected the colloidal stability of the NPs in aqueous medium. While C-Mn_3O_4 NPs (zeta potential, -21.7 mV) were completely solubilized in water, (stable for more than

two years) FA-Mn_3O_4 NPs (zeta potential -10.3 mV) gradually started to settle down at the bottom of the solution within few hours (Figure 7.6.e and 7.7.e).

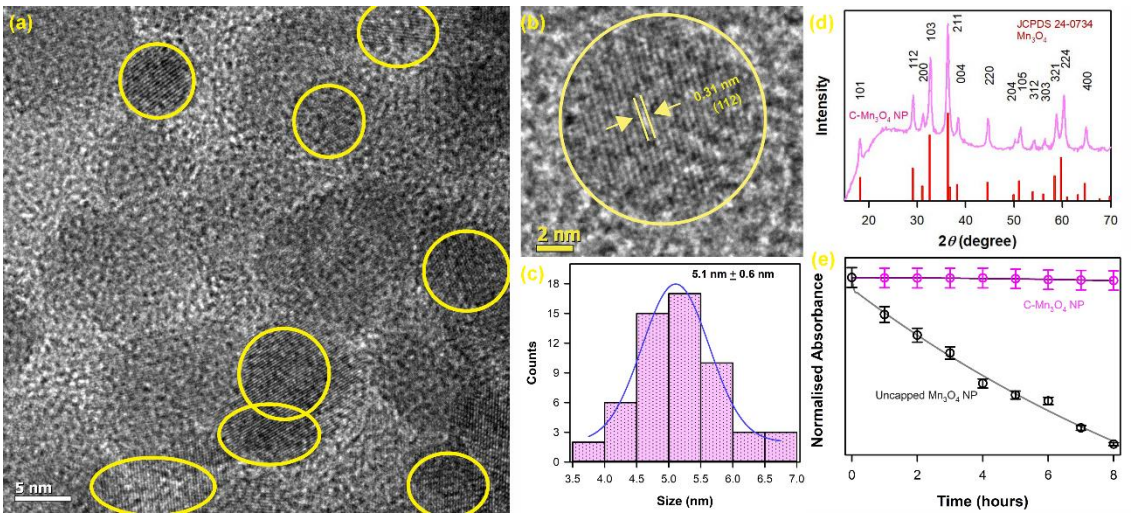

Figure 7.7: *Characterization of C-Mn_3O_4 nanoparticles. (a) The particle distribution of the nanoparticles (NPs) recorded under transmission electron microscopy (TEM). (b) The particle size distribution is shown with average size of 5.181 ± 0.667 nm and (c) High resolution electron micrograph (HRTEM) of the NPs with a clear interplaner distance of 0.31 nm for (112) planes in the Mn_3O_4 NPs is evident. (d) XRD pattern of synthesized C-Mn_3O_4 NPs which exactly matches to that of library spectra. (e) Capping with folate increases the colloidal stability of the NPs as illustrated in time dependent absorbance studies.*

Another factor that may attribute to the lesser colloidal stability of FA-Mn_3O_4 NPs is the hydrophobic nature of folate. As folate is more hydrophobic than citrate it converts the NPs attached to it hydrophobic in nature. In this regard, it has to be noted the pristine Mn_3O_4 NPs (~190 nm) are insoluble in water and functionalization with both the ligands increased it stability in aqueous media. Functionalization with citrate and folate generated exciting differential characteristics in optical properties of otherwise featureless Mn_3O_4 NPs. Both FA-Mn_3O_4 NPs and C-Mn_3O_4 NPs exhibited a high energy absorption band around 300 nm (Figure 7.8.a and 7.8.d), which can be assigned to ligand-to-metal charge transfer (LMCT) due to the i.e., the interaction between the ligand and Mn^{2+}/Mn^{3+} present at the surface of NPs [5]. It is evident from Figure 7.8.a and 7.8.d that the intensity of LMCT band (~300 nm) is higher for C-Mn_3O_4 NPs compared to the folate functionalized one. This may be due to the higher extent of charge delocalization in case of citrate in comparison to folate. A detailed explanation about the charge density delocalization is provided in the computational studies section of this manuscript. The other expected LMCT band around 385 nm has not been observed

in the absorption spectrum presumably because of the more intense absorption at 300 nm has masked it. Functionalization with folate gave rise to a single d-d transition band at ~400 nm, while, functionalization with citrate resulted in appearance of two d-d transition bands at ~450 nm and ~500 nm.

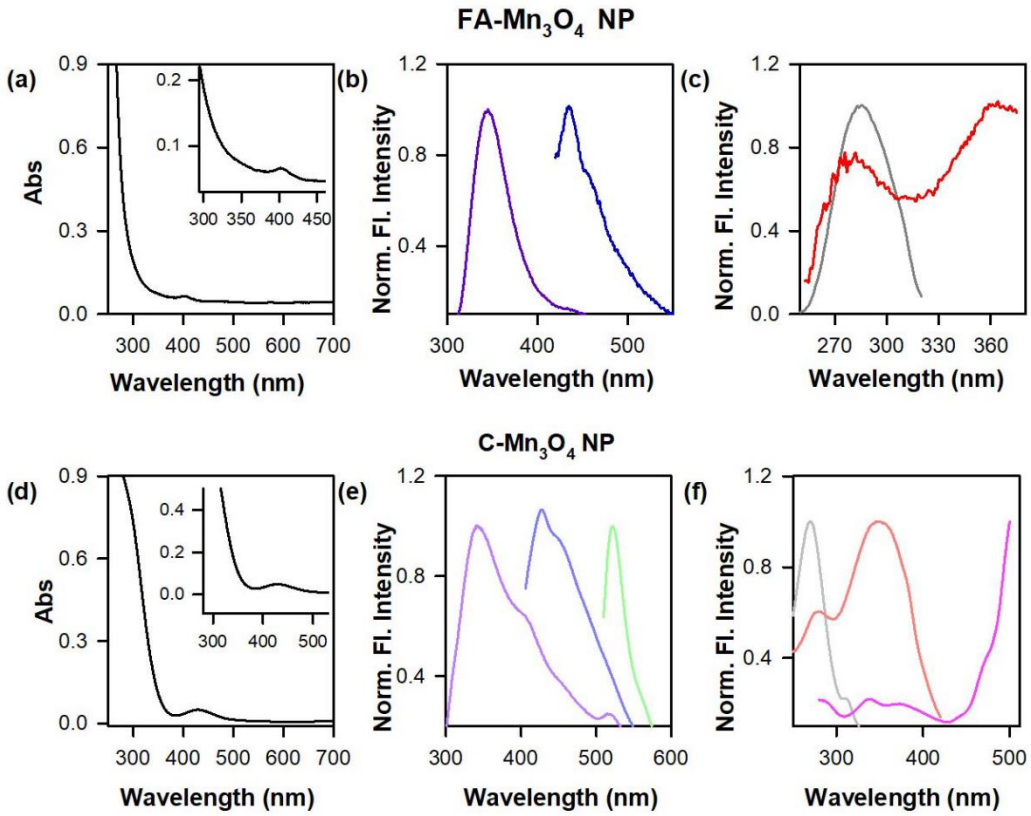

Figure 7.8: *Spectroscopic characterization of FA-Mn_3O_4 NPs and C-Mn_3O_4 NPs. (a) The absorption spectra of folate-capped NPs (FA-Mn_3O_4 NPs). A magnified version of the absorption spectrum of the NPs in the rage of 300–450 nm is shown in the inset. (b) The corresponding emission FA-Mn_3O_4 NPs. (c) The corresponding excitation spectra of FA-Mn_3O_4 NPs. (d) The absorption spectra of citrate-capped NPs (C-Mn_3O_4 NPs). A magnified version of the absorption spectrum of the NPs in the rage of 300–500 nm is shown in the inset. (e) The corresponding emission C-Mn_3O_4 NPs. (f) The corresponding excitation spectra of C-Mn_3O_4 NPs.*

The ~400 nm d-d band of FA-Mn_3O_4 NPs could be attributed to the degeneracy of ^5E_g ground state term of d^4 (Mn^{3+}) high-spin octahedral environment, which has been lifted by the Jahn–Teller effect, that ultimately leads to a tentative assignment of the observed band to the transitions $^5B_{1g} \rightarrow {}^5E_g$. The other possible low energy transitions e.g., $^5B_{1g} \rightarrow {}^5B_{2g}$, and $^5B_{1g} \rightarrow {}^5A_{1g}$ are not evident for FA-Mn_3O_4 NPs as previous studies have shown these transitions are more likely to take place only in presence of ligands having alpha hydroxy carboxylate groups [98]. Likewise, in C-Mn_3O_4 NPs, $^5B_{1g} \rightarrow {}^5E_g$ (450 nm) and low energy transition $^5B_{1g} \rightarrow {}^5B_{2g}$ (500 nm) are distinctly present

as citrate contains alpha hydroxy carboxylate groups. Emission spectra of both NPs suggested that both of them have multiple fluorescence (Figure 7.8.b; 7.8.e). FA-Mn_3O_4 NPs have emission in the UV and cyan regions (λ_{em}: 370 nm and 470 nm) when excited at 280 nm and 410 nm, respectively. In contrast, C-Mn_3O_4 NPs have distinct emissions in the UV, blue, cyan, and green region (λ_{em}: 380 nm, 440 nm, 480 nm, 550 nm) against excitation at different wavelengths (280 nm, 410 nm, 500 nm). For C-Mn_3O_4 NPs excitation spectra (Figure 7.8.f) indicates the presence of two LMCT bands (300 nm and 380 nm) and two d-d transition bands (400 nm and 500 nm) but in case of FA-Mn_3O_4 NPs (Figure 7.8.c) two LMCT (300 nm and 380 nm) and only one d-d transition (400 nm) were observed. Thus, it is evident from our studies that alteration in the functionalizing ligands significantly affected the optical properties of Mn_3O_4 NPs.

7.2.2.2. Effect of Functionalization on ROS Generation Ability: Next, we evaluated the effect of the functionalizing ligands on the ROS generation capability of Mn_3O_4 NPs. It is worth mentioning here that a plethora of studies have demonstrated that ROS generation by nanoparticles results in cellular oxidative stress which is one of the key underlying mechanisms of cytotoxicity [107]. Here, ROS generation by surface functionalized Mn_3O_4 NPs were measured with spectroscopic methods by monitoring the conversion of DCFH to DCF, a well-known ROS indicator. FA-Mn_3O_4 NPs did not generate ROS at room temperature (Figure 7.9.a) and the amount of ROS generated showed an upward trend with increase in temperature (till 37ºC). Interestingly, after 37ºC the amount of ROS generation became constant and did not increase with increasing temperature. In contrast, C-Mn_3O_4 NPs were able to generate ROS at room temperature and the amount of generated ROS was directly proportional to the temperature (Figure 7.9.b). In order to get further insight, we calculated the activation energies of ROS generation for both the NPs. From Figure 7.9.c it is evident that the activation energy was much higher in the case FA-Mn_3O_4 NPs compared to C-Mn_3O_4 NPs which explains the inability of FA-Mn_3O_4 NPs to generate room temperature ROS. From these results it can be hypothesised, in FA-Mn_3O_4 NPs some structural alterations were taking place at lower temperature (7ºC-37ºC) that facilitated the ROS generation. However, beyond 37ºC, the optimum structural features were perturbed

and as a result the amount of ROS generation did not increase with temperature and remained unaltered.

7.2.2.3. Consequence of Functionalization on the Charge Transfer: In order to further investigate the influence of different functionalizing agents in the observed temperature dependency of ROS generation ability of Mn_3O_4 NPs and to understand the underlying mechanism, we performed comprehensive computational studies with the optimised nanostructures of FA-Mn_3O_4 NPs and C-Mn_3O_4 NPs. DFT results showed that the citrate and folate binding with the Mn_3O_4 nanosurface occurs via the carboxylic oxygen.

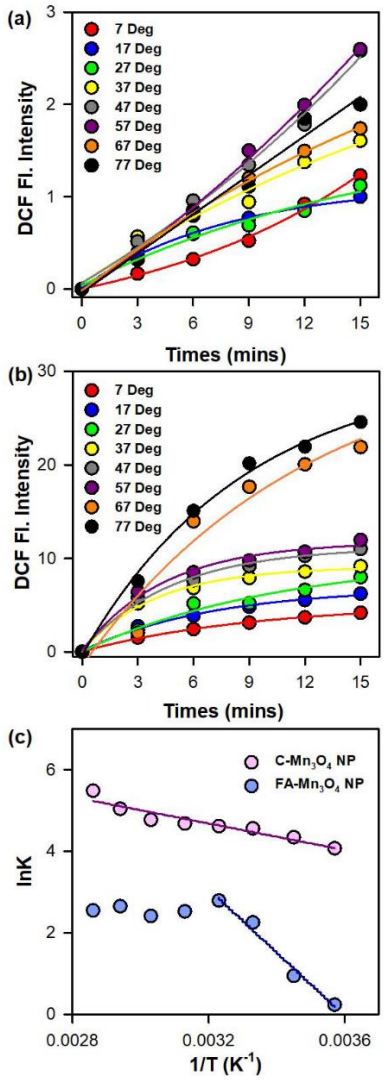

Figure 7.9: *Temperature dependent dark ROS generation ability of FA-Mn_3O_4 NP and C-Mn_3O_4 NP. (a and b) DCFH oxidation with respect to time in different temperature for FA-Mn_3O_4 NP and C-Mn_3O_4 NP respectively. (c) Activation energy plot of dark ROS generation for the respective nanohybrids.*

The carboxylic oxygen in the ligand (citrate and folate) form coordination bonds with the exposed Mn on the Mn_3O_4 nanosurface. Figure 7.10 showed the lowest energy binding conformations of citrate and folate on the nanosurface. Charge density difference plot shows the formation of coordination bonds and the extent of charge delocalization in citrate and folate bound structures. It is evident from the plots that charge delocalization occurs more in case of citrate (also observed in our spectroscopic studies). As citrate is more negatively charged than folate, charge transfer is higher in citrate.

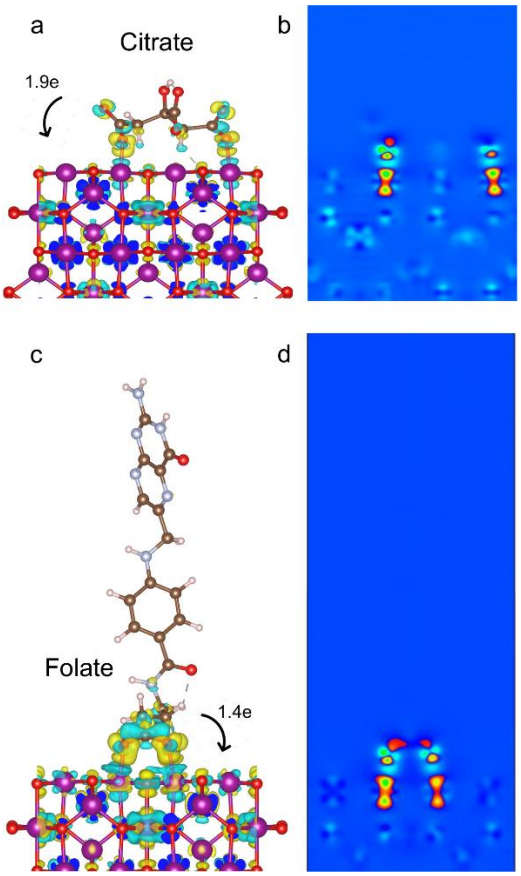

Figure 7.10: *Binding of Citrate and folate on Mn_3O_4 nano surface. (a) Citrate binding on the Mn_3O_4 nanosurface. Charge density difference is shown.(b) Density histogram showing the charge delocalization in citrate Mn_3O_4 complex. (c) Folate binding on the Mn_3O_4 nanosurface. Charge density difference is shown. (d) Density histogram showing the charge delocalization in folate Mn_3O_4 complex.*

Analysis of the (Mulliken) partial charges suggests that ground state charge transfer from citrate to a Mn(III) centre is 1.915e, whereas for folate bound through the carboxylic group the charge transfer is 1.443e. When the folate is bound only through the pteridine ring, the amount of charge transfer is 0.985e. This difference in charge transfer resulted in weaker LMCT band for FA-Mn_3O_4 NPs. Experimental

data points that charge transfer (i.e., the cause of ROS generation) in citrate is not temperature dependent, however, folate showed temperature dependency (Figure 7.9 a and 7.9.b).

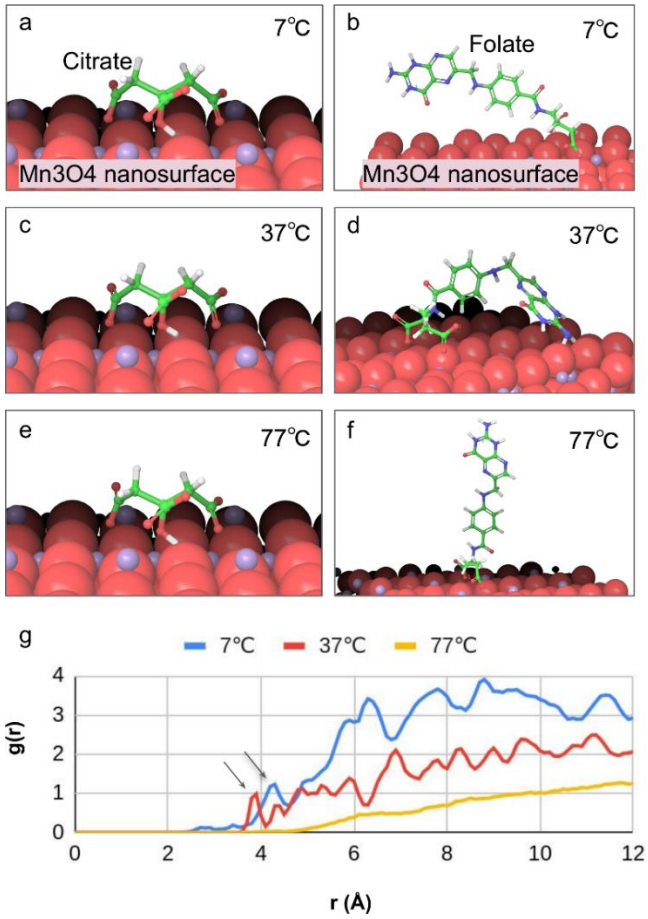

Figure 7.11: *Dynamics of citrate and folate on Mn_3O_4 nanosurface at different temperatures. (a,c,e) Most observed conformation of citrate on the Mn_3O_4 nanosurface at three different temperatures. (d,b,f) Most observed conformation of folate on the Mn_3O_4 nanosurface at three different temperatures. (g) Radial distribution function Mn centers from the pteridine ring of folate.*

To address that observation, we subjected the citrate and folate bound conformations to MD simulation at three different temperatures (7, 37 and 77 °C). Major conformations observed in MD are depicted in Figure 7.11. For citrate, the bound conformation remained stable at all the three different temperatures, however, the large side chain of folate showed increased fluctuations depending on the temperature. To probe how the pteridine ring of folate interacts with the nanosurface, radial distribution function (RDF) between the pteridine ring and Mn was calculated and is shown in Figure 7.11.g. RDF showed that at 37 °C the pteridine ring of folate comes closest to the surface giving rise to a peak at less than 4 Å increasing the probability of pi-electron transfer from the pteridine ring to the

nanoparticle. A hydrogen bonding via the terminal amine group of folate keeps the pteridine ring in position, thus, sharp peaks in the RDF plot are observed. At 7°C, as well, the pteridine ring comes close to the surface however, not as close as observed at 37°C. Due to the lack of stable hydrogen bonding, the fluctuation is more that resulting in broad peaks in the RDF plot. At 77 °C, folate showed large fluctuations and the pteridine ring came close to the nanosurface only very transiently and no peak was observed in the RDF plot (Figure 7.11.g). Therefore, at 37 °C, additional charge transfer becomes more favourable from folate to the nanoparticle via the pteridine ring. The results of the computational studies showed that for C- Mn_3O_4 NPs the charge transfer from ligand (citrate) to Mn (III) centre is higher, which makes it more reactive centre compared to the Mn(III) centre of FA-Mn_3O_4 NPs. Hence, in C-Mn_3O_4 NPs, the highly reactive Mn centres facilitates the ROS generation in room temperature and the charge distribution process is not hampered with increasing temperature. For FA-Mn_3O_4 NPs the computational results strongly supports the experimental findings. The less active Mn (III) centre is in FA-Mn_3O_4 NPs results in its inability to generate ROS at room temperature. Moreover, the charge distribution is highly temperature dependent as the structure fluctuates to a greater extent depending on the temperature. As evident from the computational results, the charge transfer from folate to Mn(III) centres is highest at 37ºC which makes the centre highly reactive (highest ROS generation). While, at higher temperature (77ºC) the centre is the least reactive as the charge transfer is lowest due to high fluctuation of pteridine ring. These results also demonstrate and explain the faster charge transfer at higher temperature for FA-Mn_3O_4 NPs. As the pteridine ring becomes more dynamic at higher temperature and the transition of electrons from excited state to ground state becomes faster. Interestingly, despite such loss of reactive centres, the experimental data showed that the amount of ROS generation by FA-Mn_3O_4 NPs at higher temperatures were almost similar to that of 37ºC. The probable reason behind this phenomenon is the increase in the kinetic energy of dissolved O_2, as previous studies have shown that generation of ROS by surface functionalized Mn_3O_4 NPs is greatly dependent upon its interaction with dissolved O_2. At higher temperature (77ºC) surplus O_2 comes in contact with the metal centres in comparison to lower temperature resulting in production of more ROS which in turn compensate the relative inactivity of Mn (III) centres. In contrast, both the

structural integrity and the lifetime of excited state electrons in C-Mn_3O_4 NPs remain constant and the increased kinetic energy of dissolved O_2 together with highly active Mn(III) centres result in the observed increase in ROS generation with temperature. In order to support our theoretical findings about the temperature dependent structural variabilities of the two differently functionalized NPs, we have measured the pico-second resolved fluorescence transient for both the NPs at different temperatures using an excitation source of 375 nm.

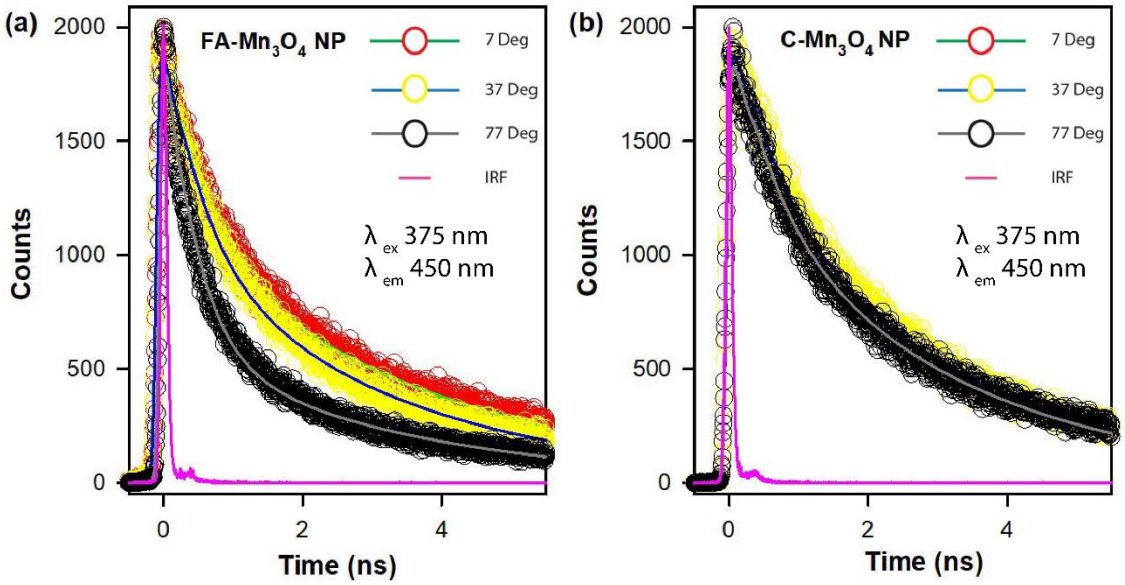

Figure 7.12. *Temperature dependent picosecond resolved fluorescence transients of the nanohybrids. (a) Lifetime of the FA-Mn_3O_4 NP in different temperature. (b) Lifetime of the C-Mn_3O_4 NP in different temperature.*

Figure 7.12.a indicated temperature dependent decrease in lifetime of FA-Mn_3O_4 NPs suggesting the charge transfer process from folate to the Mn^{2+}/Mn^{3+} of nanosurface to become faster with increasing temperature. In contrast, the lifetime of C-Mn_3O_4 NPs remain similar at all temperatures. Therefore, the charge transfer process in C-Mn_3O_4 NPs didn't show any temperature dependence (Figure 7.12.b), which corroborates our *in silico* predictions. Thus, the pico-second resolved study data also suggest the appearance of structural fluctuations in the FA-Mn_3O_4 NPs with increasing temperature.

7.2.2.4. Anti-microbial Activity of the NPs: We evaluated the implications of the ligand dependent variations in the physico-chemical properties of differently functionalized Mn_3O_4 NPs on their toxicity effect. We used *S. hominis*, a gram

Table 7.3: *Fitted Decay Time Constants of FA-Mn_3O_4 NPs and C-Mn_3O_4 NPs from Picosecond Experiments. (Values in Parentheses Represent the Relative Weight Percentage of the Time Components.)*

System	Temperature (^{0}C)	Excitation wavelength (λ_{ex})	Emission wavelength (λ_{em})	τ_1(ps)	τ_2(ps)
FA-Mn_3O_4 NP	7	375 nm	450 nm	520 (48)	3584 (52)
	37			520 (52)	3106 (48)
	77			415.20 (73)	3249.90 (26.9)
C-Mn_3O_4 NP	7	375nm	450 nm	564.70 (34.6)	3024.40 (65.3)
	37			564.70 (34.6)	3024.40 (65.3)
	77			564.70 (34.6)	3024.40 (65.3)

bacteria as the model biological system [53]. *S. hominis*, were incubated with both the FA-Mn_3O_4 NPs and C-Mn_3O_4 NPs for 2 hours in LB broth and then stained with DAPI and PI. While, DAPI stains all the cells in the medium, PI is specific to the dead cells as it cannot cross the intact cell membrane. So the ratio of DAPI stained cells to PI stained cells reveals the viability of the cells. Figure 7.13 shows the results of the microbial studies. Figure 7.13.a(i)-7.13.a(iii) are the microscopic images of control cells after staining with DAPI and PI. As expected, here the number of viable cells was more than the dead cells (ratio ~ 1.7). The microscopic images of FA-Mn_3O_4 NPs (Figure 7.13.b(i)-7.13.b(iii)) incubated bacteria showed an inverse ratio i.e. dead cells were more in numbers than the live cells (ratio ~ 0.36). Interestingly, the group of bacteria treated with C-Mn_3O_4 NPs (Figure 7.13.c(i)-7.13.c(iii)) showed higher viability as compared to FA-Mn_3O_4 NPs treated bacteria. The ratio for this C-Mn_3O_4 NP-treated group was similar to the control group (ratio ~ 1.3). Therefore, the microscopic studies revealed that the FA-Mn_3O_4 NPs exerted toxic effects and effectively killed *S. hominis*, whereas the C-Mn_3O_4 NPs did not show any cytotoxic effect towards *S. hominis*.

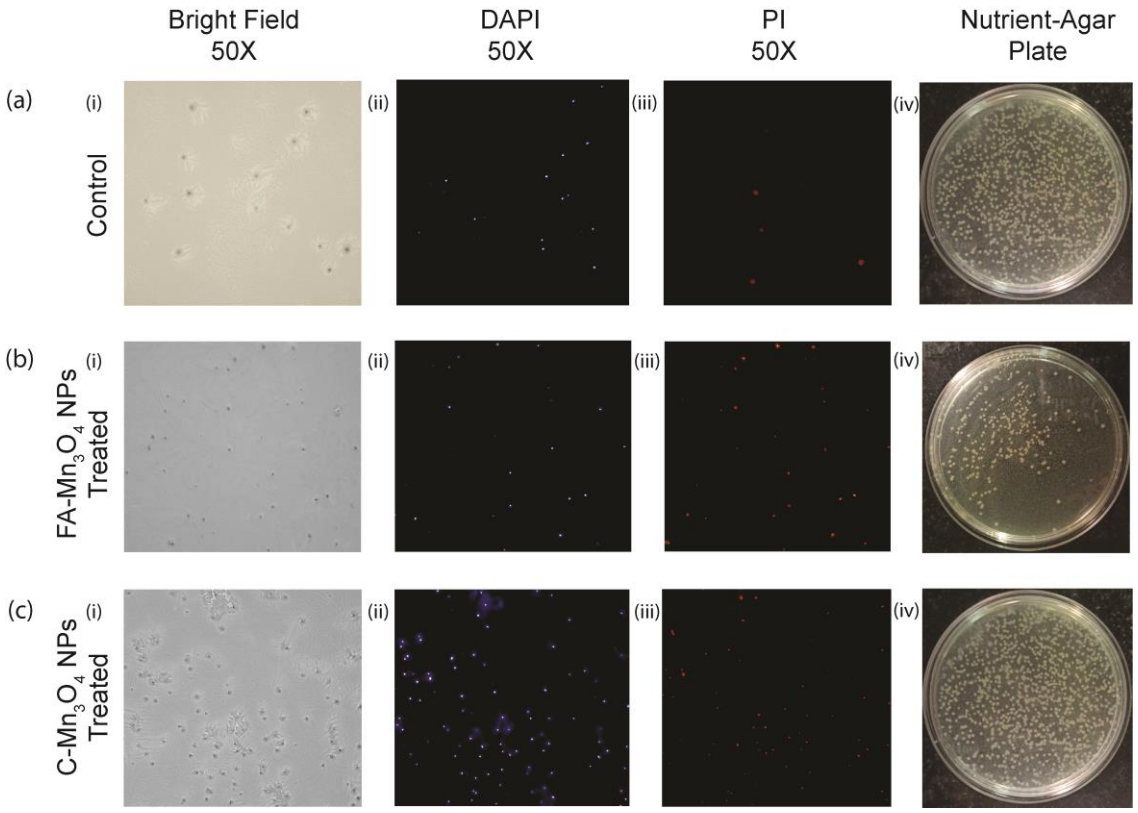

Figure 7.13: *Antibacterial activities of FA-Mn_3O_4 and C-Mn_3O_4 nanoparticles on S. hominis. (a) Control (b) FA-Mn_3O_4 treated. (c) C-Mn_3O_4 Treated. (i) are bright field microscopic images. (ii) are fluorescence micrographs of bacteria stained with DAPI. (iii) are fluorescence micrographs of bacteria stained with PI. (iv) Agar-plate colony count assay.*

To confirm the findings of the microscopic studies we performed plate count assay. *S. hominis* (in LB broth) incubated with FA-Mn_3O_4 NPs and C-Mn_3O_4 NPs for 2 hours 37ºC and then transferred to LB agar plate and incubated for 24 hours (37ºC). As shown in Figure 7.13.a(iv)-7.13.c(iv), the maximum decrease in bacterial colony count was observed for FA-Mn_3O_4 NPs. The viable colony count for FA-Mn_3O_4 NP-treated bacteria was 2.8×10^7 CFU/mL which is 72% lower compared to the number of viable colonies in control group (1.02×10^8 CFU/mL) and 60.56% lower compared to the C-Mn_3O_4 NP-treated group (7.1×10^7 CFU/mL). From both the studies, it is clear that the FA-Mn_3O_4 NPs exerted more toxic effect on *S. hominis* than C-Mn_3O_4 NPs. The findings further suggest that though the chemical core composition for the two NPs is same, their cytotoxic property is completely poles apart probably due to the contrasting features originated from the structural dissimilarities of the surface functionalizing ligands. However, the results of the cytotoxicity studies conflict with the ROS generation characteristics of the NPs described in earlier section. Considering the higher ROS generation ability of C-

Mn_3O_4 NPs, it was expected that it would exhibit greater cytotoxicity in comparison to the FA-Mn_3O_4 NPs. But in reality the opposite happened. One possible explanation of the huge cytotoxic effect shown by FA-Mn_3O_4 NPs can be drawn from difference in the hydrophobicity of Mn_3O_4 NPs generated due to the nature of the functionalizing ligands. From Figure 7.6.e and 7.7.e it is evident that FA-Mn_3O_4 NPs is much more hydrophobic than C-Mn_3O_4 NPs. Earlier studies have demonstrated that hydrophobic particles are readily engulfed by the hydrophobic cell membranes ('Film-tension model'), while the hydrophilic particles tends to go to cytosol by means of phagocytosis or active transport across the membrane [108].

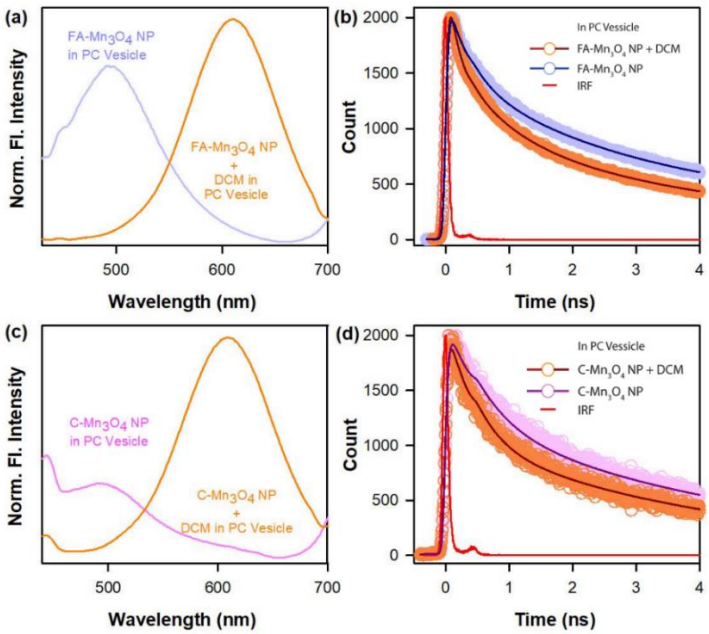

Figure 7.1: *FRET Study. (a) Steady state fluorescence spectra of FA-Mn_3O_4 (donor) in PC vesicle in the absence and presence of DCM (acceptor). (b) Picosecond-resolved PL transients of FA- Mn_3O_4 NPs (donor) in PC vesicle in the absence and presence of DCM (acceptor). (c) Steady state fluorescence spectra of C-Mn_3O_4 (donor) in PC vesicle in the absence and presence of DCM (acceptor). (d) Picosecond-resolved PL transients of C- Mn_3O_4 NPs (donor) in PC vesicle in the absence and presence of DCM (acceptor).*

As FA-Mn_3O_4 NPs are more hydrophobic in nature, it can easily be translocated to the bacterial cell wall via interaction with constituent hydrophobic peptidoglycans of the wall. Moreover, as the ROS generation gets activated at physiological temperature, the effective killing of bacterial cells takes place once the NPs enter through bacterial cell wall. The highly dense population of NPs in the cells results to a pleotropic effect in ROS generation. In contrast, the C-Mn_3O_4 NPs cannot readily translocate to the membrane as it is hydrophilic in nature, rather internalized in the

cytosol at relatively lower concentrations. Moreover, in cytosol the cellular antioxidant defence system plays a greater role to protect the cells from oxidative damages. Together these factors, result in lower ROS generation by C-Mn_3O_4 NPs yielding lesser cytotoxicity.

Different translocations of the NPs (either cytosol or cell membrane) became further evident from the measurements of fluorescence resonance energy transfer efficiency (FRET) from NPs as a donor to DCM (4-(dicyanomethylene)-2-methyl-6-(4-dimethylaminostyryl)-4H-pyran) as an acceptor in phosphatidylcholine lipid (PC) vesicles since PC lipid vesicles resemble most closely a biological cell membrane. Generally, DCM stays in the hydrophobic hydrocarbon chain of the liposomal bilayer of the PC lipid vesicles [109]. NPs translocation towards hydrophobic hydrocarbon chain of the lipid vesicles became evident from the measurements of the energy transfer efficiency from NPs (donor) to DCM (acceptor) and from the calculation of distance distributions between donor-acceptor pair in PC lipid vesicles. In the study of Forster resonance energy transfer (FRET) DCM was chosen as an acceptor because, NPs fluorescence spectrum overlaps reasonably well with the absorption spectrum of the DCM in lipid vesicles (Figure 7.14). Time-resolved decay profile of NPs in phospholipid vesicles in absence and in presence of DCM clearly indicates the possibility of energy transfer from NPs to DCM. The energy transfer efficiency from NPs to DCM in PC lipid vesicles was found to be more efficient for FA-Mn_3O_4/DCM (~42%) relative to (~23.6%) in lipid vesicles (Table 7.4). As a consequence of that, donor-acceptor distances varied from 28.8Å to 37.2Å for FA-Mn_3O_4 and C-Mn_3O_4/DCM respectively. Thus, molecular recognition of

Table 7.4: *FRET parameter in PC vesicles.*

System	**τ_{DA} (ns)**	**τ_D (ns)**	**E(%)**	**J(λ)/$M^{-1}cm^{-1}nm^4$**	**R_0/Å**	**r/Å**
FA-Mn_3O_4 NP in PC vesicle+DCM	2.10	3.60	42	$1.41X10^{15}$	27.30	28.80
C-Mn_3O_4 NP in PC vesicle+DCM	2.10	2.70	23.6	$2.90X10^{15}$	30.60	37.20

DCM by NPs in PC lipid vesicles is relatively less efficient for C-Mn_3O_4 NPs, which, however became more efficient for FA-Mn_3O_4 NPs. Together the microbial and FRET studies suggest the possibility of strong hydrophobic interactions of FA-Mn_3O_4 NPs with the bacterial cell membrane lipids might have resulted in their accumulation and ROS burst, leading to the peroxidation of the membrane lipids and eventually cytotoxicity.

7.2.2.5. X-ray Contrast of the NPs: Then we explored the diagnostic property of the two functionalized NPs. We have used X-ray imaging technique as a diagnostic tool. The X-ray imaging depends on the absorption or scattering of photons by the sample when collimated X-ray beam penetrates (I_0) it. The resultant X-ray intensity reduced to I, which can be expressed as:[110]

$$I=I_0 e^{\frac{-x\mu}{\rho}} \quad (7.1)$$

Where I_0 is the initial intensity of the X-ray beam, x denotes the thickness of the sample, μ is the linear X-ray attenuation coefficient (cm^{-1}) of sample, ρ is the material density (gm/cm^3).

To evaluate the theranostic ability of both the NPs we have used X-ray imaging technique. From Figure 7.15.a it is clear that both the NPs can be used as X-ray contrast agent due to their X-ray opaque nature. The opacification of FA-Mn_3O_4 NPs is greater than that of C-Mn_3O_4 NPs (Figure 7.15.b). So it can be stated from the X-Ray images that FA-Mn_3O_4 NPs can be a better X-ray contrast agent than C-Mn_3O_4 NPs. DLS study can give us some insight on the reason for this differential X-ray contrast. As it is evident from the DLS (Figure 7.15.c) that FA-Mn_3O_4 NPs tends to aggregate when present in solution (hydrodynamic diameter ~ 293 nm) so the bulk density increase in case of FA-Mn_3O_4 NPs compared to C-Mn_3O_4 NPs (hydrodynamic diameter ~ 19 nm). As shown in equation 7.1 the resultant X-ray intensity will increase if the bulk density of the sample is increased. So from the outcome of the above studies it can be concluded that functionalization can modify the therapeutic potential, diagnostic property and most importantly toxicity of the NPs. The NPs functionalized with hydrophobic ligand, i.e., FA-Mn_3O_4 NPs will be

better theranostic anti-microbial agent against bacterial infection compared to C-Mn_3O_4 NPs.

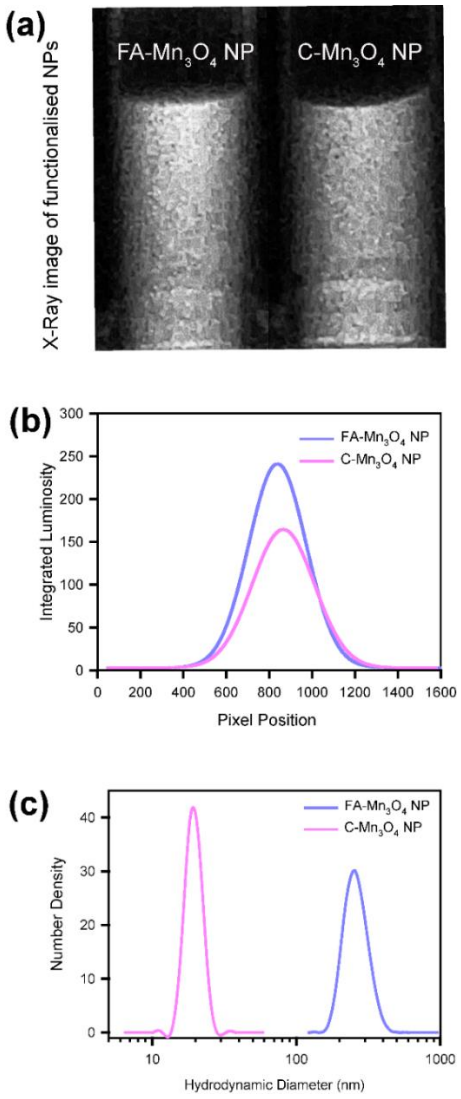

Figure 7.15: *X-ray imaging. (a) X-ray image of FA-Mn_3O_4 NPs (Left) and C-Mn_3O_4 NPs (right). (b) Quantification of X-ray integrated luminosity of FA-Mn_3O_4 NPs and C-Mn_3O_4 NPs. (c) Hydrodynamic study of FA-Mn_3O_4 NPs and C-Mn_3O_4 NPs measured by DLS.*

Regarding the biocompatibility of the both NPs, we have explored the toxicity of these NPs in our previous studies and found that the toxicity is negligible [4, 52, 97, 106, 111].

7.2.3. Functionalised Two Dimension Carbon Nitride Nanodots Detect and Reverse Lead Toxicity In The Physiological Milieu [112]: Figure 7.16.a and 7.16.b represent the TEM images of the polymeric graphitic Carbon Nitride NS (g-C_3N_4 NS) samples before and after citrate capping. Before citrate capping, the existence of

g-C_3N_4 as 2D NS can be clearly observed in Figure 7.16.a. The wrinkles and folding at the edges confirm the formation of few layered g-C_3N_4 NS. Earlier researchers have observed that polycondensation in g-C_3N_4 improves with increase in pyrolysis temperature. Thus, to achieve better polycondestaion and complete removal of constituent sulphur, the pyorlysis temperature was kept at 620ºC [113-115]. The TEM image of the g-C_3N_4 nanosheets shows the presence of holes that results from the formation of vacancies due to pyrolysis. On the other hand, the ultra-small dot like regions [marked in red circles in Figure 7.16.b] indicate the formation of g-C_3N_4 nanostructures as a result of citrate mediated etching of 2D NS. The morphology of the nanodot structure can be expressed as 2D circles. Since the starting material is 2D g-C_3N_4 nanosheets, the etched out portions will have a circular shape with flat surfaces. Additionally the dot structure exhibit significant surface properties as a result of surface functionalization rather than the bulk properties like spherical nanostructures.

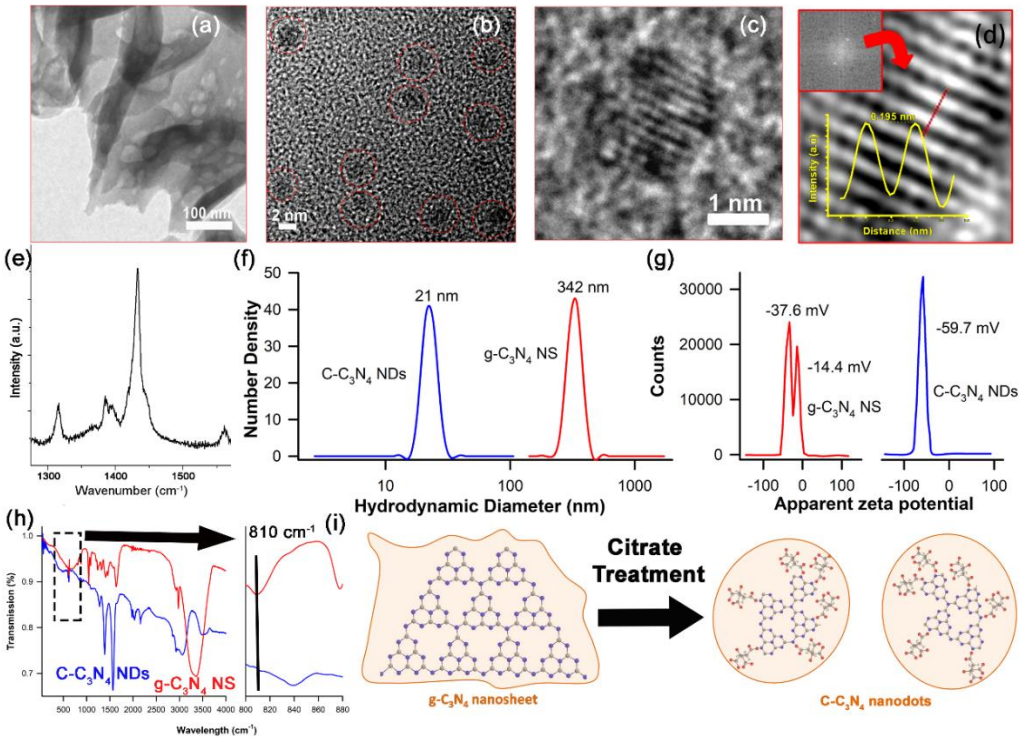

Figure 7.16: *Characterisation of Citrate capped carbon nitride nanodots (C-C_3N_4 NDs). (a) Distribution of NS in TEM. (b) Circular nanodots are marked in TEM. (c) HR-TEM of a single C-C_3N_4 ND. (d) Fringe distance of C-C_3N_4 ND. (e) Raman Spectrum of C-C_3N_4 NDs. (f) DLS of g-C_3N_4 Ns and C-C_3N_4 NDs. (g) Zeta potential of g-C_3N_4 Ns and C-C_3N_4 NDs. (h) FTIR spectrum of g-C_3N_4 NS and C-C_3N_4 NDs. (i) Schematic of synthesis of C-C_3N_4 NDs from precursor g-C_3N_4 Ns through citrate treatment.*

The average size of the NDs is estimated to be ~3.5 nm. Further, the HRTEM of a single ND reveals the existence of the lattice fringes of g-C_3N_4 (Figure 7.16.c). The bright spots in the Fast Fourier Transformation (FFT) of the particular dot (Figure 7.16.d) and the lattice spacing calculated from the reconstruction of inverse FFT indicate the lattice spacing to be ~0.19 ±.005 nm. It may be noted that such a lattice spacing has been reported for N-doped Graphene quantum dots (N-GQDs) and thus indicates the microstructural similarity between citrate capped C-C_3N_4 NSs and N-GQDs [57].

Further, the micro-Raman spectra (Figure 7.16.e) captured on the ND samples indicate the various vibrational modes corresponding to g-C_3N_4 configuration. The peak at 1316 cm^{-1} indicates the vibration due to semi-circle stretching (E') of heptazine ring [57]. Again, the peaks at 1385 and 1432 cm^{-1} correspond to the CN breathing mode ($A1'$), while the vibration due to ring stretching can be located at ~1560 cm^{-1} [60]. It can be noted that these aforementioned peaks are slightly shifted to the lower wavenumber region compared to the values for g-C_3N_4 NSs. This observation indicates the variation in vibrational features as a result of lowered conjugation of C-N network due to the fragmentation from sheet to dot like morphology. Further, this fragmentation process has been verified from dynamic light scattering studies of the samples. The hydrodynamic radius of the bare NS is estimated to be ~ 342 nm, while that of the citrate functionalised C_3N_4 NDs is found to be ~ 21 nm (Figure 7.16.f) and supports the event of fragmentation of the sheets to dots. Now the attachment of the citrate ions on the surface of the NDs can be determined from the apparent zeta potential measurements. The dots are characterized by a higher zeta potential compared to the sheets and can be assigned to the negative charges contributed by the surface attached citrate ions (Figure 7.16.g). The presence of two peaks in the zeta potential of the g- C_3N_4 NSs is due to the different zeta potential for the edge and the surface of the 2D materials. In the FTIR Spectrum (Figure 7.16.h) for pure g-C_3N_4 nanosheets the peak at 810 cm^{-1} indicates the characteristics absorption of triazine unit, while the absorption features ranging from 1200 cm^{-1} to 1700 cm^{-1} correspond to the stretching mode of CN heterocycles [58]. It can be seen that the peak associated to absorption of triazine unit is shifted to higher frequency region and thus indicates the modification in vibrational features due to the attachment of citrate ions with triazine units. Again,

the slight deformation in the vibrational features related to CN heterocycles indicates the deformation of these structural units as a result of etching out of the larger nanosheet. Further, the appearance of the strong peak at~1575 cm^{-1} indictaes the formation of an N-O bond in the citrate capped samples [116-118]. Therefore, the oxygen of the carboxy group present in citrate possibly forms a covalent bond with the terminal N of triazine unit. Formation of coordinate covalent bond between N and O is unlikely due to the dense electron cloud around the carboxy group and triazine unit. Further, the generation of intensed vibrational peaks within 2900-3100 cm^{-1}, denotes carboxylic acid O-H Stretching [119].

The additional OH may have originated from the unbound carboxyl group of citrate ions, which confirms the presence of citrate in the functionalised material. The formation of nanodots from 2D nanosheet has been shown in Figure 7.16.i. The XPS study of g- C_3N_4 NSs (Figure 7.17) confirms the presence of nitrogen and carbon. The presence of oxygen in the nanosheet may be due to the surface of absorption of oxygen or from the water that was used in the time of synthesis. Also no presence of Sulfur has been detected in the XPS study (inset, Figure 7.17).

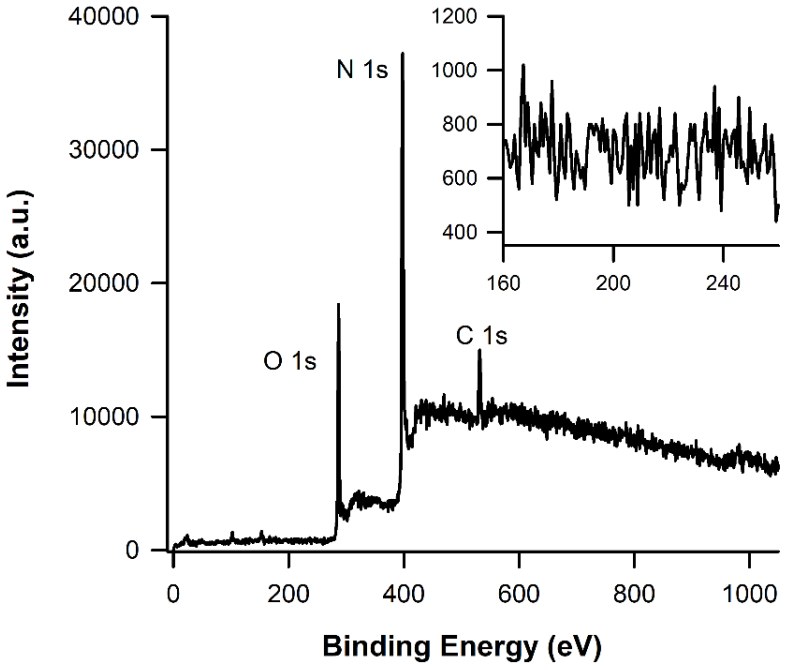

Figure 7.17: *XPS study of g-C_3N_4 NS confirms the presence of nitrogen and carbon in the in the as prepared nanosheet.*

The influence of citrate attachment on the surface of the dots can also be realized in terms of absorption and emission spectroscopy techniques. In general, g-C_3N_4 shows

an absorption peak at ~ 380 nm due to a π-π* transition, while the δ-δ* transition related peak is observed at ~ 325 nm (Figure 7.18.a) [120]. In addition, the contribution of lone pair related n-π* transition can be observed in a relatively higher position beyond 400 nm [120]. However, the overlapping of the π-π* and n-π* related absorption features leads to a broad absorption peak. The absorption characteristics of the bare NS as shown in Figure 7.18.a, show a similar trend. In contrast to that, in the absorption spectrum for the dots, the π-π* transition related absorption peak can be seen with a blue-shift leading to the distinct evolution of absorption peak at ~ 426 nm. The evolution of this peak can be assigned to the creation of electronic states within the highest occupied molecular orbitals (HOMO) and lowest unoccupied molecular orbitals (LUMO) bands of g-C_3N_4 due to the attachment of citrate ions. Further, the photoluminescence spectra of the samples confirm this inference of modification in the electronic states. As shown in Figure 7.18.b, the fluorescence spectra (excitation at 280 nm) of the bare NS and citrate treated ND shows a significant difference. In bare NS, the peak positioned at ~351 nm originates due to the transitions from δ* states to n or π states, while the transitions from π* to n or π states give rise to an emission peak at ~439 nm [120]. It is worth mentioning that, in bare C_3N_4 NS, the partial overlapping of π* and δ* states leads to significant electron transfer from δ* states to π* states. Consequently, the photoexcited electron concentration gets lowered in δ* states, leading to a suppressed emission at ~351 nm compared to emission at ~439 nm. Now in the dot like structures, the fluorescence spectrum is relatively broad where the emission peak at ~370 nm is found to be prominent while the peak at ~435 nm is missing. It can be expected that the introduction of new electronic states disrupts the path for electron relaxation from δ* states to π* states and hence the emission due to π* to n or π transitions are missing. Following that the asymmetrically stretched emission peak can be split into two peaks through deconvolution. The two peaks can be assigned to the radiative transition from δ* states to n or π states via the citrate induced electronic states. Next, to ensure the presence of additional states, photoluminescence excitation spectra have been recorded with emission wavelength as 375 nm (Figure 7.18.c). It can be observed that the spectrum for bare g-C_3N_4 NS shows a peak at ~ 275 nm which corresponds to the δ-δ* related transition. On the other hand, the emission peak at ~ 282 nm for the dots indicates the transition from δ to additional states lying below

δ* states. Further, excitation with 320 nm light (Figure 7.18.d), the excitation spectrum of bare g-C_3N_4 NS is dominant by the π* to n or π transitions (emission peak at ~ 439 nm), while the spectrum of the dots is contributed by the emission involving the citrate induced electronic states (peaking at ~ 423 nm). Further for bare g-C_3N_4 NS, the excitation spectrum with emission 435 nm (Figure 7.18.e), reveals the presence of a continuous band like feature and indicates the transition to an overlapping position of π* and δ* states.

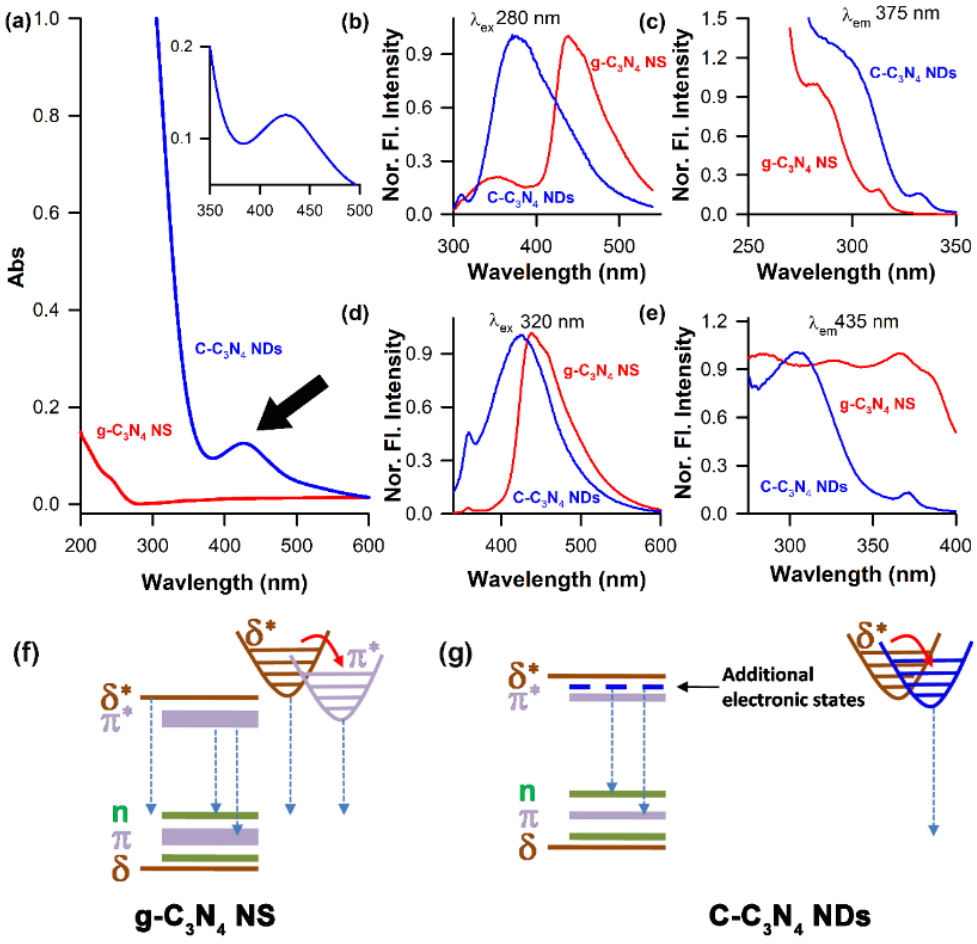

Figure 7.18: *Optical Characterization of C-C_3N_4 NDs. (a) Comparative absorbance between g-C_3N_4 NS and C-C_3N_4 NDs. (b) Comparative emission spectra of g-C_3N_4 Ns and C-C_3N_4 NDs, excited at 280nm. (c) Comparative excitation spectra of g-C_3N_4 Ns and C-C_3N_4 NDs, emission at 375nm. (d) Comparative emission spectra of g-C_3N_4 Ns and C-C_3N_4 NDs, excited at 320nm. (e) Comparative excitation spectra of g-C_3N_4 Ns and C-C_3N_4 NDs, emission at 435nm. (f) Electronic configuration of g-C_3N_4 NS. (g) Electronic configuration of C-C_3N_4 NDs.*

On the contrary, for dots the firm distinct peak at ~305 nm indicates the transition up to the additional electronic states lying below δ* states and thus confirms the role of citrate in modification of the electronic structure of g-C_3N_4 NS. The probable

transition of electrons for g-C_3N_4 NS and C-C_3N_4 NDs are depicted in Figure 7.18.f and 7.18.g.

Next, the ROS generation property of the C- C_3N_4 NDs was evaluated using DCFH. In the presence of ROS the non-fluorescent DCFH is converted to fluorescent DCF that has a strong emission at 520 nm (λ_{ex} 480 nm). From Figure 7.19.a and 7.19.b, it is evident that DCF intensity in the case of the dot like structures are higher compared to bare g-C_3N_4 NS, indicating that the C-C_3N_4 NDs have acquired the ability to generate reactive oxygen species (ROS) at room temperature. This ROS generation ability can be assigned to an increment in the surface charge of the dots upon citrate attachment. In general several functional groups like H, OH, etc remain adsorbed on the g-C_3N_4 NS originating from the precursor and processing solvents. In particular, H remains attached on the terminating N creating NH- groups.

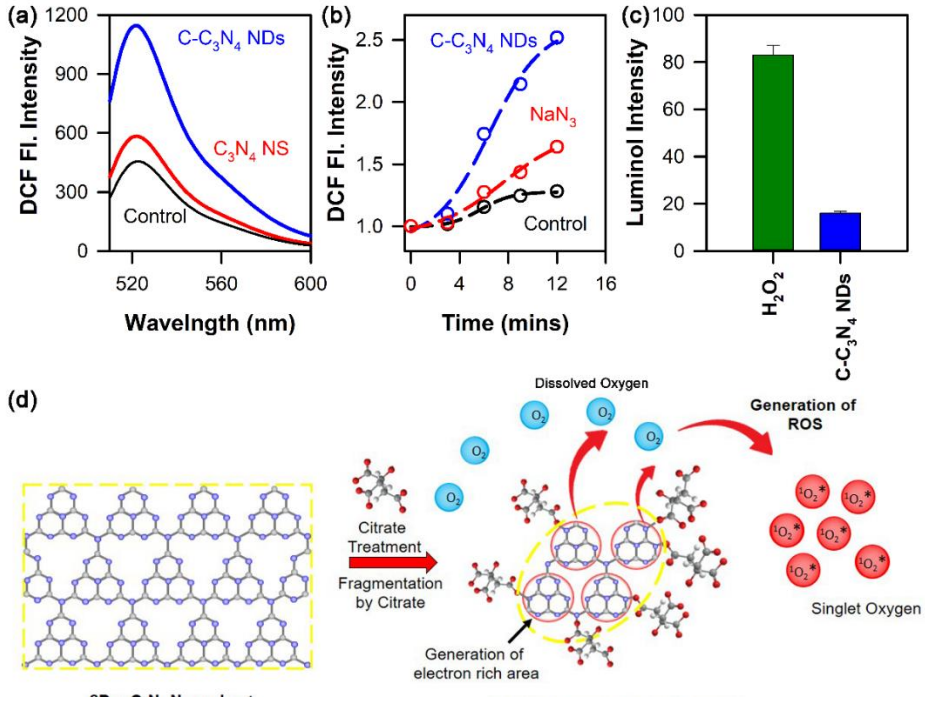

Figure 7.19: *ROS Generation ability. (a) Emission of DCF after addition of g-C_3N_4 NS and C-C_3N_4 NDs. (b) Rate of DCF production after addition of C-C_3N_4 NDs and NaN_3. (c) Chemiluminescence study for spotential superoxide generation. (d) Schematic representation of ROS generation mechanism.*

However, the fragmentation by citrate ions leads to the detachment of terminal NH-groups, which result in the evolution of a structure with a large number of unsaturated bonds i.e., dangling bonds. Thus the increment in unsaturated bonds and also the presence of negatively charged carboxy group results in the increase in the electron density. So, the non-bonded electrons will reacts with the dissolved

oxygen of the reaction medium and lead to the formation of higher content of oxygen radical. To evaluate the class of ROS, we have used sodium azide (NaN_3), a well-known singlet oxygen quencher [106]. From Figure 7.19.b it is clear that the addition of NaN_3 lowers the amount of ROS generated by C-C_3N_4 NDs. So, C-C_3N_4 NDs predominantly generate singlet oxygen. Involvement of superoxide has been examined using a chemiluminescence assay [106, 121]. Figure 7.19.c indicates that when added to luminol (in presence of NaOH), the C-C_3N_4 NDs generate a very nominal amount of superoxide. So, the possibility of superoxide generation by C-C_3N_4 NDs can be excluded from Figure 7.19.c.

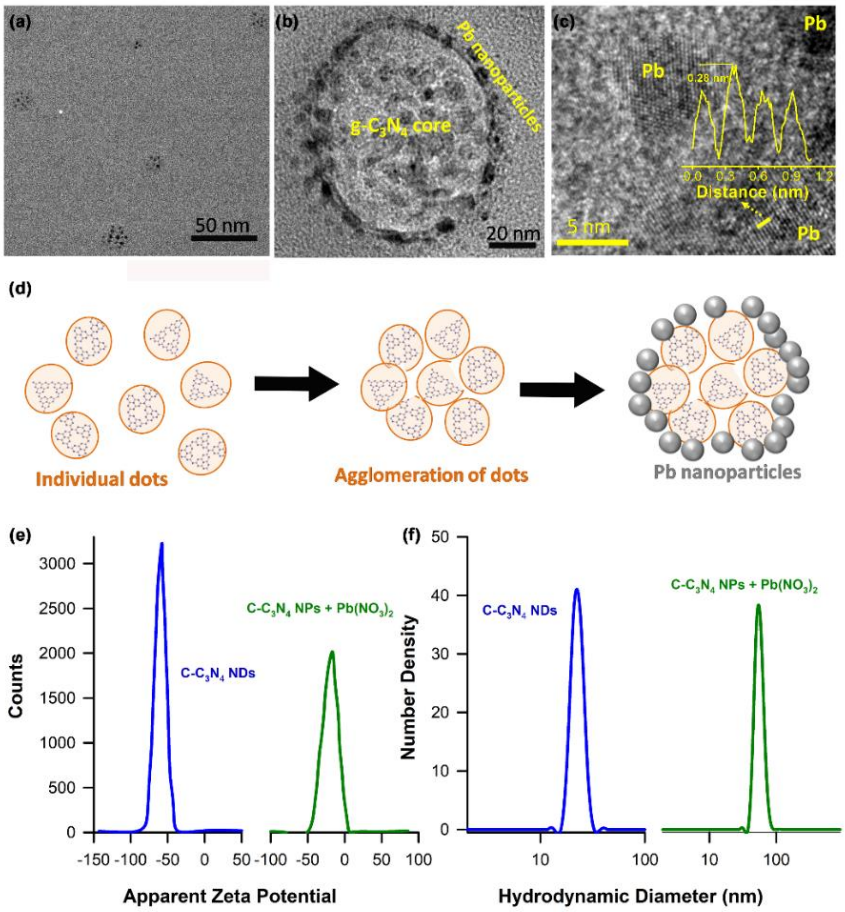

Figure 7.20: *Characterization of C-C_3N_4 NDs-Pb(II) complex. (a) Distribution of C-C_3N_4 NDs-Pb(II) complex. (b) Microscopic images of C-C_3N_4 NDs-Pb(II) complex. (c) HRTEM of C-C_3N_4 NDs-Pb(II) complex. (d) Schematic for C-C_3N_4 NDs-Pb(II) complex formation. (e) Zeta potential of C-C_3N_4 NDs and C-C_3N_4 NDs-Pb(II) complex. (f) DLS for C-C_3N_4 NDs and C-C_3N_4 NDs-Pb(II) complex.*

Figure 7.20.a represents the TEM image of the dots treated with lead nitrate [$Pb(NO_3)_2$,36 mM] which depicts the formation of circular features with an assembly of nanoparticles. A close look at such assembly, reveals that the C-C_3N_4 NDs are

agglomerated at the core, while Pb(II) nanoparticles are situated on the outer circumference of the agglomerated dots in a circular fashion (Figure 7.20.b). Further HRTEM image of the Pb interacting with citrate capped CN nanodots has been included. The distinct grains of the nanostrcutures and the interpnar spacing of ~ 0.28 nm indicates the (111) plane of cubic phased Pb and thus confirms the formation of Pb nanoparticles (Figure 7.20.c) [122]. It is expected that with time the individual dots agglomerate to reduce their surface energy maintaining an adequate surface charge on the circumference of the assembly. The positively charged ions can be reduced on the surface of such assembly and thus lead to the formation of Pb(II) nanoparticles. The right shift in zeta potential (Figure 7.20.e) suggests increase in positive charge due to the interaction with Pb(II). The comparison in hydrodynamic diameter for C-C_3N_4 NDs and C-C_3N_4 NDs-Pb(II) complex reveal that the size has increased from ~10nm to ~100 nm after the complex formation (Figure 7.20.f). Furthermore, the intimate contact of the Pb(II) and C-C_3N_4 NDs has been verified by spectroscopic techniques. Figure 7.21.a shows the UV-Visible absorption spectra of the dots treated with different amounts of Pb(II) precursor. As can be seen in the Figure 7.21.a, the MLCT band related to Pb(II) at ~300 nm becomes prominent with an increment in Pb(II) concentration. From the absorbance study, the binding constant for C-C_3N_4 NDs and Pb(II) complex formation (K_b= 0.155X10^2 M^{-1}) has been determined using Benesi–Hildebrand equation (Equation 7.2).

$$\log\frac{A-A_0}{A_f-A_0} = \log[Pb^{2+}] + logK_b \qquad (7.2)$$

The inset of Figure 7.21.a is indicating the Benesi–Hildebrand plot for the interaction of C-C_3N_4 NDs and Pb(II). Where, A_0, A, and A_f are the initial (without Pb(II)), intermediate (with Pb(II)) and final absorbance (with saturated amount of Pb(II)) at 300 nm respectively. However, the PL spectra (Figure 7.21.b) show a continual reduction in PL intensity of emission band 424 nm (λ_{ex} 375 nm) with increment in Pb(II) concentration. This fluorescence quenching can be attributed due to various reasons like molecular rearrangements, ground-state complex formation, energy transfer, excited-state reactions, collisional quenching etc [123]. For C-C_3N_4 NDs, there is no shift in the emission spectra, and the after careful analysis it was found that the quenching behaviour is following the Stren-Volmer equation (S-V) (Equation 7.3)

$$\frac{F_0}{F} - 1 = K_{SV}[Q] = K_q \tau_0 [Q] = \frac{\tau_0}{\tau} - 1 \qquad (7.3)$$

Here F indicates the fluorescence intensity in presence of quencher, and F_0 is the fluorescence intensity in the absence of quencher. [Q] denotes the quencher concentration, K_{SV} is known as the SV quenching constant, k_q is the bimolecular quenching rate constant, τ_0 refers to the fluorescence lifetime of fluorophore in the absence of quencher while τ is the fluorescence lifetime of fluorophore in the presence of quencher. The linearity of the S-V plot (K_{SV}=0.21X10^2 M^{-1}) (Figure 7.21.c) states that the quenching is a single type of quenching, either static or dynamic [124].

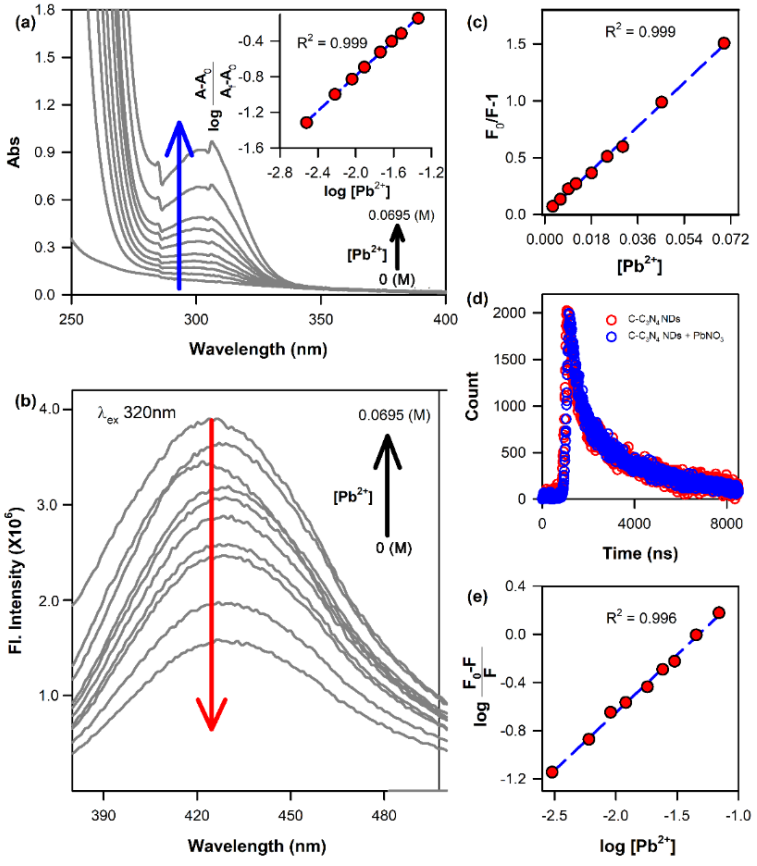

Figure 7.21: *Interaction of C-C_3N_4 NDs with Pb(II). (a) Absorbance of C-C_3N_4 NDs with addition of increasing concentration of $Pb(NO_3)_2$ (0 to 6.95X10^{-2} M). Inset shows the Benesi-Hildebrand plot for the determination of binding constant. (b) Fluorescence spectra of C-C_3N_4 NDs with addition of increasing concentration of $Pb(NO_3)_2$ (0 to 6.95X10^{-2} M). (c) Stren-Volmer(S-V) Plot. (d) Lifetime of C-C_3N_4 NDs in the presence and absence of Pb(II). (e) Modified Stern-Volmer plot.*

To, figure out the type of quenching, the C-C_3N_4 NDs and Pb(II) treated C- C_3N_4 NDs were subjected to pico-second resolved lifetime analysis. From Figure 7.21.d it is eminent that the lifetimes of C-C_3N_4 NDs before and after Pb(II) treatment show

no significant change (Table 7.5), indicating that the quenching is static in nature [121, 123]. The value of biomolecular constant ($K_q=K_{SV}/\tau_0$) was estimated to be $0.629X10^{11}$ $M^{-1}S^{-1}$, which is higher than diffusion control rate (10^{10} $M^{-1}S^{-1}$). The value of K_q along with lifetime data confirming the static nature of the quenching. Figure 7.21e depicts the double logarithmic plot (Equation 7.4). Using the equation 7.3 the association constant (K_a) has been found to be 0.159 X 10^2 M^{-1}(similar with the K_b value found from absorbance study) and the number of binding site (n=0.96) was calculated.

$$log\frac{F_0-F}{F} = \log K_a + nlog[Q] \quad (7.4)$$

Therefore the luminescence quenching effect indicates the intimate contact of C-C_3N_4 NDs with Pb(II) and confirms the event of reduction of Pb(II) ions through negatively charged C-C_3N_4 NDs.

So, in short we have started with a 2D nanosheet of g-C_3N_4 (~342 nm) and using the reducing agent, citrate we have successfully formed a water soluble nanodots (~21 nm). The presence of negatively charged carboxy group in the nonadots can interact with the positively charged Pb(II) that can lead to the elimination of that harmful ions from the medium.

Table 7.5: *Decay Time Constants of C-C_3N_4 NDs and C-C_3N_4 NDs with Pb(II) from Picosecond Experiments.*

System	τ_1(ps)	τ_2 (ps)	A_1(%)	A_2 (%)	τ_{avg} (ps)
C-C_3N_4 NDs	60	2480	88.6	11.3	340
C-C_3N_4 NDs + Pb(II)	60	2440	87.9	12.1	340

Next, the ability of C-C_3N_4 NDs to ameliorate the Pb and Pb assisted damages in physiological milieu has been evaluated using hemolysis assay. Heparinised venous blood from human has been collected to carry out the hemolysis assay. Figure 7.22.a.i depicts the microscopic image of RBC after Pb(II) treatment for 30 minutes.The microscopic image shows significant shrinkage and distortion of the structure of RBC due to Pb(II) treatment. However, upon treating RBCs with Pb(II) and C- C_3N_4 NDs, no significant shrinkage or distortion of RBCs has been found (Figure 7.22.a.ii).

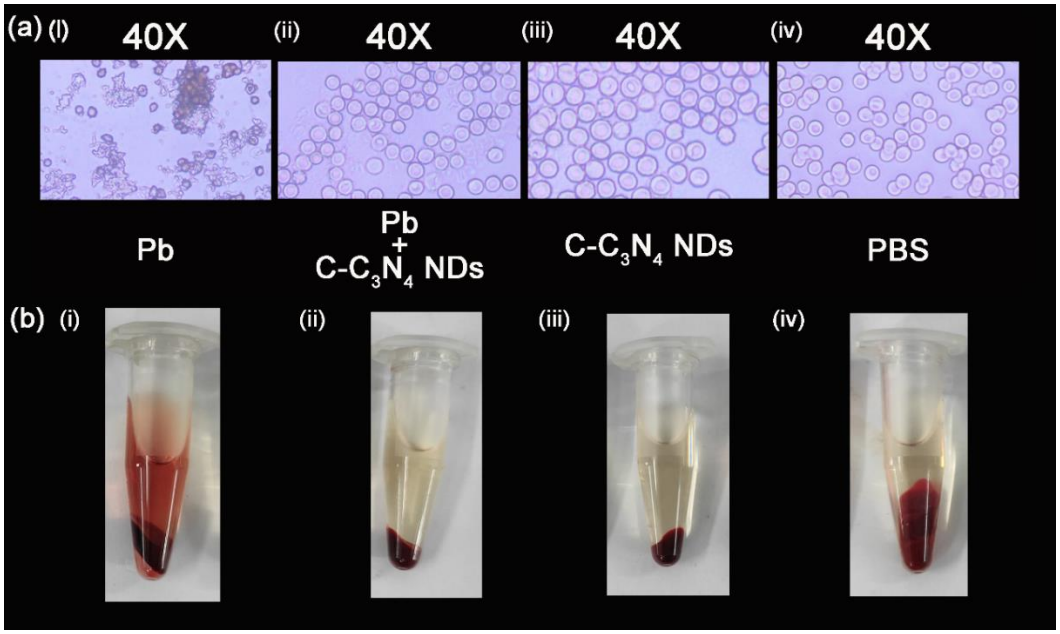

Figure 7.22: *Haemolysis Study. (a) (i-iv) Microscopic images of RBCs of respective treatment group. (b) (i-iv) Image of whole blood of respective treatment group after 30 minutes.*

The structure of co-treated RBCs is similar to that of PBS treated group (Figure 7.22.a.ii and Figure 7.22.a.iv). Recent studies have shown that Pb(II) accelerates the generation of ROS (i.e. superoxide, singlet oxygen, hydroperoxides, hydrogen peroxide) that leads to the oxidative damage of the biological entities [77, 81, 125]. Hence, from these two microscopic images (Figure 7.22.a.i and 7.22.a.ii), it can be ensured that the C-C_3N_4 NDs are effective to protect the RBCs against the Pb(II) and its oxidation associated damages. From Figure 7.22.a.iii, it is evident that the set of RBCs treated with C- C_3N_4 NDs maintains their structural integrity, indicating the bio-compatible nature of C-C_3N_4 NDs. As already mentioned, the C-C_3N_4 NDs has the potential to generate room temperature ROS. In fact these ROS leads to the passivation of the Pb(II) induced oxidative damages (Figure 7.22.a.ii) and maintain the RBCs in an oxidative eustress condition [94, 95, 126].

7.3. Conclusion:

In summary, our study demonstrates that C-Mn_3O_4 NPs can be a potential theranostic agent against hyperbilirubinemia and related diseases. The spectroscopic studies reveal that C-Mn_3O_4 NPs directly degrade unconjugated bilirubin and convert it to a relatively non-toxic product MVM. The pico-second resolved study and the Langmuir-Hinshelwood study demonstrates that the ROS dependent degradation of bilirubin by C-Mn_3O_4 NPs rather than surface mediated catalysis.

These studies altogether suggested that C-Mn_3O_4 NPs is an effective therapeutic solution for hyperbilirubinemia and associated diseases. The linear sweep voltammetry and the chronoamperometry measurements indicate that utilization of C-Mn_3O_4 NPs as an electrochemical probe can formulate a unique and cost beneficiary technology for bilirubin detection. The inability of the C-Mn_3O_4 NPs to detect and degrade the bilirubin when complexed with HSA depicts the selectivity of the nano probe towards the unconjugated bilirubin. Overall, this study unveiled a potent and multifunctional nanohybrid that can be easily packaged into a unique, cost-effective, and facile theranostic tool against hyperbilirubinemia and related diseases.

The second study demonstrates that the nature of the surface functionalizing ligand greatly influences the interaction of the nanomaterial with biological systems and determines its biocompatibility and cytotoxicity. The combined spectroscopic and computational studies for the first time shows that the interaction between surface functionalizing ligands and the nanomaterial significantly alters the activation energy of the ROS generation ability of the nanomaterial. The microbial studies depicts the hydrophobicity (ligand) dependent translocation of nanomaterials in the membrane or cytosol and downstream cytotoxic outcomes due to the pleotropic effect of differential distribution and ROS generation ability. Therefore, many properties of nanoparticles (optical characteristics, structural stability, chemical properties and most importantly the interaction with biological system) depend on the nature of the surface functionalizing ligands. Thus, surface functionalization is one of the most important factors that needed to be considered in the time of synthesis of nanomaterials for biological use. We have also shown that the FA-Mn_3O_4 NPs offer better X-ray contrast compared to that of the C-Mn_3O_4 NPs for their lower zeta potential leading to self-aggregation of the FA-Mn_3O_4 NPs. The FA-Mn_3O_4 NPS are shown to offer PDT effect in cellular milieu [106]. A functionalised NP can enter inside a bacterial cell (*S. Hominis*) and offers X-ray contrast. The intruded NPs can simultaneously generate reactive oxygen species inside the cells for bacterial remediation. It has to be noted that the class of NP used in this study has also been employed as X-ray induced radical generators for cancer treatment [18, 127]. Thus, a synergistic effect of ROS and X-ray induced free radical is expected to accelerate bacterial remediation. The work is under progress in our group. We are

currently also exploring the effect of these NPs on Gram negative bacteria. Overall our studies indicate that FA-Mn_3O_4 NPs are a potential theranostic agent for dual-mode targeting, X-ray imaging, and antimicrobial therapy.

Next, the study regarding the carbon based organic nanoparticle reports a newly developed, bio-compatible polymeric carbon nitride two dimensional (2D) nanomaterial (i.e. citrate functionalized C_3N_4 nanodots) out of two dimensional (2D) graphitic carbon nitride (g-C_3N_4) nanosheets. The comprehensive microscopic and spectroscopic characterisation indicate the synthesis of the bio-compatible nanomaterial with citrate capping, and this synthesis leads to the development of a new physiological, chemical and optical properties. It has found to be that the newly developed 2D nanodots interacts with heavy metal such as Pb and chelate this bivalent cation. The spectroscopic study on the interaction of C-C_3N_4 NDs and Pb(II) suggests that this NDs form a complex with a single Pb(II) with an association constant of $0.159X10^2$ M^{-1}. The change in the spectrum due to the complex formation is an effective detection method of Pb(II) in a reaction medium. This complex formation results in the elimination of Pb(II) from physiological milieu. Further, it also ameliorates the Pb induced oxidative damages to red blood cells through ROS generation and maintains the eustress of the cellular environment. Overall the present study demonstrates that citrate functionalized C_3N_4 nanodots (synthesized from two dimensional (2D) graphitic carbon nitride (g-C_3N_4) nanosheets) are bio-compatible and have the potential to ameliorate the lead toxicity.

Reference:

[1] F. Chen, E.B. Ehlerding, W. Cai, Theranostic nanoparticles, *J. Nucl. Med.*, 55 (2014) 1919.

[2] X. Ma, Y. Zhao, X.-J. Liang, Theranostic Nanoparticles Engineered for Clinic and Pharmaceutics, *Acc. Chem. Res.*, 44 (2011) 1114.

[3] S. Mondal, R. Ghosh, A. Adhikari, U. Pal, D. Mukherjee, P. Biswas, S. Darbar, S. Singh, S. Bose, T. Saha-Dasgupta, In vitro and microbiological assay of functionalized hybrid nanomaterials to validate their efficacy in nanotheranostics: A combined spectroscopic and computational study, *ChemMedChem*, 16 (2021) 3739.

[4] A. Adhikari, S. Mondal, M. Das, P. Biswas, U. Pal, S. Darbar, S.S. Bhattacharya, D. Pal, T. Saha-Dasgupta, A.K. Das, Incorporation of a biocompatible nanozyme in cellular antioxidant enzyme cascade reverses huntington's like disorder in preclinical model, *Adv. Healthc. Mater.*, 10 (2021) 2001736.

[5] S. Mondal, A. Adhikari, M. Das, S. Darbar, A. Alharbi, S.A. Ahmed, S.S. Bhattacharya, D. Pal, S.K. Pal, Novel one pot synthesis and spectroscopic characterization of a folate-Mn_3O_4 nanohybrid for potential photodynamic therapeutic application, *RSC Adv.*, 9 (2019) 30216.

[6] Z. Shen, T. Chen, X. Ma, W. Ren, Z. Zhou, G. Zhu, A. Zhang, Y. Liu, J. Song, Z. Li, Multifunctional theranostic nanoparticles based on exceedingly small magnetic iron oxide nanoparticles for T 1-weighted magnetic resonance imaging and chemotherapy, *ACS nano*, 11 (2017) 10992.

[7] S.M. Dadfar, K. Roemhild, N.I. Drude, S. von Stillfried, R. Knüchel, F. Kiessling, T. Lammers, Iron oxide nanoparticles: Diagnostic, therapeutic and theranostic applications, *Adv. Drug Deliv. Rev.*, 138 (2019) 302.

[8] J. Xie, J. Huang, X. Li, S. Sun, X. Chen, Iron oxide nanoparticle platform for biomedical applications, *Curr. Med. Chem.*, 16 (2009) 1278.

[9] R. Nandi, S. Mishra, T.K. Maji, K. Manna, P. Kar, S. Banerjee, S. Dutta, S. Sharma, P. Lemmens, K.D. Saha, A novel nanohybrid for cancer theranostics: Folate sensitized Fe_2O_3 nanoparticles for colorectal cancer diagnosis and photodynamic therapy, *J. Mater. Chem. B*, 5 (2017) 3927.

[10] E. Alphandéry, Iron oxide nanoparticles for therapeutic applications, *Drug Discov. Today*, 25 (2020) 141.

[11] R. Mazgaj, P. Lipiński, M. Szudzik, A. Jończy, Z. Kopeć, A.M. Stankiewicz, M. Kamyczek, D. Swinkels, B. Żelazowska, R.R. Starzyński, Comparative evaluation of sucrosomial iron and iron oxide nanoparticles as oral supplements in iron deficiency anemia in piglets, *Int. J. Mol. Sci.*, 22 (2021) 9930.

[12] L.G. Remsen, C.I. McCormick, S. Roman-Goldstein, G. Nilaver, R. Weissleder, A. Bogdanov, I. Hellström, R. Kroll, E. Neuwelt, MR of carcinoma-specific monoclonal antibody conjugated to monocrystalline iron oxide nanoparticles: The potential for noninvasive diagnosis, *AJNR Am J Neuroradiol.*, 17 (1996) 411.

[13] S. Khoei, S.R. Mahdavi, H. Fakhimikabir, A. Shakeri-Zadeh, A. Hashemian, The role of iron oxide nanoparticles in the radiosensitization of human prostate carcinoma cell line DU145 at megavoltage radiation energies, Int. J. Radiat. Biol., 90 (2014) 351.

[14] F. Xiong, H. Wang, Y. Feng, Y. Li, X. Hua, X. Pang, S. Zhang, L. Song, Y. Zhang, N. Gu, Cardioprotective activity of iron oxide nanoparticles, *Sci. Rep.*, 5 (2015) 8579.

[15] S. Mondal, R. Ghosh, A. Adhikari, U. Pal, D. Mukherjee, P. Biswas, S. Darbar, S. Singh, S. Bose, T. Saha-Dasgupta, S.K. Pal, In vitro and microbiological assay of functionalized hybrid nanomaterials to validate their efficacy in nanotheranostics: A combined spectroscopic and computational study, *ChemMedChem*, 16 (2021) 3739.

[16] A. Adhikari, S. Mondal, T. Chatterjee, M. Das, P. Biswas, R. Ghosh, S. Darbar, H. Alessa, J.T. Althakafy, A. Sayqal, Redox nanomedicine ameliorates chronic kidney disease (CKD) by mitochondrial reconditioning in mice, *Commun. Biol.*, 4 (2021) 1013.

[17] A. Adhikari, S. Mondal, S. Darbar, S. Kumar Pal, Role of nanomedicine in redox mediated healing at molecular level, *Biomol. Concepts*, 10 (2019) 160.

[18] M.H. Cho, E.-S. Choi, S. Kim, S.-H. Goh, Y. Choi, Redox-responsive manganese dioxide nanoparticles for enhanced MR imaging and radiotherapy of lung cancer, *Front. Chem.*, 5 (2017) 109.

[19] H. Yang, Y. Zhuang, H. Hu, X. Du, C. Zhang, X. Shi, H. Wu, S. Yang, Silica-coated manganese oxide nanoparticles as a platform for targeted magnetic resonance and fluorescence imaging of cancer cells, *Adv. Funct. Mater.*, 20 (2010) 1733.

[20] C. Shao, S. Li, W. Gu, N. Gong, J. Zhang, N. Chen, X. Shi, L. Ye, Multifunctional gadolinium-doped manganese carbonate nanoparticles for targeted MR/fluorescence imaging of tiny brain gliomas, *Anal. Chem.*, 87 (2015) 6251.
[21] A. Kalakonda, B.A. Jenkins, S. John, Physiology, bilirubin, *StatPearls,* St. Petersburg 2017.
[22] G.J. Maghzal, M.-C. Leck, E. Collinson, C. Li, R. Stocker, Limited role for the bilirubin-biliverdin redox amplification cycle in the cellular antioxidant protection by biliverdin reductase, *J. Biol. Chem.*, 284 (2009) 29251.
[23] L.C. Mireles, M.A. Lum, P.A. Dennery, Antioxidant and cytotoxic effects of bilirubin on neonatal erythrocytes, *Pediatr. Res.*, 45 (1999) 355.
[24] J. Kapitulnik, Bilirubin: An endogenous product of heme degradation with both cytotoxic and cytoprotective properties, *Mol. Pharmacol.*, 66 (2004) 773.
[25] N. Polley, S. Saha, A. Adhikari, S. Banerjee, S. Darbar, S. Das, S.K. Pal, Safe and symptomatic medicinal use of surface-functionalized Mn_3O_4 nanoparticles for hyperbilirubinemia treatment in mice, *Nanomedicine (Lond).* 10 (2015) 2349.
[26] R. Harb, D.W. Thomas, Conjugated hyperbilirubinemia: Screening and treatment in older infants and children, *Pediatr. Rev.*, 28 (2007) 83.
[27] M.-A. Mahtab, Liver: A complete book on hepato-pancreato-biliary diseases-e-book, *Elsevier Health Sciences,* Amsterdam, 2009.
[28] S.M. Shapiro, Chronic bilirubin encephalopathy: diagnosis and outcome, in: Seminars in Fetal and Neonatal Medicine, *Elsevier,* Amsterdam, 2010, pp. 157.
[29] G. Inamori, U. Kamoto, F. Nakamura, Y. Isoda, A. Uozumi, R. Matsuda, M. Shimamura, Y. Okubo, S. Ito, H. Ota, Neonatal wearable device for colorimetry-based real-time detection of jaundice with simultaneous sensing of vitals, *Sci. Adv.*, 7 (2021) eabe3793.
[30] P.A. Dennery, D.S. Seidman, D.K. Stevenson, Neonatal hyperbilirubinemia, *N. Engl. J. Med.*, 344 (2001) 581.
[31] C. Van der Veere, M. Sinaasappel, A.F. McDonagh, P. Rosenthal, P. Labrune, M. Odievre, J. Fevery, J. Otte, P. McClean, G. Bürk, Current therapy for Crigler-Najjar syndrome type 1: Report of a world registry, *Hepatol.*, 24 (1996) 311.
[32] B. Xia, G. Zhang, F. Zhang, Bilirubin removal by Cibacron Blue F3GA attached nylon-based hydrophilic affinity membrane, *J. Membr. Sci.*, 226 (2003) 9.

[33] A. Halder, A. Adhikari, R. Ghosh, S. Singh, A. Banerjee, N. Ghosh, A.M. Bhattacharya, S. Mandal, P. Chakrabarti, D. Bhattacharyya, Large scale validation of a new non-invasive and non-contact bilirubinometer in neonates with risk factors, *Sci. Rep.*, 10 (2020) 11149.

[34] J. Davies, D. Davies, Origins and evolution of antibiotic resistance, *Microbiol. Mol. Biol. Rev.*, 74 (2010) 417.

[35] P. Liu, L.Q. Xu, G. Xu, D. Pranantyo, K.-G. Neoh, E.-T. Kang, pH-sensitive theranostic nanoparticles for targeting bacteria with fluorescence imaging and dual-modal antimicrobial therapy, *ACS Appl. Nano Mater.*, 1 (2018) 6187.

[36] R.J. Worthington, C. Melander, Combination approaches to combat multidrug-resistant bacteria, *Trends Biotechnol.*, 31 (2013) 177.

[37] M. Vaillancourt, P. Jorth, The unrecognized threat of secondary bacterial infections with COVID-19, *MBio.*, 11 (2020) e01806.

[38] E. Sharifipour, S. Shams, M. Esmkhani, J. Khodadadi, R. Fotouhi-Ardakani, A. Koohpaei, Z. Doosti, S. Ej Golzari, Evaluation of bacterial co-infections of the respiratory tract in COVID-19 patients admitted to ICU, *BMC Infect. Dis.*, 20 (2020) 1.

[39] J.S. Kim, E. Kuk, K.N. Yu, J.-H. Kim, S.J. Park, H.J. Lee, S.H. Kim, Y.K. Park, Y.H. Park, C.-Y. Hwang, Y.-K. Kim, Y.-S. Lee, D.H. Jeong, M.-H. Cho, Antimicrobial effects of silver nanoparticles, *Nanomed.: Nanotechnol. Biol. Med.*, 3 (2007) 95.

[40] G. Ren, D. Hu, E.W.C. Cheng, M.A. Vargas-Reus, P. Reip, R.P. Allaker, Characterisation of copper oxide nanoparticles for antimicrobial applications, *Int. J. Antimicrob. Agents*, 33 (2009) 587.

[41] S.A. Ahmed, M. Nur Hasan, D. Bagchi, H.M. Altass, M. Morad, I.I. Althagafi, A.M. Hameed, A. Sayqal, A.E.R.S. Khder, B.H. Asghar, H.A. Katouah, S.K. Pal, Nano-MOFs as targeted drug delivery agents to combat antibiotic-resistant bacterial infections, *Royal Soc. Open Sci.*, 7 (2020) 200959.

[42] J.T. Seil, T.J. Webster, Antimicrobial applications of nanotechnology: Methods and literature, *Int. J. Nanomedicine.*, (2012) 2767.

[43] A.M. Allahverdiyev, K.V. Kon, E.S. Abamor, M. Bagirova, M. Rafailovich, Coping with antibiotic resistance: Combining nanoparticles with antibiotics and other antimicrobial agents, *Expert. Rev. Anti. Infect. Ther.*, 9 (2011) 1035.

[44] M.A. Zoroddu, S. Medici, A. Ledda, V.M. Nurchi, J.I. Lachowicz, M. Peana, Toxicity of nanoparticles, *Curr. Med. Chem*, 21 (2014) 3837.
[45] S.E. McNeil, Nanotechnology for the biologist, *J. Leukoc. Biol.*, 78 (2005) 585.
[46] A.E. Nel, L. Mädler, D. Velegol, T. Xia, E.M.V. Hoek, P. Somasundaran, F. Klaessig, V. Castranova, M. Thompson, Understanding biophysicochemical interactions at the nano–bio interface, *Nat. Mater.*, 8 (2009) 543.
[47] A. Sasidharan, L.S. Panchakarla, P. Chandran, D. Menon, S. Nair, C.N.R. Rao, M. Koyakutty, Differential nano-bio interactions and toxicity effects of pristine versus functionalized graphene, *Nanoscale*, 3 (2011) 2461.
[48] A. Nel, T. Xia, L. Mädler, N. Li, Toxic potential of materials at the nanolevel, *Science*, 311 (2006) 622.
[49] R.R. Mercer, J. Scabilloni, L. Wang, E. Kisin, A.R. Murray, D. Schwegler-Berry, A.A. Shvedova, V. Castranova, Alteration of deposition pattern and pulmonary response as a result of improved dispersion of aspirated single-walled carbon nanotubes in a mouse model, Am. J. Physiol. - Lung Cell. Mol. Physiol., 294 (2008) L87.
[50] A. Bekdemir, S. Liao, F. Stellacci, On the effect of ligand shell heterogeneity on nanoparticle/protein binding thermodynamics, *Colloids Surf. B: Biointerfaces*, 174 (2019) 367.
[51] A. Giri, N. Goswami, C. Sasmal, N. Polley, D. Majumdar, S. Sarkar, S.N. Bandyopadhyay, A. Singha, S.K. Pal, Unprecedented catalytic activity of mn_3o_4 nanoparticles: Potential lead of a sustainable therapeutic agent for hyperbilirubinemia, *RSC Adv.*, 4 (2014) 5075.
[52] A. Adhikari, N. Polley, S. Darbar, D. Bagchi, S.K. Pal, Citrate functionalized Mn_3O_4 in nanotherapy of hepatic fibrosis by oral administration, *Future Sci. OA*, 2 (2016) FSO146.
[53] A.M. Schneider, A.M. Nelson, Skin microbiota: Friend or foe in pediatric skin health and skin disease, *Pediatr. Dermatol.*, 36 (2019) 815.
[54] F. Chaves, M. García-Álvarez, F. Sanz, C. Alba, J.R. Otero, Nosocomial spread of a *Staphylococcus hominis* subsp. n*ovobiosepticus* strain causing sepsis in a neonatal intensive care unit, *J. Clin. Microbiol.*, 43 (2005) 4877.
[55] J. Yang, L.-S. Tang, R.-Y. Bao, L. Bai, Z.-Y. Liu, B.-H. Xie, M.-B. Yang, W. Yang, Hybrid network structure of boron nitride and graphene oxide in shape-

stabilized composite phase change materials with enhanced thermal conductivity and light-to-electric energy conversion capability, *Sol. Energy Mater Sol. Cells.*, 174 (2018) 56.

[56] S. Yu, L. Zhao, R. Liu, C. Zhang, H. Zheng, Y. Sun, L. Li, Performance enhancement of Cu-based AZO multilayer thin films via graphene fence engineering for organic solar cells, *Sol. Energy Mater Sol. Cells.*, 183 (2018) 66.

[57] R. Das, K.K. Paul, P.K. Giri, Highly sensitive and selective label-free detection of dopamine in human serum based on nitrogen-doped graphene quantum dots decorated on Au nanoparticles: Mechanistic insights through microscopic and spectroscopic studies, *Appl. Surf. Sci.*, 490 (2019) 318.

[58] S. Bayan, N. Gogurla, A. Midya, S.K. Ray, White light emission characteristics of two dimensional graphitic carbon nitride and ZnO nanorod hybrid heterojunctions, *Carbon*, 108 (2016) 335.

[59] J. Zhu, P. Xiao, H. Li, S.A.C. Carabineiro, Graphitic carbon nitride: Synthesis, properties, and applications in catalysis, *ACS Appl. Mater. Interfaces.*, 6 (2014) 16449.

[60] Y. Yuan, L. Zhang, J. Xing, M.I.B. Utama, X. Lu, K. Du, Y. Li, X. Hu, S. Wang, A. Genç, R. Dunin-Borkowski, J. Arbiol, Q. Xiong, High-yield synthesis and optical properties of g-C_3N_4, *Nanoscale*, 7 (2015) 12343.

[61] J. Barrio, S. Barzilai, N. Karjule, P. Amo-Ochoa, F. Zamora, M. Shalom, Fluorescent carbon nitride macrostructures derived from triazine-based cocrystals, *Adv. Opt. Mater.*, 9 (2021) 2100683.

[62] C. Yang, K. Folens, G. Du Laing, F. Artizzu, R. Van Deun, Improved quantum yield and excellent luminescence stability of europium-incorporated polymeric hydrogen-bonded heptazine frameworks due to an efficient hydrogen-bonding effect, *Adv. Funct. Mater.*, 30 (2020) 2003656.

[63] Z. Song, Z. Li, L. Lin, Y. Zhang, T. Lin, L. Chen, Z. Cai, S. Lin, L. Guo, F. Fu, X. Wang, Phenyl-doped graphitic carbon nitride: Photoluminescence mechanism and latent fingerprint imaging, *Nanoscale*, 9 (2017) 17737.

[64] H.J. Kwon, K. Shin, M. Soh, H. Chang, J. Kim, J. Lee, G. Ko, B.H. Kim, D. Kim, T. Hyeon, Large-scale synthesis and medical applications of uniform-sized metal oxide nanoparticles, *Adv. Mater.*, 30 (2018) 1704290.

[65] S. Andreescu, M. Ornatska, J.S. Erlichman, A. Estevez, J. Leiter, Biomedical applications of metal oxide nanoparticles, *Springer,* Berlin, 2012.

[66] M.J. Martín, C. Gentili, V. Lassalle, In vitro biological tests as the first tools to validate magnetic nanotheranostics for colorectal cancer models, *ChemMedChem*, 15 (2020) 1003.
[67] L. Jia, X. Li, H. Liu, J. Xia, X. Shi, M. Shen, Ultrasound-enhanced precision tumor theranostics using cell membrane-coated and pH-responsive nanoclusters assembled from ultrasmall iron oxide nanoparticles, *Nano Today*, 36 (2021) 101022.
[68] Z. Wang, R. Qiao, N. Tang, Z. Lu, H. Wang, Z. Zhang, X. Xue, Z. Huang, S. Zhang, G. Zhang, Y. Li, Active targeting theranostic iron oxide nanoparticles for MRI and magnetic resonance-guided focused ultrasound ablation of lung cancer, *Biomater.*, 127 (2017) 25.
[69] H.L. Karlsson, M. Toprak, B. Fadeel, Toxicity of Metal and Metal Oxide Nanoparticles, in: Handbook on the toxicology of metals: Fourth edition, *Elsevier BV,* Amsterdam, 2015, pp. 75.
[70] K. Girigoswami, Toxicity of metal oxide nanoparticles, *Mol. Cell Toxicol.*, (2018) 99.
[71] S.J. Soenen, P. Rivera-Gil, J.-M. Montenegro, W.J. Parak, S.C. De Smedt, K. Braeckmans, Cellular toxicity of inorganic nanoparticles: Common aspects and guidelines for improved nanotoxicity evaluation, *Nano Today*, 6 (2011) 446.
[72] L. Yildirimer, N.T.K. Thanh, M. Loizidou, A.M. Seifalian, Toxicology and clinical potential of nanoparticles, *Nano Today*, 6 (2011) 585.
[73] E.G. Gillan, Synthesis of nitrogen-rich carbon nitride networks from an energetic molecular azide precursor, *Chem. Mater.*, 12 (2000) 3906.
[74] J.O. Duruibe, M. Ogwuegbu, J. Egwurugwu, Heavy metal pollution and human biotoxic effects, *Int. J. Phys. Sci.*, 2 (2007) 112.
[75] X. Xu, S. Nie, H. Ding, F.F. Hou, Environmental pollution and kidney diseases, *Nat. Rev. Nephrol.*, 14 (2018) 313.
[76] S. World Health Organization. Water, T. Health, Guidelines for drinking-water quality. , in, *World Health Organization,* Geneva, 2004.
[77] H. Gurer, N. Ercal, Can antioxidants be beneficial in the treatment of lead poisoning?, *Free Radic. Biol. Med.*, 29 (2000) 927.
[78] H. Horiguchi, M. Sato, N. Konno, M. Fukushima, Long-term cadmium exposure induces anemia in rats through hypoinduction of erythropoietin in the kidneys, *Arch. Toxicol.*, 71 (1996) 11.

[79] A. Budimir, Metal ions, Alzheimer's disease and chelation therapy, *Acta Pharm.*, 61 (2011) 1.

[80] V.N. Uversky, H.-J. Lee, J. Li, A.L. Fink, S.-J. Lee, Stabilization of partially folded conformation during α-synuclein oligomerization in both purified and cytosolic preparations, *J. Biol. Chem.*, 276 (2001) 43495.

[81] N.C. Papanikolaou, E.G. Hatzidaki, S. Belivanis, G.N. Tzanakakis, A.M. Tsatsakis, Lead toxicity update. A brief review, *Med. Sci. Monit.*, 11 (2005) RA329.

[82] A. Wani, A. Ara, J. Usmani, Lead toxicity: A review, *Interdiscip. Toxicol.*, (2015).

[83] D.A. Gidlow, Lead toxicity, *Occup. Med.*, 54 (2004) 76.

[84] P. Pan, J.-X. Fan, X.-N. Wang, J.-W. Wang, D.-W. Zheng, H. Cheng, X.-Z. Zhang, Bio-orthogonal bacterial reactor for remission of heavy metal poisoning and ROS elimination, *Adv. Sci.*, 6 (2019) 1902500.

[85] M.B. Gumpu, S. Sethuraman, U.M. Krishnan, J.B.B. Rayappan, A review on detection of heavy metal ions in water – An electrochemical approach, *Sens. Actuators B: Chem.*, 213 (2015) 515.

[86] K. Sakthithasan, P. Lévy, J. Poupon, R. Garnier, A comparative study of edetate calcium disodium and dimercaptosuccinic acid in the treatment of lead poisoning in adults, *Clin. Toxicol.*, 56 (2018) 1143.

[87] C.-H. Weng, C.-W. Hsu, C.-C. Hu, T.-H. Yen, M.-J. Chan, W.-H. Huang, Blood lead level is a positive predictor of uremic pruritus in patients undergoing hemodialysis, *Ther. Clin. Risk Manag.*, (2017) 717.

[88] G. Liu, M.R. Garrett, P. Men, X. Zhu, G. Perry, M.A. Smith, Nanoparticle and other metal chelation therapeutics in Alzheimer disease, *Biochim. Biophys. Acta - Mol. Basis Dis.*, 1741 (2005) 246.

[89] P. Kumar, G.P. Rai, S.J.S. Flora, Immunomodulation following zinc supplementation during chelation of lead in male rats, *Biometals*, 7 (1994) 41.

[90] Curtis D. Klaassen, a. Jie Liu, S. Choudhuri, Metallothionein: An intracellular protein to protect against cadmium toxicity, *Annu. Rev. Pharmacol. Toxicol.*, 39 (1999) 267.

[91] A. T. Townsend, K. A. Miller, S. McLean, S. Aldous, The determination of copper, zinc, cadmium and lead in urine by high resolution ICP-MS, *J. Anal. At. Spectrom.*, 13 (1998) 1213.

[92] H.N. Kim, W.X. Ren, J.S. Kim, J. Yoon, Fluorescent and colorimetric sensors for detection of lead, cadmium, and mercury ions, *Chem. Soc. Rev.*, 41 (2012) 3210.
[93] F. Arduini, J.Q. Calvo, G. Palleschi, D. Moscone, A. Amine, Bismuth-modified electrodes for lead detection, *TrAC, Trends Anal. Chem.*, 29 (2010) 1295.
[94] H. Sies, Oxidative eustress and oxidative distress: Introductory remarks, in: Oxidative Stress, Elsevier, 2020, pp. 3.
[95] H. Sies, D.P. Jones, Reactive oxygen species (ROS) as pleiotropic physiological signalling agents, *Nat. Rev. Mol. Cell Biol.*, 21 (2020) 363.
[96] S. Mondal, N. Pan, R. Ghosh, A. Bera, D. Mukherjee, T.K. Maji, A. Adhikari, S. Ghosh, C. Bhattacharya, S.K. Pal, Interaction of a jaundice marker molecule with a redox-modulatory nano-hybrid: A combined electrochemical and spectroscopic study toward the development of a theranostic tool, *ChemMedChem*, 17 (2022) e202100660.
[97] A. Adhikari, M. Das, S. Mondal, S. Darbar, A.K. Das, S.S. Bhattacharya, D. Pal, S.K. Pal, Manganese neurotoxicity: Nano-oxide compensates for ion-damage in mammals, *Biomater. Sci.*, 7 (2019) 4491.
[98] A. Giri, N. Goswami, M. Pal, M.T.Z. Myint, S. Al-Harthi, A. Singha, B. Ghosh, J. Dutta, S.K. Pal, Rational surface modification of Mn_3O_4 nanoparticles to induce multiple photoluminescence and room temperature ferromagnetism, *J. Mater. Chem. C*, 1 (2013) 1885.
[99] P.A. Zunszain, J. Ghuman, A.F. McDonagh, S. Curry, Crystallographic analysis of human serum albumin complexed with 4Z, 15E-bilirubin-IXα, Journal of molecular biology, 381 (2008) 394.
[100] N. Polley, S. Saha, A. Adhikari, S. Banerjee, S. Darbar, S. Das, S.K. Pal, Safe and symptomatic medicinal use of surface-functionalized Mn3O4 nanoparticles for hyperbilirubinemia treatment in mice, Nanomedicine, 10 (2015) 2349.
[101] W.E. Kurtin, Spectroscopy and photochemistry of bilirubin photoproducts. I. Methylvinylmaleimide, *J. Photochem. Photobiol.*, 27 (1978) 503.
[102] J. Raveendran, J. Stanley, T.S. Babu, Voltammetric determination of bilirubin on disposable screen printed carbon electrode, *J. Electroanal. Chem.*, 818 (2018) 124.
[103] T. Takashima, K. Hashimoto, R. Nakamura, Mechanisms of pH-dependent activity for water oxidation to molecular oxygen by MnO_2 electrocatalysts, *J. Am. Chem. Soc.*, 134 (2012) 1519.

[104] M. Purdey, Ecosystems supporting clusters of sporadic TSEs demonstrate excesses of the radical-generating divalent cation manganese and deficiencies of antioxidant co factors Cu, Se, Fe, Zn, *Med. Hypotheses*, 54 (2000) 278.
[105] S. Lei, K. Tang, Z. Fang, H. Zheng, Ultrasonic-assisted synthesis of colloidal Mn_3O_4 nanoparticles at normal temperature and pressure, *Cryst. Growth Des.*, 6 (2006) 1757.
[106] S. Mondal, A. Adhikari, M. Das, S. Darbar, A. Alharbi, S.A. Ahmed, S.S. Bhattacharya, D. Pal, S.K. Pal, Novel one pot synthesis and spectroscopic characterization of a folate-Mn3O4 nanohybrid for potential photodynamic therapeutic application, RSC Advances, 9 (2019) 30216.
[107] R.J. Wydra, P.G. Rychahou, B.M. Evers, K.W. Anderson, T.D. Dziubla, J.Z. Hilt, The role of ROS generation from magnetic nanoparticles in an alternating magnetic field on cytotoxicity, *Acta Biomater.*, 25 (2015) 284.
[108] H. Chen, R. Langer, D.A. Edwards, A film tension theory of phagocytosis, *J. Colloid Interface Sci.*, 190 (1997) 118.
[109] S.K. Pal, D. Sukul, D. Mandal, S. Sen, K. Bhattacharyya, Solvation dynamics of dcm in dipalmitoyl phosphatidylcholine lipid, *Tetrahedron*, 56 (2000) 6999.
[110] L.E. Cole, R.D. Ross, J.M. Tilley, T. Vargo-Gogola, R.K. Roeder, Gold nanoparticles as contrast agents in X-ray imaging and computed tomography, *Nanomedicine (Lond.)*, 10 (2015) 321.
[111] A. Adhikari, P. Biswas, S. Mondal, M. Das, S. Darbar, A.M. Hameed, A. Alharbi, S.A. Ahmed, S. Sankar Bhattacharya, D. Pal, S. Kumar Pal, A smart nanotherapeutic agent for in vitro and in vivo reversal of heavy-metal-induced causality: Key information from optical spectroscopy, *ChemMedChem*, 15 (2020) 420.
[112] S. Mondal, S. Bayan, R. Ghosh, M. Das, A. Adhikari, D. Mukherjee, A.K. Mallick, S.K. Ray, S.K. Pal, Functionalized two-dimensional carbon nitride nanodots detect and reverse lead toxicity in the physiological milieu, *ACS Appl. Mater. Interfaces.*, 14 (2022) 27002.
[113] B. Zhang, Q. Dong, C.E. Korman, Z. Li, M.E. Zaghloul, Flexible packaging of solid-state integrated circuit chips with elastomeric microfluidics, *Sci. Rep.*, 3 (2013) 1098.

[114] F. Dong, L. Wu, Y. Sun, M. Fu, Z. Wu, S.C. Lee, Efficient synthesis of polymeric g-C_3N_4 layered materials as novel efficient visible light driven photocatalysts, *J. Mater. Chem. A*, 21 (2011) 15171.
[115] J. Xu, Y. Li, S. Peng, G. Lu, S. Li, Eosin Y-sensitized graphitic carbon nitride fabricated by heating urea for visible light photocatalytic hydrogen evolution: The effect of the pyrolysis temperature of urea, *Phys. Chem. Chem. Phys.*, 15 (2013) 7657.
[116] M.B. Dawadi, L. Degliumberto, D.S. Perry, H.D. Mettee, R.L. Sams, High-resolution infrared spectroscopy of the asymmetric NO stretch band of jet-cooled nitromethane and assignment of the lowest four torsional states, *J. Mol. Spectrosc.*, 343 (2018) 85.
[117] S. Farmer, D. Kennepohl, W. Reusch, W. Reusch, Infrared spectra of some common functional groups, in, 2022.
[118] B. University of Colorado, IR Spectroscopy Tutorial, in, 2011.
[119] B.C.F.a.T.R.o.U.o.C. Craig A. Merlic, WebSpectra , Problems in NMR and IR Spectroscopy, (2000).
[120] S. Bayan, A. Midya, N. Gogurla, A. Singha, S.K. Ray, Origin of modified luminescence response in reduced graphitic carbon nitride nanosheets, *J. Phys. Chem. C*, 121 (2017) 19383.
[121] A. Adhikari, S. Mondal, T. Chatterjee, M. Das, P. Biswas, R. Ghosh, S. Darbar, H. Alessa, J.T. Althakafy, A. Sayqal, S.A. Ahmed, A.K. Das, M. Bhattacharyya, S.K. Pal, Redox nanomedicine ameliorates chronic kidney disease (CKD) by mitochondrial reconditioning in mice, *Commun. Biol.*, 4 (2021) 1013.
[122] M.A. Kusiak, D.J. Dunkley, R. Wirth, M.J. Whitehouse, S.A. Wilde, K. Marquardt, Metallic lead nanospheres discovered in ancient zircons, *Proc. Natl. Acad. Sci. U.S.A.*, 112 (2015) 4958.
[123] J.R. Lakowicz, Principles of fluorescence spectroscopy, *Springer,* Berlin, 2006.
[124] A. Adhikari, S. Darbar, T. Chatterjee, M. Das, N. Polley, M. Bhattacharyya, S. Bhattacharya, D. Pal, S.K. Pal, Spectroscopic studies on dual role of natural flavonoids in detoxification of lead poisoning: Bench-to-bedside preclinical trial, *ACS Omega*, 3 (2018) 15975.
[125] P.-C. Hsu, Y.L. Guo, Antioxidant nutrients and lead toxicity, *Toxicology*, 180 (2002) 33.

[126] P.M. Quirós, A. Mottis, J. Auwerx, Mitonuclear communication in homeostasis and stress, *Nat. Rev. Mol. Cell Biol.*, 17 (2016) 213.
[127] W. Fan, W. Tang, J. Lau, Z. Shen, J. Xie, J. Shi, X. Chen, Breaking the depth dependence by nanotechnology-enhanced x-ray-excited deep cancer theranostics, *Adv. Mater.*, 31 (2019) 1806381.

CHAPTER 8

Developments of Nanoparticles and their Biochemical and Molecular Aspects in Preclinical Disease Model

8.1. Introduction:

Ulcerative colitis, a chronic idiopathic gastro-intestinal disease characterized by dysregulated immune response and persistent inflammation in the colonic and rectal mucosae [1], is the dominant subtype (Crohn's disease being the other) of inflammatory bowel disease (IBD) having a prevalence of ~0.25% of the population in North America, Europe, and Oceania [2]. The direct and indirect annual healthcare expenditure associated with ulcerative colitis are estimated to be as high as USD 12.8-29.8 billion in Europe and USD 8.1-14.9 billion in the United States [3]. With no proper cure, ulcerative colitis often poses increased risk of numerous digestive and malignant pathologies (e.g., colorectal cancer) associated with uncontrolled inflammation leading to significant disability-adjusted life years, morbidity, and mortality [4, 5]. The available conventional treatment options are 5-amino aminosalicylic acid (ASA), corticosteroids, immunosuppressant (e.g., azathioprine, 6-mercathioprine, methotrexate) and molecular targeting of inflammatory cascades (e.g., anti-TNF-α drugs infliximab, adalimumab, and golimumab) [6-9]. For mild to moderate disease 5-ASA is effective but for severe cases 5-ASA has been proved to be ineffective [8, 10, 11]. Administration of corticosteroids (intravenous or oral) are practiced for severe cases of UC [8]. Use of corticosteroids can provide primary remission for some cases but cannot completely remediate the UC. Previous reports on corticosteroid use suggested involvement of many genetic factors regarding its clinical efficacy [12, 13]. The other mentioned options are inadequate, expensive, have potentially life-threatening side effects and can only induce clinical remission (not cure) [4, 14-16]. Thus, it is of considerable interest to develop newer therapeutic modalities preferably with higher biocompatibility and lesser off-target adverse effects.

The etiology of ulcerative colitis is complex, multifaceted and exposome dependent involving genetic predisposition, epithelial barrier defects, dysbiosis of gut microflora, dysregulated immune response, irregular lifestyle (smoking, high-sugar and high-fat diet, stress etc.) and environmental factor [3, 17]. In conjunction with the inappropriate activation of pro-inflammatory signaling cascades, recent findings insinuated the key involvement of reactive oxygen species (ROS) in the pathogenesis and progression of ulcerative colitis [18, 19]. During the disease phase, infiltrated leukocytes, on activation, generates excess ROS (along with wide-spectrum of pro-inflammatory cytokines)and shifts the redox equilibrium of the intestinal mucosa toward oxidative distress, which in turn maintains active inflammation through induction of redox-sensitive signaling pathways and transcription factors [20]. Additionally, numerous pro-inflammatory molecules generate further oxidation products, leading to a self-sustaining and auto-amplifying vicious cycle that eventually disrupts the intestinal epithelial barrier [18]. Interestingly, both excessive and insufficient ROS contributes to the pathophysiology of ulcerative colitis [20]. For instance, a recent clinical study identified the defective superoxide ($O_2^{\bullet-}$) generation as one of the major risk factors in intestinal inflammation [21]. Considering the causal relationship between ROS and inflammation in the disease pathogenesis, we hypothesized that a combination strategy involving scavenging of ROS and down-regulation of pro-inflammatory mediators would be beneficial for the treatment of ulcerative colitis. However, trials with conventional non-selective small molecule antioxidants at high doses have generally failed in prevention or treatment of ROS related disease processes, likely owing to their inability to reach sufficient stoichiometric concentration inside cells or failure to maintain physiological ROS level (i.e., oxidative eustress) leading to disruption of vital redox-signaling pathways that controls processes like cellular metabolism, energetics, and survival [22]. One of the emerging solutions to this unique paradox about pleiotropic role of ROS in disease progression is the introduction of redox-modulating nanomaterials with potential electron donating as well as accepting capability to maintain precise balance between cellular oxidative eustress and distress (i.e., redox buffering; see ref. [23] for details). In the recent years, some inorganic nanoparticles with anti-oxidant properties showed some promising results in the management of UC. Au and Zn nanoparticles achieved significant success by exhibiting anti-oxidant

properties [24-26]. So, it can be hypothesized that the advancing nanotechnology can provide a more successful way forward to the remission of UC via balancing the cellular redox state. In this regard, ligand functionalized biocompatible tri-manganese tetroxide (Mn_3O_4) nanoparticles could be a practical choice. Several contemporary studies illustrated the efficacy of citrate functionalized Mn_3O_4 nanoparticles as redox medicine against a number of ROS-mediated disorders like neurodegenerative diseases [27, 28], hepatic fibrosis [29], chronic kidney disease [30], and neonatal hyperbilirubinemia [31]. In addition, our recent study has showed how ROS generation ability of folate functionalized Mn_3O_4 nanoparticles could be used in photo-dynamic therapy of adenocarcinoma [32]. Thus, this transition metal oxide nanomaterial is an ideal example of redox buffer not only because of its ability to act as a catalytic antioxidant to protect mitochondria, the master regulator of cellular redox homeostasis [27] but also for its micro-environment dependent pro-oxidant activity [23]. Moreover, the nanomaterial is biocompatible and do not exert any detrimental effect to cellular components or biomolecules [23].

In this study, our primary aims were i) to synthesize a biocompatible ligand (i.e., chitosan) functionalized Mn_3O_4 nanoparticle (Ch-Mn_3O_4 NP) that can efficiently function as cellular redox buffer; ii) to evaluate its safety and efficacy as a potential redox medicine against ulcerative colitis in a well-established animal model i.e., dextran sulfate sodium (DSS) intoxicated BALB/c mice; and iii) to understand the underlying mechanism of therapeutic action. The choice of surface functionalizing ligand i.e., chitosan (a polysaccharide composed of randomly arranged β-linked D-glucosamine and N-acetyl-D-glucosamine [33]) was primarily dictated by a) its stability in the pH range of gastro-intestinal tract making it suitable for oral administration [34]; b) biocompatibility with LD_{50} value close to sugar (16 g kg^{-1}) [35]; and c) specific and easy absorption in the colon due to the interaction between its positively charged primary amines and the negatively charged sialic acid substructures present in colonic mucus [36, 37]. Here, we have successfully synthesized Ch-Mn_3O_4 NPs, thoroughly characterized its physico-chemical properties using electron microscopic and UV-Vis spectroscopic techniques, and evaluated *in vitro* redox buffering capacity (i.e., pro-oxidant and antioxidant activities). In animal experiments, clinical and histopathological signs of ulcerative colitis were markedly reduced after treatment with Ch-Mn_3O_4 NPs. Further

molecular studies illustrated significant reduction in intestinal pro-inflammatory cytokines, decreased macrophage activity and preservation of cellular redox homeostasis through mitochondrial protection. A 28-day repeated dose sub-chronic toxicity study demonstrated biocompatibility and safety of this treatment strategy. In summary, our preclinical animal study provides a proof of concept for the use of a nanomaterial (i.e., Ch-Mn_3O_4 NPs) with synergistic anti-inflammatory and redox buffering capacity as redox medicine to prevent and treat ulcerative colitis.

8.2. Results and Discussion:

8.2.1. Chitosan Functionalized Mn_3O_4 Nanoparticles Counteracts Ulcerative Colitis in Mice through Modulation Of Cellular Redox State [38]:

8.2.1.1. Development of an Orally Administrable Nanomaterial (i.e., Ch-Mn_3O_4 NPs) to Target Colon: The surface functionalizing ligands, size, and surface charge are three important factors that determine specific distribution pattern of a nanomaterial inside living organisms.

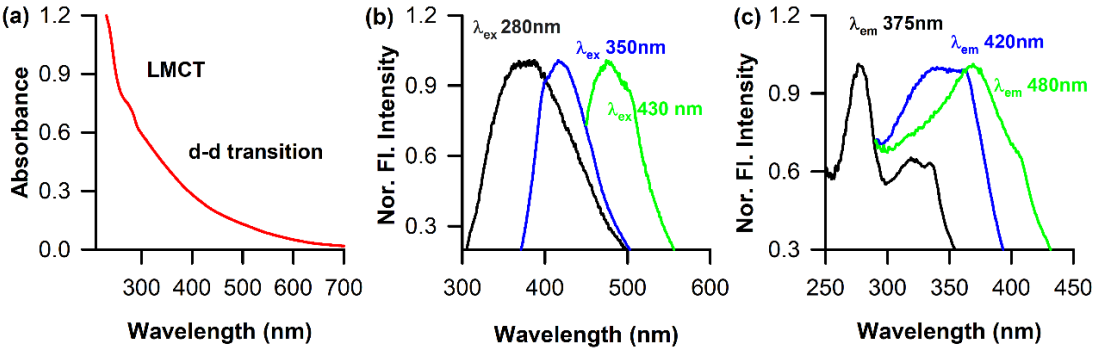

Figure 8.1: *(a) Absorbance Spectrum of Ch-Mn_3O_4 NPs showing LMCT and d-d transition bands. (b) Fluorescence emission spectra of Ch-Mn_3O_4 NPs. (c) Corresponding excitation spectra of Ch-Mn_3O_4 NPs.*

Here, we have functionalized Mn_3O_4 NPs with biocompatible ligand chitosan considering the prior knowledge about its well-known ability to specifically target and be absorbed in the colonic tissues. UV-Vis spectroscopic studies (Figure 8.1.a) revealed signatures of ligand to metal charge transfer (LMCT) from chitosan to Mn^{2+}/Mn^{3+} of the NPs, degeneracy of ground state d^4 (Mn^{3+}) electrons(e.g., Jahn-Teller effect) and multiple photoluminescence at room temperature, the unique features otherwise absent in pristine non-functionalized Mn_3O_4 NPs (Figure 8.1.b).The transmission electron micrographs (TEM) show the spherical shape and

homogeneous distribution of Ch-Mn_3O_4 NPs (Figure 8.2.a).The selected area electron diffraction (SAED) pattern shows the diffraction rings corresponding to (101) planes (Figure 8.2.b), confirming the spinel hausmannite structure of Ch-Mn_3O_4 NPs [39].

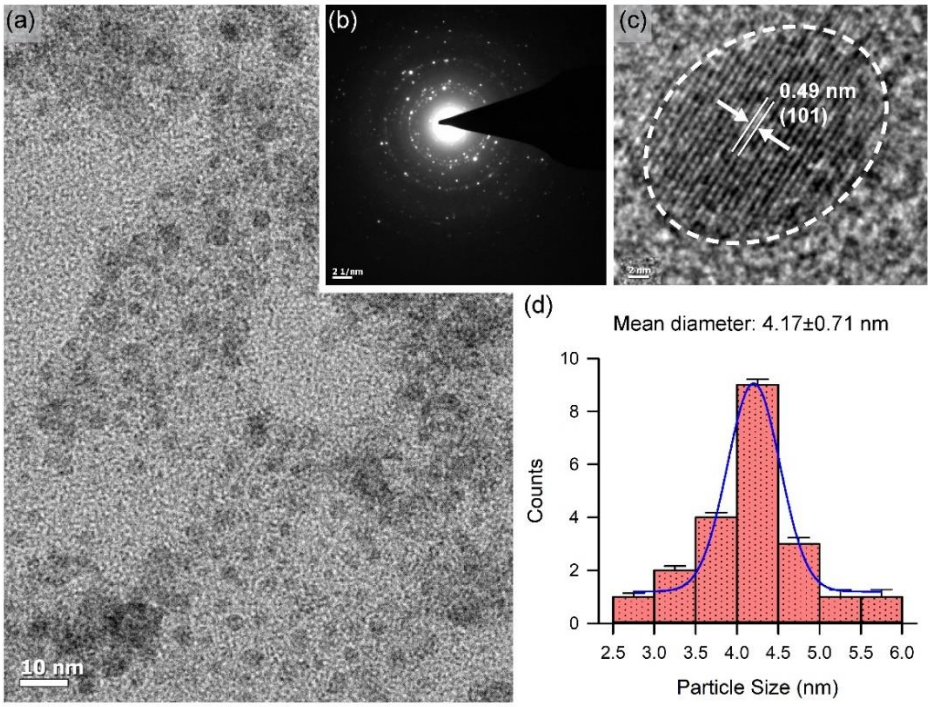

Figure 8.2: *(a) Transmission electron microscopy (TEM) image of Ch-Mn_3O_4 NPs. (b) SAED pattern of the same. (c) High-resolution TEM (HRTEM) image of a single nanoparticle. (d) Size-distribution of Ch-Mn_3O_4 NPs as measured from TEM.*

The inter-fringe distance from high-resolution TEM (HR-TEM) was determined to be 4.9 Å (Figure 8.2.c), corresponding to the (101) plane of Mn_3O_4 crystal lattice [40]. Figure 8.2.d suggests monomodal size distribution of spherical Ch-Mn_3O_4 NPs with a median diameter of 4.17±0.71 nm. It has to be noted that, specific care was taken during optimization of the synthesis method to confine the size of the NPs within 8.0 nm (majority of the particles were in 2.5-6.0 nm size range) as a diameter <8.0 nm facilitates elimination of NPs through renal excretory system, one of the major determinants of biocompatibility [41]. To check the effect of pH in the structure of the NPs, we have performed the TEM study at different pH (Figure 8.3.c-8.3.f). It is evident from the TEM results that the variation in pH does not significantly affect the overall shape or size of the NPs. The aqueous stability of Ch-Mn_3O_4 NPs, as determined by sequential monitoring of absorbance at 280 nm, was found to be excellent (pH 2.5-6.5) (Figure 8.3.a), But at higher pH (pH~ 7.5) the NPs

were precipitating out from the aqueous solution. This is due to the tendency of the chitosan molecule to be aggregated at higher pH.

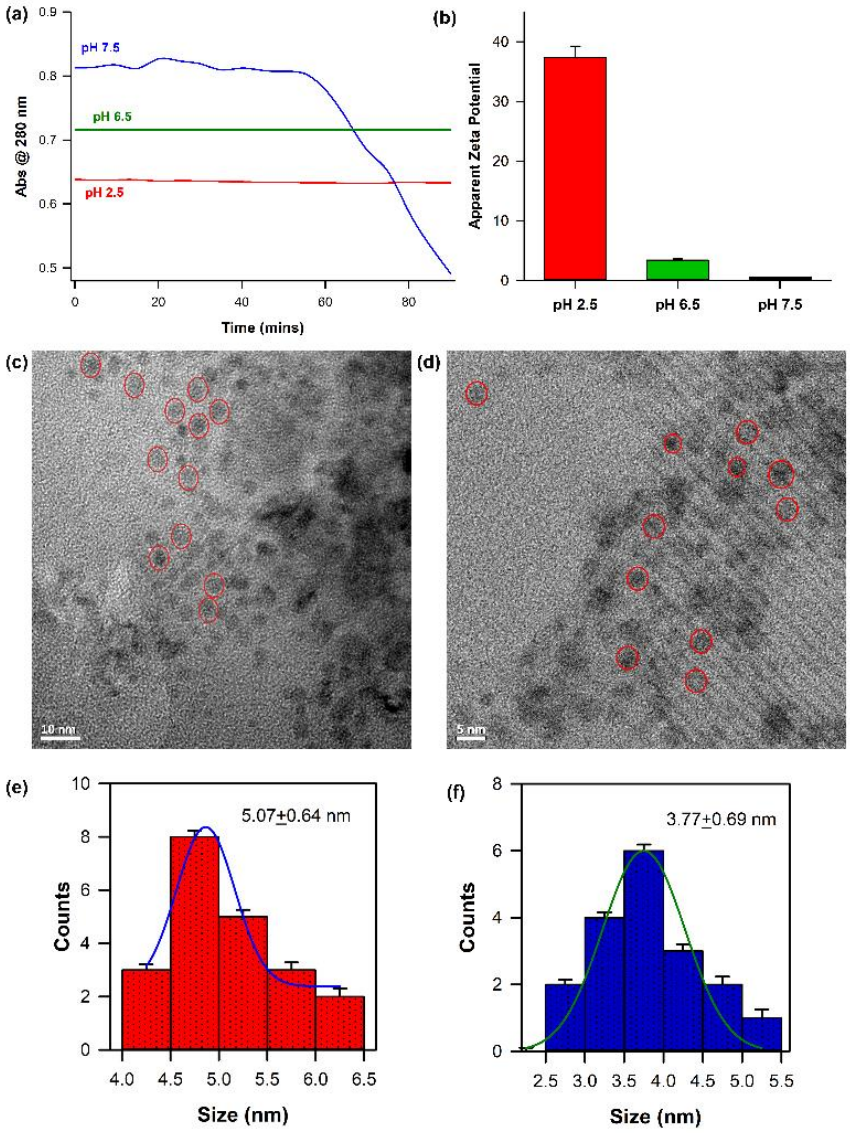

Figure 8.3: *(a) Aqueous stability at different pH. (b) Zeta Potential at different pH. (c) TEM image of the Ch-Mn_3O_4 NPs at pH 3. (d) TEM image of the Ch-Mn_3O_4 NPs at pH 7.5. (e) Size distribution of Ch-Mn_3O_4 NPs at pH 3. (f) Size distribution of Ch-Mn_3O_4 NPs in pH 7.5.*

Moreover, the pH dependent zeta potential study showed the similar trend (Figure 8.3.b). At pH more than 7, Ch-Mn_3O_4 NPs were found to be aggregated and precipitate out from the solution. Due to this characteristic, Ch-Mn_3O_4 NPs become efficient ligand for colon targeted drugs as at colonic pH (~ 7.2) it will be separated out from the solution and will be adhere to the colonic mucosal layer [42].

8.2.1.2. Ch-Mn_3O_4 NPs Function as a Redox Buffer: In order to maintain the cellular oxidative eustress condition, rapid sensing and adjustment of the redox environment is essential for redox buffering. According to our previous studies, Ch-Mn_3O_4 NPs has the ability to function as a redox buffering agent by sensing the cellular redox state and swiftly shifting the redox equilibrium to the eustress condition [23]. This behavior of Ch-Mn_3O_4 NPs as a redox modulator is analogous to that of pH buffers, where the pH buffering system can adjust the pH of a solution by sensing the H^+ concentration of the medium. In this study, by utilizing the 2′,7′-dichloro-dihydro-fluorescein (DCFH) assay we evaluated the pro-oxidant activity of Ch-Mn_3O_4 NPs (Figure 8.4.a). Next, we investigated the radical scavenging activity of the NPs using ABTS [2,2′-azino-bis(3-ethylbenzothiazoline-6-sulfonic acid)] assay (Figure 8.4.b). The Ch-Mn_3O_4 NPs can effectively scavenge the $ABTS^{\bullet+}$ radical cation (0.5 $\mu g ml^{-1}$ NPs showed anti-oxidant potential equivalent to 0.43 mM Trolox solution, water-soluble vitamin E analog).

After getting the insight about the ROS generation and radical scavenging activity of the NPs, we evaluated the *in vitro* redox buffering capacity of the synthesized NPs using H_2O_2 as an oxidant molecule. With the increase in the concentration of H_2O_2, the rate of 2′,7′- dichloro-dihydro-fluorescein oxidation increased within the medium (Figure 8.4.c). However, on introduction of Ch-Mn_3O_4 NPs in the action medium, a significant alteration in the 2′,7′- dichloro-dihydro-fluorescein intensity signifies the quenching of the ROS generated by the H_2O_2, acting as an oxidant in the medium. It is worthwhile to mention that Ch-Mn_3O_4 NPs always a maintained a base level of ROS concentration within the reaction medium, rather than eliminating all the ROS molecules. Prior findings have shown that a strong relationship exists between the intracellular H_2O_2 concentration and cellular oxidative state, and regular cellular functions are maintained up to 0.1 μM H_2O_2 concentration, beyond that triggers detrimental pathways that lead to cell death.

Here, we have determined the concentration of Ch-Mn_3O_4 NPs equivalent to the intracellular concentration of H_2O_2 in terms of ROS generation (Figure 8.4.d). Figure 8.4.e shows the cell response pattern associated to intracellular Ch-Mn_3O_4 NP concentration. In summary, the *in vitro* studies clearly describe the ability of Ch-Mn_3O_4 NPs to maintain oxidative eustress, i.e., persistent maintenance of the

cellular ROS level for proper physiological functioning (oxidative eustress) while evading the excess ROS from the medium (oxidative distress).

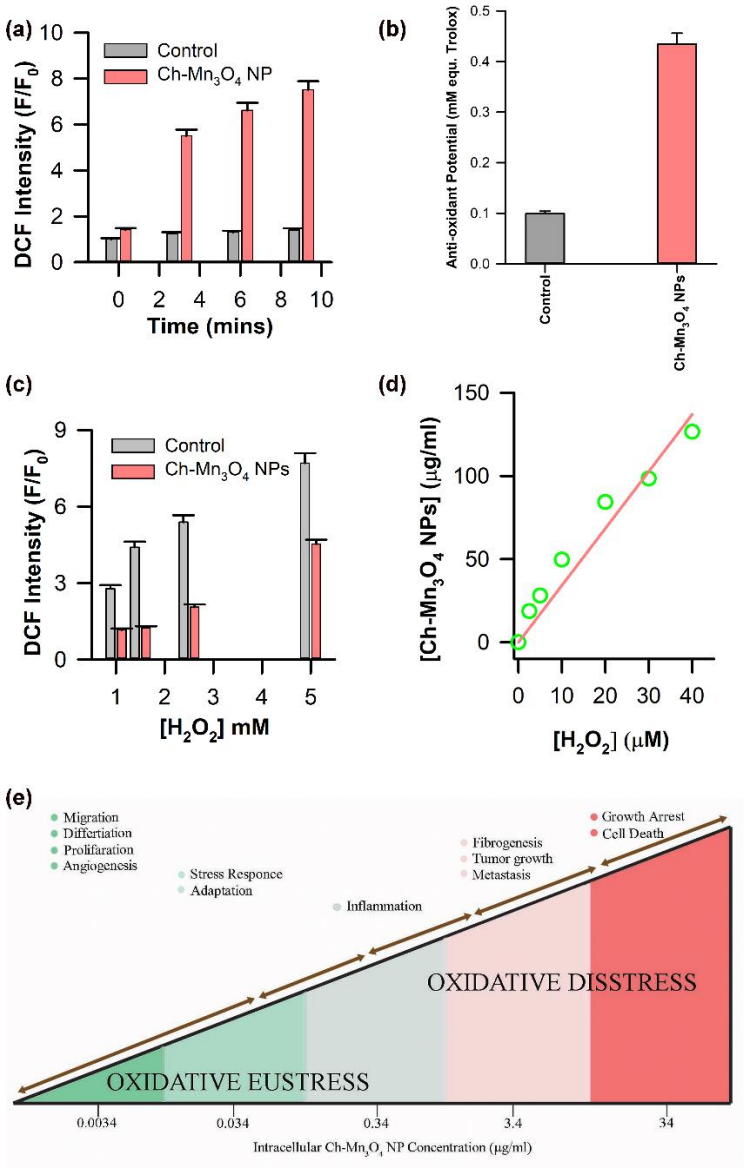

Figure 8.4: *(a) ROS generation by Ch-Mn_3O_4 NPs in room temperature. (b) Anti-oxidant activity of the NPs. (c) In-vitro redox buffering by Ch-Mn_3O_4 NPs. (d) Concentration equivalency between Ch-Mn_3O_4 NPs and H_2O_2 in term of ROS generation. (e) Relationship between concentration of Ch-Mn_3O_4 NPs and redox state of cells.*

8.2.1.3. Ch-Mn_3O_4 NPs Improved Clinical Symptoms in Animal Model of Acute Ulcerative Colitis: Promising redox buffering capability and favourable physico-chemical properties of Ch-Mn_3O_4 NPs propelled us to move forward and initiate preclinical animal studies. Here, we evaluated the treatment outcomes of Ch-Mn_3O_4 NPs in dextran sulfate sodium (DSS) induced BALB/c mice, a well-established

animal model for testing therapeutic interventions against ulcerative colitis [43]. Severely elevated disease activity index (DAI), a combined score comprising of three prominent clinical parameters weight loss, stool consistency, and fecal blood content [44], in DSS (5% in drinking water) intoxicated mice (DAI: 9.60±0.96 compared to 0.0±0.0 of control littermates, $p<0.0001$, one-way ANOVA, $F(3, 24.24)=310.0$) at day 12 indicates successful induction of ulcerative colitis (Figure 8.5.a).

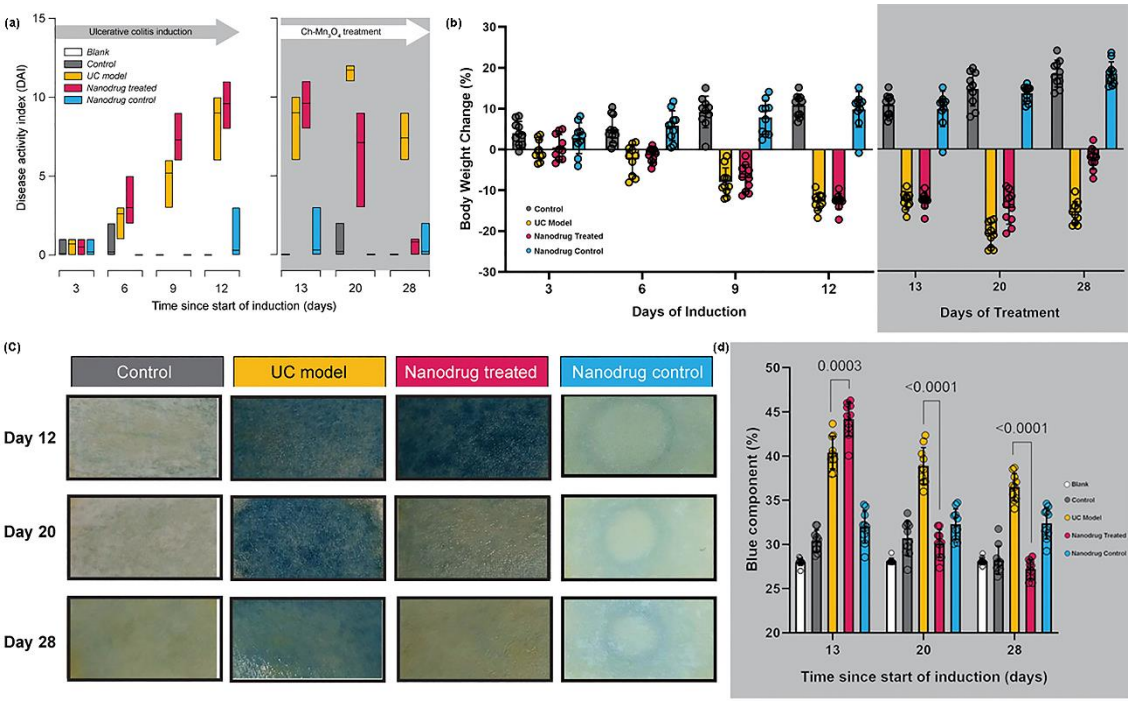

Figure 8.5: *(a) DAI score throughout the ulcerative colitis induction and the treatment phase. Treatment with Ch-Mn_3O_4 NPs successfully prevented as well as reduced the DAI score to normal level. (b) Body weight change across all the groups during the induction and Ch-Mn_3O_4 NPs treatment phase. (c) Picture of OBT test strips. (d) Fecal blood indices (Blue component analysis of OBT test strips). The amount of blood in faeces significantly reduced after treatment with Ch-Mn_3O_4 NPs. In bar plots data were expressed as Mean ± SD (n=10). In box plots, center lines show the medians; box limits indicate the 25th and 75th percentiles, whiskers extend 1.5 times the interquartile range from the 25th and 75th percentiles. One-way analysis of variance (ANOVA) followed by by correction of false discovery rate (post hoc FDR: two stage step up method of Benjamini, Krieger and Yekutieli) for multiple comparisons was performed for comparison between multiple groups. $p < 0.05$ is considered significant.*

Drastic reduction in body weight (BW change: -12.70±1.91% in DSS-intoxicated group compared to 10.81±2.74% in control, $p<0.0001$, one-way ANOVA, $F(3, 24.13)=205.2$) further supports acute colitis induction (Figure 8.5.b). For the therapeutic settings, treatments were administered daily starting on day 13 and final outcomes were assessed on day 28. Oral administration of Ch-Mn_3O_4 NPs (0.25 mg

kg^{-1} BW, single dose daily) for 15 consecutive days significantly reduced the DAI (0.80±0.42 compared to 7.40±1.07 of ulcerative colitis model cohort, p<0.0001, one-way ANOVA, F (3, 17.71)=290.8) (Figure 8.5.a) and prevented body weight loss (BW change:-2.31±2.69% vs -15.69±2.71% of ulcerative colitis model cohort, p<0.0001, one-way ANOVA, F (3, 34.93)=332.1) (Figure 8.5.b).

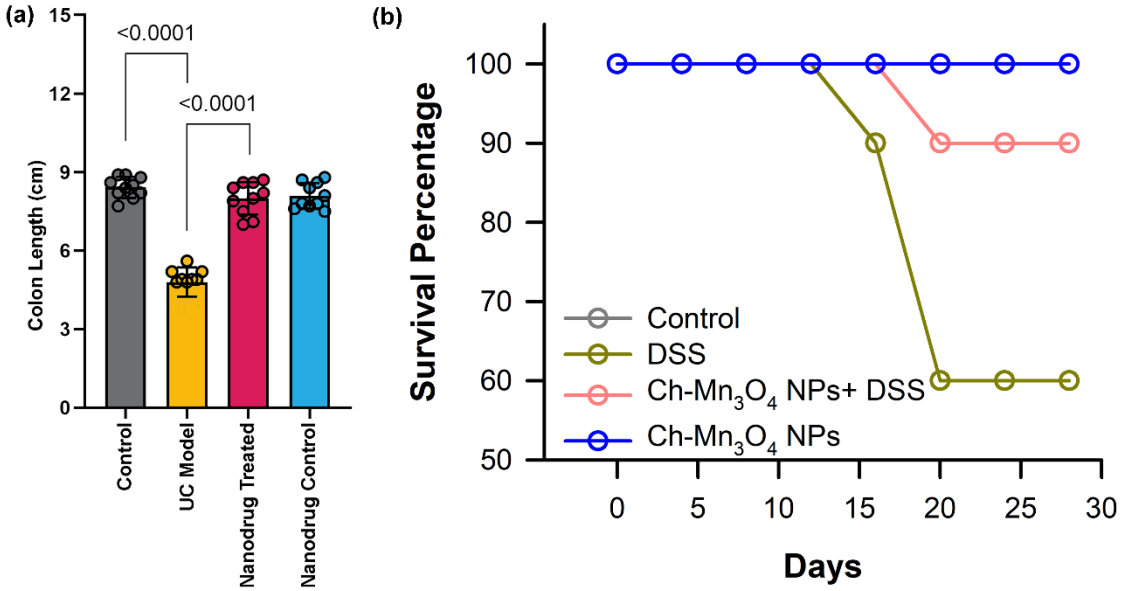

Figure 8.6: *(a) Colon length of all study groups. Data are expressed as mean ± SD (n=10). One-way analysis of variance (ANOVA) followed by correction of false discovery rate (post hoc FDR: two stage step up method of Benjamini, Krieger and Yekutieli) for multiple comparisons was performed for comparison between multiple groups. $p < 0.05$ is considered significant. (b) Survival curve of the experimental mice in all the four groups.*

The body weight changes were similar in control and Ch-Mn_3O_4 NPs control cohort (BW change: 18.51±2.91% vs 18.50±3.30% of control cohort, p=0.9941, one-way ANOVA, F (3, 34.93)=332.1) (Figure 8.5.b). As bloody diarrhea is one of the primary and well-reported symptoms of acute colitis [44, 45], we monitored the fecal blood content throughout the experimental period. At day 12, the DSS-intoxicated mice showed large amount of blood in their feces (Figure 8.5.c & Figure 8.5.d). While the fecal blood content remained high in the ulcerative colitis model cohort for the rest of the treatment period (day 13 – 28), in Ch-Mn_3O_4 NPs treated cohort it started to reduce from day 20 and disappeared on day 28 (Figure 8.5.c & Figure 8.5.d). Bloody diarrhea was accompanied by reduced colon length, another typical characteristics of acute colitis, in the ulcerative colitis model (Colon length: 4.80±0.55 cm vs 8.42±0.39 cm of control cohort, p<0.0001, one-way ANOVA, F

(3, 32.88)=105.1). Treatment with Ch-Mn_3O_4 NPs significantly improved the colon length comparable to control mice (Colon length: 8.00±0.62 cm vs 8.42±0.39 cm of control cohort, p=0.09, one-way ANOVA, F (3, 32.88)=105.1) (Figure 8.6.a). Also treatment of NPs reduces the significant mortality rate from the induced disease (Figure 8.6.b).

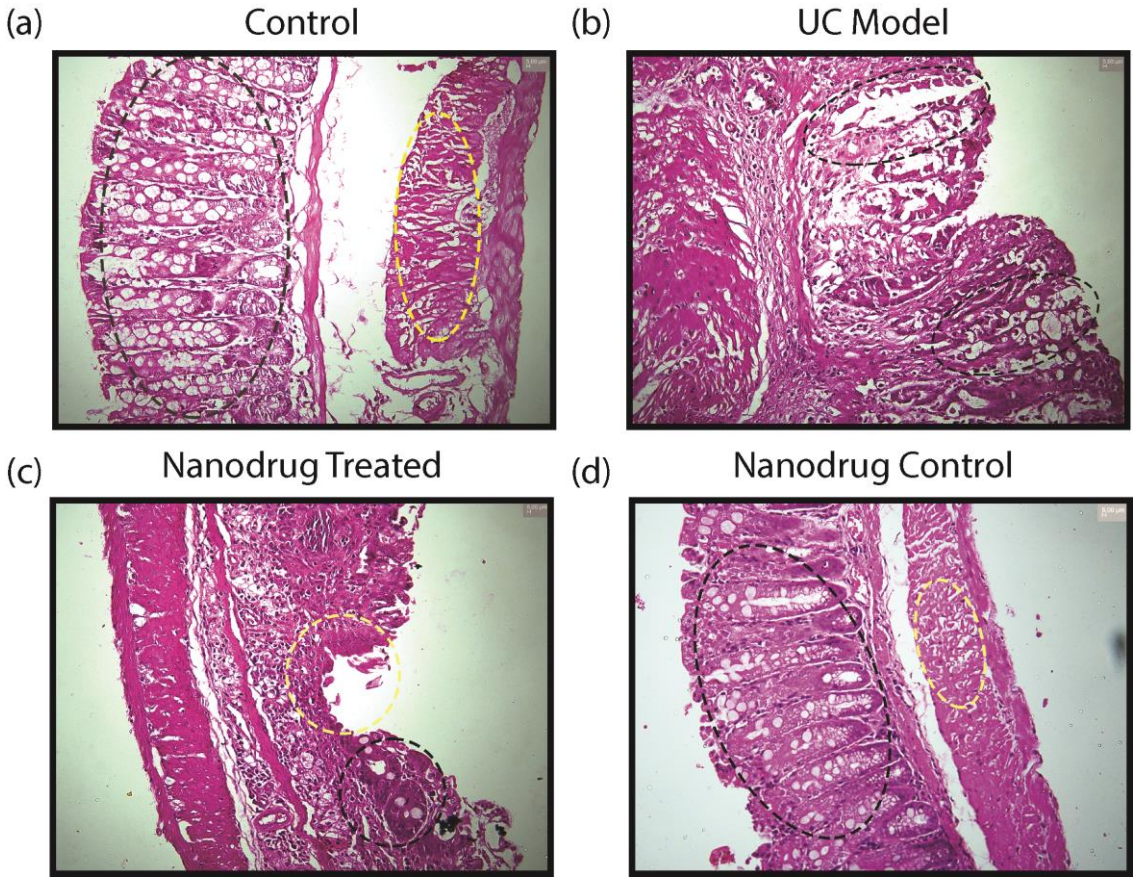

Figure 8.7: *(a) Micrographs of hematoxylin and eosin stained colon section of control mice. Black oval: Mucosal layer; Yellow oval: Muscularispropia. (b) Micrographs of hematoxylin and eosin stained colon section of DSS intoxicated diseased group. Black oval: infiltration of inflammatory cells. (c) Micrographs of hematoxylin and eosin stained colon section of Ch-Mn_3O_4 NPs treated group. Colon section of Ch-Mn_3O_4 NPs treated mice shows the healed ulcerated area covered by regenerating epithelium and other important glands (Black circle: Regenerative glands; Yellow circle: Healing region). (d) Micrographs of hematoxylin and eosin stained colon section of Ch-Mn_3O_4 NPs control group. Black oval: Mucosal layer; Yellow oval: Muscularis propia.*

8.2.1.4. Ch-Mn_3O_4 NPs Bolstered Histological Healing and Formation of Regenerative Glands: Along with resolution of clinical symptoms (i.e., cessation of rectal bleeding and improvement in bowel habits), the primary end point of all treatment strategies for ulcerative colitis comprises histopathological healing (i.e., amelioration of mucosal damages and inflammation) as they improve long-term

remission, decrease risk of colectomy, and limit corticosteroid use [46, 47]. In this study, hematoxylin and eosin (H & E)-stained colon tissue sections isolated from both control and Ch-Mn_3O_4 NPs control cohorts show normal histological features of colon like healthy mucosal and submucosal layer, typical muscularis propria and serosa (Figure 8.7.a and Figure 8.7.d).

In contrast, colon tissue section from the ulcerative colitis model cohort shows prominent pathological features of ulcerative colitis like well demarcated superficial mucosal ulceration and massive infiltration of inflammatory cells within lamina propria. In addition, presence of severe cryptitis and crypt abscesses, moderate increase in the number of neutrophils in lamina propria along with the presence of small areas of granulation tissues and mucosal fibrosis in lamina propria indicate towards severe architectural abnormalities in colon (Figure 8.7.b). Treatment with Ch-Mn_3O_4 NPs for 15 days lead to remarkable improvements in the histopathological features of damaged colon. The extent of inflammatory cells infiltration reduced significantly along with normal looking crypt cells, usual number of neutrophiles in lamina propria and epithelium, and regenerating epithelial layer with negligible level of adjacent inflammation. The H &E-stained colon section from this group (Figure 8.7.c) clearly shows the healed ulcerated area covered by regenerating epithelium along with several regenerative glands, indicating the initiation of regenerative pathways. In brief, colon from the Ch-Mn_3O_4 NPs treated group shows almost healthy mucosal layer, muscularis propria, submucosal layer and serosa with mild abnormalities. To get an objective, semiquantitative, reproducible depiction of the histopathological healing described in the above section, we have evaluated the histology score of H & E stained colon tissue sections according to the Geboes Score, the most commonly used histological score in ulcerative colitis (Figure 8.8) [47, 48]. The Geboes Score for ulcerative colitis model cohort was significantly high indicating severity of colonic damage i.e. architectural abnormalities, chronic inflammatory cells infiltration, presence of neutrophils in lamina propria and epithelium, destruction of the crypts and presence of ulcer and granulation tissue (Geboes Score: 14.00±0.81 vs 0.10±0.31 of control cohort, $p<0.0001$, one-way ANOVA, $F(3, 22.10)=844.7$). (Figure 8.8). Treatment with Ch-Mn_3O_4 NPs decreased the score within the normal range (Geboes Score:3.00±1.00 vs 14±0.81 of ulcerative colitis model cohort, $p<0.0001$, one-way ANOVA, F (3,

22.10)=844.7) which is the confirmation of the histological healing of the colonic lesions, reduced inflammation and restoration of architectural integrity (Figure 8.8).

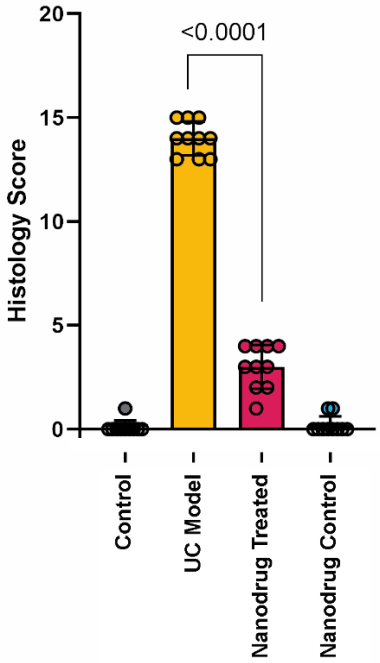

Figure 8.8: *Histology score of all study groups. Data are expressed as mean ± SD (n=10). One-way analysis of variance (ANOVA) followed by correction of false discovery rate (post hoc FDR: two stage step up method of Benjamini, Krieger and Yekutieli) for multiple comparisons was performed for comparison between multiple groups. $p < 0.05$ is considered significant.*

The Geboes Score for control and Ch-Mn_3O_4 NPs control cohorts were similar (0.20+0.42 vs 0.10+0.31 of control cohort, p=0.5566, one-way ANOVA, F (3, 22.10)=844.7) (Figure 8.8). So, treatment with Ch-Mn_3O_4 NPs did not cause any kind of architectural abnormality in colon of Ch-Mn_3O_4 NPs control cohorts (Figure 8.7.d).

8.2.1.5. Ch-Mn_3O_4 NPs Reduce Markers of Inflammation: Pro-Inflammatory Cytokines and Macrophage Infiltration: Activation of pro-inflammatory cytokines particularly IL-1β and IL-12 play pivotal role in the induction, pathogenesis, and relapse of ulcerative colitis [49-51]. As illustrated in Figure 8.9.a and 8.9.b, serum levels of both cytokines were severely elevated representing induction of intense inflammation. In agreement with the histopathological observations, administration of Ch-Mn_3O_4 NPs drastically reduced the levels of both IL-1β (IL-1β: 447.7±112.3 $pgml^{-1}$; p<0.0001, F (3, 15.8)=786.6, one-way ANOVA, compared to diseased model IL-1β: 2882±252.4 pg ml^{-1}) Figure 8.9.a and IL-12 (IL 12: 34.17±3.49 pg ml^{-}

[1]; p<0.0001, F (3, 33.10)= 417.2, one-way ANOVA, compared to diseased model IL-1β: 72.45±4.16 pg ml^{-1}) Figure 8.9.b.

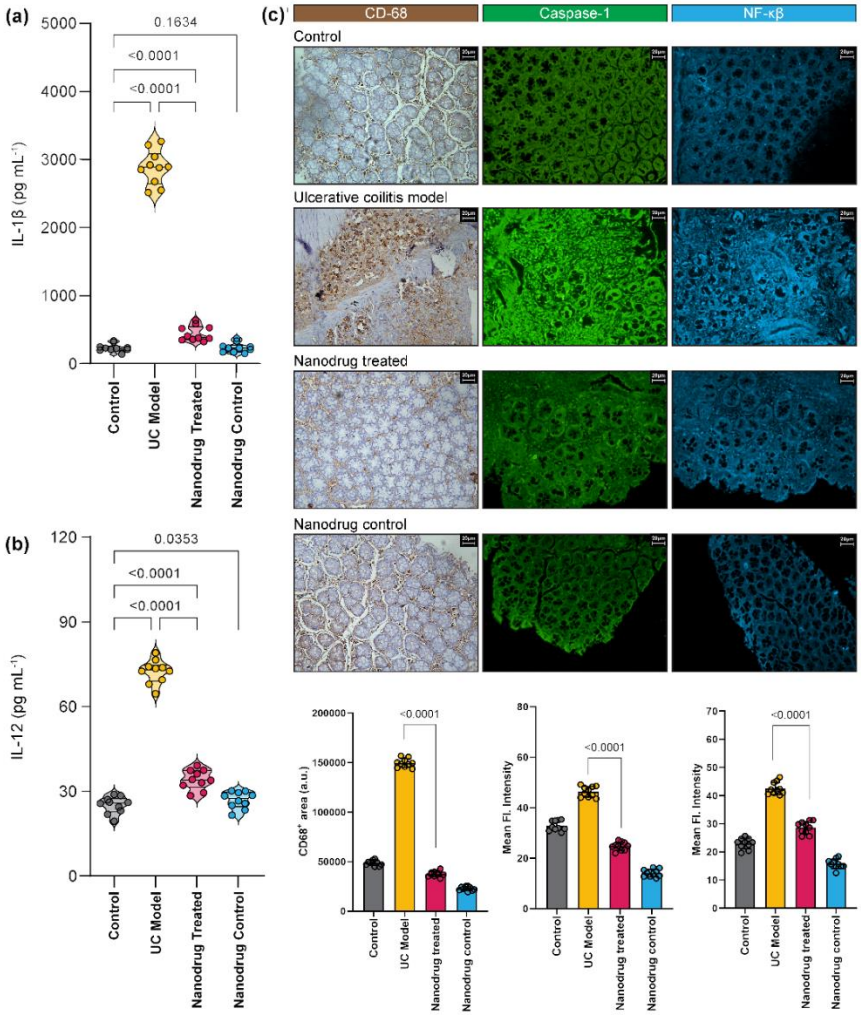

Figure 8.9. *(a) Amount of IL-1β in blood samples collected from each study groups. (b) Amount of IL-12 in blood samples collected from each study groups. c) Colonic tissue section stained with anti CD-68 antibody. Treatment with Ch-Mn_3O_4 NPs shows mild no of positive cells indicating prevention of the infiltration of M1 macrophage leading to reduced inflammation. Section also stained with anti-caspase-1 antibody. Treatment with Ch-Mn_3O_4 NPs successfully prevents caspase-1 activation which indicates cessation of inflammasome assembly. Further section stained with anti-NF-κβ p65 antibody. Micrographs shows lower presence of the protein indicating the down regulation of free NF-κβ in mice treated with NPs. CD-68 positive area and mean fluorescence intensity incase of anti-caspase-1 and anti-NF-κβ stained area also mentioned. Violins depict kernel density estimation of the underlying data distribution with the width of each violin scaled by the number of observations at that Y-value. Three lines (from the bottom to the top) in each violin plot show the location of the lower quartile (25th), the median, and the upper quartile (75th), respectively. The shaded area indicates the probability distribution of the variable. Individual data points are represented as colored circles (n= 10). One-way analysis of variance (ANOVA) followed by correction of false discovery rate (post hoc FDR: two stage step up method of Benjamini, Krieger and Yekutieli) for multiple comparisons was performed for comparison between multiple groups. The numbers inside the plots indicate numerical p values. p < 0.05 is considered significant.*

Neither of the other two experimental cohorts show signs of inflammation. Macrophages are one of the most abundant leukocytes found in luminal gastrointestinal mucosa and plays vital role in maintaining intestinal mucosal homeostasis [52]. Infiltration of macrophages in lamina propria and subsequent induction of pro-inflammatory cascades is a major event in progression of both ulcerative colitis and Crohn's disease [53, 54]. Prior studies have also proposed potential benefits for the therapeutic targeting of macrophages in IBD [55]. Here, we stained the colon tissue sections with anti-CD68 antibody, a popular marker for M1 macrophages, to visualize the level of macrophage infiltration. In control cohort, accumulation of CD-68$^+$ macrophages were seen beneath the colonic mucosa forming a dense sub-epithelial bandand only a small fraction CD-68$^+$ macrophages were present in thelamina propria (Figure 8.9.c). In the colitis model cohort, hefty number of CD-68$^+$ macrophages were detected in both sub-epithelial and lamina propria region (Figure 8.9.c). Such infiltration of macrophages reflected in the observed large CD-68$^+$ positive region (Figure 8.9.c). The Ch-Mn_3O_4 NPs treated cohort showed minimal CD-68$^+$ macrophages in the lamina propria and lesser dense subepithelial band even compared to the control ones. The CD-68$^+$ positive region was also smaller in this group. Ch-Mn_3O_4 NPs control cohort showed similar staining like the control group.

8.2.1.6. Ch-Mn_3O_4 NPs Inhibits Inflammasome Mediated Caspase-1 Activation and Down Regulates NF-Kβ Expression in Colonic Tissue: To get further insight into the upstream regulators of the anti-inflammatory phenomena displayed by Ch-Mn_3O_4 NPs, we investigated the expression profiles of two key proteins namely Caspase-1, responsible for cell death [56, 57], and NF- κβ, major transcription factor regulating the pro-inflammatory cytokines [58-60]. The strong green fluorescence from the cytosolic regions of the colon tissues stained with anti-Caspase-1 antibody from ulcerative colitis model mice clearly reveals high expression of Caspase-1 (Mean Fl. intensity: 46.36±2.09; $p<0.0001$, $F(3, 33.61)=557.1$, one-way ANOVA, compared to control Mean Fl. intensity: 32.86±1.98) (Figure 8.9.c) compared to the control mice. In contrast, Caspase-1 expression was much lesser in Ch-Mn_3O_4 NPs treated group than the diseased ones as illustrated by lower intensity of the green fluorescence (Mean Fl. intensity: 24.77±1.64; $p<0.0001$, $F(3, 33.61)=557.1$, one-way ANOVA, compared to diseased model Mean Fl. intensity: 46.36±2.09).

Similarly, we monitored the expression profile of NF-κβ in colon tissues using fluorescent tagged anti-NF-κβ p65 subunit antibody. In ulcerative colitis model group, the presence of NF-κβ was abundant in both cytosol and nuclei of the colonic epithelial cells compared to control one (Figure 8.9.c) indicating up-regulation of this transcription factor (Mean Fl. intensity: 42.54±2.17; $p<0.0001$, $F(3, 34.48)=322.3$, one-way ANOVA, compared to control Mean Fl. intensity: 22.98±1.88). Whereas, the Ch-Mn_3O_4 NP treated group showed much lower fluorescence intensity (Mean Fl. intensity: 28.65±2.19; $p<0.0001$, $F(3, 34.48)=322.3$, one-way ANOVA, compared to diseased model Mean Fl. intensity: 42.54±2.17) indicative of down regulated NF-κβ expression.

8.2.1.7. Ch-Mn_3O_4 NPs Mitigates Redox-Mediated Inflammation through Protection of Mitochondria from Oxidative Damages: Recent evidence suggests that mitochondria lie at the heart of immunity and mitochondrial alterations play central role in the pathogenesis of a plethora of inflammation mediated acute and chronic diseases including ulcerative colitis [61, 62]. Oxidative damage to intestinal mitochondria may lead to initiation of NF-κβ pathway, formation of NRLP3 inflammasome and caspase-1 activation [61, 63]. Therefore, we evaluated the mitochondrial 'health' in different experimental cohorts. The results clearly suggests that induction of ulcerative colitis triggered detrimental alterations to important mitochondrial health indicators resulting into degenerative redox signaling. Induction of ulcerative colitis led to increased mitochondrial membrane permeabilization i.e., mitochondrial swelling or mPTP formation. The time dependent sharp decrease in the 540 nm absorbance (Figure 8.10.a) of mitochondria isolated from ulcerative colitis model cohort upon Ca^{2+} sensitization is a clear manifestation of this phenomena. This was accompanied by deregulated mitochondrial membrane potential ($\Delta\psi_m$: 68.81±4.57 %; $P<0.0001$, $F(3, 27.56)=178$, one-way ANOVA, compared to control $\Delta\psi_m$: 100±3.02%) (Figure 8.10.b), decreased ATP level (ATP content: 16.00±2.40 nmol mg-1 protein; $P<0.0001$, $F(3, 35.55)=127.9$, one-way ANOVA, compared to control ATP content: 33.17±2.30 nmol mg-1 protein) (Figure 8.10.c),and increased mitochondrial ROS formation (mt ROS: 139.3±6.25 %; $p<0.0001$, $F(3, 29.22)=140.5$, one-way ANOVA, compared to control mt ROS: 100±2.33 %) (Figure 8.10.d).

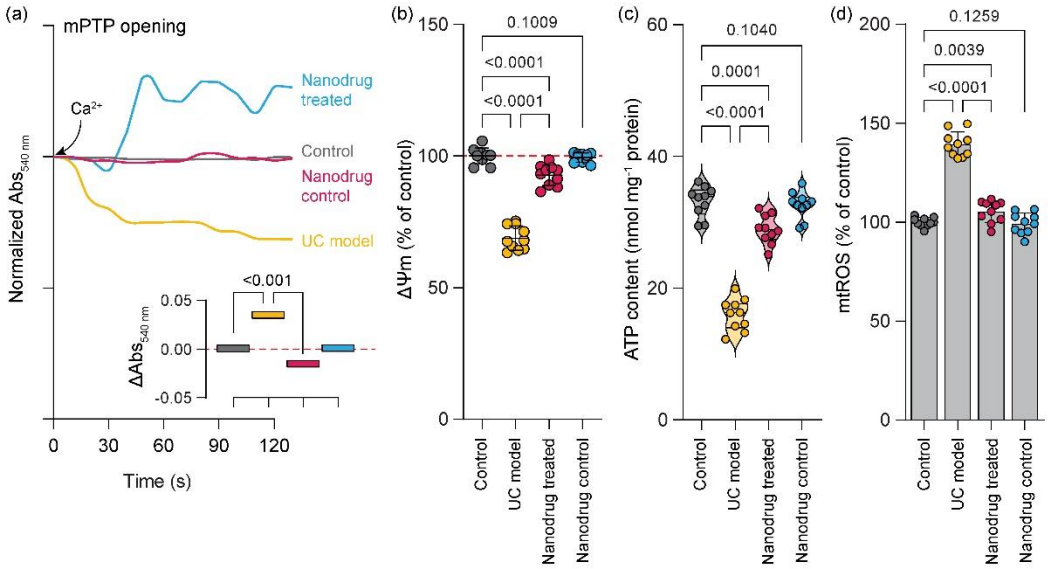

Figure 8.10. *(a) Effect on mitochondria permeability transition, measured as a decrease in absorbance at 540 nm. (b) Change in mitochondrial membrane potential (ΔΨm). (c) ATP content. (d) Mitochondrial ROS (mtROS) as measured using DCFH assay. Ch-Mn_3O_4 NPs efficiently protect the mitochondria from the oxidative damages. In bar plots data were expressed as Mean ± SD (n=10). Violins depict kernel density estimation of the underlying data distribution with the width of each violin scaled by the number of observations at that Y-value. Three lines (from the bottom to the top) in each violin plot show the location of the lower quartile (25th), the median, and the upper quartile (75th), respectively. The shaded area indicates the probability distribution of the variable. Individual data points are represented as colored circles (n= 10). One-way analysis of variance (ANOVA) followed by by correction of false discovery rate (post hoc FDR: two stage step up method of Benjamini, Krieger and Yekutieli) for multiple comparisons was performed for comparison between multiple groups. The numbers inside the plots indicate numerical p values. $p < 0.05$ is considered significant.*

These alterations were abrogated by Ch-Mn_3O_4 NP treatment; regulated mitochondrial membrane potential ($\Delta\psi_m$: 92.72±3.89 %; p<0.0001, F (3, 27.56)=178, one-way ANOVA, compared to ulcerative colitis model cohort $\Delta\psi_m$: 68.81±4.57%), increased ATP level (ATP content: 28.91±2.18 nmol mg^{-1} protein; p<0.0001, F (3, 35.55)=127.9, one-way ANOVA, compared to ulcerative colitis model cohort ATP content: 16.00±2.40 nmol mg^{-1} protein), decreased mitochondrial ROS formation (mt ROS: 105.4±5.50 %; p<0.0001, F (3, 29.22)=140.5, one-way ANOVA, compared to ulcerative colitis model cohort mt ROS: 139.3±6.25 %) (Figure 8.10.a-8.10.d].

8.2.1.8. Biocompatibility of Ch-Mn_3O_4 NPs: We evaluated the bio-compatibility of the prepared Ch-Mn_3O_4 NPs in *in-cellulo* model.

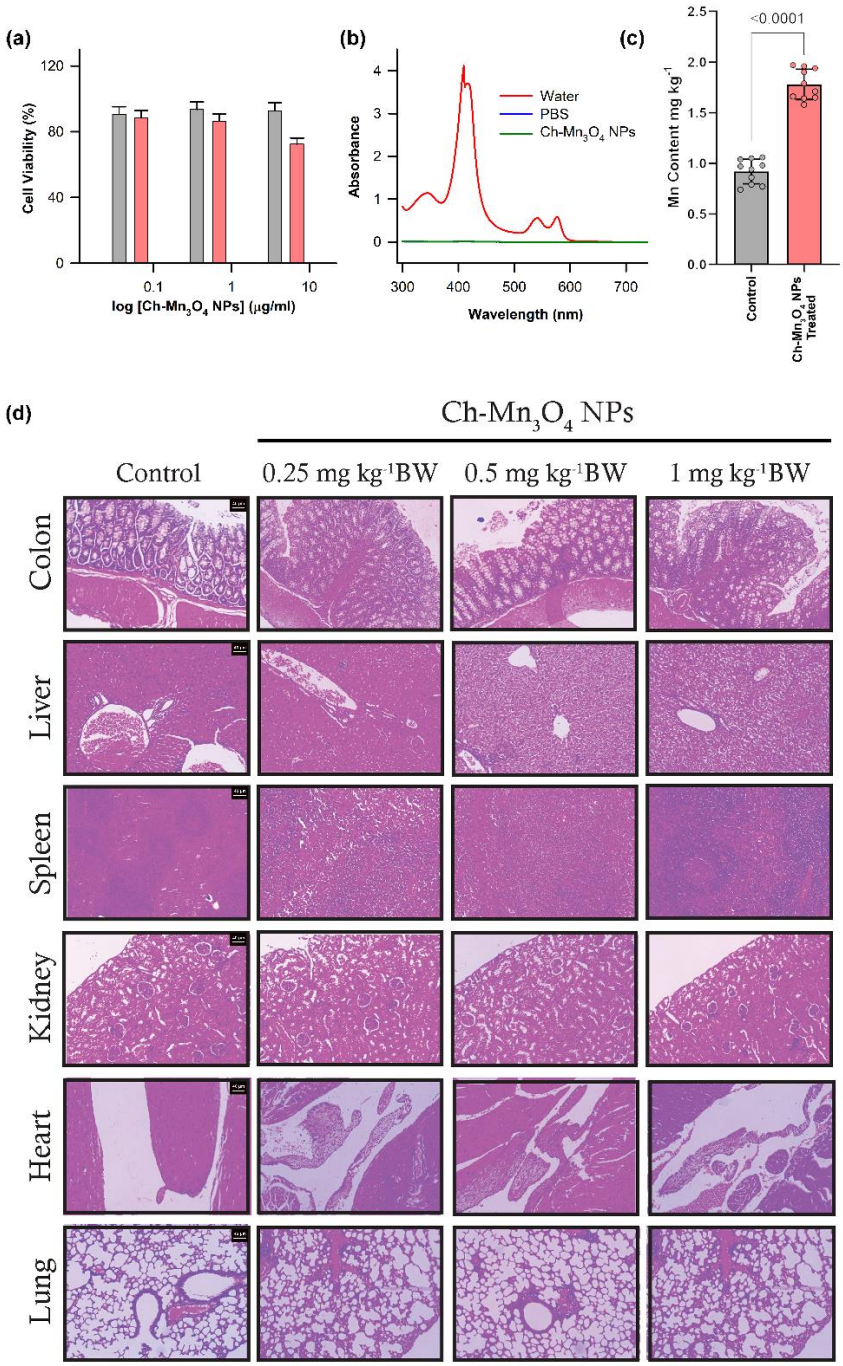

Figure 8.11: *(a) Cell-viability assay using HEK 293 cell line. (b) Hemolysis assay. (c) Mn-Content of control mice and Ch-Mn_3O_4 Treated mice. In bar plots data were expressed as Mean ± SD (n=10). An unpaired, parametric t test with Welch's correction was performed. $p<0.05$ is considered significant. (d) Sub-chronic toxicity of Ch-Mn_3O_4 NPs. Micrographs of hematoxylin and eosin stained sections of colon, liver, spleen and kidney after 28 days treatment with Ch-Mn_3O_4 NPs at three dose levels i.e. 0.25 mg kg^{-1} BW, 0.5 mg kg^{-1} BW and 1 mg kg^{-1} BW. Colon sections show large guts comprising of healthy mucosa layer, muscularis propria and submucosa layer across the all groups. Control and all the NPs treated groups liver section shows normal looking central vein, portal tracts, hepatocytes arranged in cords with normal sinusoidal space. Spleen sections of the control and NPs treated groups show normal histological features which comprised ideal red and white pulp region. Kidney sections show normal looking medulla and cortex in all four groups. Lung and heart sections of the control and NPs treated groups show normal histological features.*

In the first step, we used the human embryonic kidney (HEK 293) cell line, a normal epithelial cell line, for this purpose. First, we have treated the HEK 293 cell line with three different concentration (0.05 μgml^{-1}, 0.5 μgml^{-1}, 5 μgml^{-1}) of NPs and incubated them for 6 hours. Then using MTT assay, we have determined the cell viability. Figure 8.11.a exhibits the cell viability for three different concentrations of NPs. It is evident from the Figure 8.11.a that the cells those received 0.05 μgml-1and 0.5 μgml^{-1} of NPs show similar cell viability as the control group. But the cells treated with 5 μgml^{-1} of NPs showed significant cell viability (~70%) compared to control cells.

To understand this phenomenon of lower cell viability at higher concentration NPs, we have established a relation between the amount of ROS generated by a certain concentration of NPs and ROS produced by a certain concentration of H_2O_2. Figure 8.4.d depicts that the concentration of NPs equivalent to the concentration of H_2O_2 in term of ROS generation. The graph shows a linear relation. Previous studies have shown that a strong relationship exists between the intracellular [H_2O_2] and cells oxidative state [22]. It is reported that the cells perform their normal function up to 0.1 μM of intracellular H_2O_2 concentration (oxidative eustress). An increase in intracellular H_2O_2 concentration beyond 0.1 μM triggers the detrimental pathways that lead to cell death (oxidative distress) [22]. This intracellular concentration of H_2O_2 varies from cell type to cell type. From our calculation, we have created a similar cell response pattern with increasing intracellular NPs concentration (Figure 8.4.e). This picture gives a comprehensible idea regarding the outcome of our cell viability assay. As the cells treated with 0.05 μgml^{-1} and 0.5 μgml^{-1} of NPs maintain oxidative eustress, no significant cell death was observed. However, the cells that received 5 μgml^{-1} of NPs showed significant cell death because at that NP concentration cells failed to retain its oxidative eustress condition and excess ROS generation damaged the cell components. So, from the above discussion it is evident that this NPs can effectively buffer the redox state of the cells and help them to perform their normal physiological function. But beyond a certain level it also creates oxidative distress due to its ROS generation ability in room temperature.

Hemolysis study (Figure 8.11.b) has also been performed using 0.5 μgml^{-1} of NPs. RBCs were incubated with NPs, water and phosphate buffer saline (PBS) for 3 hours. The study set with NPs no visible hemolysis like the PBS one. Further, the

spectroscopic assessment of the supernatant also confirm that NPs did not exert any toxic effect on RBCs.

Further we carried out the bio-distribution of the NPs in different organs using ICPOES (Figure 8.11.c). After 7 days of treatment, the manganese content in colon tissue sample of Ch-Mn_3O_4 NPs treated mice (Mn content: 1.78±0.15 mg kg^{-1}; $P<0.0001$, $t=14.05$, $df=17.22$; Unpaired t test, compared to control Mn content: 0.92±0.12 mg kg^{-1}) is significantly higher in comparison to untreated control cohort. But there was no significant accumulation of NPs in any organs other than colon. So, the results of bio-distribution study suggest the high affinity of Ch-Mn_3O_4 NPs towards colon which is the primary target organ of this study.

A sub-chronic toxicity study to evaluate the bio-compatibility and toxicity of Ch-Mn_3O_4 NPs in the preclinical mice model was performed (Figure 8.11.d). We have chosen three dose of NPs, 0.25mg kg^{-1} Body weight (BW), 0.5 mg kg^{-1} BW & 1 mg kg^{-1} BW. Three group of mice were orally treated with a single dose of NPs on a daily basis. A fourth group of mice were treated with saline water (oral administration) that serves as a control study group. After 28 days, we have collected organs from all the study groups and performed histological analysis to check any structural abnormalities in the organs of NPs treated mice. Figure 8.11.d shows the histological structure of colon, liver, spleen and kidney of all four groups. No structural abnormality is observed in histological examination of any organs of the NPs treated mice. All the organs of NPs treated mice successfully retained their normal architecture as compared to the control study group. Further we performed analysis of haematological parameters across all the groups. And the results show all the parameters are in normal range in all NPs treated groups (Table 8.1). So, it can be concluded that Ch-Mn_3O_4 NPs is safe and biocompatible in physiological milieu.

Hence, this study was designed to determine whether an orally administrable novel nanodrug, Ch-Mn_3O_4 NPs, could be used as a redox medicine or the treatment of severe ulcerative colitis, a crucial clinical question considering the growing prevalence of the disease and non-availability of safe and effective therapeutic strategy. Our results provide direct evidence that treatment with the nanodrug (0.25 mg kg^{-1} BW, daily for 15 days) ameliorates both clinical symptoms (e.g., weight loss, shortening of colon length, rectal bleeding, inconsistent stool, DAI) and histological

damages (e.g., intestinal epithelial barrier disruption, goblet cell depletion, granulocyte infiltration, crypt cell damage) of acute ulcerative colitis in DSS-intoxicated BALB/c mice. The extensive restoration of regular intestinal histological features (i.e., 'histological healing') accomplished through Ch-Mn_3O_4 NP treatment is immensely important in clinical management of ulcerative colitis as available data indicate that histologic healing is associated with better outcomes in ulcerative colitis, including lower relapse rates and cancer risk [64].

Table 8.1: *Summary of hematology parameters studied across the groups.*

Parameters	**Control**	**Ch-Mn_3O_4 NPs 1 mg kg^{-1} BW**	**Ch-Mn_3O_4 NPs 0.5 mg kg^{-1} BW**	**Ch-Mn_3O_4 NPs 0.25 mg kg^{-1} BW**
Hb (g/dl)	13.56 ± 0.50	13.50 ±0.44	13.81 ±0.72	13.38 ±0.38
RBC ($\times 10^6/\mu l$)	6.48 ±0.48	6.44 ±0.36	6.83 ±0.41	6.44 ±0.36
HCT (%)	41.87±1.09	42.61 ±1.74	42.53 ±1.36	41.08 ±1.30
MCV (fl)	63.27 ±3.67	64.91 ±3.04	62.29 ±4.29	63.37 ±2.23
MCH (pg)	22.36 ±1.45	21.42 ±0.96	23.58 ±1.86	21.84 ±1.31
MCHC (g/dl)	34.24 ±1.16	33.31 ±1.25	33.22 ±1.09	33.72 ±1.16
Platelets ($\times 10^3/\mu l$)	6.72 ± 0.79	6.49 ± 0.52	6.64 ± 0.88	6.45 ± 1.02
WBC ($\times 10^5/\mu l$)	8.68 ± 0.55	9.72 ± 0.41	9.17 ± 0.67	8.92 ± 0.69

Interestingly, most of the currently available treatment options are incapable of instigating histological healing. As a result, mucosal healing, routinely assessed by endoscopy, has emerged as the major therapeutic target though microscopic evidence of inflammation is common even in patients with clinically and sigmoidoscopically quiescent colitis [65], suggesting that endoscopy may underestimate the extent of the disease and possibly alter the clinical follow-up scheme [66]. Thus, development of new age therapies like the one investigated in

this study will not only improve the treatment outcome but also support the emerging argument about raising the bar of drug activity assessment by implementing histologic remission as the ultimate treatment goal in clinical practice [64, 66].

The favorable therapeutic effects illustrated by Ch-Mn_3O_4 NPs may perhaps been stemmed from suppressed local inflammation and maintenance of cellular redox equilibrium as manifested by decreased proinflammatory cytokines and reduced mediators of oxidative damage. The reduction in intestinal inflammation due to Ch-Mn_3O_4 NP treatment is consistent with our previous results [30] where a kidney targeted different ligand functionalized manganese oxide nanoparticle reduced renal inflammation and cured chronic kidney disease. This study also provides a piece of direct evidence that Ch-Mn_3O_4 NPs can scavenge ROS, particularly H_2O_2, the longest living one in the physiological milieu. Furthermore, it can generate ROS depending on the microenvironment, in turn, functions as redox buffer. Considering the inseparable correlation between uncontrolled, persistent oxidative stress and inflammation, we postulate that the redox buffering activity of Ch-Mn_3O_4 NPs is the underlying reason behind the observed anti-inflammatory activity. This also supports our histological finding that Ch-Mn_3O_4 NPs prevents damage to the intestinal epithelium and restores regular colon architecture as several external and internal stimuli induce the formation of ROS in the gut, resulting in lipid peroxidation and apoptosis and colonic mucosal damage.

Our observation that prevention of mitochondrial damage from oxidative distress is one of the key molecular events in the therapeutic mechanism of Ch-Mn_3O_4 NPs provides proof-of-concept in support of the emerging hypothesis that mitochondrial redox homeostasis could be putative drug target for prevention of inflammation-associated disorders like ulcerative colitis [67]. It is well-known that mitochondria are coordinators of cellular homoeostasis via their role in energy production and oxidative metabolism, induction of apoptosis, regulation of calcium, production of ROS, and regulation of signal transduction and epigenomic intermediates [68]. In the intestine, mitochondrial metabolism and function play key roles in immune cell activation, intestinal epithelial cell barrier integrity and differentiation programs and stemness [69]. Several prior studies have revealed the involvement of mitochondrial stress in the pathophysiology of ulcerative colitis but whether this is a cause or consequence of the disease is not known [70]. While mitochondria function as a

platform for pro-inflammatory signaling cascade through activation of NF-κβ pathway [61], the pro-inflammatory mediators also alter mitochondrial function [63]. Interestingly, both processes increase mitochondrial oxidative distress or in other words dysregulates mitochondrial redox homeostasis, promoting a vicious inflammatory cycle. Furthermore, damage-associated molecular patterns (DAMPs) derived from mitochondria leads to NRLP3 inflammasome formation and caspase-1 activation, the processing of pro-IL-1β and pro-IL-18, and pyroptotic cell death [61, 63]. In this study, the observed increase in mtROS, opening of mPTP, deregulation of mitochondrial membrane potential and depletion in ATP levels due to disease pathogenesis functioned as mitochondrial stress response leading to activation of NF-κβ pathway and induction of multiple pro-inflammatory genes and interleukins (ILs).Observed overexpression of NF- κβ in lamina propria and increased IL--1β and IL-12 levels further supports this argument. The DAMPs released from mitochondria due to loss of membrane integrity activated the NRLP3 inflammasome, thereby driving caspase-1 activation, also illustrated in the immunofluorescence study. On the other hand, Ch-Mn_3O_4 NPs regulated the cellular and mitochondrial ROS to homeostatic level, in turn protected structural and functional integrity of mitochondria (reflected in low mPTP, regular $\Delta\psi_m$, and normal ATP content), thereby obstructed the causal vicious cycle of inflammation. The observed inhibition of mPTP opening by Ch-Mn_3O_4 NPs is a critical event in the therapeutic mechanism because recent studies have demonstrated a large pore formed by oligomerization of the voltage-dependent anion channel 1 (VDAC1), the mPTP formation mechanism, mediates DAMP movement across the outer mitochondrial membrane (OMM) for immune cell activation, with a pathogenic role [71]. The down regulation of pro-inflammatory cytokines further supports this argument. The findings that Ch-Mn_3O_4 NPs maintains cellular redox homeostasis and prevents pro-inflammatory signaling cascades through mito-protection corroborates our previous study that elucidated a similar redox-mediated nephroprotective mechanism by citrate-functionalized-Mn_3O_4 NPs in treatment of chronic kidney disease.

The origin of the catalytic mechanisms behind ROS generation by Ch-Mn_3O_4 NPs lies in the unique electronic structure of the nanodrug having closely packed tetrahedral and octahedral sites within a face-centered cubic oxygen framework. The

valence band of the structure is dominated by tetrahedral Mn^{2+}, while the octahedral Mn-ions are in a Jahn-Tellar distorted, high-spin Mn^{3+} state (also evident in the UV-Vis spectra) [29, 72]. The high-energy tetrahedral Mn^{2+} spontaneously oxidizes to Mn^{3+}, followed by the removal of electron from octahedral site, forming Mn^{4+}. When three electrons per formula unit are removed, the valence band becomes dominated by oxygen states and electrons are extracted from O2p orbitals instead of tetrahedral Mn^{3+}, resulting in the formation of oxygen holes on the nanodrug surface. The holes generates transient free radicals upon interaction with dissolved molecular oxygen. On the other hand, when in abundance ROS are readily adsorbed by the nanodrug to replenish its initial electronic configuration.

The limitations of this study provide scope for future work. Comprehensive investigation about the molecular mechanism of action and effect to other inflammatory pathways and mediators of ulcerative colitis would be beneficial to translate this work into clinical trial. Use of genetically modified rodent model or extending it to treatment of IBD could also provide further information. One huge advantage of this therapeutic strategy is the apparent non-toxicity of this nanodrug. However, more detailed toxicity study particularly at molecular level is important to meet the FDA endorsement requirements.

8.3. Conclusion:

There are very few published articles in contemporary literature that report a promising alternative approach for the treatment of ROS induced inflammatory diseases like ulcerative colitis. On the other hand, many new reports are confirming the involvement of redox imbalance behind the pathogenesis of ulcerative colitis. Our study suggests that Ch-Mn_3O_4 NPs could be an efficient redox medicine to attenuate colon injury and ulcer formation as evidenced by the reduction in clinical symptoms, restoration of normal colon length, decrease in the infiltration of immune cells, reduction in molecular markers of inflammation, down regulated pro-inflammatory cytokines, and initiation of regenerative glands at the site of ulcer. The molecular mechanism involves the redox buffering of cellular redox state by Ch-Mn_3O_4 NPs and protects the mitochondria from ROS damages. The findings strongly suggest the translational potential of Ch-Mn_3O_4 NPs as a redox nanoparticle for the treatment of UC.

Reference

[1] W.J. Sandborn, B.G. Feagan, G. D'Haens, D.C. Wolf, I. Jovanovic, S.B. Hanauer, S. Ghosh, A. Petersen, S.Y. Hua, J.H. Lee, Ozanimod as induction and maintenance therapy for ulcerative colitis, *N. Engl. J. Med.*, 385 (2021) 1280.

[2] G.G. Kaplan, The global burden of IBD: From 2015 to 2025, *Nat. Rev. Gastroenterol. Hepatol.*, 12 (2015) 720.

[3] J. Torres, S. Mehandru, J.-F. Colombel, L. Peyrin-Biroulet, Crohn's disease, *Lancet*, 389 (2017) 1741.

[4] D.C. Baumgart, C. Le Berre, Newer biologic and small-molecule therapies for inflammatory bowel disease, *N. Engl. J. Med.*, 385 (2021) 1302.

[5] K. Taku, S. Britta, W.S. Chen, M. Ferrante, B. Shen, C.N. Bernstein, D. Silvio, P.-B. Laurent, H. Toshifumi, Ulcerative colitis (Primer), *Nat. Rev. Dis. Primers*, 6 (2020).

[6] J.P. Gisbert, F. Gomollón, J. Maté, J.M. Pajares, Role of 5-aminosalicylic acid (5-ASA) in treatment of inflammatory bowel disease: A systemic review, *Dig. Dis. Sci.*, 47 (2002) 471.

[7] E. Mao, G. Hazlewood, G. Kaplan, L. Peyrin-Biroulet, A. Ananthakrishnan, Systematic review with meta-analysis: Comparative efficacy of immunosuppressants and biologics for reducing hospitalisation and surgery in crohn's disease and ulcerative colitis, *Aliment. Pharmacol. Ther.*, 45 (2017) 3.

[8] J. Li, F. Wang, H.-J. Zhang, J.-Q. Sheng, W.-F. Yan, M.-X. Ma, R.-Y. Fan, F. Gu, C.-F. Li, D.-F. Chen, Corticosteroid therapy in ulcerative colitis: Clinical response and predictors, *World J. Gastroenterol.*, 21 (2015) 3005.

[9] G. Falasco, R. Zinicola, A. Forbes, Immunosuppressants in distal ulcerative colitis, *Aliment. Pharmacol. Ther.*, 16 (2002) 181.

[10] L. Aspenvall, E. Aadland, Severe ulcerative colitis, *Tidsskr Nor Laegeforen.*, 110 (1990) 1520.

[11] S. Travis, The management of mild to severe acute ulcerative colitis, *Aliment. Pharmacol. Ther.*, 20 (2004) 88.

[12] T. Creed, C. Probert, Steroid resistance in inflammatory bowel disease–mechanisms and therapeutic strategies, *Aliment. Pharmacol. Ther.*, 25 (2007) 111.

[13] J.H. Cho, The genetics and immunopathogenesis of inflammatory bowel disease, *Nat. Rev. Immunol.*, 8 (2008) 458.

[14] J.D. Feuerstein, K.L. Isaacs, Y. Schneider, S.M. Siddique, Y. Falck-Ytter, S. Singh, K. Chachu, L. Day, B. Lebwohl, T. Muniraj, AGA clinical practice guidelines on the management of moderate to severe ulcerative colitis, *Gastroenterol.*, 158 (2020) 1450.

[15] S. Targan, S. Hanauer, S. Van Deventer, L. Mayer, D. Present, T. Braakman, K. DeWoody, T. Schaible, P. Rutgeerts, Crohn's Disease cA2 Study Group. A short-term study of chimeric monoclonal antibody cA2 to tumor necrosis factor alpha for Crohn's disease, *N. Engl. J. Med.*, 337 (1997) 1029.

[16] J.P. Terdiman, C.B. Gruss, J.J. Heidelbaugh, S. Sultan, Y.T. Falck–Ytter, American gastroenterological association institute guideline on the use of thiopurines, methotrexate, and anti–tnf-α biologic drugs for the induction and maintenance of remission in inflammatory crohn's disease, *Gastroenterol.*, 145 (2013) 1459.

[17] S.D. Thapa, H. Hadid, M. Usman, W. Imam, A. Hassan, J. Schairer, S.-M.R. Jafri, N. Kaur, Predictors of thiopurine treatment failure in biologic-naive ulcerative colitis patients, *Dig. Dis. Sci.*, 61 (2016) 230.

[18] F. Biasi, G. Leonarduzzi, P. Oteiza, G. Poli, Mechanisms, redox considerations, and therapeutic targets., *Antioxid. Redox Signal.*, 19 (2018) 1711.

[19] G. Jena, P.P. Trivedi, B. Sandala, Oxidative stress in ulcerative colitis: An old concept but a new concern, *Free Radic. Res.*, 46 (2012) 1339.

[20] E.L. Campbell, S.P. Colgan, Control and dysregulation of redox signalling in the gastrointestinal tract, *Nat. Rev. Gastroenterol. Hepatol.*, 16 (2019) 106.

[21] C. Huang, S.S. De Ravin, A.R. Paul, T. Heller, N. Ho, L. Wu Datta, C.S. Zerbe, B.E. Marciano, D.B. Kuhns, H.A. Kader, B.S. R, Genetic risk for inflammatory bowel disease is a determinant of Crohn's disease development in chronic granulomatous disease, *Inflamm. Bowel Dis.*, 22 (2016) 2794.

[22] H. Sies, D.P. Jones, Reactive oxygen species (ROS) as pleiotropic physiological signalling agents, *Nat. Rev. Mol. Cell Biol.*, 21 (2020) 363.

[23] S. Mondal, A. Adhikari, R. Ghosh, M. Singh, M. Das, S. Darbar, S.S. Bhattacharya, D. Pal, S.K. Pal, Synthesis and spectroscopic characterization of a target-specific nanohybrid for redox buffering in cellular milieu, *MRS Adv.*, 6 (2021) 427.

[24] J. Li, H. Chen, B. Wang, C. Cai, X. Yang, Z. Chai, W. Feng, ZnO nanoparticles act as supportive therapy in DSS-induced ulcerative colitis in mice by maintaining gut homeostasis and activating Nrf2 signaling, *Sci. Rep.*, 7 (2017) 1.
[25] A.M. Abdelmegid, F.K. Abdo, F.E. Ahmed, A.A. Kattaia, Therapeutic effect of gold nanoparticles on DSS-induced ulcerative colitis in mice with reference to interleukin-17 expression, *Sci. Rep.*, 9 (2019) 10176.
[26] Y. Cheng, C. Cheng, J. Yao, Y. Yu, Y. Liu, H. Zhang, L. Miao, H. Wei, Mn_3O_4 nanozyme for inflammatory bowel disease therapy, *Adv. Ther.*, 4 (2021) 2100081.
[27] A. Adhikari, S. Mondal, M. Das, P. Biswas, U. Pal, S. Darbar, S.S. Bhattacharya, D. Pal, T. Saha-Dasgupta, A.K. Das, A.K. Mallick, S.K. Pal, Incorporation of a biocompatible nanozyme in cellular antioxidant enzyme cascade reverses huntington's like disorder in preclinical model, *Adv. Healthc. Mater.*, 10 (2021) 2001736.
[28] A. Adhikari, M. Das, S. Mondal, S. Darbar, A.K. Das, S.S. Bhattacharya, D. Pal, S.K. Pal, Manganese neurotoxicity: nano-oxide compensates for ion-damage in mammals, *Biomater. Sci.*, 7 (2019) 4491.
[29] A. Adhikari, N. Polley, S. Darbar, D. Bagchi, S.K. Pal, Citrate functionalized Mn_3O_4 in nanotherapy of hepatic fibrosis by oral administration, *Future Sci. OA*, 2 (2016) FSO146.
[30] A. Adhikari, S. Mondal, T. Chatterjee, M. Das, P. Biswas, R. Ghosh, S. Darbar, H. Alessa, J.T. Althakafy, A. Sayqal, Redox nanomedicine ameliorates chronic kidney disease (CKD) by mitochondrial reconditioning in mice, *Commun. Biol.*, 4 (2021) 1.
[31] A. Adhikari, V.K. Bhutani, S. Mondal, M. Das, S. Darbar, R. Ghosh, N. Polley, A.K. Das, S.S. Bhattacharya, D. Pal, A.K. Mallick, S.K. Pal, Chemoprevention of bilirubin encephalopathy with a nanoceutical agent, *Pediatr. Res.*, 93 (2022) 827.
[32] S. Mondal, A. Adhikari, M. Das, S. Darbar, A. Alharbi, S.A. Ahmed, S.S. Bhattacharya, D. Pal, S.K. Pal, Novel one pot synthesis and spectroscopic characterization of a folate-Mn_3O_4 nanohybrid for potential photodynamic therapeutic application, *RSC Adv.*, 9 (2019) 30216.
[33] V. Zargar, M. Asghari, A. Dashti, A review on chitin and chitosan polymers: Structure, chemistry, solubility, derivatives, and applications. , *ChemBioEng Rev.*, 2 (2015) 204.

[34] R. Ghosh, S. Mondal, D. Mukherjee, A. Adhikari, S.A. Ahmed, R.I. Alsantali, A.S. Khder, H.M. Altass, Z. Moussa, R. Das, Oral drug delivery using a polymeric nanocarrier: chitosan nanoparticles in the delivery of rifampicin, *Mater. Adv.*, (2022).
[35] V. Dodane, V.D. Vilivalam, Pharmaceutical applications of chitosan, *Pharm. Sci. Technol. Today*, 1 (1998) 246.
[36] M.M.T. Ways, W.M. Lau, V.V. Khutoryanskiy, Chitosan and its derivatives for application in mucoadhesive drug delivery systems, *Polymers*, 10 (2018) 267.
[37] N. Kulkarni, P. Jain, A. Shindikar, P. Suryawanshi, N. Thorat, Advances in the colon-targeted chitosan based drug delivery systems for the treatment of inflammatory bowel disease, *Carbohydr. Polym.*, (2022) 119351.
[38] S. Mondal, M. Das, R. Ghosh, M. Singh, A. Adhikari, S. Darbar, A. Kumar Das, S.S. Bhattacharya, D. Pal, D. Bhattacharyya, Chitosan functionalized Mn_3O_4 nanoparticles counteracts ulcerative colitis in mice through modulation of cellular redox state, *Commun. Biol.*, 6 (2023) 647.
[39] S. Lei, K. Tang, Z. Fang, H. Zheng, Ultrasonic-assisted synthesis of colloidal Mn_3O_4 nanoparticles at normal temperature and pressure, *Cryst. Growth Des.*, 6 (2006) 1757.
[40] T. Imboon, J. Khumphon, K. Yotkuna, I. Tang, S. Thongmee, Enhancement of photocatalytic by Mn_3O_4 spinel ferrite decorated graphene oxide nanocomposites, *SN Appl. Sci.*, 3 (2021) 1.
[41] A.E. Nel, L. Mädler, D. Velegol, T. Xia, E. Hoek, P. Somasundaran, F. Klaessig, V. Castranova, M. Thompson, Understanding biophysicochemical interactions at the nano–bio interface, *Nat. Mater.*, 8 (2009) 543.
[42] M. Kurakula, S. Gorityala, K. Moharir, Recent trends in design and evaluation of chitosan-based colon targeted drug delivery systems: Update 2020, *J. Drug Deliv. Sci. Technol.*, 64 (2021) 102579.
[43] C. Benoit, D. Jesse, M. Madhu, V. Matam, Dextran sulfate sodium (DSS)-induced colitis in mice, *Curr. Protoc. Immunol.*, 25 (2014) 1.
[44] D.J. Friedman, B.M. Künzli, Y.I. A-Rahim, J. Sevigny, P.O. Berberat, K. Enjyoji, E. Csizmadia, H. Friess, S.C. Robson, CD39 deletion exacerbates experimental murine colitis and human polymorphisms increase susceptibility to inflammatory bowel disease, *Proc. Natl. Acad. Sci. U.S.A.*, 106 (2009) 16788.

[45] U. Colitis-Pathophysiology, Inflammatory bowel disease part I : Ulcerative colitis-pathophysiology and conventional and alternative treatment options, *Altern. Med. Rev.*, 8 (2003) 247.

[46] S.P. Costello, P.A. Hughes, O. Waters, R.V. Bryant, A.D. Vincent, P. Blatchford, R. Katsikeros, J. Makanyanga, M.A. Campaniello, C. Mavrangelos, Effect of fecal microbiota transplantation on 8-week remission in patients with ulcerative colitis: a randomized clinical trial, *JAMA*, 321 (2019) 156.

[47] A. Jauregui-Amezaga, A. Geerits, Y. Das, B. Lemmens, X. Sagaert, T. Bessissow, T. Lobatón, M. Ferrante, G. Van Assche, R. Bisschops, A simplified Geboes score for ulcerative colitis, *J. Crohns Colitis.*, 11 (2017) 305.

[48] M.H. Mosli, B.G. Feagan, G. Zou, W.J. Sandborn, G. D'Haens, R. Khanna, L.M. Shackelton, C.W. Walker, S. Nelson, M.K. Vandervoort, Development and validation of a histological index for UC, *Gut*, 66 (2017) 50.

[49] N. Kaneko, M. Kurata, T. Yamamoto, S. Morikawa, J. Masumoto, The role of interleukin-1 in general pathology, *Inflamm. Regen.*, 39 (2019) 1.

[50] Y. Arai, H. Takanashi, H. Kitagawa, I. Okayasu, Involvement of interleukin-1 in the development of ulcerative colitis induced by dextran sulfate sodium in mice, *Cytokine*, 10 (1998) 890.

[51] B. Egger, M. Bajaj-Elliott, T.T. MacDonald, R. Inglin, V.E. Eysselein, M.W. Buchler, Characterisation of acute murine dextran sodium sulphate colitis: Cytokine profile and dose dependency, *Digestion*, 62 (2000) 240.

[52] A.M. Smith, F.Z. Rahman, B.H. Hayee, S.J. Graham, D.J. Marks, G.W. Sewell, C.D. Palmer, J. Wilde, B.M. Foxwell, I.S. Gloger, Disordered macrophage cytokine secretion underlies impaired acute inflammation and bacterial clearance in Crohn's disease, *J. Exp. Med.*, 206 (2009) 1883.

[53] P. Foubert, M.M. Kaneda, J.A. Varner, Pi3kγ activates integrin α4 and promotes immune suppressive myeloid cell polarization during tumor progressionmyeloid cell integrin α4 controls cancer immune suppression, *Cancer Immunol. Res.*, 5 (2017) 957.

[54] J. Rugtveit, P. Brandtzaeg, T. Halstensen, O. Fausa, H. Scott, Increased macrophage subset in inflammatory bowel disease: Apparent recruitment from peripheral blood monocytes, *Gut*, 35 (1994) 669.

[55] S. Dharmasiri, E.M. Garrido-Martin, R.J. Harris, A.C. Bateman, J.E. Collins, J.F. Cummings, T. Sanchez-Elsner, Human intestinal macrophages are involved in the pathology of both ulcerative colitis and Crohn disease, *Inflamm. Bowel Dis.*, 27 (2021) 1641.

[56] L. Wang, X. Dong, S. Feng, H. Pan, X. Jang, L. Chen, Y. Zhao, W. Chen, Z. Huang, VX765 alleviates dextran sulfate sodium-induced colitis in mice by suppressing caspase-1-mediated pyroptosis, *Int. Immunopharmacol.*, 102 (2022) 108405.

[57] J. Li, C.M. Ma, D.L. Di, A narrative review of pyrolysis and its role in ulcerative colitis, *Eur. Rev. Med. Pharmacol. Sci.*, 26 (2022) 1156.

[58] A.S. Baldwin Jr, The nf-κb and iκb proteins: New discoveries and insights, *Annu. Rev. Immunol.*, 14 (1996) 649.

[59] M. Islam, T. Murata, M. Fujisawa, R. Nagasaka, H. Ushio, A. Bari, M. Hori, H. Ozaki, Anti-inflammatory effects of phytosteryl ferulates in colitis induced by dextran sulphate sodium in mice, *Br. J. Pharmacol.*, 154 (2008) 812.

[60] M.J. May, S. Ghosh, Signal transduction through NF-κB, *Immunol. Today*, 19 (1998) 80.

[61] E.L. Mills, B. Kelly, L.A. O'Neill, Mitochondria are the powerhouses of immunity, *Nat. Immunol.*, 18 (2017) 488.

[62] A. Verma, S. Pittala, B. Alhozeel, A. Shteinfer-Kuzmine, E. Ohana, R. Gupta, J.H. Chung, V. Shoshan-Barmatz, The role of the mitochondrial protein VDAC1 in inflammatory bowel disease: A potential therapeutic target, *Mol. Ther.*, 30 (2022) 726.

[63] M.J. López-Armada, R.R. Riveiro-Naveira, C. Vaamonde-García, M.N. Valcárcel-Ares, Mitochondrial dysfunction and the inflammatory response, *Mitochondrion*, 13 (2013) 106.

[64] L. Peyrin–Biroulet, A. Bressenot, W. Kampman, Histologic remission: The ultimate therapeutic goal in ulcerative colitis?, *Clin. Gastroenterol. Hepatol.*, 12 (2014) 929.

[65] S. Riley, V. Mani, M. Goodman, S. Dutt, M. Herd, Microscopic activity in ulcerative colitis: What does it mean?, *Gut*, 32 (1991) 174.

[66] B. Lemmens, I. Arijs, G. Van Assche, X. Sagaert, K. Geboes, M. Ferrante, P. Rutgeerts, S. Vermeire, G. De Hertogh, Correlation between the endoscopic and

histologic score in assessing the activity of ulcerative colitis, *Inflamm. Bowel Dis.*, 19 (2013) 1194.
[67] G. Aviello, U. Knaus, Ros in gastrointestinal inflammation: Rescue or sabotage?, *Br. J. Pharmacol.*, 174 (2017) 1704.
[68] A.S. Sreedhar, P. Csermely, Heat shock proteins in the regulation of apoptosis: New strategies in tumor therapy: A comprehensive review, *Pharmacol. Ther.*, 101 (2004) 227.
[69] E. Rath, A. Moschetta, D. Haller, Mitochondrial function—Gatekeeper of intestinal epithelial cell homeostasis, *Nat. Rev. Gastroenterol. Hepatol.*, 15 (2018) 497.
[70] D.N. Jackson, M. Panopoulos, W.L. Neumann, K. Turner, B.L. Cantarel, L. Thompson-Snipes, T. Dassopoulos, L.A. Feagins, R.F. Souza, J.C. Mills, Mitochondrial dysfunction during loss of prohibitin 1 triggers Paneth cell defects and ileitis, *Gut*, 69 (2020) 1928.
[71] J. Kim, R. Gupta, L.P. Blanco, S. Yang, A. Shteinfer-Kuzmine, K. Wang, J. Zhu, H.E. Yoon, X. Wang, M. Kerkhofs, VDAC oligomers form mitochondrial pores to release mtDNA fragments and promote lupus-like disease, *Science*, 366 (2019) 1531.
[72] A. Adhikari, P. Biswas, S. Mondal, M. Das, S. Darbar, A.M. Hameed, A. Alharbi, S.A. Ahmed, S.S. Bhattacharya, D. Pal, S.K. Pal, A smart nanotherapeutic agent for in vitro and in vivo reversal of heavy-metal-induced causality: Key information from optical spectroscopy, *ChemMedChem*, 15 (2020) 420.

CHAPTER 9

Use of Theranostic Nanomaterials in Preclinical Mice Model

9.1. Introduction:

The pressing need for more accurate and robust detection of relevant clinical parameters (i.e. diagnosis) to construct an improved strategy for disease management has led to the concept of a 'theranostic platform'. The term 'theranostics' refers to an integrated cutting-edge platform that can simultaneously perform the diagnosis and therapy of diseases [1, 2]. Nanotechnology is one of the pioneer sectors of science that immensely contribute towards this theranostics aspect [2-4]. The introduction of theranostic nanoagent in the bio-medical field has radically transformed disease management approaches [5, 6]. In this regard, transition metal oxide nanoparticles, especially the manganese and iron oxide NPs, have exhibited the most promising results [7-12]. These NPs exert a therapeutic effect in several ways including the increase in the conventional drug localization (by using the physical stimuli or by emerging as the target specific agent) [3] or their intrinsic physiological properties (ROS generation, radical scavenging activity) [7, 9, 13-16]. On the other hand, the diagnostic function is enabled through deliberate engineering of the physic-chemical (i.e., electronic, magnetic and optical) properties of these NPs to take advantage of the latest imaging techniques (e.g. MRI imaging, X-ray imaging, fluorescence imaging) [9, 17-20].

X-ray is one of the oldest and convenient (i.e. cost effective) imaging techniques widely used in the diagnosis of several clinical disorders. The biomedical X-ray image analysis depends on the differential X-ray absorption capacity (i.e. the contrast) of the biological system. In the attenuation based X-ray imaging, different shades of gray (i.e., combination of black and white) are generated on the X-ray plate or detector due the absorption or scattering of photons by the sample (i.e., biological organ under investigation) when collimated X-ray beam (initial intensity = I_0) penetrates it. The resultant X-ray intensity after penetration (I) can be expressed as, [21]

$$I = I_0 e^{\frac{-x\mu}{\rho}} \quad (9.1)$$

Where I_0 is the initial intensity of the X-ray beam, x denotes the thickness of the sample, μ is the linear X-ray attenuation coefficient (cm^{-1}) of the sample, ρ is the material density (gm/cm^3).

As air and gases (e.g. oxygen, carbon-dioxide, nitrogen) tend not to absorb X-ray due to the absence of radiographic density (i.e. radiolucent), they generate no shadow on X-ray film and appeared black [22, 23]. On the other hand, bones are micro-porous structures made of calcium and tend to absorb the highest amount of X-ray photons resulting in dense white shadow on the X-ray film [24, 25]. The soft tissue and water present in the mammalian body create a varying degree of gray shadow[23, 24, 26, 27] depending on the thickness and the density of the tissue [26, 28]. Many times, the usual contrast of the plain film radiography sufficiently demarks the lesion area. However, there are numerous situations where the use of contrast agents (i.e., materials that accentuate specific structures by increasing the contrast of X-ray image) becomes necessary to reveal lesions (or deformities) with greater certainty and accuracy. For example, demonstration of abdominal and pelvic disease entities by X-ray computed tomography (CT) depends to a large extent on their clear differentiation from the adjacent structure [29]. The optimal delineation of abdominal structures (e.g. pancreas) with contrast agent is a double-edged sword. While the use of positive contrast agents (i.e. that increase the attenuation of X-ray photon) is required to differentiate the abdominal organs from the fluid-filled intestine, they (i.e. positive contrast agents) severely hinder the accuracy of delineation by increasing streak artifacts associated with motion (i.e., respiration, bowel peristalsis, patient movement etc.) [29].

A similar problem is often faced in imaging lungs and brain lobes. In this regard, low density negative contrast agents (i.e., that are X-ray translucent) such as poly-unsaturated fats have been suggested as an alternative [29, 30]. However, side effects (e.g. cramps, mid diarrhea etc.) and contradictions (e.g., acute fulminant pancreatitis, acute cholecystitis, biliary colic, brittle diabetes etc.) limited their use [29]. Therefore, it is of considerable interest to the biomedical community to develop an X-ray contrast agent that is devoid of side effects, has differential

absorptive power, can stay sufficient time in the target organ, can excrete thoroughly and provide accurate delineation of organs.

Here, we are proposing a biocompatible water-soluble nanoparticle (citrate-functionalized Mn_3O_4 NPs; C-Mn_3O_4 NPs) as an alternative X-ray contrast agent. This bio-compatible NPs can generates room temperature reactive oxygen species (ROS; which eventually maintains cellular redox homeostasis by promoting oxidative stress)[16, 31-33] without external stimulation (e.g., light, heat etc.) [6, 34-36]. Our observation reveals that the ROS generated by the NPs are making the site more radiolucent. Using a similar manganese oxide nanoparticle (folate-functionalized Mn_3O_4 NPs; FA-Mn_3O_4 NPs) that lacks the room temperature ROS generation ability as control, we are confirming that the ROS generated by C-Mn_3O_4 NPs are playing the pivotal role that consequently contrasting its shadow in the X-ray film appears less dense than its surroundings. Previously we described the therapeutic efficacy against several diseases like hepatic fibrosis, neuro-degeneration, chronic kidney disease etc. makes C-Mn_3O_4 NPs further suitable as a nano-theranostic platform [15, 16, 35]. To our understanding, this work can serve as a template for development of the newer approaches to enhance the clarity of conventional X-ray radiography along with possibilities of simultaneous therapeutics.

9.2. Results and Discussion:

9.2.1. Organ Specific Therapeutic Nanoparticles Generates Radiolucent Reactive Species for Potential Nanotheranostics using Conventional X-ray Technique in Mammals [37]: Figure 9.1.a and 9.1.b quantify the room temperature ROS generation ability of C-Mn_3O_4 NPs with respect to folate functionalized Mn_3O_4 NPs (FA-Mn_3O_4 NPs). It is evident, from this experiment and also from the previous studies that the FA-Mn_3O_4 NPs cannot generate room temperature ROS [17, 38] whereas C-Mn_3O_4 NPs are capable of generating ROS at room temperature [14, 15, 39, 40]. Using these two contrasting NPs we have studied the effect of ROS in X-ray attenuation. X-ray images of these two NPs were collected using a conventional X-ray machine. Figure 9.1.c exhibits the X-ray images of NPs in centrifuge tube. The brightness or luminosity analysis of the images shows that the

image of FA-Mn_3O_4 NPs more brighter than the other one, which suggests the FA-Mn_3O_4 NPs attenuate more X-ray beam than the C-Mn_3O_4 NPs.

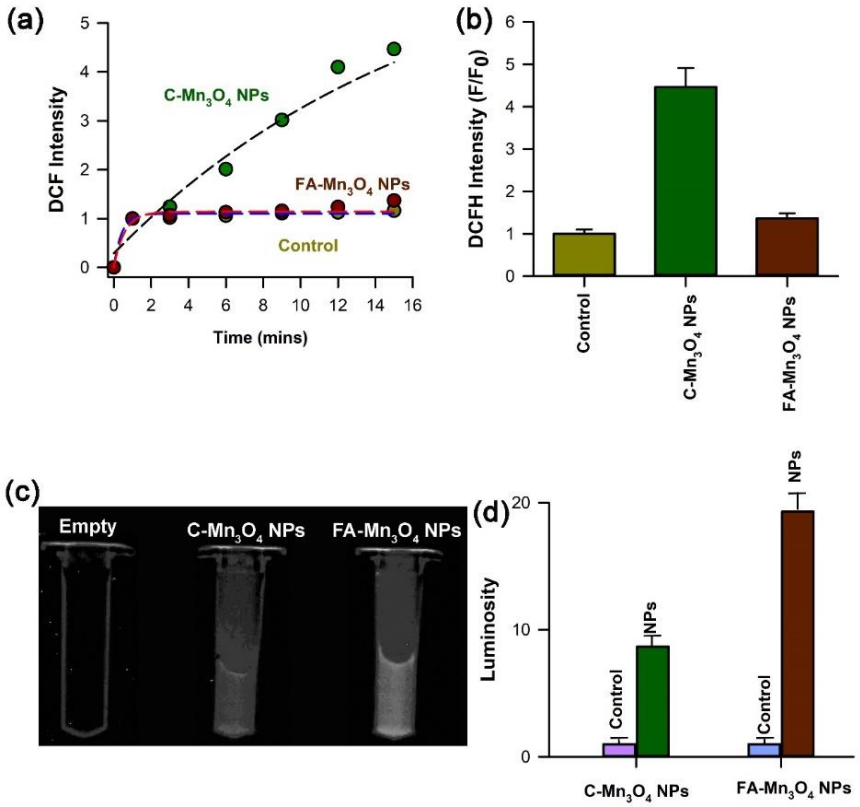

Figure 9.1: *In-vivo ROS generation and X-ray imaging of NPs. (a) DCFH oxidation and ROS production by the C-Mn_3O_4 NPs, FA-Mn_3O_4 NPs at room temperature. (b) Quantification of ROS generation by the C-Mn_3O_4 NPs, FA-Mn_3O_4 NPs at room temperature. (c) X-ray image of the NPs in centrifuge tube. (d) Measured luminosity of the both NPs quantified from the X-ray images.*

As mentioned earlier, the brightness of the images depends on the attenuation of the X-ray, more the attenuation more the brighter image [21]. On the other hand, radiolucency can occur due to the presence of air or gases or due to the X-ray fluorescence phenomenon (XRF) [22, 24]. The contrast analysis (Figure 9.1.d) of the X-ray images for the control and NP treated reveals that FA-Mn_3O_4 NPs attenuate more X-ray than C-Mn_3O_4 NPs. Not only that, the increased radiolucency in the case of C-Mn_3O_4 NPs results from the different ability of ROS generation not due to XRF as both the NPs should generate a comparable amount of XRF because of their similarity in the composition of the chemical core [41, 42]. This observation about ROS increasing radiolucency can be supported by the conventional diagnosis of apical periodontitis. The presence of periodical lucency in the radiograph of a tooth is diagnosed as apical periodontitis.[43-45] Recent studies have shown that ROS activity is increased in the lesion area in apical periodontitis [46-48]. We are

proposing that this ROS presence in the tissue alters the X-ray attenuation properties of it and makes it radiolucent. For evaluating the interaction between ROS and X-ray in physiological milieu, we have used a preclinical mouse model and injected a well-known intercellular ROS generator NPs C-Mn_3O_4 NPs [13, 15, 16, 40] and took the X-ray images of mice in different positions. Previous preclinical studies from our group showed that this C-Mn_3O_4 NP is bio-compatible and do not exert any significant toxic effect on any organs [13, 15, 49].

Figure 9.2.a & 9.2.c show the X-ray image of Swiss albino mouse (in ventral position) before and after injecting (through tail vain) the C-Mn_3O_4 NPs. It is evident that the organ of the animal has become more radiolucent after treating with the NPs. From these images we have taken the lung as our topic of interest and analyzed the differential brightness before and after injecting the NPs. It is important to note that, previously the bio-distribution studies of these NPs in a preclinical mouse model have been done by our group [14, 16]. It is reported that C-Mn_3O_4 NPs can enter into the lung and generate a basal level of ROS that does not cause any kind of toxicity in the lungs [14].

From the detailed histogram analysis of the lungs it has been shown in Figure 9.2.b that for the control lung the brightness level can be divided into three regions (respective regions are shown in the image). On the other hand, the image of the lung after treating with NPs only exhibits two regions of brightness level (Figure 9.2.d) and all the regions are shifted to the left side of the histogram (darker shaded area). In the NP treated lung the intensity first and the second region (darker) have been increased in comparison to the control lungs. For the first region the signal to noise ratio (SNR) is close to 2 and for the second region it is more than 2. As the third region is not present in the treatment group so the SNR for this region is very high (infinite). These findings manifest that after NP treatment there is an alteration in the X-ray attenuation capacity of the tissues i.e. the tissues become more radiolucent. As a result, the unwanted contrasts are eliminated, providing a distinct picture of the lung.

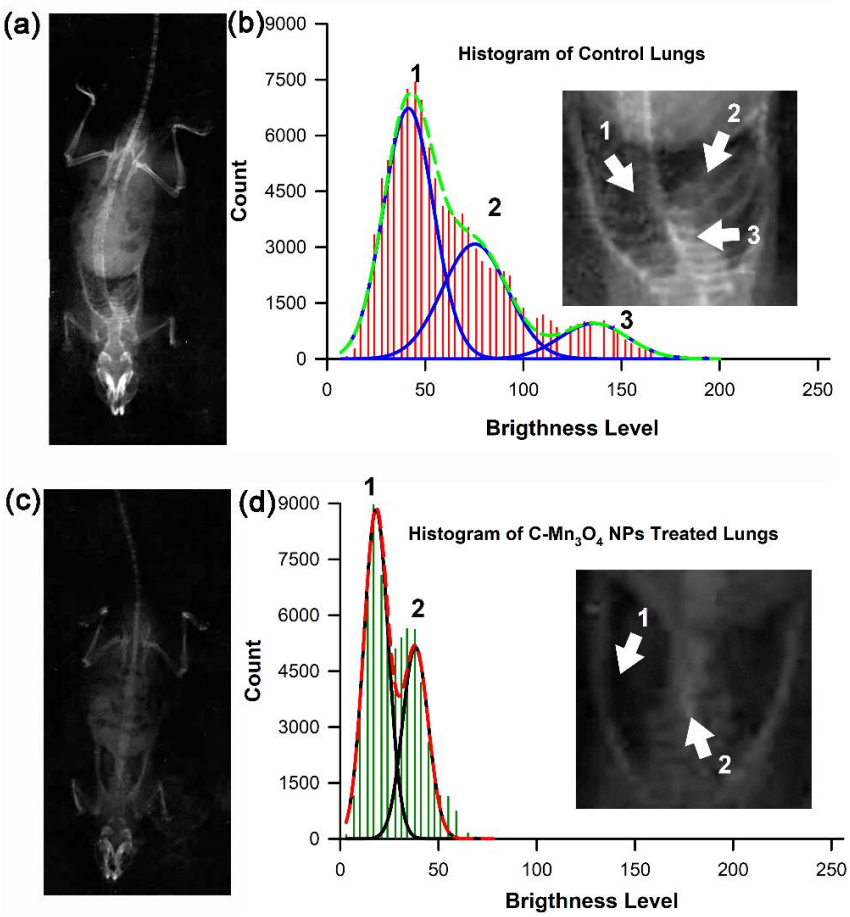

Figure 9.2: *X-ray image of Swiss Albino Mouse in ventral position. (a) X-ray image of mouse before C-Mn_3O_4 NPs treatment. (b) Histogram of control lung. Three different regions of brightness levels are indicated in the X-ray image. X-ray image of control lung (inset). (c) X-ray image of mouse after C-Mn_3O_4 NPs treatment. (b) Histogram of treated lung. Two different regions of brightness levels are indicated in the X-ray image. X-ray image of treated lung (inset).*

So, any change in lung morphology will be more prominent not only that from our previous studies we can state that the ROS (by redox buffering) will also provide therapeutic effect in the said organ [14].

Our next target organ was the brain as brain imaging is still a very complicated and expensive affair. For analyzing the brain with conventional X-ray, we have placed the mouse laterally and take the X-ray image. Figure 9.3.a and 9.3.c show the image of the animal before and after treating with NPs respectively. Here also the radiolucency of the brain for the treated group is much higher than the control one. Histogram analysis of the two images depicts that there are three widely spread different regions of brightness level in the control group whereas for the treatment group image the regions become more constricted to the left side of the histogram i.e. to the darker shades (respective regions are shown in the image, Figure 9.3.b &

9.3.d). The intensity of the less bright regions is higher in the case of the treatment group. The most prominent change in intensity level for brain can be found at the second region. The corresponding SNR for this region is close to 4.

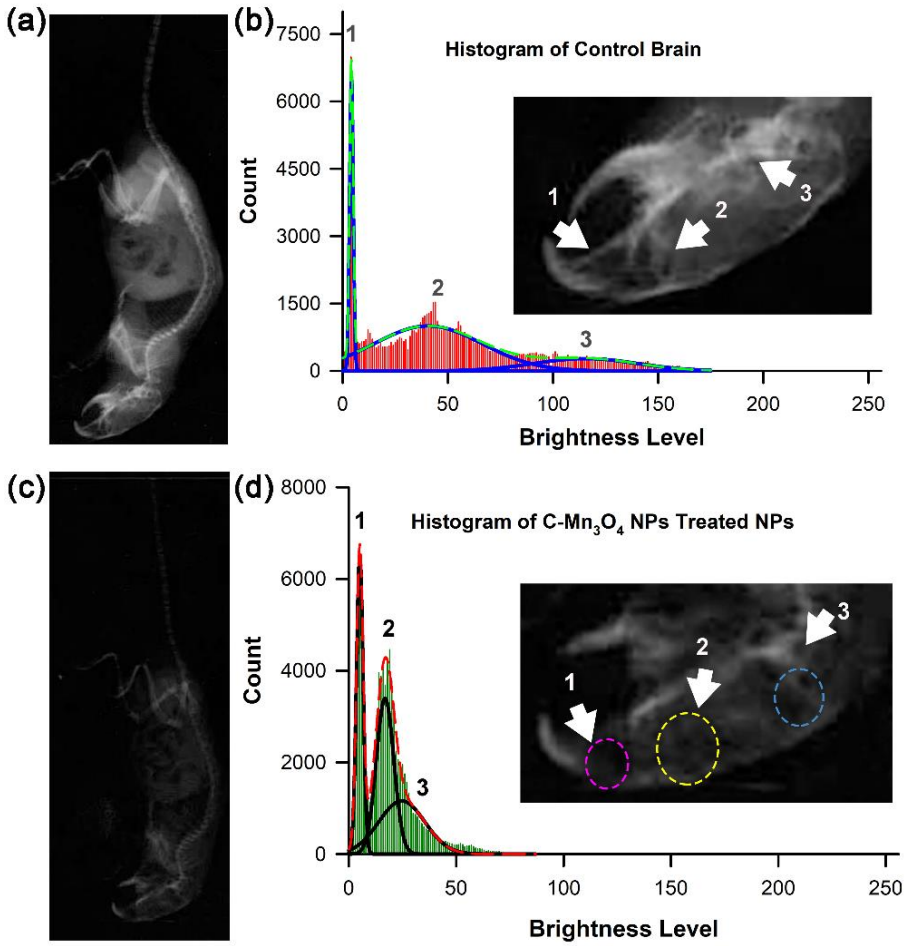

Figure 9.3: *X-ray image of Swiss Albino Mouse in lateral position. (a) X-ray image of mouse before C-Mn_3O_4 NPs treatment. (b) Histogram of control brain. Three different regions of brightness levels are indicated in the X-ray image. X-ray image of control brain (inset). (c) X-ray image of mouse after C-Mn_3O_4 NPs treatment. (b) Histogram of treated brain. Two different regions of brightness levels are indicated in the X-ray image. X-ray image of treated brain (inset). The purple region is the olfactory bulb, the yellow region defines the cerebral cortex and the cyan region denotes the cerebellum.*

Also, careful scanning of the X-ray images of the brain reveals the appearance of different brain lobes such as the purple region is the olfactory bulb, the yellow region defines the cerebral cortex and the cyan region denotes the cerebellum in NPs treated group (Figure 9.3.d).

To further rationalize our results, X-ray images of FA-Mn_3O_4 NPs treated (through tail vain injection) mice were taken. As mentioned earlier, these NPs do not generate the room temperature ROS so this NPs cannot work as a negative contrast agent if our hypothesis is correct [17, 38].

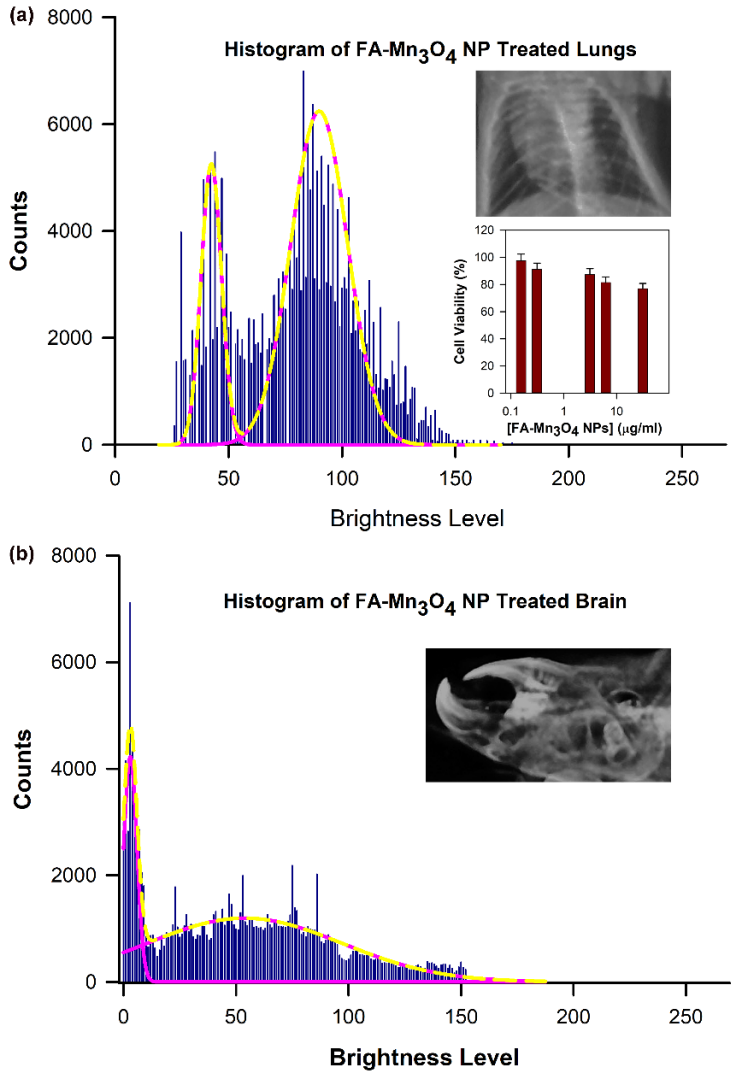

Figure 9.4: *X-ray image of Swiss Albino Mouse treated with FA-Mn_3O_4 NP. (a) Histogram of FA-Mn_3O_4 NP treated lungs. X-ray image of FA-Mn_3O_4 NP treated lungs (upper inset). Cytotoxicity study of FA- Mn_3O_4 NP using HEK cell line (lower inset) (b) Histogram of FA-Mn_3O_4 NP treated brain. X-ray image of FA-Mn_3O_4 NP treated brain (inset).*

X-ray images of lungs and brain of FA-Mn_3O_4 NPs treated mice strongly agree with our hypothesis (Figure 9.4.a and 9.4.b). Figure 9.4.a shows the contrast of lungs after the treatment of FA-Mn_3O_4 NPs. It is evident from the images that the radiolucency is less in the case of FA-Mn_3O_4 NPs treated mice compared to C-Mn_3O_4 NPs treated mice. The histogram analysis of the lungs reveals that two

different widely spread brightness regions are present in the case of FA-Mn_3O_4 NPs treated lungs.

These regions mostly overlap with the control group region as it contains brighter regions (i.e., right side of the histogram). The same trend has been noticed for an X-ray image of FA-Mn_3O_4 NPs treated brain. The histogram of the brain possesses two widely spread regions, one of which mostly falls on the right side of the histogram (Figure 9.4.a & 9.4.b). The different lobes of the brains are not clear enough in FA-Mn_3O_4 NPs treated group compared to the C-Mn_3O_4 NPs treated group. This finding actually indicates that the ROS generated by the C-Mn_3O_4 NPs is making the sites more radiolucent. It has to be noted that FA-Mn_3O_4 NPs also do not show any toxicity as evidenced from our MTT assay (Figure 9.4.a, lower inset). With the help of these results we can identify only the effect of ROS on increased radiolucency eliminating all the contribution generated by the phenomenon of XRF (As mentioned previously, XRF must be similar for two NPs as the core NP is the same) [41, 42].

9.3. Conclusion:

From the outcomes above the experiments, we can conclude that this study is introducing two important findings. This study is the first study to reveal a relationship between the oxidative state of the tissue and the ROS concentration. The *in-vitro* ROS experiment and in-vivo experiments prove that the presence of ROS in soft tissues actively interferes with its X-ray attenuation capacity and allows X-ray to penetrate easily through the tissue, i.e., making them more radiolucent. In summary the C-Mn_3O_4 NPs can act as a theranostics nanoagent by generating ROS that increases the radiolucency of the targeted organ or tissue thereby providing a better X-ray image for accurate diagnosis and also by exerting its therapeutic effect through buffering redox state of the target organ or tissue [14-16, 50]. Furthermore, as ROS is modifying the X-ray attenuation ability of the tissue, so the disorders caused by excess ROS generation can be diagnosed by tracing the alteration of radiolucency of the site promoted by the excess ROS. Additionally, this strategy can be used to avoid unwanted interference of the soft tissues and to enhance the contrast of the image that can help in the diagnosis of complicated bone fracture [24]. Not only that, due to enhancement of contrast any alteration in the organ or

tissue morphology can be detected easily. The future aspect of the study is to visualize other soft tissues like blood vessels, lymph nodes, muscles, etc. and their architectural changes in both disease and normal condition. So, basically this NP can be used as a potent biocompatible negative contrast agent in conventional X-ray imaging techniques.

Reference

[1] K.-T. Chen, K.-C. Wei, H.-L. Liu, Theranostic strategy of focused ultrasound induced blood-brain barrier opening for CNS disease treatment, *Front. Pharmacol.*, 10 (2019) 86.

[2] F. Chen, E.B. Ehlerding, W. Cai, Theranostic nanoparticles, *J. Nucl. Med.*, 55 (2014) 1919.

[3] X. Ma, Y. Zhao, X.-J. Liang, Theranostic nanoparticles engineered for clinic and pharmaceutics, *Acc. Chem. Res.*, 44 (2011) 1114.

[4] K.T. Nguyen, Y. Zhao, Engineered hybrid nanoparticles for on-demand diagnostics and therapeutics, *Acc. Chem. Res.*, 48 (2015) 3016.

[5] J.V. Jokerst, S.S. Gambhir, Molecular imaging with theranostic nanoparticles, *Acc. Chem. Res.*, 44 (2011) 1050.

[6] S. Mondal, R. Ghosh, A. Adhikari, U. Pal, D. Mukherjee, P. Biswas, S. Darbar, S. Singh, S. Bose, T. Saha-Dasgupta, S.K. Pal, In-vitro and microbiological assay of functionalized nano-hybrids to validate their differential efficacy in nano-theranostics: A combined spectroscopic and computational study, *ChemMedChem*, 16 (2021) 3739.

[7] M.H. Cho, E.-S. Choi, S. Kim, S.-H. Goh, Y. Choi, Redox-responsive manganese dioxide nanoparticles for enhanced MR imaging and radiotherapy of lung cancer, *Front. Chem.*, 5 (2017) 109.

[8] X. Qian, X. Han, L. Yu, T. Xu, Y. Chen, Manganese-based functional nanoplatforms: Nanosynthetic construction, physiochemical property, and theranostic applicability, *Adv. Funct. Mater.*, 30 (2020) 1907066.

[9] R. Nandi, S. Mishra, T.K. Maji, K. Manna, P. Kar, S. Banerjee, S. Dutta, S. Sharma, P. Lemmens, K.D. Saha, A novel nanohybrid for cancer theranostics: Folate sensitized Fe_2O_3 nanoparticles for colorectal cancer diagnosis and photodynamic therapy, *J. Mater. Chem. B*, 5 (2017) 3927.

[10] S.M. Dadfar, K. Roemhild, N.I. Drude, S. von Stillfried, R. Knüchel, F. Kiessling, T. Lammers, Iron oxide nanoparticles: Diagnostic, therapeutic and theranostic applications, *Adv. Drug Deliv. Rev.*, 138 (2019) 302.

[11] Z. Shen, T. Chen, X. Ma, W. Ren, Z. Zhou, G. Zhu, A. Zhang, Y. Liu, J. Song, Z. Li, Multifunctional theranostic nanoparticles based on exceedingly small

magnetic iron oxide nanoparticles for T 1-weighted magnetic resonance imaging and chemotherapy, *ACS nano*, 11 (2017) 10992.

[12] M. Kermanian, S. Sadighian, A. Ramazani, M. Naghibi, M. Khoshkam, P. Ghezelbash, Inulin-Coated Iron Oxide Nanoparticles: A Theranostic Platform for Contrast-Enhanced MR Imaging of Acute Hepatic Failure, *ACS Biomater. Sci. Eng.*, 7 (2021) 2701.

[13] A. Adhikari, S. Mondal, T. Chatterjee, M. Das, P. Biswas, R. Ghosh, S. Darbar, H. Alessa, J.T. Althakafy, A. Sayqal, Redox nanomedicine ameliorates chronic kidney disease (CKD) by mitochondrial reconditioning in mice, *Commun. Biol.*, 4 (2021) 1.

[14] A. Adhikari, S. Mondal, M. Das, R. Ghosh, P. Biswas, S. Darbar, S. Singh, A.K. Das, S.S. Bhattacharya, D. Pal, Redox buffering capacity of nanomaterials as an index of ros-based therapeutics and toxicity: A preclinical animal study, *ACS Biomater. Sci. Eng.*, 7 (2021) 2475.

[15] A. Adhikari, S. Mondal, M. Das, P. Biswas, U. Pal, S. Darbar, S.S. Bhattacharya, D. Pal, T. Saha-Dasgupta, A.K. Das, Incorporation of a biocompatible nanozyme in cellular antioxidant enzyme cascade reverses huntington's like disorder in preclinical model, *Adv. Healthc. Mater.*, 10 (2021) 2001736.

[16] S. Mondal, A. Adhikari, R. Ghosh, M. Singh, M. Das, S. Darbar, S.S. Bhattacharya, D. Pal, S.K. Pal, Synthesis and spectroscopic characterization of a target-specific nanohybrid for redox buffering in cellular milieu, *MRS Adv.*, 6 (2021) 427.

[17] S. Mondal, R. Ghosh, A. Adhikari, U. Pal, D. Mukherjee, P. Biswas, S. Darbar, S. Singh, S. Bose, T. Saha-Dasgupta, *In vitro* and microbiological assay of functionalized hybrid nanomaterials to validate their efficacy in nanotheranostics: A combined spectroscopic and computational study, *ChemMedChem*, 16 (2021) 3739.

[18] A. Patel, D. Asik, E.M. Snyder, A.E. Dilillo, P.J. Cullen, J.R. Morrow, Binding and release of feiii complexes from glucan particles for the delivery of t1 mri contrast agents, *ChemMedChem*, 15 (2020) 1050.

[19] Z. Cai, C. Wu, L. Yang, D. Wang, H. Ai, Assembly-controlled magnetic nanoparticle clusters as mri contrast agents, *ACS Biomater. Sci. Eng.*, 6 (2020) 2533.

[20] P. Reineck, A.N. Abraham, A. Poddar, R. Shukla, H. Abe, T. Ohshima, B.C. Gibson, C. Dekiwadia, J.J. Conesa, E. Pereiro, Multimodal imaging and soft X-ray tomography of fluorescent nanodiamonds in cancer cells, *Biotechnol. J.*, 16 (2021) 2000289.

[21] L.E. Cole, R.D. Ross, J.M. Tilley, T. Vargo-Gogola, R.K. Roeder, Gold nanoparticles as contrast agents in X-ray imaging and computed tomography, *Nanomedicine (Lond).*, 10 (2015) 321.

[22] D.G. Lloyd-Jones, Chest X-ray Anatomy, in (2020).

[23] D. Rhinehart, Air and gas in the soft tissues: A radiologic study, *Radiology.*, 17 (1931) 1158.

[24] F. Pfeiffer, M. Bech, O. Bunk, P. Kraft, E.F. Eikenberry, C. Brönnimann, C. Grünzweig, C. David, Hard-X-ray dark-field imaging using a grating interferometer, *Nat. Mater.*, 7 (2008) 134.

[25] B. Kevles, Naked to the bone: Medical imaging in the twentieth century, *Rutgers University Press*, New Brunswick, 1997.

[26] D.G. Lloyd-Jones, Basics of X-ray Physics, in (2016).

[27] N.I.o.B.I.a.B. (NIBIB), X-rays, in (2022)

[28] J.F. Griffith, H.K. Genant, R. Marcus, D. Feldman, D.W. Dempster, M. Luckey, J.A. Cauley (Eds.), Imaging of Osteoporosis, Osteoporosis (Fourth Edition), *Academic Press,* San Diego, 2013, 1505.

[29] D.J. Hamlin, F.A. Burgener, Positive and negative contrast agents in CT evaluation of the abdomen and pelvis, *J. Comput. Assist. Tomogr.*, 5 (1981) 82.

[30] G.N. Baldwin, Computed tomography of the pancreas: Negative contrast medium, *Radiology.*, 128 (1978) 827.

[31] H. Sies, D.P. Jones, Reactive oxygen species (ROS) as pleiotropic physiological signalling agents, *Nat. Rev. Mol. Cell Biol.*, 21 (2020) 363.

[32] H. Sies, Oxidative eustress and oxidative distress: Introductory remarks, Oxidative Stress, *Elsevier*, Amsterdram (2020) 3.

[33] B. D'Autréaux, M.B. Toledano, ROS as signalling molecules: mechanisms that generate specificity in ROS homeostasis, *Nat. Rev. Mol. Cell Biol.*, 8 (2007) 813.

[34] A. Giri, N. Goswami, M. Pal, M.T.Z. Myint, S. Al-Harthi, A. Singha, B. Ghosh, J. Dutta, S.K. Pal, Rational surface modification of Mn_3O_4 nanoparticles to

induce multiple photoluminescence and room temperature ferromagnetism, *J. Mater. Chem. C*, 1 (2013) 1885.

[35] A. Adhikari, N. Polley, S. Darbar, D. Bagchi, S.K. Pal, Citrate functionalized Mn_3O_4 in nanotherapy of hepatic fibrosis by oral administration, *Future Sci. OA*, 2 (2016) FSO146.

[36] N. Polley, S. Saha, A. Adhikari, S. Banerjee, S. Darbar, S. Das, S.K. Pal, Safe and symptomatic medicinal use of surface-functionalized mn_3o_4 nanoparticles for hyperbilirubinemia treatment in mice, *Nanomedicine (Lond.)*, 10 (2015) 2349.

[37] S. Mondal, M. Das, R. Ghosh, S. Singh, S. Darbar, N. Bhattacharyya, A. Adhikari, A.K. Das, S.S. Bhattacharya, D. Pal, Organ-specific therapeutic nanoparticles generates radiolucent reactive species for potential nanotheranostics using conventional X-ray technique in mammals, *Appl. Nanosci.*, 12 (2022) 3851.

[38] S. Mondal, A. Adhikari, M. Das, S. Darbar, A. Alharbi, S.A. Ahmed, S.S. Bhattacharya, D. Pal, S.K. Pal, Novel one pot synthesis and spectroscopic characterization of a folate-Mn_3O_4 nanohybrid for potential photodynamic therapeutic application, *RSC Adv.*, 9 (2019) 30216.

[39] A. Giri, N. Goswami, C. Sasmal, N. Polley, D. Majumdar, S. Sarkar, S.N. Bandyopadhyay, A. Singha, S.K. Pal, Unprecedented catalytic activity of Mn_3O_4 nanoparticles: potential lead of a sustainable therapeutic agent for hyperbilirubinemia, *RSC Adv.*, 4 (2014) 5075.

[40] A. Adhikari, M. Das, S. Mondal, S. Darbar, A.K. Das, S.S. Bhattacharya, D. Pal, S.K. Pal, Manganese neurotoxicity: nano-oxide compensates for ion-damage in mammals, *Biomater. Sci.*, 7 (2019) 4491.

[41] M.J. Pushie, I.J. Pickering, M. Korbas, M.J. Hackett, G.N. George, Elemental and Chemically Specific X-ray Fluorescence Imaging of Biological Systems, *Chem. Rev.*, 114 (2014) 8499.

[42] T.D.T. Oyedotun, X-ray fluorescence (XRF) in the investigation of the composition of earth materials: A review and an overview, *Geol. Ecol. Landsc.*, 2 (2018) 148.

[43] S. Huumonen, D. Ørstavik, Radiological aspects of apical periodontitis, *Endod. Topics.*, 1 (2002) 3.

[44] J.G. Pak, S. Fayazi, S.N. White, Prevalence of periapical radiolucency and root canal treatment: A systematic review of cross-sectional studies, *J. Endod.*, 38 (2012) 1170.
[45] M.N. Chapman, R.N. Nadgir, A.S. Akman, N. Saito, K. Sekiya, T. Kaneda, O. Sakai, Periapical lucency around the tooth: Radiologic evaluation and differential diagnosis, *Radiographics.*, 33 (2013) E15.
[46] A. Georgiou, P.C. Ulloa, G. Van Kessel, W. Crielaard, S. Van der Waal, Reactive oxygen species can be traced locally and systemically in apical periodontitis: A systematic review, *Arch. Oral Biol.*, (2021) 105167.
[47] P. Hernández-Ríos, P.J. Pussinen, R. Vernal, M. Hernández, Oxidative stress in the local and systemic events of apical periodontitis, *Front. Physiol.*, 8 (2017) 869.
[48] A. Jakovljevic, M. Andric, M. Miletic, K. Beljic-Ivanovic, A. Knezevic, S. Mojsilovic, J. Milasin, Epstein-Barr virus infection induces bone resorption in apical periodontitis via increased production of reactive oxygen species, *Med. Hypotheses*, 94 (2016) 40.
[49] A. Adhikari, S. Mondal, M. Das, R. Ghosh, P. Biswas, S. Darbar, S. Singh, A.K. Das, S.S. Bhattacharya, D. Pal, Redox buffering capacity of nanomaterials as an index of ROS-based therapeutics and toxicity: a preclinical animal study, *ACS Biomater. Sci. Eng.*, 7 (2021) 2475.
[50] A. Adhikari, P. Biswas, S. Mondal, M. Das, S. Darbar, A.M. Hameed, A. Alharbi, S.A. Ahmed, S. S. Bhattacharya, D. Pal, A smart nanotherapeutic agent for in vitro and in vivo reversal of heavy-metal-induced causality: Key information from optical spectroscopy, *ChemMedChem*, (2020) 420.

List of Publications

A. In Peer Reviewed International Journal

1. **S. Mondal,** M. Das, R. Ghosh, M. Singh, A. Adhikari, S. Darbar, A. K. Das, S. S. Bhttacharya, D. Pal, D. Bhattacharyya, A. S. A. Ahmed, A. K. Mallick, M. M. Al-Rooqi, Z. Moussa, S. A. Ahmed and S. K. Pal
   "Chitosan functionalized Mn_3O_4 nanoparticles counteracts ulcerative colitis in mice through modulation of cellular redox state"
   Communications Biology 6 (2023) 647.

2. **S. Mondal,** M. Das, R. Ghosh, S. Singh, S. Darbar, N. Bhattacharyya, A. Adhikari, A. K. Das, S. Sankar Bhattacharya, D. Pal, A. K. Mallick and S. K. Pal
   "Organ Specific therapeutic nanoparticles generates radiolucent reactive species for potential nanotheranostics using conventional X-Ray technique in mammals"
   Applied Nanoscience 12 (2022) 3851.

3. **S. Mondal,** N. Pan, R. Ghosh, A. Bera, D. Mukherjee, T.K. Maji, A. Adhikari, S. Ghosh, C. Bhattacharya and S. K. Pal
   "Interaction of a jaundice marker molecule with redox modulatory nano-hybrid: A combined electrochemical and spectroscopic study towards development of a theranostics tool"
   ChemMedChem 17 (2022) e202100660.

4. **S. Mondal,** S. Bayan, R. Ghosh, M. Das, A. Adhikari, D. Mukherjee, A. K. Mallick, S. K. Ray and S. K. Pal
   "Functionalised two dimension carbon nitride nanodots detect and reverse lead toxicity in the physiological milieu"
   ACS Applied Materials & Interfaces 14 (2022) 27002.

5. **S. Mondal,** R. Ghosh, A. Adhikari, U. Pal, D. Mukherjee, P. Biswas, S. Darbar, S. Singh, S. Bose, T. Saha-Dasgupta, S. K. Pal
   "In-vitro and microbiological assay of functionalized hybridnanomaterials to validate their efficacy in nano-theranostics: A combined spectroscopic and computational study" *ChemMedChem* 16 (2021) 1.

6. **S. Mondal,** A. Adhikari, R. Ghosh, M. Singh, M. Das, S. Darbar, S. S. Bhattacharya, D. Pal and S. K. Pal
"Synthesis and spectroscopic characterization of a target-specific nanohybrid for redox buffering in cellular milieu"
MRS Advances 6 (2021) 1.

7. **S. Mondal,** A. Adhiakari, M. Das, S. Darbar, A. Alharbi, S. A. Ahmed, S. S. Bhattacharya, D. Pal, and S. K. Pal
"Novel one pot synthesis and spectroscopic characterization of folate-Mn_3O_4 nanohybrid for potential photodynamic therapeutic application"
RSC Advances 9 (2019) 30216.

8.* L. Roy, A. Banerjee, N. Bhattacharyya, **S. Mondal,** R. Ghosh, M. Das, R. T. Goswami, K. Bhattacharya, A. K. Mallick, A. Chattopadhyay and S. K. Pal

"Radiolucency in conventional X-ray imaging leads potential diagnosis of hypoxia in human organ"
Journal of Medical Case Reports 4 (2023) 2261.

9.* A. Banerjee, R. Ghosh, S. Singh, A. Adhikari, **S. Mondal**, L. Roy, S. Midya, S. Mukhopadhyay, S. S. Chowdhury, S. Chakraborty, R. Das, J. H. Al-Fahemi, Z. Moussa, A. K. Mallick, A. Chattopadhyay, S. A. Ahmed and S. K. Pal

"Spectroscopic studies on a natural biomarker for the identification of origin and quality of tea extracts for the development of a portable and field deployable prototype"
Spectrochimica Acta Part A: Molecular and Biomolecular Spectroscopy 299 (2023) 122842.

10.* A. Adhikari, V. K. Bhutani, **S. Mondal,** M. Das, S. Darbar, R. Ghosh, N. Polley, A. K. Das, S. S. Bhattacharya, D. Pal, A. K. Mallick and S. K. Pal

"A nanoceutical agent for chemoprevention of bilirubin encephalopathy"

Pediatric Research 93 (2023) 827.

11.* A. Banerjee, N. Bhattacharyya, R. Ghosh, S. Singh, A. Adhikari, **S. Mondal,** L. Roy, A. Bajaj, N., Ghosh, A. Bhushan, M. Goswami, A. S. A. Ahmed, Z. Moussa, P. Mondal, S. Mukhopadhyay, D. Bhattacharyya, A. Chattopadhyay, S. A. Ahmed, A. K. Mallick and S. K. Pal

"Non-invasive estimation of hemoglobin, bilirubin and oxygen saturation of neonates simultaneously using whole optical spectrum analysis at point of care"
Scientific Reports 13 (2023) 2370.

12.* P. Biswas, A. Adhikari, U. Pal, **S. Mondal,** D. Mukherjee, R. Ghosh, R. J. Obaid, Z. Moussa, S. S. Choudhury, S. A. Ahmed, R. Das and S. K. Pal

"A combined spectroscopic and molecular modeling study on structure-function-dynamics under chemical modification: Alpha-chymotrypsin with formalin preservative"
Frontiers in Chemistry 10 (2022) 1.

13.* A. Banerjee, D. Mukherjee, A. Bera, R. Ghosh, **S. Mondal,** S. Mukhopadhyay, R. Das, H. M. Altass, S. S. A. Natto, Z. Moussa, S. A. Ahmed, A. Chattopadhyay and S. K Pal

"Molecular co-localization of multiple drugs in a nanoscopic delivery vehicle for potential synergistic remediation of multi-drug resistant bacteria"
Scientific Reports 12 (2022) 18881.

14.* M. Das, **S. Mondal,** R. Ghosh, P. Biswas, Z. Moussa, S. Darbar, S. A. Ahmed, A. K. Das, S. S. Bhattacharya, D. Pal, A. K. Mallick, P. Chakrabarti, J. K. Kundu, A. Adhikari and S. K. Pal

"A nano erythropoiesis stimulating agent (Nano-ESA) for the treatment of anemia and associated disorders"
iScience 25 (2022) 105021.

15.* R.Ghosh, **S. Mondal,** D. Mukherjee, A. Adhikari, M. Bhattacharyya and S. K. Pal

"Inorganic-organic synergy in nano-hybrids makes a new class of drug with targeted delivery: Glutamate functionalization of iron nanoparticles for potential bone marrow delivery and x-ray dynamic therapy"
Current Drug Delivery 19 (2022) 991.

16.* R. Ghosh, **S. Mondal,** D. Mukherjee, A. Adhikari, S. A. Ahmed, R. A. Alsantali, A.S. Khder, H. M. Altass, Z. Moussa, R. Das, M. Bhattacharyya and S. K .Pal

"Oral drug delivery using a polymeric nano carrier: Chitosan Nanoparticles in the delivery of rifampicin"
Materials Advances 3 (2022) 4622.

17.* R. Ghosh, S. Singh, D. Mukherjee, **S. Mondal,** M. Das, U. Pal, A. Adhikari, A. Bhushan, S. Bose, S. S. Bhattacharyya, D. Pal, T. Saha-Dasgupta, M. Bhattacharyya, D. Bhattacharyya, A. K. Mallick, R, Das and S. K. Pal

"Host-assisted delivery of a model drug to genomic DNA: Key information from ultrafast spectroscopy and *in silico* study"
ChemBioChem 23 (2022) e202200109.

18.* N. Bhattacharyya, S. Singh, D. Mukherjee, N. Das, A. Chatterjee, A. Halder, A. Adhikari, **S. Mondal**, D. Shikha, A. Bajaj, P. Mondal, P. Chakrabarti, A. K. Mallick and S. K. Pal

"Picosecond-resolved fluorescence resonance energy transfer (fret) in diffuse reflectance spectroscopy explores biologically relevant hidden molecular contacts in a non-invasive way"
Physical Chemistry Chemical Physics 24 (2022) 6176.

19.* P. Biswas, U. Pal, A. Adhikari, **S. Mondal,** D. Mukherjee, R Ghosh, T. Saha-Dasgupta, S. S. Chowdhury, R. Das and S. K. Pal

"Essential loop dynamics modulates catalytic activity in α-Chymotrypsin"
Chemistry Select 7 (2022) e202104262.

20.* A. Adhikari, **S. Mondal,** T. Chatterjee, M. Das, P. Biswas, R. Ghosh, S. Darbar, H. Alessa, J. T. Althakafy, A. Sayqal, S. A. Ahmed, S. K.Pal

"Redox nanomedicine ameliorates chronic kidney disease (CKD) by mitochondrial reconditioning in mice"
Communications Biology 4 (2021) 1.

21.* A. Adhikari**, S. Mondal,** M. Das, R. Ghosh, P. Biswas, S. Darbar, S. Singh, A. K. Das, S. S. Bhattacharya, D. Pal, A.K. Mallick, S. K. Pal

"Redox buffering capacity of nanomaterials as an index of ROS-based therapeutics and toxicity: A preclinical animal study"
ACS Biomaterials Science. & Engineering 7 (2021) 2475.

22.* S. Bayan, A. Adhikari, U. Pal, R. Ghosh, **S. Mondal,** S. Darbar, T. Saha-Dasgupta, S. K. Ray, S. K. Pal

"Development of triboelectroceutical fabrics for potential applications in self-sanitizing personal protective equipment"
ACS Applied Bio Materials 4 (2021) 5485.

23. A. Adhikari U. Pal, S. Bayan, **S. Mondal**, R. Ghosh, S. Darbar, T. Saha-Dasgupta, S. K. Ray, S. K. Pal

"Nanoceutical fabric prevents COVID-19 spread through expelled respiratory droplets: a combined computational, spectroscopic, and antimicrobial study"
ACS Applied Bio Materials 4 (2021) 5471.

24.* A. Adhikari, **S. Mondal,** M. Das, P. Biswas, U. Pal, S. Darbar, S. S. Bhattacharya, D. Pal, T. Saha-Dasgupta, A. K. Das, A. K. Mallick and S. K. Pal

"Incorporation of a biocompatible nanozyme in cellular antioxidant enzyme cascade reverses huntington like disorder in preclinical model"
Advanced Healthcare Materials (2020) 2001736.

25.* A. Adhikari, S. Darbar, M. Das, **S. Mondal,** S. S. Bhattacharya, D. Pal and S. K. Pal

"Rationalization of a traditional liver medicine using systems biology approach and its evaluation in preclinical trial"
Computational Biology and Chemistry 84 (2020) 107196.

26.* A. Adhikari, P. Biswas, **S. Mondal,** M. Das, S. Darbar, A. M. Hameed, A. Alharbi, S. A. Ahmed, S. S. Bhattacharya, D. Pal and S. K. Pal

"Smart nanotherapeutic agent for in vitro and in vivo reversal of heavy metal induced causality: Key information from optical spectroscopy"
ChemMedChem 15 (2020) 420.

27.* A. Adhikari, **S. Mondal**, S. Darbar, and S. K. Pal

"Role of nanomedicine in redox mediated healing at molecular level"
Biomolecular Concepts 10 (2019) 160.

28.* A. Adhiakari, M. Das, **S. Mondal,** S. Darbar, A. K. Das, S. S. Bhattacharya, D. Pal and S. K. Pal,

"Manganese neurotoxicity: Nano-oxide compensates the ion-damage in mammals"

Biomaterials Science 7 (2019) 4491.

B. Conference Proceeding/Symposium

1. **S. Mondal,** A. Adhikari, M. Singh, R. Ghosh, M. Goswami, P. Biswas and S. K. Pal

"Spectroscopic study on the interaction of Co^{2+} with citrate-Mn_3O_4: Towards the development of nanotherapy against cobalt toxicity"

Materials Today: Proceedings 43 (2020) 3692.

2.* R. Ghosh, S. Singh, A. Adhikari, **S. Mondal,** D. Mukherjee, N. Bhattacharyya, A. Halder, M. Bhattacharyya and S. K. Pal

"Synthesis and characterization of a nano-formulation for long lasting sterilization effect",

Materials Today: Proceedings 80 (2023) 1846.

3.* P. Biswas, A. Adhikari, **S. Mondal,** M. Das, S. S. Bhattacharya, D. Pal, S. S. Choudhury and S. K. Pal

"Synthesis and spectroscopic characterization of a zinc oxide-polyphenol nanohybrid from natural resources for enhanced antioxidant activity with less cytotoxicity"

Materials Today: Proceedings 43 (2020) 3481.

**Marked publications are not included in the Thesis*

List of National/International Conference/Workshop

1. **Oral Presentation** at "BOSE FEST – 2021", (Virtual).
2. **Oral presentation** delievered at "2020 IEEE International Conference on Nanoelectronics, Nanophotonics, Nanomaterials, Nanobioscience & Nanotechnology - (5NANO 2020)", (Virtual).
3. **Oral presentation** delievered at "BeSCHON – 2020", Kolkata, India.
4. **Poster presentation** delivered at "International Conference on Nano Science and Technology – 2020" Kolkata, India.
5. **Poster presentation** delivered at "BOSE FEST – 2020" Kolkata, India.